

**DEVELOPMENT AND  
CHARACTERIZATION OF BIOMEDICAL  
POROUS Ti–Nb–Ag ALLOY THROUGH  
POWDER METALLURGY METHOD**

Thesis

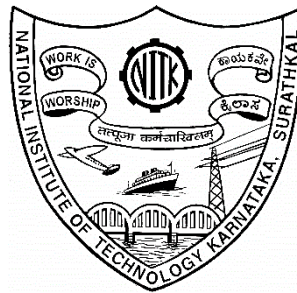
Submitted in partial fulfilment of the requirements for the degree of

**DOCTOR OF PHILOSOPHY**

by

**SHIVARAM M.J**

**(145038MT14F08)**



**DEPARTMENT OF METALLURGICAL AND**

**MATERIALS ENGINEERING**

**NATIONAL INSTITUTE OF TECHNOLOGY KARNATAKA**

**SURATHKAL, MANGALORE, INDIA - 575025**

**October-2021**




## DECLARATION

I hereby *declare* that the Research Thesis entitled “**Development and Characterization of Biomedical porous Ti–Nb–Ag alloy through Powder Metallurgy Method**” which is being submitted to the National Institute of Technology Karnataka, Surathkal in partial fulfillment of the requirements for the award of the Degree of **Doctor of Philosophy** in the Department of Metallurgical and Materials Engineering, is a *bonafide report of the research work carried out by me*. The material contained in this Research Thesis has not been submitted to any University or Institution for the award of any degree.

Register Number : **145038MT14F08**

Name of the Research Scholar : **Shivaram M. J.**

Signature of the Research Scholar : 

Place: NITK, Surathkal

Date:

## CERTIFICATE

This is to *certify* that the Research Thesis entitled “**Development and Characterization of Biomedical porous Ti–Nb–Ag alloy through Powder Metallurgy Method**” submitted by **Mr. Shivaram M J (Register Number: 145038MT14F08)** as the record of the research work carried out by him, is *accepted as the Research Thesis submission* in partial fulfillment of the requirements for the award of degree of **Doctor of Philosophy**.

### Research Guides

**Dr. Shashi Bhushan Arya**

Assistant Professor

Department of Metallurgical

and Materials Engineering

**Prof. Jagannatha Nayak**

Professor

Department of Metallurgical

and Materials Engineering

Chairman - DRPC

Date:



## ACKNOWLEDGEMENT

I would like to express my deep heart felt feelings of gratitude to my guides **Dr. Shashi Bhushan Arya**, Assistant Professor and **Dr. Jagannatha Nayak**, Professor, Department of Metallurgical and Materials Engineering for their excellent guidance and support throughout the work. Both of them have been an excellent mentor and a constant source of energy, ideas and enthusiasm. I cannot thank them enough for the support they have given me and for their patience as I worked through this thesis.

With sense of pride and dignity, my largest appreciation to my Research Progress Assessment Committee members, **Dr. Mrityunjay Doddamani**, Department of Mechanical Engineering, NITK and **Dr. Ravishankar K. S.**, Department of Metallurgical and Materials Engineering, NITK, for their remarkable support, thoughtful comments, and constructive suggestions on the research work.

I owe a very important debt to the great souls that unite to accomplish this work: **Prof. Bharat Bhushan Panigrahi**, **Dr. Rahul B Mane**, Department of Materials Science and Metallurgical Engineering, Indian Institute of Technology Hyderabad, Telangana and **Dr. M R Ramesh**, Department of Mechanical Engineering, NITK, and their research team for valuable aid of different facilities required for this work.

I also thank for extending generous support to all the Head of Department: **Prof. K. N. Prabhu**, **Prof. Jagannath Nayak**, **Prof. Udaya Bhat**, and **Prof. S. Anandhan**, and entire faculty of Department of Metallurgical and Materials Engineering, NITK, in the course of this work.

I am thankful to Ministry of Human Resource Development, New Delhi, and NITK for their financial assistance to conduct my research work in the form of contingency and for the research fellowship.

I am pleased and thankful to Alumni Association, NITK, for granting International Travel Support scheme, for their financial support to present part of this research work entitled, 'Influence of Ball milling times on mechanical properties of

porous Ti-Nb-Ag alloy, in *International Conference on "Powder Metallurgy and Particulate Technology" (IPMPC-19)*, at Paris, France from 21-24<sup>th</sup> September 2017.

I would like to show my greatest appreciation to the technicians and non-teaching staffs in Department of Metallurgical and Materials Engineering, without their timely boundless help, this work or journey was dreadful. With immense pleasure I record my gratitude to **Mrs. Sharmila Dinesh** for her constant support in all clerical works, **Mrs. Vinaya D. Shettigar, Mr. Sundra Shettigar, Mr. Dinesha Shettigar, Mr. Ismail, Mr. Sachin, Mr. Yashvanth K. S and Mr. Satish P** for their kind assistance in laboratories and office.

My special appreciation to my colleagues who had been a giant shoulder to enjoy journey with meticulous assistance and technical discussions and cooperation of **Dr. Bhaskan T, Mr. Ajmal, Dr. Melby Chacko, Mr. Vinay B. U, Mr. Freddy Jems, Mr. Atul singh, Ms. Ranju Kumari, Ms. Preethi.**

I'm always grateful to my well-wishers for their continuous support Mr. Kemparaju C. R, Mr. Vinay, Mr. Nuthan S, Mr. Sooraj Kuamr, Mrs. Roopa Ms. Priya, Mr. Anand babu, Mr. Harshvardhan, Dr. Sharath P. C, Dr. Mahantesh matapathi, Dr. Mallikarjuna Balichakra, Dr. Gopi K.R, Dr. Gajanan Anne, Dr. Bharath kumar, Dr. Basavaraj Nainegali, Dr. Sachin Kumar B, Mr. Pavankumar R. Sondar, Mr. Gurudath B and Mr. Chethan Kumar B are only a few among them.

I am indeed delighted to extend my honest thanks to my all well-wishers for their love and affection, who kept my spirits high during my research work, Mr. Shashi Kumar K. S, Eranna H, Ramadas, Rajesh T. R, Dr. Sangamesh Rajole, Mrs. Suma, Mrs. Thara, Mr. Pradeep Kumar D, Dr. Nagaraju M. K, Mrs. Latha and Ms. Divya for their support, love and affection.

I take this opportunity to thank all my teachers, Mrs. Nagarathamma, Mrs. Saraswathamma, Mr. Kagerappa, Mrs. Shailaja, Mrs. Indira, Mr. D. Anandappa, Dr. Girish C, and to everyone who has passed on their knowledge to me.

The dissertation must surely bear the imprint of the prayers, sacrifices made, love, and affection showered on me by my family members. It is my esteemed duty to reserve my high regards to my grandfather **Mr. Siddalingaih, Mrs. Doddamma**, my dad, Mr. Jayaramaiah, my mom Mrs. Jayamma H. H and my brother Mr. Rajesh., along with my family members (Mr. Krishnamurthy, Mrs. Gangamma, Mr. Basavarju, Mr. Jayamma) and dedicate this work to them for believing in me that I would accomplish this work.

**SHIVARAM M.J**

*DEDICATED*  
*TO*  
*MY BELOVED*  
*GRAND PARENTS*  
*AND*  
*PARENTS*

## ABSTRACT

One of the major concerns in biomedical implants is the mismatch in the elastic modulus of the implant material and the bones leading to stress shield effect. The present investigation focuses on the development of low elastic modulus, porous Ti–Nb–Ag alloy through powder metallurgy (PM) space holder method.

Elemental powders of Ti, Nb and Ag with varying amounts were mixed with the powders of space holder ( $\text{NH}_4\text{HCO}_3$ ). These powders are blended using ball milling for 1h, 5h, 10 h, 15 h, and 20 h. The powders were compacted by applying a load of 500 MPa. These compacts were initially calcinated at 200°C for 2 h to remove the space holder and then finally sintered at 1200°C for 3 h under ultrahigh vacuum sintering furnace. Microstructure of the porous alloys exhibited micropores, macropores and interconnected pore structures. It was found that with increasing ball milling time, the porosity and pore size decreased while the mechanical properties and electrochemical corrosion properties [in simulated body fluid (SBF)] were improved. XRD results indicated formation of small amount  $\alpha''$  martensite phase and intermetallic compound of  $\text{Ti}_2\text{Ag}$  along with the  $\alpha$  and  $\beta$  phases.

Role of Nb was studied with various Nb content ( $x = 25, 30$  and  $35$  wt%) in Porous Ti– $x$ Nb–5Ag alloys. Increase in Nb content led to decrease in porosity, reduction in both the elastic modulus and compression strength but improved corrosion resistance in SBF.

Samples with different porosity levels (22% to 68%) with pore size ranging from 98  $\mu\text{m}$  to 130  $\mu\text{m}$  were fabricated by varying the amount of space holder. Increase in porosity further leads to the reduction in the compression strength, elastic modulus and also corrosion resistance in SBF.

Tribocorrosion behaviour of porous Ti–20Nb–5Ag alloys were evaluated in SBF solution by applying various loads (0 N, 1N, 5N, 10N). The results indicate that increasing the applied loads lead to a material degradation and corrosion.

The porous Ti–20Nb–5Ag samples are alkali-heat treated using 5 M NaOH, to aid the hydroxyapatite formation in SBF. Alkali treated samples were immersed in SBF for 7, 14 and 21 days at 37 °C to examine the hydroxyapatite formation. The Ca/P ratio confirmed the formation of adequate hydroxyapatite coating. Further, the electrochemical corrosion test was conducted on hydroxyapatite coated porous alloy in SBF. The hydroxyapatite coated porous

alloy after 21 days of immersion in SBF shows excellent corrosion resistance. The cytotoxicity test was conducted on the porous Ti–20Nb–5Ag alloy using MG-63 human osteoblast cells by incubating for 1, 4, and 7 days. The results indicated excellent cell growth and proliferation on porous alloy surface. Cytotoxicity test confirms that developed porous sample has non-toxic in nature and highly suitable for implant application.

**Keywords:** Porous alloys, Powder Metallurgy, Microstructure, Mechanical Properties, Electrochemical corrosion behavior, Tribocorrosion Properties, Surface modification, Hydroxyapatite formation, MG-63 osteoblast human cells.

# CONTENTS

---

<b>ACKNOWLEDGEMENT</b>	
<b>ABSTRACT</b>	
<b>CONTENTS</b>	i
<b>LIST OF FIGURES</b>	v
<b>LIST OF TABLES</b>	xii
<b>NOMENCLATURE</b>	xv
<b>CHAPTER 1</b> .....	1
<b>1. INTRODUCTION</b> .....	1
1.1 Objectives of the present work .....	5
1.2 Organization of the present work .....	5
<b>CHAPTER 2</b> .....	7
<b>2. LITERATURE REVIEW</b> .....	7
2.1 Introduction of biomaterials .....	7
2.2 Design consideration for developing biomaterials .....	7
2.2.1 Biocompatibility .....	8
2.2.2 Osseointegration .....	8
2.2.3 Mechanical properties .....	8
2.2.4 Corrosion behavior .....	9
2.2.5 Tribocorrosion properties .....	9
2.3 Currently used metallic biomaterials .....	10
2.4 Titanium and its alloys for biomedical applications .....	12
2.5 Metallic porous alloys for biomedical application .....	19
2.5.1 Processing methods of porous Ti and its alloys .....	21
2.5.1.1 Liquid state processing .....	21
2.5.1.2 Solid state sintering processing .....	22
2.5.2 Powder metallurgy space holder method .....	23
2.5.2.1 Powder selection and preparation .....	24

2.5.2.2	Blending .....	25
2.5.2.3	Compaction .....	25
2.5.2.4	Space holder removal .....	26
2.5.2.5	Sintering process .....	26
2.5.3	Advantages and disadvantages of PM method .....	27
2.6	Development and characterization of porous Ti alloys .....	27
2.6.1	Microstructural and Mechanical properties .....	27
2.6.2	Electrochemical corrosion behavior .....	32
2.6.3	Tribocorrosion properties .....	35
2.6.4	Surface modification and hydroxyapatite formation .....	37
2.6.4.1	Surface modification technique .....	38
2.6.4.2	Chemical methods .....	39
2.6.4.3	Hydroxyapatite formation .....	41
2.6.5	Cytotoxicity performance .....	48
2.7	Motivation .....	51
<b>CHAPTER 3 .....</b>		<b>53</b>
<b>3.</b>	<b>EXPERIMENTAL DETAILS .....</b>	<b>53</b>
3.1	Raw materials .....	53
3.2	Synthesis of Ti–Nb–Ag alloy powder using ball mill .....	55
3.3	Preparation of porous Ti-Nb-Ag alloy through powder metallurgy .....	55
3.4	Characterization of developed porous Ti–Nb–Ag alloy .....	56
3.4.1	Porosity, density and mechanical properties .....	56
3.4.2	Electrochemical corrosion properties .....	56
3.4.3	Tribocorrosion behavior .....	57
3.4.4	Surface modification through alkali treatment .....	58
3.4.5	Evaluation of hydroxyapatite formation .....	58
3.4.6	In-vitro corrosion behavior .....	59
3.4.7	Cytotoxicity performance .....	59
3.5	Microstructural analysis .....	60



<b>CHAPTER 4 .....</b>	<b>63</b>
<b>4. RESULTS AND DISCUSSION .....</b>	<b>63</b>
4.1 Effect of ball milling times on sintered porous Ti–20Nb–5Ag alloys.....	63
4.1.1 Microstructure analysis of ball milled powders.....	63
4.1.2 XRD analysis .....	70
4.1.3 Microstructure analysis of sintered porous alloys.....	75
4.1.4 XRD analysis .....	78
4.1.5 Mechanical properties of sintered porous alloys .....	85
4.1.6 In vitro electrochemical corrosion properties .....	86
4.2 Influence of addition of various Nb content on sintered porous Ti–xNb–5Ag alloys .....	91
4.2.1 Synthesis and characterization of Ti–xNb–5Ag alloys powders .....	91
4.2.2 XRD analysis .....	94
4.2.3 Microstructural characterization of sintered porous alloys .....	95
4.2.4 Mechanical properties of sintered porous alloys .....	100
4.2.5 Role of Nb content on in-vitro corrosion study .....	101
4.3 Effects of addition of various amount of space holder material .....	109
4.3.1 Microstructural analysis .....	109
4.3.2 Mechanical properties porous alloys .....	112
4.3.3 Effect of porosity on electrochemical corrosion properties .....	115
4.4 Tribocorrosion properties of porous Ti–20Nb–5Ag alloy under various applied loads .....	121
4.4.1 Microstructure of the porous Ti–20Nb–5Ag alloy .....	121
4.4.2 Effect of applied loads on open circuit potential .....	122
4.4.3 Electrochemical corrosion study under the applied load .....	123
4.4.4 Mechanism of material removal from porous alloy .....	126
4.5 Surface modification, Surface bioactivity and cytotoxicity behavior .....	131
4.5.1 Surface modification via alkali treatment .....	133
4.5.2 Surface bioactivity in simulated body fluid .....	123
4.5.3 AFM and XPS analysis of analysis of hydroxyapatite coated surface..	138

4.5.4 Effect of hydroxyapatite coating on the electrochemical corrosion behavior .....	142
4.5.5 Cytotoxicity performance .....	149
<b>5. CONCLUSIONS .....</b>	<b>155</b>
<b>REFERENCES</b>	<b>159</b>
<b>LIST OF PUBLICATIONS</b>	
<b>BIO-DATA</b>	

## LIST OF FIGURES

<b>Fig. No.</b>	<b>Contents</b>	<b>Page No.</b>
1.1	Various implant materials	1
2.1	Various causes for failure of biomaterials implants which leads to revision surgery	11
2.2	Schematic representation of the effect of alloying elements on phase diagrams of titanium alloys	13
2.3	Typical Ti–Nb phase diagram	15
2.4	Schematic diagram of sintering behaviour and formation of Kirkendall type pore in the Ti–Nb alloy	17
2.5	The comparison of elastic modulus of various Ti–based alloys with human bone	18
2.6	Schematic representation of stress shielding and stress shielding zone at hip joint replacement	19
2.7	A comparison of the stress-strain curves between the bulk metal and the porous material	20
2.8	Illustration of bone formation in the porous structure and interfaces of bone ingrowth and porous implants	20
2.9	Classification of processing methods of metallic porous alloys	21
2.10	Different processing methods for porous Ti alloys; (a) gas entrapment technique, (b) hollow sphere sintering, (c) replication method and (d) loose powder sintering	22
2.11	Schematic illustration of fabrication method of porous titanium with the space holder method	24
2.12	SEM micrographs of porous Ti with porosity level of 39% and 45%.	28

2.13	(a) Compressive strength, (b) Elastic modulus of sintered porous titanium as function of porosity.	28
2.14	Compressive stress–strain curves of the porous Ti–20Nb–15Zr with various porosity level	29
2.15	Electrochemical corrosion behavior of porous Ti–16Nb alloy with different porosities in SBF solution at 37 °C	33
2.16	Schematic diagram of Wear of implant	36
2.17	Tribocorrosion result of porous Ti-Nb alloy under the various loads in physiological solution; (a) OCP recorded with respect to time, (b) potentiodynamic polarization curves	37
2.18	Reasons for the research on surface modification and new alloys	38
2.19	Classification of surface modification techniques for titanium and titanium alloys	39
2.20	Schematic representation of surface structural change of Ti metal during alkali and heat treatments	41
2.21	Schematic representation of changes in surface structure as hydroxyapatite formation on the surface of Ti alloy after immersion in SBF	42
2.22	Porous Ti-Mo alloy after immersion in SBF for 7, 14, and 21 days: (a) SEM microstructure of hydroxyapatite formation, and (b) AFM tomography	44
2.23	Porous Ti-42Nb alloys immersed in Hanks' solution for 1, 168, and 360 h: (a) potentiodynamic polarization curves, (b) Nyquist, (c) Bode magnitude and phase angle plot, and (d) equivalent circuit model	46
2.24	XPS survey spectra of the surface of porous Ti-42Nb alloy after immersion in Hanks' solution for 360 h	48
2.25	Confocal micrographs of cell growth on the porous Ti-Nb-Zr alloy; (a) inside pores of porous Ti-Nb-Zr alloy and (b) on the surface of the porous alloy	49
3.1	Schematic representation of development of synthesis of Ti–Nb–Ag alloy powders, porous Ti-Nb-Ag alloys and characterization	53
3.2	SEM and EDX analysis of as-procured elemental powders SEM and EDX: (a	54

	& d) Ti, (b & e) Nb, and (c & f) Ag	
3.3	SEM micrograph of as-procured ammonium bicarbonate ( $\text{NH}_4\text{HCO}_3$ ) used as space holder material	54
3.4	Schematic representation of fabrication of porous Ti-Nb-Ag alloys through PM method	55
3.5	(a) Photographs of electrochemical potentiostat (Biologic-150), and (b) temperature controlled water bath.	57
3.6	Schematic diagram of custom-made Tribometer	58
3.7	Photograph of X-ray diffractometer	61
3.8	Photograph of X-ray photoelectron spectroscopy	62
4.1	SEM images of Ti-20Nb-5Ag alloy powders developed by ball milling at different times of (a) 1 h, (b) 5 h, (c) 10 h, (d) 15 h and (e) 20 h.	64
4.2	A corelationship of particle size with ball milling time for developed Ti-20Nb-5Ag alloy powders	65
4.3	Backscattered SEM images of the Ti-20Nb-5Ag alloy powders developed from different ball milling times: (a) 1 h, (b) 5 h, (c) 10 h and (d) 15 h.	66
4.4	(a) EDX elemental mapping of Ti-20Nb-5Ag alloy powders obtained after 1 h of ball milling time	67
	(b) EDX elemental mapping of Ti-20Nb-5Ag alloy powders obtained after 5 h of ball milling time	68
	(c) EDX elemental mapping of Ti-20Nb-5Ag alloy powders obtained after 10 h of ball milling time	68
	(d) EDX elemental mapping of Ti-20Nb-5Ag alloy powders obtained after 15 h of ball milling time	69
	(e) EDX elemental mapping of Ti-20Nb-5Ag alloy powders obtained after 20 h of ball milling time	69
4.5	XRD diffraction patterns of Ti-20Nb-5Ag alloy powders with different ball milling times	70

4.6	SEM micrographs of porous Ti–20Nb–5Ag alloy developed from various ball milled powders for: (a) 1 h, (b) 5 h, (c) 10 h (d) 15 h, and (e) 20 h	76
4.7	Backscattered SEM microstructure of the porous Ti–20Nb–5Ag alloy with different ball milling times: (a) 1 h, (b) 5 h, (c) 10 h (d) 15 h, and (e) 20 h	77
4.8	XRD patterns of sintered porous Ti–20Nb–5Ag alloy developed using different ball milling time	78
4.9	Optical images of the sintered porous Ti–20Nb–5Ag alloy made from the 15 h of ball milled powder	84
4.10	Porosity and density of the sintered porous Ti–20Nb–5Ag alloy developed with various ball milling times for 1, 5, 10, 15 h and 20 h	84
4.11	Sintered porous Ti–20Nb–5Ag alloy made from the various ball mill powders (a) Typical compressive stress–strain curve and (b) mechanical properties	85
4.12	Potentiodynamic polarization curves in SBF solution at 37 °C for the sintered porous Ti–20Nb–5Ag alloy made from various ball milling times	87
4.13	SEM micrographs of porous Ti–20Nb–5Ag alloy after corrosion test in SBF solution: (a) low and (b) high magnification region, (c) EDX analysis after corrosion test	89
4.14	SEM micrographs of developed Ti–xNb–5Ag alloy powders after 20 h ball milling: (a) 25 wt. %, (b) 30 wt. %, and (c) 35 wt. %	91
4.15	Backscattered SEM images of developed Ti–xNb–5Ag alloy powders after 20 h ball milling: (a) 25 wt.% Nb, (b) 30 wt.% Nb, and (c) 35 wt.% Nb	92
4.16	Particle size distribution of Ti–xNb–5Ag alloy powders developed with addition of various Nb content after 20 h of ball milling	93
4.17	SEM morphology of developed Ti–xNb–5Ag alloy powders with the addition of various Nb content after 20 h ball milling: (a) 25 wt. %, (b) 30 wt. %, and (c) 35 wt. %	94
4.18	SEM morphology of developed porous Ti–xNb–5Ag alloys after 1200 °C: (a) 25 wt. %, (b) 30 wt. %, and (c) 35 wt. %	95
4.19	(a) Elemental mapping of developed porous Ti–25Nb–5Ag alloys sintered at 1200 °C for 3 h	96

	(b) Elemental mapping of developed porous Ti–30Nb–5Ag alloys sintered at 1200 °C for 3 h	97
	(c) Elemental mapping of developed porous Ti–35Nb–5Ag alloys sintered at 1200 °C for 3 h	97
4.20	XRD analysis of developed porous Ti– <i>x</i> Nb–5Ag alloys after sintered at 1200 °C for 3 h: (a) 25 wt. % Nb, (b) 30 wt. Nb %, and (c) 35 wt. Nb%	98
4.21	Porosity and density values of porous Ti– <i>x</i> Nb–5Ag alloy with the addition of various Nb content ( <i>x</i> =25, 30 and 35 wt. %) after sintered at 1200 °C	99
4.22	Stress-strain curves of porous Ti– <i>x</i> Nb–5Ag alloy with the addition of various Nb content ( <i>x</i> =25, 30 and 35 wt. %), and (b) Compression strength and elastic modulus of porous alloys	100
4.23	Potentiodynamic polarization curves of porous Ti– <i>x</i> Nb–5Ag alloy with the addition of various Nb content ( <i>x</i> =25, 30 and 35 wt. %)	102
4.24	EIS plots of porous Ti– <i>x</i> Nb–5Ag alloys ( <i>x</i> =25, 30 and 35 wt. %) in SBF solution at 37 °C: (a) Nyquist impedance plot, (b) Bode magnitude plot, (c) Bode phase plot, and (d) equivalent circuit model	105
4.25	SEM images of porous Ti–20Nb–5Ag samples synthesized using different amounts of NH <sub>4</sub> HCO <sub>3</sub> (wt. %): (a) 15%, (b) 30% (c) 45% and (d) 60%.	110
4.26	Pore size distribution of porous Ti–20Nb–5Ag samples synthesized using different amounts of NH <sub>4</sub> HCO <sub>3</sub> (wt. %): (a) 15%, (b) 30% (c) 45% and (d) 60%	111
4.27	Influence of different amount of NH <sub>4</sub> HCO <sub>3</sub> (wt. %) on porosity and density of porous Ti–20Nb–5Ag alloy	112
4.28	Compressive stress-strain curve of the porous Ti–20Nb–5Ag alloy with different porosity; prepared using different amounts of NH <sub>4</sub> HCO <sub>3</sub> (wt. %)	113

4.29	SEM micrograph of fractured surface of 43% porous Ti–20Nb–5Ag sample: (a) fracture of pore cell walls were indicated by arrows, (b) magnified view of region shown by rectangle in Fig. 6.9 (a): brittle rupture (shown in circle) and ductile failure (region 1) and shear lips (region 2)	115
4.30	Potentiodynamic polarization curves of porous Ti–20Nb–5Ag alloy with different porosity in SBF at 37 °C	116
4.31	Electrochemical impedance spectroscopy results of porous Ti–20Nb–5Ag alloy having various porosity in SBF at 37 °C: (a) Nyquist plot; (b) Bode magnitude; (c) Bode phase angle; (d) Equivalent circuit used to analysis EIS data	118
4.32	SEM micrographs of the porous Ti–20Nb–5Ag alloy used for tribocorrosion study	121
4.33	Open circuit potential (OCP) scan for porous Ti–20Nb–5Ag alloy at static and various applied loading conditions	122
4.34	Potentiodynamic polarization curves of porous Ti–20Nb–5Ag alloy at various applied loads: 0 N, 1 N, 5 N and 10 N	124
4.35	SEM images of porous Ti–20Nb–5Ag alloy after tribocorrosion at the various applied loads	126
4.36	Mechanism of tribocorrosion process of porous Ti–20Nb–5Ag alloy in SBF	127
4.37	SEM images of porous Ti-20Nb-5Ag alloy: (a) untreated, (b) after alkali-heat treatment, (c) EDS analysis of the porous surface shown in Fig. (b) and (d) XRD pattern of the surface shown in Fig. (b).	132
4.38	SEM micrographs of porous Ti-20Nb-5Ag alloy after immersion in SBF solution: (a) 7 days, (b) 14 days, (c) 21 days, and (d) XRD analysis of porous alloy after 21 days of immersion in SBF	134
4.39	EDX analysis of porous Ti–20Nb–5Ag alloy after immersion for various time in SBF: (a) 7 days, (b) 14 days, and (c) 21 days	135
4.40	EDX elemental mapping of porous Ti-20Nb-5Ag alloy after 21 days immersion in SBF.	136



4.41	Ca/P ratio of hydroxyapatite coated porous Ti-20Nb-5Ag alloy after immersion for various time in SBF: (a) 7 days, (b) 14 days, (c) 21 days	137
4.42	Schematic representation of hydroxyapatite formation on the porous Ti-20Nb-5Ag alloy in SBF	138
4.43	Surface topography of porous Ti-20Nb-5Ag alloy after immersion in SBF for: (a) 7 days, (b) 14 days, (c) 21 days, and (d) variation in the surface roughness (Ra) and root mean square (Rms)	139
4.44	XPS high-resolution survey spectra obtained for porous Ti-20Nb-5Ag alloy surface after 21 days immersion in simulated body fluids at 37 °C	140
4.45	XPS high resolution individual element spectra of (a) Ti2p, (b) Nb 3d, (c) Ag 3d, (d) O 1s and Ca 2p	141
4.46	Potentiodynamic polarization curves of porous Ti-20Nb-5Ag alloys in SBF solution at 37 °C as a function of immersion time (7, 14 and 21 days)	143
4.47	EIS plots of porous Ti-20Nb-5Ag alloys in SBF solution at 37 °C after 7, 14 and 21 days of immersion: (a) Nyquist impedance plot, (b) Bode magnitude plot, and (c) Bode phase plot	146
4.48	Physical model of porous Ti-20Nb-5Ag alloy/hydrogel layer/hydroxyapatite layer/ solution interface at 37 °C	148
4.49	Fluorescence images of MG-63 human osteoblast cell cultured for different duration: (a) control and, (b) porous Ti-20Nb-5Ag alloy	151
4.50	Human osteoblast MG-63 cell attachments on porous Ti-20Nb-5Ag alloy at different incubation duration: growth of cells with respect to the control	152

## LIST OF TABLES

<b>Table No.</b>	<b>Contents</b>	<b>Page No.</b>
2.1	Advantages and disadvantages of type of metallic biomaterials	10
2.2	Biocompatible Ti-based alloys currently used in the biomedical sector in many applications together with their main advantages and drawbacks.	14
2.3	Space holding particles and considerations in selection for metallic biomaterials	25
2.4	Various new combination of porous Ti-based alloy and their properties	30
2.5	Electrochemical corrosion behavior of porous Ti-based alloys in SBF solution	34
2.6	Surface modification and hydroxyapatite formation on various porous Ti alloys in SBF solution	44
2.7	Cytotoxicity studies conducted on various porous Ti alloys using human osteoblast cell by means of cell growth and cell proliferation	49
3.1	Chemical reagents used to prepare 1000 ml of simulated body fluids	57
4.1	(a) Parameters obtained from the XRD analysis of the Ti-20Nb-5Ag ball milled powder for 1 h by using Williamson-Hall method.	71
	(b) Parameters obtained from the XRD analysis of the Ti-20Nb-5Ag ball milled powder for 5 h by using Williamson-Hall method.	72
	(c) Parameters obtained from the XRD analysis of the Ti-20Nb-5Ag ball milled powder for 10 h by using Williamson-Hall method.	73

	(d) Parameters obtained from the XRD analysis of the Ti-20Nb-5Ag ball milled powder for 15 h by using Williamson-Hall method.	74
	(e) Parameters obtained from the XRD analysis of the Ti-20Nb-5Ag ball milled powder for 20 h by using Williamson-Hall method.	75
4.2	(a) Parameters obtained from the XRD analysis of the sintered porous alloys using 1 h ball milled powder analysed using Williamson-Hall method	79
	(b) Parameters obtained from the XRD analysis of the sintered porous alloys using 5 h ball milled powder analysed using Williamson-Hall method	80
	(c) Parameters obtained from the XRD analysis of the sintered porous alloys using 10 h ball milled powder analysed using Williamson-Hall method	81
	(d) Parameters obtained from the XRD analysis of the sintered porous alloys using 15 h ball milled powder analysed using Williamson-Hall method	82
	(e) Parameters obtained from the XRD analysis of the sintered porous alloys using 20 h ball milled powder analysed using Williamson-Hall method	83
4.3	Potentiodynamic polarization parameters of porous Ti-20Nb-5Ag alloys made from various ball milled powders in SBF solution at 37 °C	88
4.4	Electrochemical corrosion parameters of the porous Ti-xNb-5Ag alloys (x=25, 30 and 35 wt. %) alloy in SBF solution at 37 °C	103

4.5	Impedance parameters obtained by $R_s (Q_p(R_p(Q_bR_b)))$ model to fit EIS data of porous Ti-xNb-5Ag alloy ( $x=25, 30$ and $35$ wt. %) in SBF solution at $37^\circ\text{C}$	97
4.6	The mechanical properties of the developed porous Ti-20Nb-5Ag alloy	114
4.7	Electrochemical corrosion parameter of porous Ti-20Nb-5Ag alloy having different porosity level in SBF solution.	116
4.8	Impedance parameters obtained by $R_s (Q_pR_p) (Q_bR_b)$ model to fit EIS data of porous alloys having various porosities in SBF solution at $37^\circ\text{C}$	118
4.9	Corrosion parameters of porous Ti-20Nb-5Ag alloy in SBF solution at various applied load	125
4.10	Corrosion parameters of the porous Ti-20Nb-5Ag alloy after immersion in SBF solution at $37^\circ\text{C}$ for 7, 14 and 21 days	133
4.11	Impedance parameters of porous Ti-20Nb-5Ag alloy obtained by fitting $R_s (R_aQ_a)(R_bQ_b)$ models on immersion in SBF	138

## NOMENCLATURE

PM: Powder Metallurgy

$\text{NH}_4\text{HCO}_3$ : Ammonium bicarbonate

XRD: X-Ray Diffractometer

SEM: Scanning Electron Microscopy

EDX: Energy Dispersive X-Ray

OM: Optical Microscopy

AFM: Atomic Force Microscopy

XPS: X-ray Photoelectron Spectroscopy

FM: Fluorescent Microscope

SCE: Saturated Calomel Electrode

EIS: Electrochemical Impedance Spectroscopy

SBF: Simulated Body Fluid

## CHAPTER 1

### 1. INTRODUCTION

Titanium (Ti) and its alloys are emerging biomaterials in the form of new class material to replace the damaged part of the hard bone tissues, which significantly restore the specific functions (Geetha et al. 2009; Long and Rack 1998; Wen et al. 2002). The Ti and its alloys having wide range of applications in the biomedical sector, that range from total hip replacement, knee replacement, joint replacement, dental and vascular stents (Wen et al. 2001; Wu et al. 2014; Yue-qin et al. 2010). A biomaterial are basically used to replace the damage part of human body to restore their functions. These biomaterials can have a several application such as; dental, total hip replacement, knee joints, spinal, stents, and heart valve etc., as shown in Fig. 1.1.

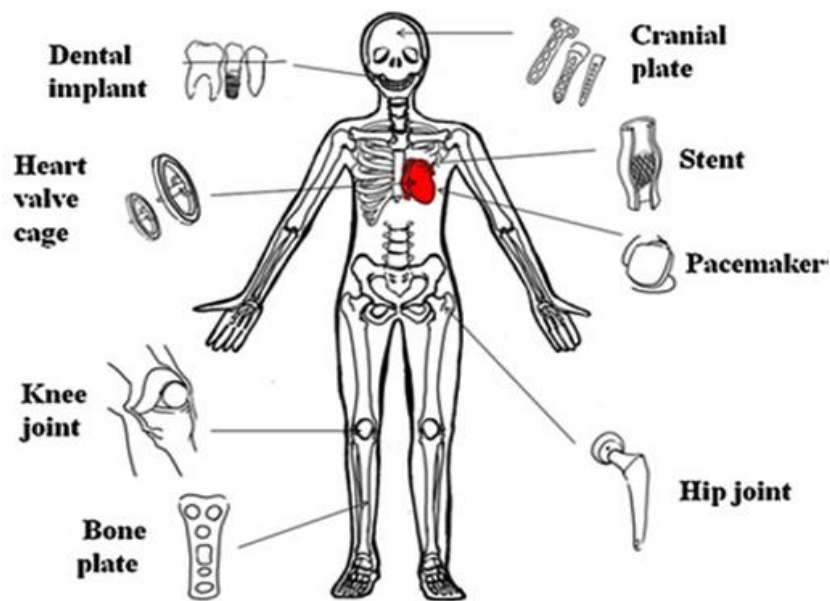


**Fig. 1.1: Various implant materials (Manivasagam et al. 2010).**

In spite of the great progress of Ti alloys in the field of clinical applications, the *stress-shielding effect* has remains a crucial use as implant materials. Stress-shielding effect may be defined as a condition of bone in which there is a reduction in bone mass that is less severe than that in osteoporosis, which caused by mismatch of elastic modulus of the implant materials. It is also leads to bone resorption, and implant

loosening which is harmful to the surrounding living tissues (Wen et al. 2002; Xiong et al. 2008b).

Many attempts have been made to reduce the elastic modulus of the titanium implant materials by addition of  $\beta$  stabilizing elements such as Mo, Nb, Ta, Zr, and Sn. Also, addition of Cu and Ag into Ti to control microbial growth on the alloy surface and which show non-toxic properties in the human body environment (Aguilar et al. 2016a; Gao et al. 2012b; Xiong et al. 2008a). When alloying these elements with Ti, they exhibit  $\alpha+\beta$ , and  $\beta$  phases and enhance the strength of implant materials with low elastic modulus, (Aguilar et al. 2016a; Gao et al. 2012b; Xiong et al. 2008a). However, it is found that Nb is a strong  $\beta$  stabilizer in Ti alloys resulting in solid solution strengthening and precipitation hardening. Many researchers have prepared Ti alloy with the addition of various Nb content to examine the relevant properties which suits for orthopaedic applications (Lee et al. 2002; Nazari et al. 2015; Rao et al. 2014a). Moreover, the corrosion and tribocorrosion behavior of Ti-based alloys is governed by  $\beta$  stabilizing elements. Most of the Ti alloys contains a naturally formed compact layer which contains  $\text{TiO}_2$  oxide layer and also it can be observe that formation of other oxides on surface of Ti alloys with the addition of various alloying elements. The presence of Nb in the alloy enhances the passivation characteristics of the film by forming  $\text{Nb}_2\text{O}_5$  and also beneficial effect of Nb addition as an alloying element in stabilizing surface films of Ti alloys. However, newly developed various Ti-based and studied the microstructure, mechanical, biocompatible, corrosion and tribocorrosion properties of the alloys.

Still, bulk Ti-based alloy possess a higher compression strength and elastic modulus (90 GPa) as compared to the natural bone of 2–200 MPa and 0.1–30 GPa respectively, which remains to causes the *stress-shielding effect* (Ryan et al. 2006). One of the best methods to minimize the elastic modulus of the implants is to introduction of pore structures in the bulk materials (Niu et al. 2009; Wang et al. 2011). Recently, porous titanium (Ti) and its alloy as implant materials have been very attractive implant materials in the field of biomedical applications. Due to their significant properties such as; low elastic modulus, good mechanical properties, high

corrosion resistance and excellent biocompatibility properties (Chen et al., 2009; Andani et al., 2014).

While designing the implants, prior understanding of the load-bearing condition is essential, which demands high strength bones, though there are several sections, where bone strength could be lower also (Long and Rack 1998; Niinomi 2002). Also, the porous structures allow transportation of body fluids, facilitate new bone ingrowth, and increase the osseointegration potential of implant materials.

Recently, additive manufacturing has also emerged as a fabrication route, which allows achieving the patient's personalized requirement. However, the conventional powder metallurgy route has still been a choice for making porous implants, using space holder materials. It offers very low processing cost and the possibility of producing near net shape component. Pore fraction, size, and properties can be tailored using appropriate space holder materials. NaCl, ammonium bicarbonate magnesium were used as the space holder materials and to create interconnected pores (Gao et al. 2012b; Torres et al. 2012, 2014a). It has also observed that achieving adequate structural and mechanical properties are not enough to employ as an implant material due to their bio inertness. Thus, it suggested that some additional surface modification is necessary to alleviate the bio-inertness problem and to improve the surface bioactivity of the implants (Butev et al. 2015; Khodaei et al. 2015). Chemical methods such as acidic and alkali (NaOH) treatments were used for controlled surface oxidation which is form a stable oxides on the surface of titanium alloys. Subsequently, this oxides are significantly enhance the surface bioactivity with the formation of the apatite layer or calcium phosphate layers on the surface of implants when interaction taking place between implants and simulated body fluids (Hazwani et al. 2017; Wang et al. 2009). Several investigations conducted to evaluate the biological compatibility of titanium implants due to the release of toxic metal ions resulting in corrosion, tribocorrosion process and cytotoxicity performances, which can significantly affect the surrounding environment (Bai et al. 2016; Ou et al. 2017). The electrochemical corrosion is one of the crucial factor in the human body environment due to toxic ions release from the implant materials and mainly this is a surface phenomenon. The corrosion behavior of the implant materials depend on the various factor such as elemental composition,



surface morphology, and corrosive environment (Chen et al. 2017; Sasikumar & Rajendran, 2012). It is well known that Ti can easily react with the oxygen from the atmosphere due to its strong affinity for oxygen. Therefore, this kind of implant materials show a tendency to form a stable and tightly adherent protective oxide layer (native oxides) on their surfaces (Sri Maha et al. 2019), which can give the protection against the corrosion. However, these materials can suffer corrosion attacks in an aggressive environment like human body fluid conditions. It is possible to further increase its corrosion resistance by modifying its surface or coating bone-like hydroxyapatite on their surface. These processes can make Ti and its alloys to withstand in the human body for long duration (Prando et al., 2018; Chen et al., 2016).

On the other hand, tribocorrosion behavior of implants is a critical one in the environment of the human body and is a phenomenon of the material degradation process under the combined effect of wear and corrosion (Injeti et al. 2019; Long and Rack 1998). After implant materials are inserted into the human body, the implants are exposed to human body fluid and are subjected to inevitable micro-motion between the interfaces over a lifetime. This can lead to a continuous removal of material due to wear and corrosion with implants and bone tissue (C Albayrak et al. 2013; Z. Wang et al., 2017). Resulting in the release of wear debris and metal ions (which can be cytotoxic) which lead to failure by means of osteolysis and loosening of implant materials. This process is very important to understand the nature of biomaterials, their structural properties, mechanical properties and interaction with the natural bone surrounding (Toptan, 2017; Z. Wang et al. 2018). Besides, the microstructure, mechanical properties, corrosion and tribocorrosion behavior that are requirements to be fulfilled by bone implants for a successful osseointegration, the main necessity is their biocompatibility. Biocompatibility is the ability to exist in contact with tissues of the human body without determining harm to the surrounding tissues and to the human body by means of cytotoxicity and antibacterial tests. However, the cytotoxicity test is performed to examine cell adhesion, and cell proliferation studies to ensure that the implants are non-toxic and used as bioimplants without any adverse reaction with the surrounding tissues (Majumdar et al. 2015; Torres-Sanchez et al. 2018).

## 1.1 OBJECTIVES OF THE PRESENT WORK

1. To study the role of ball milling times on microstructure, mechanical and electrochemical corrosion properties of sintered porous Ti–20Nb–5Ag alloy.
2. To examine the role of Nb content on the mechanical and electrochemical corrosion properties of sintered porous Ti– $x$ Nb–5Ag alloy
3. To examine the role of porosity level on microstructure, mechanical and electrochemical corrosion properties of sintered porous Ti–20Nb–5Ag alloy.
4. To study the tribocorrosion properties of optimized porous Ti–20Nb–5Ag alloy in simulated body fluid.
5. To examine the surface modification, hydroxyapatite formation and cytotoxicity behavior of optimized porous Ti–20Nb–5Ag alloy.

## 1.2 ORGANIZATION OF THE THESIS

The thesis is organised into five chapters. ‘**Chapter 1**’ presents the generic introduction of the thesis which discusses the importance of development of porous alloys for biomedical applications. The importance of these biomaterials and their microstructure, mechanical properties, electrochemical corrosion behavior, tribocorrosion properties, hydroxyapatite formation capability, and cytotoxicity characteristics of Ti alloys. ‘**Chapter 2**’ presents a detailed **Literature Review**. This chapter summarizes the technical information and research updates available till date like the development of new porous Ti based alloys and their relevant properties which suits for biomedical applications. ‘**Chapter 3**’ explains the ‘**Experimental details**’ adopted in the present research work. It explains the experimental methodologies, and instruments used to accomplish the specified objectives. The results obtained in different experiments were consolidated, analysed, and discussed in detail and presented in ‘**Chapter 4**’ as ‘**Results and discussion**’. It comprises of five parts such as; (i) study the role of ball milling times (1 to 20 h) on microstructure, mechanical and electrochemical corrosion properties of sintered porous Ti–20Nb–5Ag alloy, (ii) role of addition of Nb content on the mechanical and electrochemical corrosion properties of porous Ti– $x$ Nb–5Ag alloy ( $x= 25, 30$  and  $35$  wt.% Nb).

(iii) addition of various amount of space holder ( $\text{NH}_4\text{HCO}_3$ ) to examine the porosity level, microstructure, mechanical and electrochemical corrosion properties of sintered porous Ti–20Nb–5Ag alloy, (iv) examine the tribocorrosion properties of sintered porous Ti–20Nb–5Ag alloy at various applied loads in simulated body fluid, (v) surface modification through alkali treatment, hydroxyapatite coating by immersion in SBF for various times, and cytotoxicity behavior on the sintered porous Ti–20Nb–5Ag alloy, and The important results are summarized, and the significant conclusions drawn in the research work is consolidated in the ‘**Chapter 5**’ as ‘**conclusions**’.

## **CHAPTER 2**

### **2. LITERATURE REVIEW**

This chapter deals with the findings of previous studies which provide information relevant to present research work. These findings include the development of bio-implant materials, porous implant materials, processing methods of porous implants, electrochemical corrosion behavior, tribocorrosion properties, surface bioactivity and cytotoxicity performance of the biomaterials.

#### **2.1 Introduction of biomaterials**

Biomedical metallic materials are an important class of biomaterials owing to their excellent features like high strength and toughness, fatigue resistance, easy processing, etc., which are widely used in clinic. Metallic materials are first candidates for those hard tissues repairs in orthopaedic and dentistry that require high load bearing capacity, as well as stents in interventions, and have been used to manufacture various implant devices in these medical areas. Among these, fixation devices for bone fracture, joints, spines, teeth implants, and coronary stents are representatives of high-grade products, varying in different types and specifications. The properties of medical metallic materials can be crucial to the performances of these implant devices, even affecting their efficacies for patients. Currently, stainless steels, Co-Cr based alloys, and titanium (Ti) alloys are the main metallic implant materials that are mostly used in clinic, occupying pivotal positions in production and clinical applications of medical metallic materials. Biodegradable magnesium (Mg) based materials are a novel class of medical metallic materials that are being developed and have great potential for medical applications.

#### **2.2 Design consideration for developing of biomaterials**

The design and selection of a biomaterial depends on its specific utilization in medical application. In order to serve safely and appropriately for a long period of time without rejection, a metallic implant should possess the following essential characteristics:

- a. Biocompatibility

- b. Osseo-integration
- c. Suitable mechanical properties
- d. High corrosion and wear resistance

### **2.2.1 Biocompatibility**

Biocompatibility of material is an ability to exist in contact with tissues of the human body without causing any adverse reaction in surrounding tissues. It is not only associated to toxicity, but also capacity to promote natural tissue growth on the surface of metallic implants. Biocompatibility is a complicated process and its depend on various factors such as bio-functionality, bio-inertia, bioactivity, and bio-stability (Nasab et al. 2010). If the metallic implant is biocompatible, it allows to accept without any undesirable immunity response, allergic reactions, inflammatory or chonical problems to the surrounding tissue of the human body.

### **2.2.2 Osseointegration**

The ability of a material surface to integrate with the adjacent bone or tissue forming new bone and bone healing is known as “osseointegration”. Surface chemistry, surface roughness and surface topography which promote osseointegration between the implant and host tissue are the key factors for the new developments of metallic implants. The inability of the surface implants integrated with the micro-motions between the bone and implants, results in degradation of the surface properties and loosening effect (Nishiguchi et al. 2001). Surface roughness of the implants is helpful to enhance the bonding between the implant materials and surrounding tissues. However, pores and rough surfaces are preliminary requirement for assisting osseointegration of metallic implants.

### **2.2.3 Mechanical properties**

An important requirement for metallic implant is good mechanical compatibility with human bone. This includes well-matched mechanical strength of implant to withstand the load when inserted into human body as well as low elastic modulus similar to that of human bone to avoid or reduce the stress shielding effects.

The metallic implant is mostly suffered as premature failure because of insufficient strength or mismatch of mechanical properties between the implants and bone.

The requirements are compression strength of about 2–200 MPa, elastic modulus ranging from 0.1–30 GPa and density of bone is between 1.8–2.1 g/cm<sup>3</sup> which depending on the type of hard bone tissue (Staiger et al. 2006; Yue-qin et al. 2010). If the developed implant materials do not fall within the required range, it can be referred as biomechanical incompatibility.

#### **2.2.4 Corrosion behavior**

It is a gradual degradation of metallic implant by electrochemical corrosion reactions of implant when it is placed in the hostile electrolytic environment of the human body. The implants face severe corrosion environment which includes blood and other constituents of the body fluid which encompass several constituents like water, sodium, chlorine, proteins, plasma, amino acids along with mucin in the case of saliva. Aqueous medium in the human body consists of various anions such as chloride, phosphate, and bicarbonate ions, cations like Na<sup>+</sup>, K<sup>+</sup>, Ca<sup>2+</sup>, Mg<sup>2+</sup> etc., organic substances of low-molecular-weight species as well as relatively high-molecular-weight polymeric components, and dissolved oxygen. The biological molecules upset the equilibrium of the corrosion reactions of the implants by consuming the products due to anodic or cathodic reactions. Proteins can bind themselves to metal ions and transport them away from the implant surface upsetting the equilibrium across the surface double layer that is formed by the electrons on the surface and excess cations in the solution. In addition, proteins that are absorbed on the surface are also found to reduce the diffusion of oxygen at certain regions and cause preferential corrosion at those regions.

#### **2.2.5 Tribocorrosion properties**

Tribocorrosion is the irreversible transformation of a material due to the simultaneous action of corrosion and wear taking place in a sliding tribological contact. This involves numerous synergy effects between mechanical and electrochemical phenomena, usually leading to an accelerated material degradation. The micro-motion,

design and functionalities of load-bearing orthopedic implants leads to a continuous removal of material due to wear and corrosion with other implants and bone tissue. Inferior wear resistance can result in the release of wear debris and metal ions (which can be cytotoxic) leading to immune response and rejection of implants. Thus, development of implants with high corrosion and wear resistance is prime importance for the longevity of the material in the human system.

### 2.3 Currently used metallic biomaterials

Various metallic materials used as bioimplants include austenitic stainless steel (Type 316 SS), Co–Cr based alloys, NiTi alloy, Mg alloy and Ti and its alloys for different biomedical applications such dental, orthopedics, cardiovascular etc. It is found that the Ni, Cr and Co are released from the stainless steel and Co–Cr alloys due to the corrosion in the body environment (Geetha et al. 2009; Ibrahim et al. 2017).

In addition, these alloys possessed much higher elastic modulus than human bone which leading to insufficient stress transfer to the bone. This leads to serious cause of bone resorption and loosening of implant after implantation. Amongst the traditional biomaterials, Ti based alloys are widely used for implant applications due to the combination of their outstanding characteristics such as high strength, low density (high specific strength), high corrosion resistance, complete inertness to body environment, enhanced biocompatibility, low modulus and high capacity to join with bone and other tissues. The advantageous and limitations of the traditional metallic implants are listed in Table 2.1.

**Table 2.1: Advantages and disadvantages of type of metallic biomaterials.**

<b>Alloys</b>	<b>Advantages</b>	<b>Disadvantages</b>
Stainless steels	Good corrosion and fatigue resistance in short-term applications Low cost Easy to be machined	Corrosion issue in long-term applications High modulus (stress shielding effect) Toxicity and carcinogenicity of nickel
Co–Cr alloys	Long-term corrosion resistance Super fatigue and wear resistance Biocompatibility	Difficult to machine and thus expensive to process High modulus (stress shielding effect)

		toxicity and carcinogenic properties of hexavalent chromium (VI)
Ti and its alloys (Ti-6Al-4V)	Light weight Greatest corrosion resistance Excellent biocompatibility Relatively low Young's modulus	Lower shear strength Low wear resistance Expensive High modulus (stress shielding effect) Al and V allergy

Currently used metallic implants including the stainless steel (Type 316L), Co-Cr alloys, and Ti-based alloys have tendencies to fail after long-term use due to high elastic modulus compared to that of human bone, low wear and corrosion resistance, and lack of biocompatibility. Several reasons to cause failure of metallic implant materials is shown in Fig. 2.1. Which is revealed that the most of these failures are quite connected and responsible to each other.

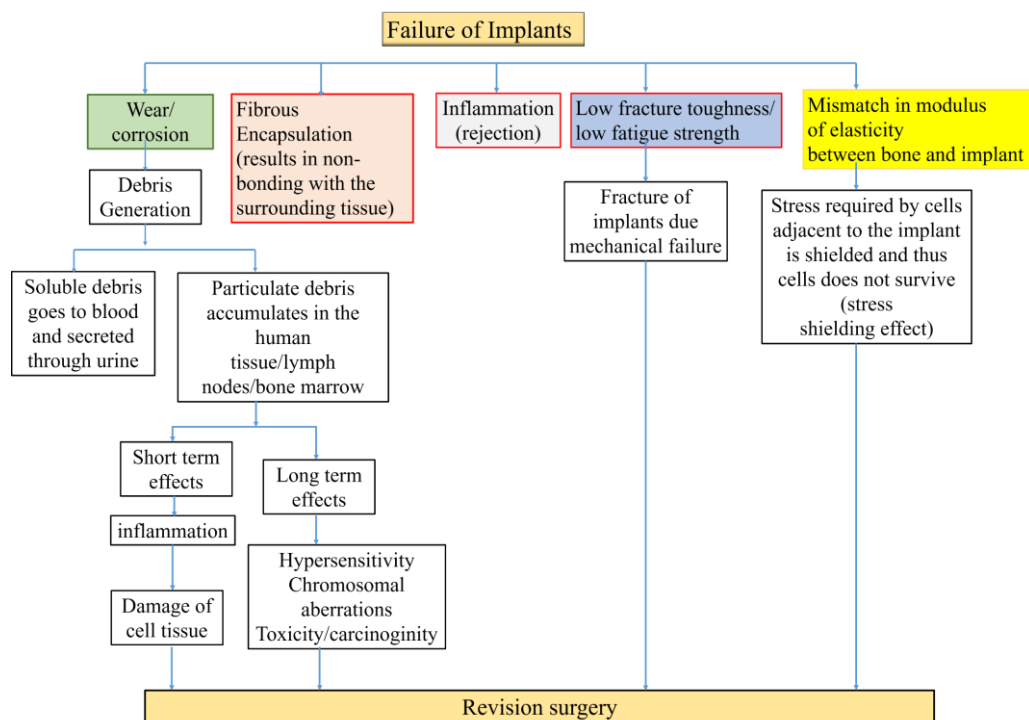


**Fig. 2.1: Various causes for failure of biomaterials implants which leads to revision surgery (Geetha et al. 2009).**

Hence, it is not possible to ignore anyone properties during the alloy design or developments. It can be seen that a low wear resistance leads to metallic ions release provoking problems on short and long term with damage of cell tissue and toxicity.



Furthermost, a mismatch of elastic modulus of implant with the bone is a crucial factor and leads to the catastrophic failure of metallic implant materials.

It significantly reduces the life span of the implants and required revision surgery and re-implantation which is an expensive and traumatic condition for the patients. Ti and its alloys exhibit elastic modulus of 110 GPa which is lower than stainless steel (210 GPa) and Co–Cr alloys (240 GPa ) (Geetha et al. 2009; Niinomi 1998). Therefore, many researchers have been attempted to reduce the elastic modulus by addition of various alloying elements such as Nb, Mo, Zr, Ta, Sn, Ag and Cu, which having the capable of reducing elastic, improve the antibacterial properties without exhibiting any adverse reactions with the surrounding tissues.

#### **2.4 Titanium (Ti) and its alloys for biomedical applications**

Ti and its alloys have been extensively employed as a bio-implant material in various parts of the human body such as heart valves, blood vessel stents or knees, hips, shoulders or spinal replacements since 1950s (Liu et al. 2004). Ti presents two different structures such as hexagonal close packed (HCP)  $\alpha$  phase at low temperature and body-centred cubic (BCC)  $\beta$  phase at high temperature. Two generation of Ti–based alloys have been emerged by the addition of various alloying elements is shown in Fig. 2.2. It shows the influence of alloying elements on phase diagram and microstructural modification by the addition of different type of alloying elements into the matrix of titanium metal. These alloying elements well known as stabilizers of phases (mainly  $\alpha$ ,  $\alpha+\beta$ , and  $\beta$  alloys) can be classified in to three types as (i)  $\alpha$ –stabilizers (alloying elements Al, O, C, N), (ii)  $\beta$ –stabilizers (alloying elements Mo, Nb, V, Ta), (iii) neutrals (alloying elements Zr, Sn). Based on these alloying elements into Ti alloys, it can be developed and classified as  $\alpha$ , near  $\alpha$ ,  $\alpha+\beta$ , metastable  $\beta$  or  $\beta$  types Ti alloys (Geetha et al. 2009).

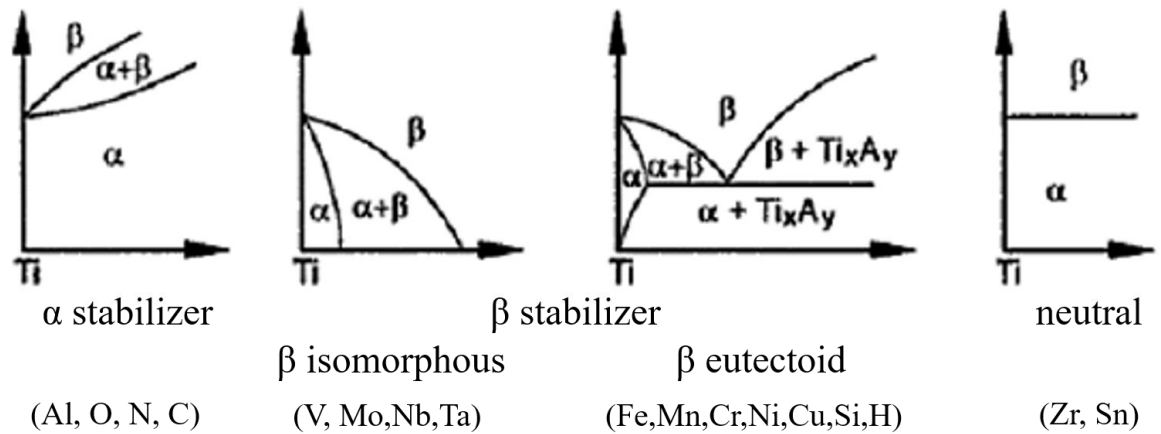


**Fig. 2.2: Schematic representation of the effect of alloying elements on phase diagrams of titanium alloys (G. Lütjering, J and Williams., 2007).**

A well-known first generation of Ti-based alloys is developed as biomaterials in year 1950 and leading so far as commercially pure (CP)-Ti ( $\alpha$ -type) and Ti-6Al-4V, Ti-6Al-7Nb or Ti-Al-Fe ( $\alpha+\beta$  type) alloys in biomedical industry. Second generation of Ti alloys were developed using  $\beta$ -stabilizers such as Nb, Mo, Zr, and Ta which are considered to be fairly safe, as compared to V and Al based alloys of first generation. However, various Ti based alloys developed using  $\beta$ -stabilizing elements such as Ti-13Nb-13Zr, Ti-12Mo-6Zr-2Fe, Ti-35Nb-7Zr-5Ta and Ti-Mo, are developed with great interest in 1990s onwards (Chen and Thouas 2015). However, the required mechanical properties of these developed alloys are depend on composition and the relative amount of  $\alpha$  and  $\beta$  phases in the microstructures.

The  $\beta$ -stabilizer elements content in Ti matrix has a direct effect on strength and elastic modulus of the alloys. It is noticed Nb, Ta, Zr, Mo and Sn chosen as safe alloying elements to Ti alloys which are quite non-toxic and non-allergic and now extensively used in the field of biomedical due to their distinctive combination of properties like superior mechanical properties, high biocompatibility, excellent corrosion and wear resistance (Niinomi 2002).

Various type of Ti-based alloys and its advantages, disadvantages with applications are shown in Table 2.2.

**Table 2.2: Biocompatible Ti-based alloys currently used in the biomedical sector in many applications together with their main advantages and drawbacks.**

Ti alloys	Advantageous	Disadvantages	Applications
CP Ti Ti-6Al-4V	High biocompatibility	High density, Poor tribological properties	Orthopedic: Joints, hip stems, total hip implant, acetabular cup,
Ti-6Al-7Nb Ti-13Nb-13Zr	Excellent corrosion resistance	Toxic effect of Al and V ion long term	hard tissue or bone substitutions, load-bearing implants
Ti-35Nb-7Zr-5Ta	Low Young's modulus		Dentistry
Ti-15Mo	Low density		Cardiovascular: stents, heart valve parts

Interestingly, Nb is identified as strong  $\beta$ -stabilizing element among the other elements. It shows solid-solution strengthening and formation of precipitation hardening (Cremasco et al. 2008) (Niinomi 2002). Also, with the addition of Nb into Ti matrix, reduces the elastic modulus of implants by increasing the  $\beta$  phase and reduction of  $\alpha$  phase. It also found that the improvement in corrosion and wear resistances of the alloys by formation the  $\text{Nb}_2\text{O}_5$  protective oxide films on the alloy surface. The phase diagram of the Ti-Nb system is shown in Fig. 2.3, revealing a possible solubility of Nb and formation of  $\beta$  phase.

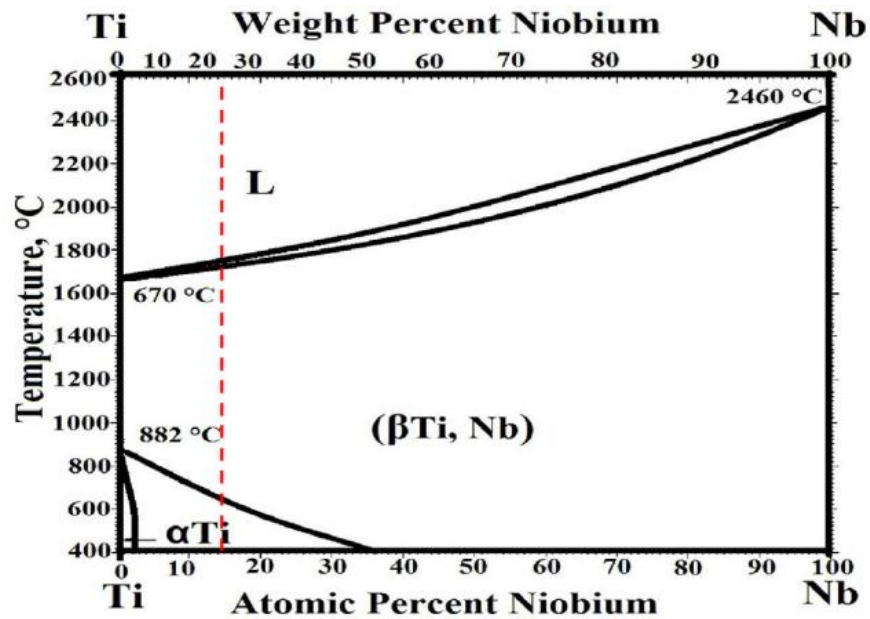


Fig. 2.3: Typical Ti–Nb phase diagram (Fellah et al. 2019b).

However, there is limitation to process Ti–based alloys with the addition of  $\beta$ –stabilizing elements due to the high melting point and also chemical segregation during the solidification. The alloying elements have high density and higher melting point than Ti, which may increase density of implant. These elements are highly reactive with oxygen which leads to oxidation problem. Hence, it requires an extra precaution and operation to process under high vacuum. There are several processing techniques have been used to develop Ti alloys including liquid metallurgy, powder metallurgy method (PM), laser melting and sintering, spark plasma sintering (SPS), and Arc-melting process. However, various bulk Ti alloys have also been developed using above techniques by various researchers is briefly discussed as:

**Nazari et al. (2015)** studied the effect of addition of Nb content on microstructure and mechanical properties of Ti–(5–40)Nb–Mo alloys developed through PM method. With different content of Nb added powders were ball milled for 1 h and compacted at an applied load of 600 MPa. The green pellets were sintered at 1150 °C to fabricate the alloys.

Microstructure of sintered alloy exhibits the  $\alpha+\beta$  type phases with significant reduction in  $\alpha$  phase on increasing Nb content. A remarkable observation is noticed that variation in porosity due to the presence of high amount of Nb into alloy. It is found high porosity, primarily due to the formation of Kirkendall's type pore in sintered alloys. These extra developed porosities directly control the mechanical properties of Ti-Nb alloy. It is reported about 14% reduction in the compression strength and 61% reduction in elastic modulus at the highest Nb content.

Zhao et al.,(2015) have developed Ti-Nb alloy and formation of Kirkendall type pores during sintering process into three distinct steps namely:

**(i) Ti-diffusion controlled step:** Pore elimination is mainly attributed to the diffusion between Ti particles, which is occurred due to the noteworthy difference between the diffusion coefficients at low temperature. Second particle (Nb) acts as diffusion barriers against the mass flow of the Ti atoms. The shrinkage of the Ti particles is inhibited by the fully dense Nb particles which leads to a stress and reduces the shrinkage. It is an initial step where residue pores can be seen between Nb and Ti particles as well as between Ti to Ti particles.

**(ii) Ti-Nb diffusion step:** In this stage, which is occurred at slightly higher temperature, the neck growth between the Ti particles and Nb particles becomes apparent. It is mainly take place due the dissolution of Nb particles which leads to the acceleration of the diffusion between the Ti particles and the mass transfer between the Ti matrix and Nb particles. It also contributes to the pore elimination at this step and a strong Kirkendall effect may lead to pore initiation at Ti-Nb boundaries.

**(iii) Matrix-diffusion step:** this step is occurred at very high temperatures where homogenization process between the Ti matrix and Nb particles would be finished. The Ti-Nb bimodal structure is transferred into the Ti-Nb matrix. Further, shrinkage is accomplished by pore elimination due to higher diffusion in the Ti-Nb matrix. However, it is found that the pores developed as round and closed types when the temperature is further raised.

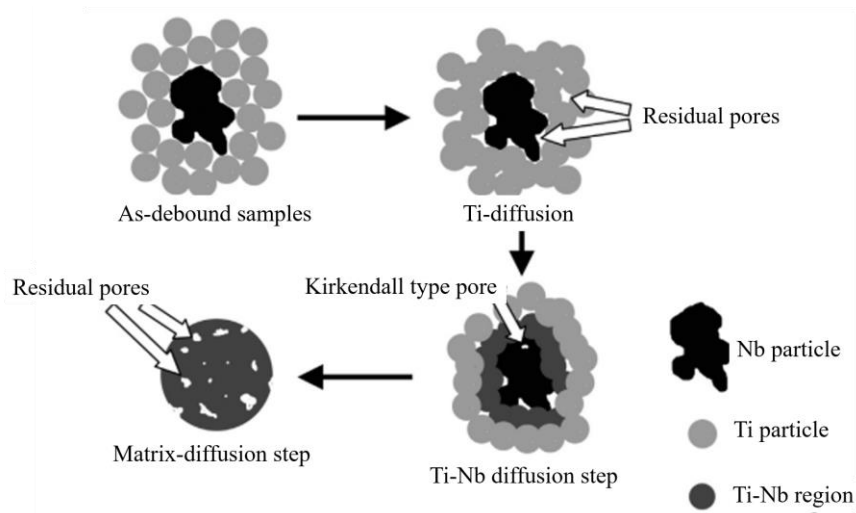


**Fig. 2.4: Schematic diagram of sintering behavior and formation of Kirkendall type pore in the Ti–Nb alloy (Zhao et al. 2015).**

Wen et al., (2014) fabricated Ti–26Nb–5Ag alloy using PM method and studied its microstructure and mechanical properties. The elemental powders blended for 20 h, and compacted at an applied load of 160 MPa to prepare the green compacts. Then, green samples were sintered in a vacuum furnace at a temperature of 1000 °C for 5 h. Compression strength of sintered alloy is found 428 MPa and the a microstructure of alloy consists of  $\alpha$ ,  $\beta$  and  $\alpha''$  phases.

Xu et al., (2013) found a dependency of mechanical properties of different Ti–15Mo– $x$ Nb alloys ( $x=5, 10, 15,$  and  $20$  wt. %) which are processed by arc-melting technique. Microstructure of the developed alloys are exhibited only  $\beta$  phase. The compression strength of developed alloys increased with the increase in Nb content from 473 MPa to 710 MPa.

Kalita et al., (2020) used spark plasma sintering to process Ti– $x$ Nb alloy ( $x = 14, 20$  and  $26$  at. %). They reported the effects of Nb content on microstructural and mechanical properties of alloys. It was reported that there was formation of  $\alpha$ ,  $\beta$  and  $\alpha''$  phases, which commonly exhibited with the addition of Nb in Ti matrix. They reported a compressive yield strength of 949 MPa, 746 MPa, and 656 MPa depending on the presence of  $\alpha$  hexagonal phase in the microstructure of the developed alloys.

As discussed above, all the developed Ti–Nb based alloys possessed superior mechanical and microstructural properties. Compression strength and elastic modulus of the developed alloys are not within the range of human bone. A successful implant should possess close elastic modulus of human bone (0.1–30 GPa) and compression strength of 2–200 MPa (Wang et al. 2011). However, in various Ti based alloys which used for biomedical application the elastic modulus is presented in Fig. 2.5.

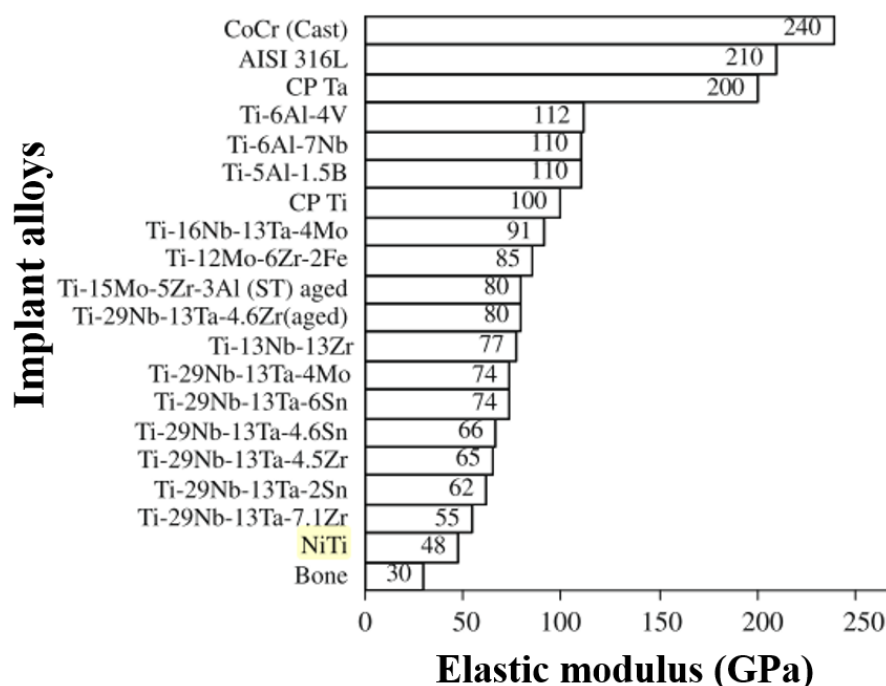


**Fig. 2.5: The comparison of elastic modulus of various Ti–based alloys with human bone (Geetha et al. 2009).**

If the implant materials have higher elastic modulus than human bone, it leads to sever stress-shielding effect. Mismatch of elastic modulus, significantly loosens the implants and leads to biomechanical incompatibility. Fig. 2.6 shows schematic representation of stress-shielding effect when an implant is inserted into human body which exhibited higher elastic modulus than human bone. Nevertheless, a great progress has been reached in biomedical applications, mismatch of elastic modulus between implants and human bone surrounding remains a critical issue, which is major reason for failure of implants due to stress shielding of bone (Ridzwan et al. 2007).

Therefore, many researchers have put an effort to minimize the stress-shielding effect by introduction of pore structures in to bulk Ti-based implants using various processing techniques (Dunand 2004; Ryan et al. 2006).

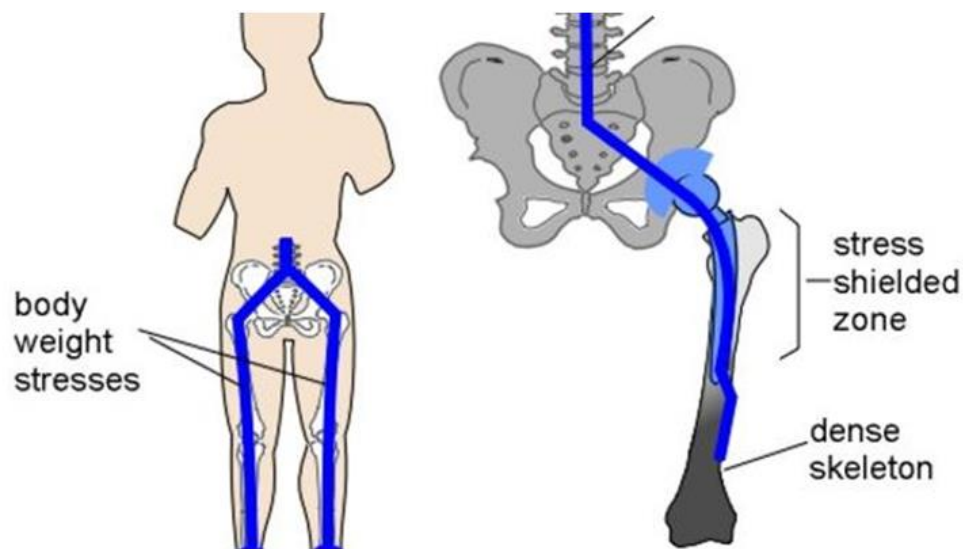


**Fig. 2.6: Schematic representation of stress shielding and stress shielding zone at hip joint replacement (Ridzwan et al. 2007).**

## **2.5. Metallic porous alloys for biomedical application**

In recent years, metallic porous materials gained a special attention as a new generation of materials for potential application in tissue engineering. Basically, a bone structure consists of a porous tissue material, which is a physiological rationale for the use of porous alloys for hard tissue replacement. Introduction of pore structures into a bulk material structure, which can significantly reduce the elastic modulus close to that of human bone. Subsequently, it provides a good load transfer ability and stimulate the formation of new bone ingrowth (Rubshtein et al. 2014; Xiong et al. 2008a).

Fig. 2.7 shows the comparison between the stress-strain curves of bulk materials and porous structure under the tensile and compressive stress. It can be seen that lower elasticity is exhibited by metallic porous material as compared to bulk which is very much essential for biomedical applications.



In addition, these porosities allow new bone tissues to grow into the porous structure, providing an adequate biological fixation. Provided that interconnected porosity exists, the pore structure can have the additional desired effect of promoting bone ingrowth, which significantly enhance the osseointegration properties of the porous implant materials. Fig. 2.8 represents the pore structures which allow the formation of new bone ingrowth into the open pore structure and assisting as a stable fixation and also creating a highly convoluted interface between the bone surrounding and porous implant alloy.

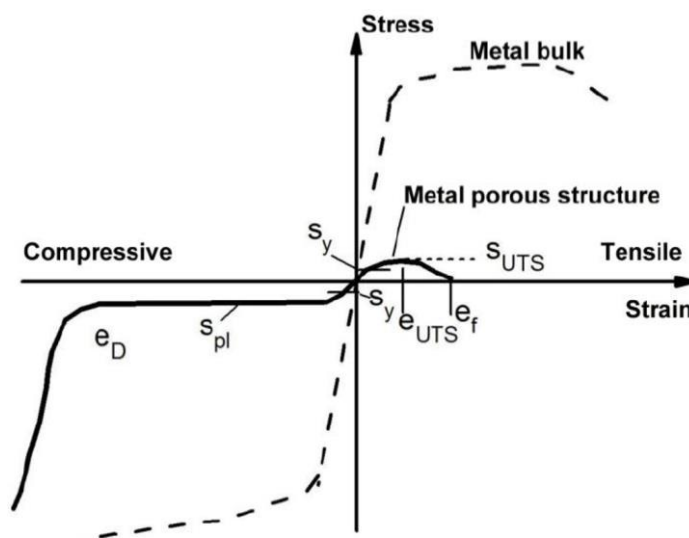


**Fig. 2.7:** A comparison of the stress-strain curves between the bulk metal and the porous metal (Ridzwan et al. 2007).

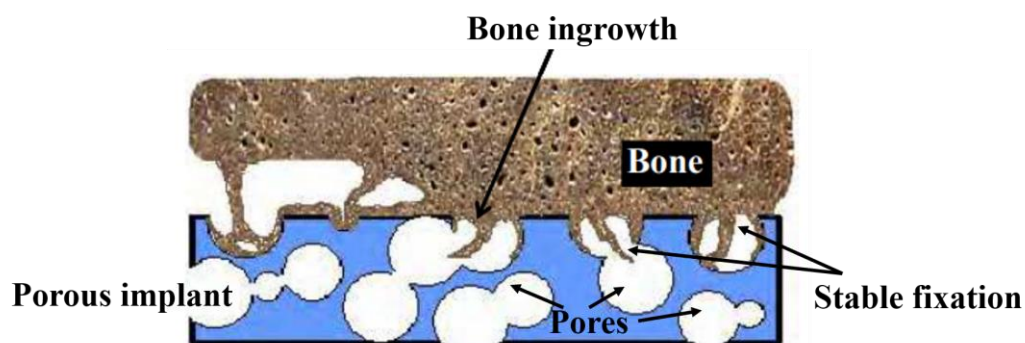


**Fig. 2.8:** Illustration of bone formation in the porous structure and interfaces of bone ingrowth and porous implants.

(<https://www.intechopen.com/books/biomimetics-learning-from-ture/biomimetic-porous-titanium-scaffolds>)

### 2.5.1 Processing methods of porous Ti and its alloys

There are a variety of production methods to produce porous Ti and its alloys. These methods can be classified into four classes, as (i) liquid state processing, (ii) solid state processing, (iii) electro-deposition technique and (iv) vapour deposition method (Murray and Dunand 2004; Ryan et al. 2008; Torres et al. 2014b; Wang et al. 2017a; Yu et al. 2019). Fig. 2.9 shows the various processing methods of porous materials. However, the liquid state, and solid-state processing techniques are most commonly used to develop the metallic porous Ti alloys and described in this section.

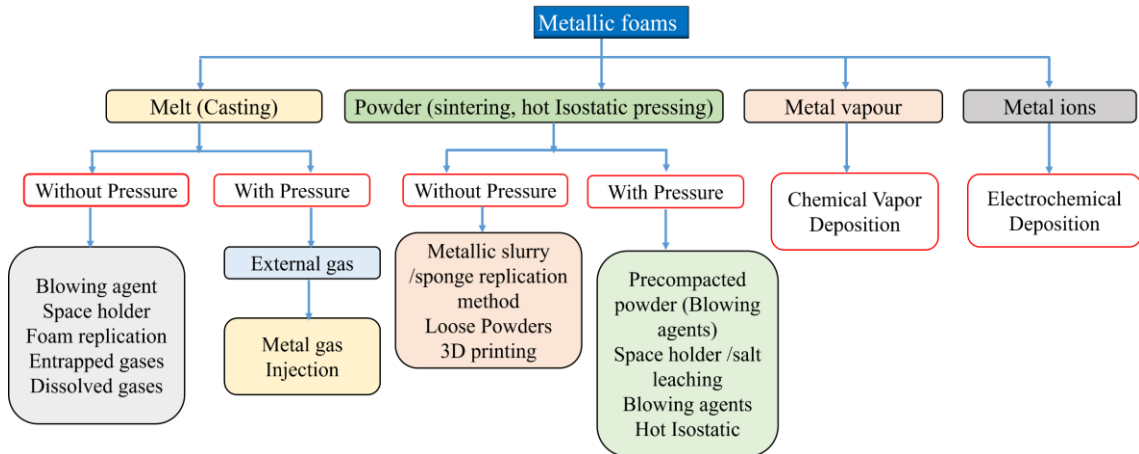


**Fig. 2.9: Classification of processing methods of metallic porous alloys (Singh and Bhatnagar 2018).**

#### 2.5.1.1. Liquid state processing

This technique mainly depends on how to develop a pores through gas bubbles. It is carried out by two methods namely, (i) direct foaming method by creating the gas bubbles, and (ii) indirect foaming method by blowing gas to generate the porous structure. Generally, this method is used for low melting point and low reactivity such as aluminium (Al) and zinc (Zn) (Srivastava and Sahoo 2007). However, it is difficult to process porous Ti due to high melting point (1668 °C) and high reactivity with the atmosphere (e.g., oxygen and nitrogen). The process costs would be high due to vacuum and liquifying as compared to solid processing techniques.

### 2.5.1.2. Solid state sintering processing

Solid state sintering processing (powder metallurgy) technique is one of the simplest and economical method which is an effective route to develop the porous Ti and its alloys. This processing technique helps to achieve a required porosity level, pore size distribution and most importantly avoid the possible oxidation on the developed porous Ti alloys. Various processing methods such as gas entrapped method, hollow sphere sintering, replication method, loose powder sintering and powder metallurgy space holder technique which are used to develop the porous Ti and its alloys are schematically presented in Fig. 2.10.

Gas entrapment processing technique is broadly used to produce porous Ti alloys for aerospace applications. In this technique, argon filled densified Ti powder is heated to high temperature which results in expansion of filled argon gas leading to formation of open and isolated pore structure as seen in Fig. 2.10 (a). It produces relatively low porosity level with the inhomogeneous pore distribution. Murray and Dunand., (2004) have developed porous Ti with the porosity of 29% and 44% using direct foaming by introduction of pressurized argon bubbles in molten metal of Ti.

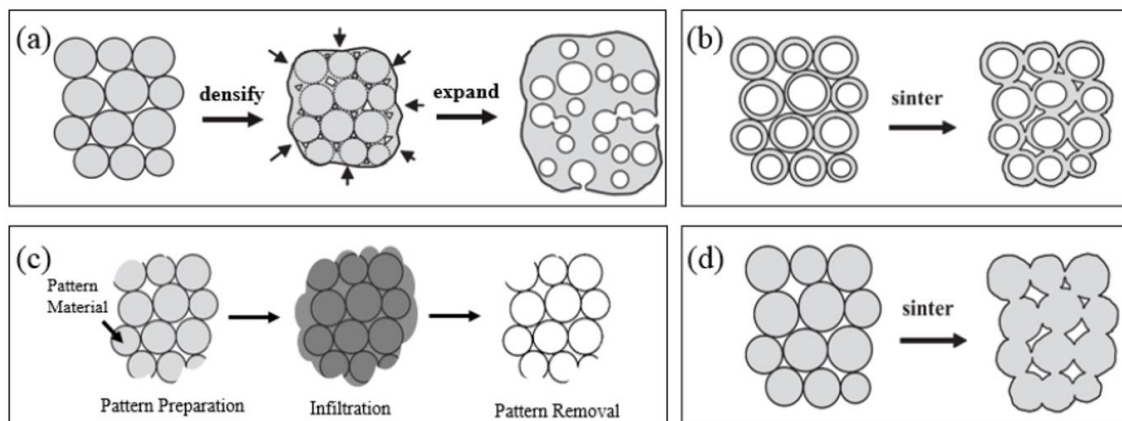


**Fig. 2.10: Different processing methods for porous Ti alloys; (a) gas entrapment technique, (b) hollow sphere sintering, (c) replication method and (d) loose powder sintering (Dunand 2004).**

Hollow sphere sintering (HSS) process is shown in Fig. 2.10 (b) for developing the porous alloys. This technique is used for producing Ni, Cu and Ti with suitable pore

structures. Yu et al.,(2019) have processed porous Ti6Al4V using HSS technique which is exhibited mixed porous structures containing open and closed pore structures. These hollow sphere structured alloys are widely used in high temperature applications.

Another solid-state sintering technique is replication method. By employing this method, a high porosity alloys can be developed using polyurethane (PU) as a template. Fig. 2.10 (c) presents the schematic representation of polymeric sponge replication method. A porous Ti scaffolds were fabricated by an improved polymeric sponge replication technique and characterized by Wang et al., (2017). Microstructure revealed uniform distribution of pores along with the interconnected macropores in the fabricated porous Ti scaffolds which is fairly suitable for biomedical applications. However, using this method for porous Ti, there is chances of getting oxidation of Ti powders during evaporation of polymeric template.

Loose powder sintering is the simplest powder metallurgy fabrication technique performed to make metallic porous implants. It is based on the partial densification of metal powders during sintering as demonstrated by Torres et al., (2014). They followed the main steps of powder preparation, compaction and sintering at relatively high temperature. They obtained the porous Ti with the porosities of 42% and 35% at the processing temperature of 1000 °C and 1100 °C respectively. Microstructure of the porous samples have irregular shaped and randomly orientated porosities as presented schematically in Fig. 2.10 (d).

### **2.5.2 Powder metallurgy space holder method**

The development of metallic porous implants with the powder metallurgy space holder method begins with the mixing of metal matrix powder and space-holding particles as depicted in Fig. 2.11. This includes the various small steps such as mixing of alloy powders and space holder materials, compaction process, removal of space holder and finally sintering process. However, it is important to note that choosing appropriate metal powder and space holder particles are a key factor in preparing the porous alloys. This is mainly because the properties of the developed porous alloys are affected by the characteristics of both metal matrix powder and space holding particles.

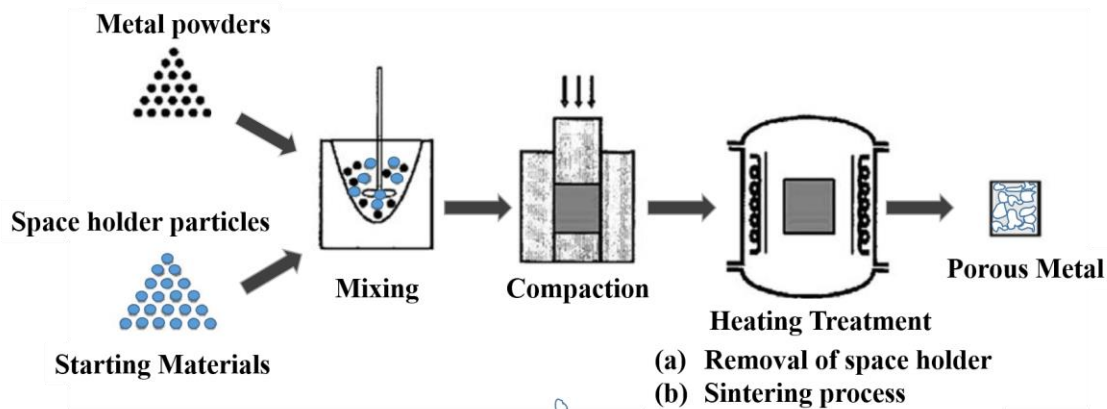


**Fig. 2.11: Schematic illustration of fabrication method of porous titanium with the space holder method (Arifvianto and Zhou 2014).**

### 2.5.2.1 Powder Selection and Preparation

There are two types of powder particles one may choose for development of porous implant alloys, (a) the pre-alloyed powders, and (b) blending of two or more elemental powders. In the pre-alloying technique, one or more elemental powders are mixed to prepare the base metal powder before the alloy is atomized into powder form (Aguilar et al. 2016b; Oh et al. 2003). In case of blending elemental technique, individual elemental powders are mixed together using ball milling process. During the ball milling, select the suitable ball to powder ratio and duration of milling to prepare the alloy powders. On the other hand, choosing the space holder particles is one of the important criteria which has direct influence on the pore morphology and mechanical properties of the porous implant alloys. Various space holder materials and their suitability to develop the porous implants are listed in Table. 2.3. The selection of space-holding particles must be based on the following criteria:

- Biocompatibility and non-toxicity
- Chemical stability
- Removal capability

**Table 2.3: Space holding particles and considerations in selection for metallic biomaterials.**

Space holder material	Reasons of selection	References
Ammonium hydrogen carbonate	Low decomposition temperature	Wang et al. (2011)
Carbamide	Highly soluble in water	Arifvianto et al. (2015)
Saccharose	Soluble in water, biocompatible	Jakubowicz et al. (2013)
Sodium chloride	Soluble in water, biocompatible	Torres et al. (2012)
Magnesium	Biocompatible	Kalantari et al.(2015)

### 2.5.2.2 Blending

Blending of both the metal powders and space holder materials are performed as the first step of development of porous alloys. The pore morphology which includes micropores, macropores, and interconnected pores are entirely depend on the characteristics and amount of space holder particles. The importance of the mixing process on the pore distribution of porous alloys was emphasized by several authors (Aguilar et al. 2016b; Li et al. 2015).

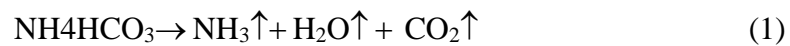
### 2.5.2.3 Compaction

Compaction process is performed after blending of metal powder and space holder particles. During compaction, blended powder particles are compacted under the uniaxial load to obtain the green compacts. The stages involved in the powder compaction process have been well described in the literature (Arifvianto et al. 2015). Many techniques have been used for compaction process. Similar to those used in the fabrication of metallic scaffolds, i.e., uniaxial die compaction (Nouri et al. 2011); isostatic compaction (You et al. 2020) and injection moulding (Zhao et al. 2015). Several studies have reported the compacting pressure ranging from 200–800 MPa to prepare the green compacts and it significantly influences on the porosity level in porous Ti alloys (Arifvianto et al. 2015; Li et al. 2015). During compaction, the number

of contact points and contact area increases, which leads to densification in green compacts (Smorygo et al. 2012).

#### **2.5.2.4 Space Holder Removal**

The removal of space holder particles from the green compacts is very much important to produce the good quality of porous alloys, in order to prevent contamination from the residual space holder particles. It also helps to obtain the micropores, macropores and interconnected pore structures in the porous alloys. Space holder removal is achieved by means of heat treatment process, which lead to evaporation of particles due to thermal decomposition. The study using ammonium bicarbonate ( $\text{NH}_4\text{HCO}_3$ ) as space holder to produce the pore structure reported that decomposition of  $\text{NH}_4\text{HCO}_3$  particles started at about  $50\text{ }^\circ\text{C}$  and the reaction continued until this space holder material was completely removed at  $175\text{ }^\circ\text{C}$ . The decomposition of  $\text{NH}_4\text{HCO}_3$  particles from the green compacts is in accordance with following equation (Li et al. 2015; Zhang et al. 2017):



#### **2.5.2.5 Sintering process**

Sintering is performed at high temperatures which increases the bonding between metal powder particles in the sintered alloys. The bonded metal powder particles build up the porous structure in porous alloys. Final pore morphology of the metallic porous alloy depends on the sintering ability. At the beginning, inter-particle bonds and necks are formed at powder particle contact points. Atoms of powder particles are thermally activated, leading to mass diffusion and neck growth at inter-particle contact points. As sintering proceeds, voids at powder particle interstices are rounded, along with densification and grain growth that occur simultaneously. At the end of sintering, powder densification keeps occurring but at a slower rate than the earlier stage of the densification process. Ti and its alloys are processed at the sintering temperature ranging from  $1000\text{ }^\circ\text{C}$  to  $1500\text{ }^\circ\text{C}$  (Karre et al. 2019; Rao et al. 2014b).

The microstructural characteristics, mechanical properties, electrochemical corrosion and tribocorrosion behavior, surface bioactivity and cytotoxicity behavior of the sintered alloys are discussed in the following sections.

### **2.5.3 Advantages and disadvantages of PM method**

There are many benefits of using powder metallurgy technique to produce the porous alloys, and few limitations of powder metallurgy as follows:

#### **Advantages**

- Rate of production is high.
- Low operating cost.
- The possibility of producing near net shape product.
- Components with wide variations in compositions and materials can be produced.
- Porosity and pore size can be tailored using appropriate space holder materials.

#### **Disadvantages**

- Rate of production is high.
- The complicated objects has to eject from the die without fracture, more complicated shapes cannot be produced.
- It is very difficult to produce homogeneous distribution of pore structures.

## **2.6 Development and characterization of porous Ti alloys**

### **2.6.1 Microstructural and Mechanical properties**

The mechanical properties of porous implant alloys used in biomedical applications can be altered with changing the porosity level. Changing the porosity level can alter the compression strength, elastic modulus and density of the implant alloy which is preliminary requirement to use for biomedical applications (Yu et al. 2019).

Xiao et al., (2013) have have fabricated porous Ti implant with the addition NaCl as space holder materials to form pore through PM method. The CP-Ti powder blended with the NaCl and compacted at applied load of 180 MPa to prepare green compacts. Then, green compacts were heat treated at 800 °C for 8 h and sintered 1200 °C for 8 h to obtain the porosities. They have reported porosities of 39%, 41%, 50%,



and 63%. Microstructure of the porous alloys exhibit micropores, macropores and interconnected pore structures with the pore size more than 100  $\mu\text{m}$ , which is essential to use as porous implant as depicted in Fig. 2.12. It was found that the elastic modulus and the compression strength decreased with increase in porosity as shown in Fig. 2.13. The compression strength and the elastic modulus are in the range from 468 to 94 MPa and 18 to 2.7 GPa, respectively. The results showed a significant influence of porosity and pore size on the compression strength and elastic modulus of the porous Ti sample.

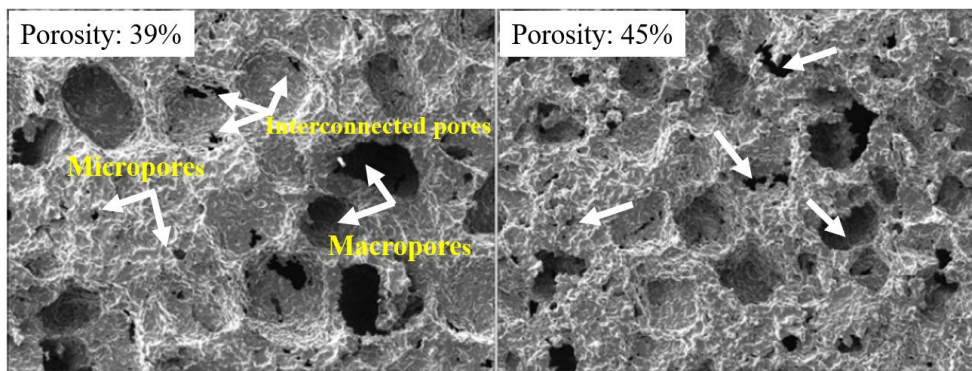


**Fig. 2.12: SEM micrographs of porous Ti with porosity level of 39% and 45% (Xiao et al. 2013).**

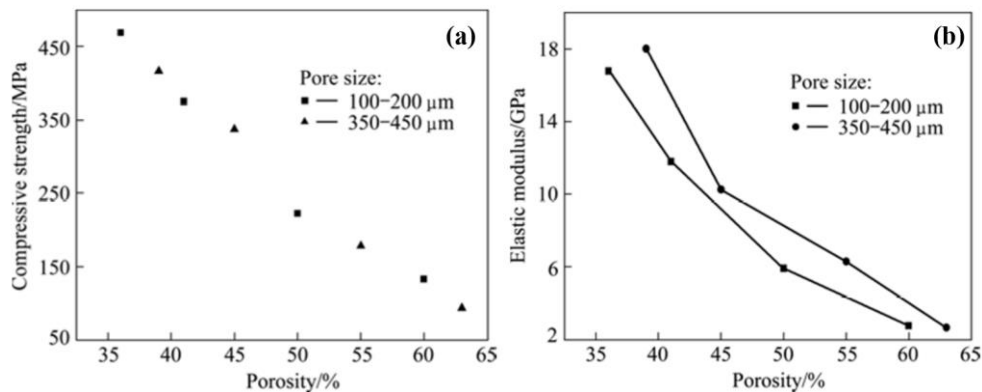


**Fig. 2.13: (a) Compressive strength, (b) Elastic modulus of sintered porous titanium as function of porosity (Xiao et al. 2013).**

Rao et al., (2014) have reported a study on porous Ti–20Nb–15Zr alloy with the porosity of 6% to 62% by the addition of  $\text{NH}_4\text{HCO}_3$  contents for 0% to 50 wt. % through PM space holder method. It was found that there was reduction in the compression strength from 1550 MPa to 65 MPa, and elastic modulus from 11 GPa to 2.5 GPa for the porosities of 6% to 62%, respectively. They also described the compression

behavior of porous alloy as depicted shown in Fig. 2.14 (insight; SEM image of porous alloy with 62% porosity).

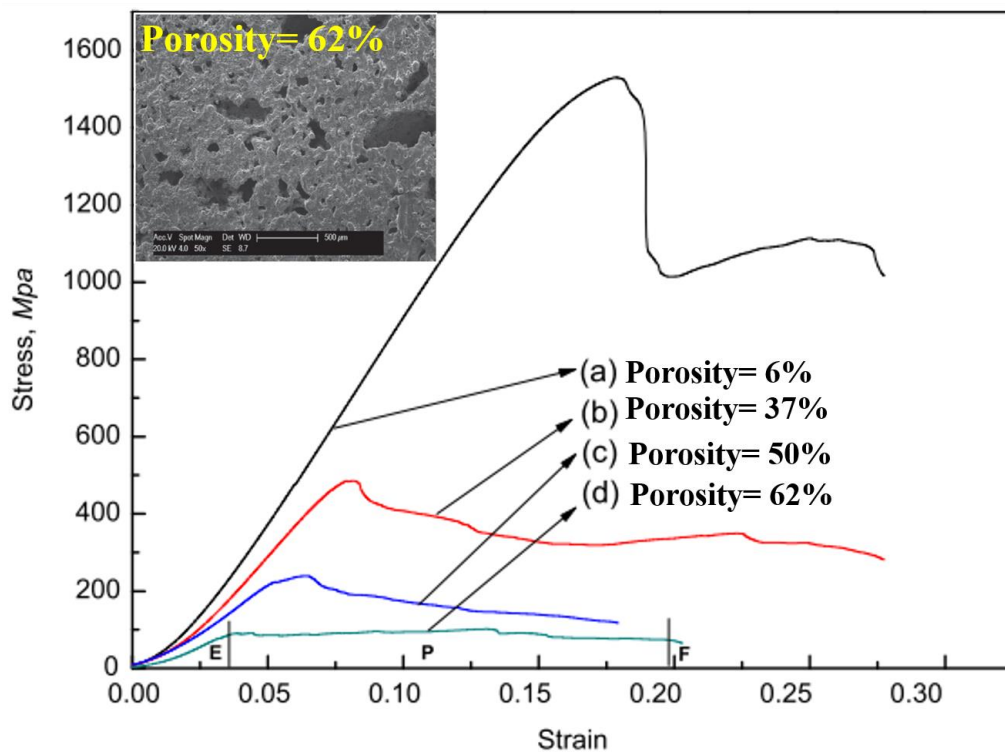


**Fig. 2.14. Compressive stress–strain curves of the porous Ti–20Nb–15Zr with various porosity level (Rao et al. 2014a).**

There are three distinct stages: (a) linear elastic deformation stage; in which the pore walls may deform elastically (E zone), (b) a plastic yield stage up to a peak stress in which the walls may deform plastically (P zone), and (c) a densification and fracture stage in which the walls may collapse (F zone). However, the P zone which corresponds to the plastic deformation taking place, where the pore structure deforms by sliding each other under the stress. Porous alloy which have low porosity can resist the sliding moment between the pores, where strength of the pore cell wall is high. While, the high porosity samples can easily deform through collapse of pores under the stress due to the low strength of cell wall. Thus, the compression behavior of porous alloy significantly depends on the porosity levels. Similarly, various researchers developed porous Ti-based alloys through PM space holder method and investigated for microstructural

characteristics and mechanical properties of the porous alloys. Table. 2.4 gives a summary of such studies.

**Table 2.4: Various new combination of porous Ti-based alloy and their properties.**

Alloys	Processing Method	Summary	References
Porous Ti-10Nb-10Zr	NH <sub>4</sub> HCO <sub>3</sub> was added with 20, 30, 40, 50 and 60 wt. % to the 4 h ball milled powder of this alloy. Mixture of this powder was compacted to prepare green compacts. Then, compacts were heated to 175 °C, and sintered at the temperature of 1200 °C for 10 h.	Porous alloys possessed the porosities of 42%, 50%, 59%, 69% and 74% for the addition of various amount of NH <sub>4</sub> HCO <sub>3</sub> . However, the porous alloy with 59% porosity showed the compatible mechanical properties. They reported compressive strength of 137 MPa and elastic modulus of 5.6 GPa.	(Wang et al. 2009)
Porous Ti-10Mg	Ti and Mg powders blended for 5 h. NH <sub>4</sub> HCO <sub>3</sub> (0-30 wt. %) added to blended powder and compacted at 300 MPa. Sintered at 1200 °C for 5 h in vacuum atmosphere.	Microstructure of alloy consists Ti and Mg phases are main constituents. Porosity obtained about of 13 to 50%. Porous alloys possessed elastic modulus and compressive strength obtained about 174-646 MPa and 20.2-43.7 GPa, respectively.	(Wang et al. 2011)
Porous	Elemental powders of Ti and Ag ball milled for 1, 2, 5 and 10 h. Then, 50 % of urea added as pore former. Mixture was compacted	Results shows that there was gradual reduction in particle size with increase in ball milling time. It was observed that the porosity reduced from 64% to 53%, while compression strength increased from 15 MPa to 53	

Ti–Ag	at 100 MPa. Compacts were heated to 250 °C for 1 h to burn urea and sintered at 1350 °C for 2 h in Ar atmosphere.	MPa, and elastic modulus increased from about 1 GPa to 1.9 GPa. This results attributed to significant reduction in powder particle size.	(Hou et al. 2013)
Porous Ti–7.5Mo	Elemental powders were ball milled for 3, 15 and 30 h. Alloy powder mixed with 60 vol. % of NH <sub>4</sub> HCO <sub>3</sub> , and compacted at an applied load of 200 MPa. Then, sintered 1100 °C for 5 h.	They observed that the reduction in average particles size for the ball milling time for 3 h and 15 h. While, remarkably increase in the average particle size for 30 h, The sintered porous alloys possessed porosity of 63%, 61% and 67%. They found the compression strength of 19, 25 and 8 MPa, and elastic modulus of 1.2, 1.7 and 0.5 GPa.	Hsu et al., (2014)
Ti–6Al–4V foams	The alloy powder ball milled for 6 h and various Mg contents (30, 45 & 60 vol. %) were added to develop various porosity level. Then, compacts were sintered at 1200 °C for 3 h.	Porous alloys obtained with the porosity ranging from 47, 54, and 64% with an average macropore size more than 400 μm. The compression strength of about 132, 97 and 72 MPa and the elastic modulus of 47, 41, 37 GPa were reported for different porosities.	(Kalantari et al. 2015a)
Porous Ti–16Nb	The elemental powders of Ti and Nb was mixed for 2 h using ball mill. The NH <sub>4</sub> HCO <sub>3</sub> with the 0, 30, 50, 70 vol. % were added to blended powders and compacted	The microstructure of sintered porous shows that the formation of α+β type phases, which helps to reduce the elastic modulus. With the addition of various amount of NH <sub>4</sub> HCO <sub>3</sub> contents porosity increased from 4% and 60%, while, the density decreased from 4.67	Eren et al., (2018)

	<p>at an applied load of 200 MPa. Compacts were sintered at 1200 °C for 3 h under vacuum atmosphere (<math>10^{-5}</math> mbar).</p>	<p><math>\text{g/cm}^3</math> to <math>1.91 \text{ g/cm}^3</math>, respectively. It was noticed that there was decrease of compression strength from 1450 MPa to 100 MPa, while elastic modulus reduced from 96 GPa to 15 GPa, respectively.</p>	
--	--	--	--

### 2.6.2 Electrochemical corrosion behavior

The reaction of the metallic ions that leaches away from the implant due to electrochemical corrosion in the human body affects several biological parameters. As a material starts to corrode, the dissolution of metal will lead to loss which in turn will eventually lead to brittleness and fracture of the implant. Once the material fractures, corrosion gets accelerated due to increase in the amount of exposed surface area and loss of protective metal oxide layers. If the metal fragments are not surgically extracted, further dissolution and fragmentation can occur, which may result in inflammation of the surrounding tissues. Many researchers have studied the effect of pore structure on the electrochemical corrosion behavior in various physiological solutions is discussed briefly as:

Eren et al., (2018) have developed and carried electrochemical corrosion properties of porous Ti–16Nb alloy with the different porosities (23% and 60%) samples in simulated body fluids (SBF) solution at 37 °C. Electrochemical corrosion behaviour of porous alloy were examined by introduction of porosity through using potentiodynamic polarization and electrochemical impedance spectroscopy (EIS) techniques as presented in Fig. 2.15. It is observed that the corrosion potential (Saturated calomel electrode as reference) and corrosion current density of  $-407 \text{ mV}$  and  $0.351 \text{ }\mu\text{A/cm}^2$  for 23% porosity, and  $-405 \text{ mV}$  and  $2.21 \text{ }\mu\text{A/cm}^2$  for 60% porosity, respectively. Similarly, Nyquist and Bode plots obtained by EIS study show that a significant reduction in semicircle radius (capacitive loop), modulus of impedance and phase angles of high porosity alloy.

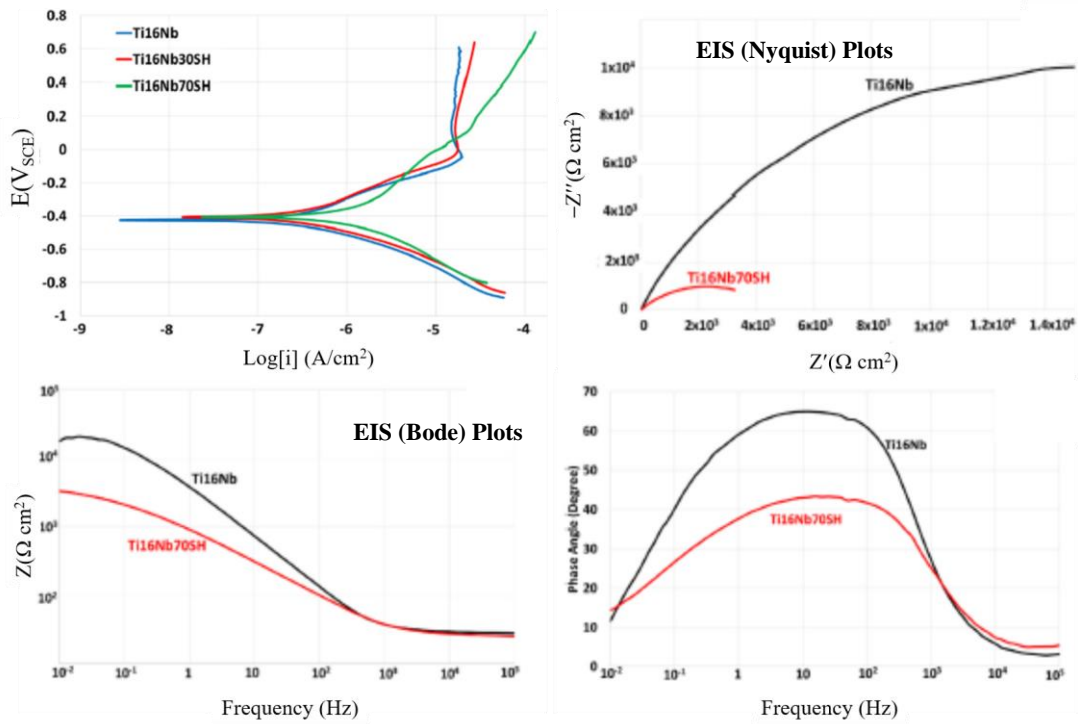


**Fig. 2.15: Electrochemical corrosion behavior of porous Ti–16Nb alloy with different porosities in SBF solution at 37 °C (Eren et al. 2018).**

It is noticed that the corrosion potential decreased, while corrosion current density increased due to introduction of porosity in the bulk alloys. It showed that the increment of the porosity lowered the corrosion resistance for reasons such as the exposure of a larger surface area to the electrolyte, heterogeneous oxide film or the insufficient thickness of oxide film due to the difficulty involved in electrolyte penetration between porosities. Similarly, various studies have demonstrated the effect of pore structure on the electrochemical corrosion behavior of porous Ti alloys in physiological solutions as listed Table. 2.5.

**Table 2.5. Electrochemical corrosion behavior of porous Ti-based alloys in SBF solution.**

Alloys	Environment	Summary	References
Porous Ti-39Nb	Corrosion properties of porous alloys (porosity ranging from 0% to 33% processed by PM method and) evaluated in Simulated body fluid at 37 °C.	The results of measurements proved the occurrence of a localized form of corrosion in the material with a porosity of 24% and 33%. Distinct localization of the corrosion process was recorded in an environment containing fluoride ions. In addition, there was formation of microcells on porous materials, which significantly influenced corrosion behaviour of material.	(Fojt 2013)
Porous Ti-(4-10)Mo	The porous alloys with the porosity ranging from 36% to 61% examined for corrosion behavior in SBF solution at 37 °C, with the exposed surface area of 1 cm <sup>2</sup> .	The electrochemical characteristics are principally controlled by porous features. Potentiodynamic polarization results reveal that $E_{corr}$ values decrease and $i_{corr}$ values increase with the increase of porosity, indicating a reduced corrosion resistance. EIS study revealed two time constants and showed that lower capacitance values and larger impedance values for samples with lesser porosity than those of higher porosity.	(Xie et al. 2015)
	Porous alloys having porosity of 24% 39% 52% were examined	Results indicated that the decreases in corrosion potential from -328 mV to -430 mV, while corrosion current	

Porous Ti-10Cu	corrosion properties using aerated electrolyte of 0.9 wt.% of NaCl	density increases from 0.1 $\mu\text{A}/\text{cm}^2$ to 0.5 $\mu\text{A}/\text{cm}^2$ with increase porosity in alloys. The higher interconnectivity of pores of the higher porosity alloy will result in the free flow of the electrolyte in the pores or cavities as well as the inhomogeneous electron transfer reaction.	(Li et al. 2017)
Porous Ti-10Mo	Corrosion properties of porous alloys having porosity level from 50–66% examined in physiological solution at 37 °C, with the exposed surface area of 1 $\text{cm}^2$ .	With rising of porosity, the corrosion potential of porous alloy in PBS shift to negative direction, while corrosion current density increases significantly. The corrosion rate of the Ti-10Mo increases exponentially with increase in porosity, and is much lower than that of CP Ti with similar porosity.	(Xu et al. 2018)

### 2.6.3 Tribocorrosion properties porous Ti alloys

Tribocorrosion behavior of implant materials is vital examination for more practical usage in biomedical sector. In this regard, various processing parameters and their effects on properties of implant alloys under the loading condition are of great concern. The synergic effect of both the wear and corrosion leads to damage of implant surface resulting in degradation of materials in the form the wear debris. However, the mixed debris can be compacted on the worn surfaces, forming oxidized patches, whereas some of these debris may adhere on counter-body surfaces that can abrade the metal leading to the formation of grooves on the worn surfaces.



The schematic diagram illustrating the wear of implant material is shown in Fig. 2.16. The summary of a few studies which have been conducted to explore the effects of pores structure and applied load on tribocorrosion properties of porous implant alloys in physiological solution are presented in this section.

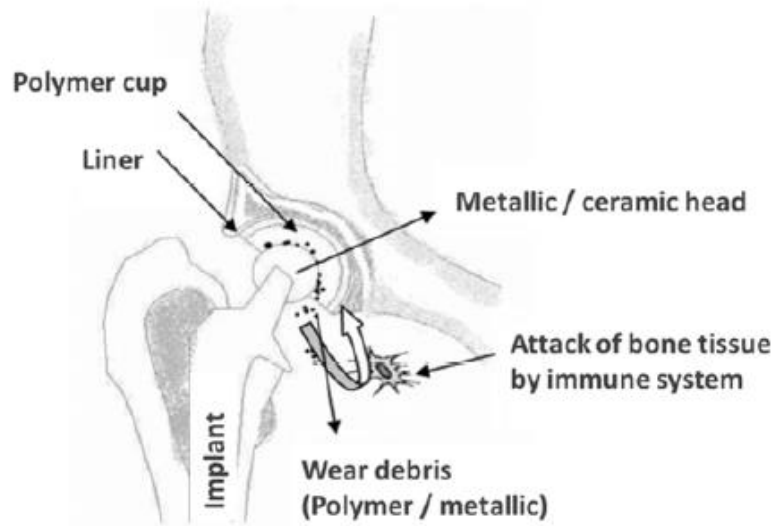


**Fig. 2.16: Schematic diagram of Wear of implant (Geetha et al. 2009).**

In a study by Fellah et al.,(2019) who carried out the preliminary tribocorrosion test on porous Ti–15Nb alloy in phosphate-buffered saline (PBS) solution. Various loads such as 3 N, 7 N and 10 N were applied on the porous sample to investigate the open circuit potential and potentiodynamic polarization behavior. It was found that the open circuit potential (OCP) was decreased in both the porous alloy with increase in applied load. However, it was observed that the reduction in OCP values from  $-310$  to  $-380$  mV (SCE) when the applied load increased from 3 to 10 N of porous Ti–15Nb alloy as shown in Fig 2.17 (a). Fig 2.17 (b) shows potentiodynamic polarization curves of porous alloy with the application of different applied loads. It is reported that the reduction in the potential values, while increase in corrosion current density with applied load increased. Result indicates that the corrosion directly contributed and also increases the wear with enhancing load, which leads to more material loss.

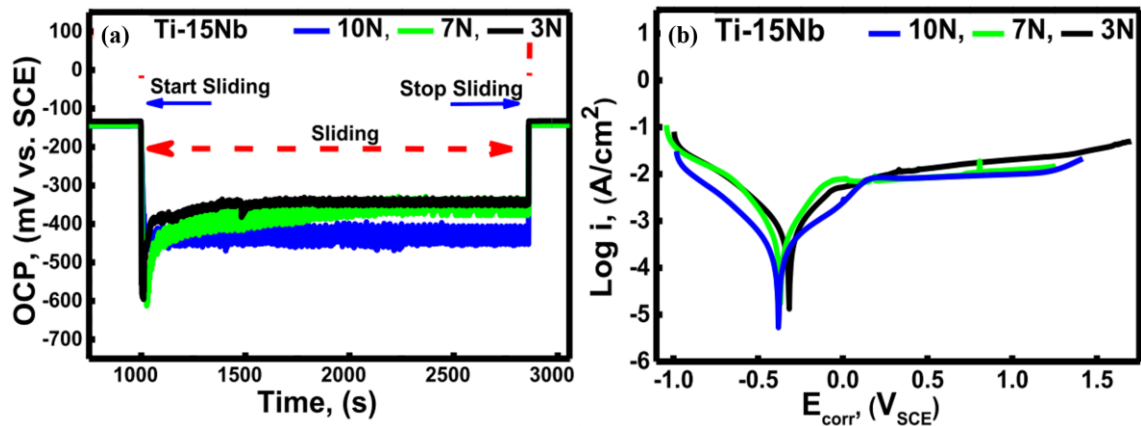


**Fig. 2.17. Tribocorrosion result of porous Ti-Nb alloy under the various loads in physiological solution; (a) OCP recorded with respect to time, (b) potentiodynamic polarization curves (Fellah et al., 2019).**

Another tribocorrosion study by Toptan.,(2017) has been reported on porous Ti have porosity of 22% and 37% developed by PM space holder method. The tribocorrosion properties of porous Ti samples examined at an applied load of 3 N against counter surface (Zirconia) pin in NaCl solution. It is noticed that the stabilization OCP values before sliding were decreased in porous Ti on increasing in porosities. This alteration may be attributed to the difference on the nature and quality of the native oxide films between the one formed on the outmost surface and on the pore surfaces. When sliding started, a sudden decrease in OCP values was observed for both porous samples, due to the mechanical damage of the passive film, leading to the formation of the active sites on the worn surfaces, that is the typical behavior of the passive metals under sliding. It is known that OCP values obtained during sliding are mixed potential values, reflecting both the active (worn) and passive (unworn) surfaces. After sliding, the OCP values were rapidly increased and stabilized as initial potential.

#### **2.6.4 Surface modification and hydroxyapatite formation**

In order to accomplish desired biological integration of Ti implants with bone tissues, surface modification methods is required. One of the reasons is to clean the contaminated materials surfaces previously formed during production due to plastic deformation which leads to the formation of non-uniform coating layer on substrate surfaces. Also, insufficient osseointegration capability is another reason for surface

modification of Ti and its alloys, since the major limitation of a metallic material for long term survival in the body is the lack of a stable biological fixation to living bone (Wang et al. 2017c). Although biomaterials are classified into bio-tolerant, bioactive or bio-reabsorbable materials, their biological response will depend on their surface properties and thus can be modified through surface treatments. This plays a crucial role in biocompatibility, where surface roughness, topography, and chemistry are the critical parameters to be evaluated in osseointegration. Further, it has been demonstrated that with suitable surface properties titanium can act as a bioactive material promoting the formation of hydroxyapatite. Fig. 2.18 summarizes the main reasons for the development of new alloys and surface treatments.

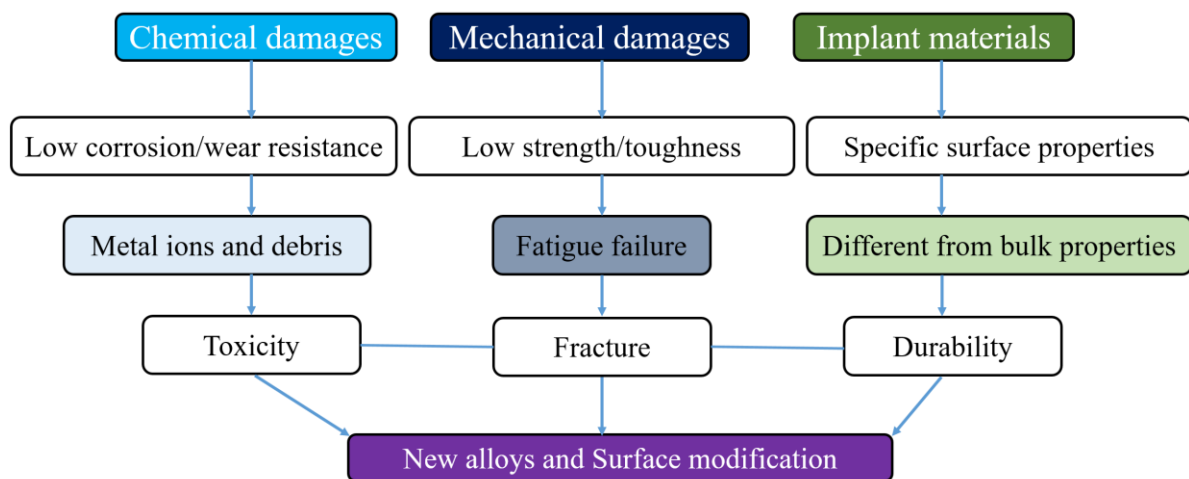


**Fig. 2.18: Reasons for the research on surface modification and new alloys (Kokubo et al. 2010).**

#### 2.6.4.1 Surface modification techniques

Various researches have been conducted to adjust the bioactivity of Ti and its alloys by common surface modification techniques such as mechanical, physical and chemical methods are summarized in Fig. 2.19. In most of the mechanical methods like machining, grinding or polishing, the purpose is to increase the surface roughness by physical forces. While, in physical methods, like thermal spraying and ion beam deposition, focus is on the deposition of a biocompatible layer by using electrical, kinetic and thermal energy.

However, these techniques are not appropriate for surface modification of Ti alloys having complex geometries in the form of porous structures due to difficulty in treating the whole surface homogeneously. Chemical methods which are relatively more suitable techniques for surface modification of porous type implant materials. These are described in the following section.

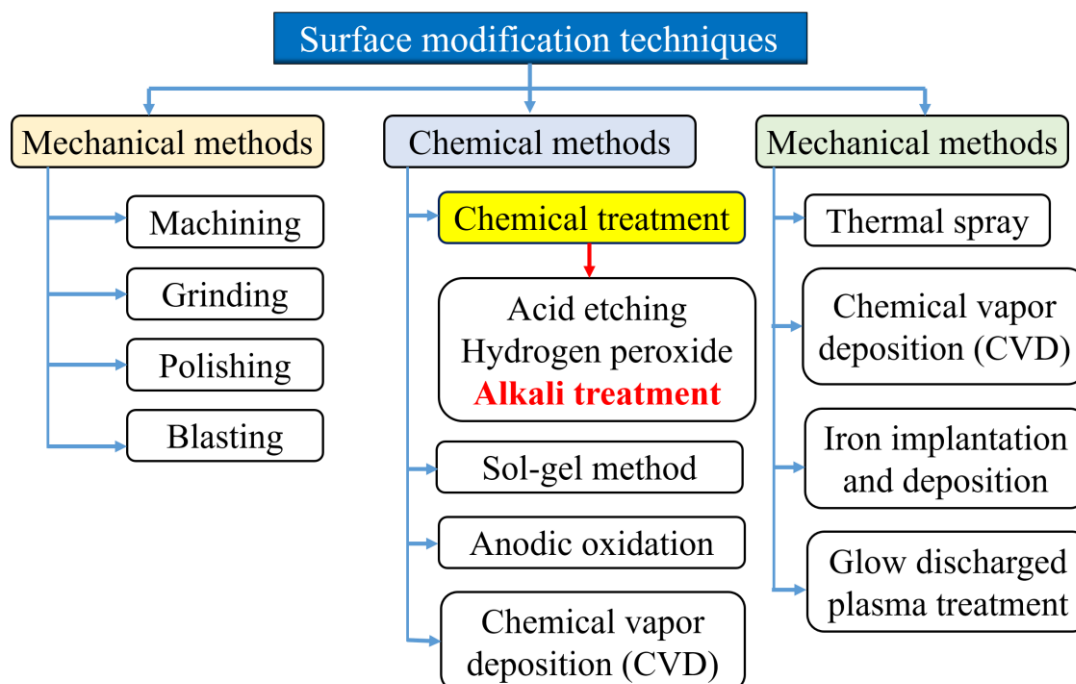


**Fig. 2.19: Classification of surface modification techniques for titanium and titanium alloys (Kokubo et al. 2010).**

#### 2.6.4.2 Chemical methods:

Chemical methods consist of chemical vapour deposition (CVD), sol-gel method, anodic oxidation, biochemical method and chemical treatments. Among, these methods chemical treatments demonstrate the excellent interaction between the interface of implant and solution. Chemical treatment such as acid etching, hydrogen peroxide ( $H_2O_2$ ) and alkali treatments (Fellah et al. 2019a) are most commonly used to modify the surface of Ti alloy which has pore structures.

Alkali treatment has become a popular technique because of its simplicity and easy to control the process parameters. Alkali treatment can be basically described as a simple surface modification technique to modify the Ti implants. By using aqueous

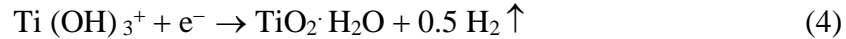
solutions containing sodium hydroxide (NaOH) or potassium hydroxide (KOH) we can obtain bioactive sodium or potassium titanate layer.

The titanate layer obtained by alkali treatment on titanium substrates allows apatite nucleation and enhances bioactivity and bone regeneration on the implant surface.

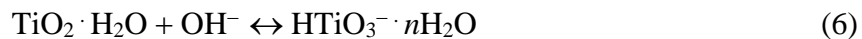
Liu et al., (2004) first reported alkali and heat treatment to improve the bioactivity. The method enables the formation of a biologically active bone-like apatite layer on the surface. In this process, implant materials are first immersed in 5–10 M NaOH or KOH solution for 24 h, followed by rinsing with distilled water and ultrasonic cleaning for 5 min. The specimens are then dried in an oven at 60 °C for 24 h and finally heated to around 600–800 °C for 1 h. During the alkali treatment, the TiO<sub>2</sub> layer partially dissolves in the alkaline solution because of the attack by hydroxyl groups.



This reaction is assumed to proceed simultaneously with hydration of Ti alloys.



Further, hydroxyl attack on the hydrated TiO<sub>2</sub> produces negatively charged hydrates on the surfaces of the substrates as follows:



These negatively charged species combine with the alkali ions in the aqueous solution to produce an alkaline titanate hydrogel layer. During heat treatment, the hydrogel layer is dehydrated and densified to form a stable amorphous or crystalline alkali titanate layer. These layers significantly influence on the formation of hydroxyapatite on the surface of Ti alloys. Fig. 2.20 shows the schematic representation of structural changes on Ti metal during alkali and heat treatments.

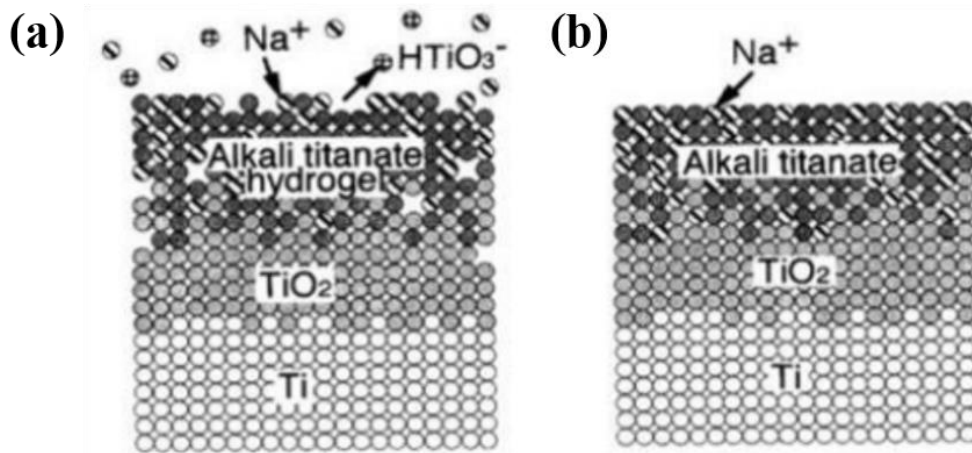


**Fig. 2.20: Schematic representation of surface structural change of Ti metal during alkali and heat treatments (Kohn 1998).**

#### 2.6.4.3 Hydroxyapatite formation

Hydroxyapatite formation on implant materials is one of the widely used methods to understand the bioactivity characteristics of implants when inserted into human body, although there is no general rule for determination of bioactivity. However, it is very much essential for most of the bio-implants like Ti alloys to investigate the bonding to living bone *in vivo*. This can be done by studying the formation of bone-like hydroxyapatite on the surface when immersed in SBF by conducting the *in-vitro* tests. The implant materials have excellent hydroxyapatite formation on their surface providing many advantageous such as good biological fixation, and corrosion resistance. Fig. 2.21 shows the schematic illustration of hydroxyapatite formation on the Ti alloys when immersed into SBF solution.

The alkali heat treated Ti alloy samples when immersed in SBF, simultaneous reactions take place between the functional group of Ti-OH and ions present in the SBF (Kokubo et al. 2003). It was found that the surface of the sodium titanate was highly negatively charged in the SBF and the formation of hydroxyapatite on the substrate surface mainly depend on the immersion time. The surface potential increased with increasing soaking time to a maximum positive value. Thereafter, it is decreased with increasing soaking time, reached a negative value again, and finally converged to a constant negative value (Raman et al. 2007). However, the Ti-OH groups formed on

the surface of sodium titanate after soaking in SBF are negatively charged and hence, combine selectively with the positively charged  $\text{Ca}^{2+}$  ions in the fluid to form calcium titanate, as demonstrated in Fig. 2.21.

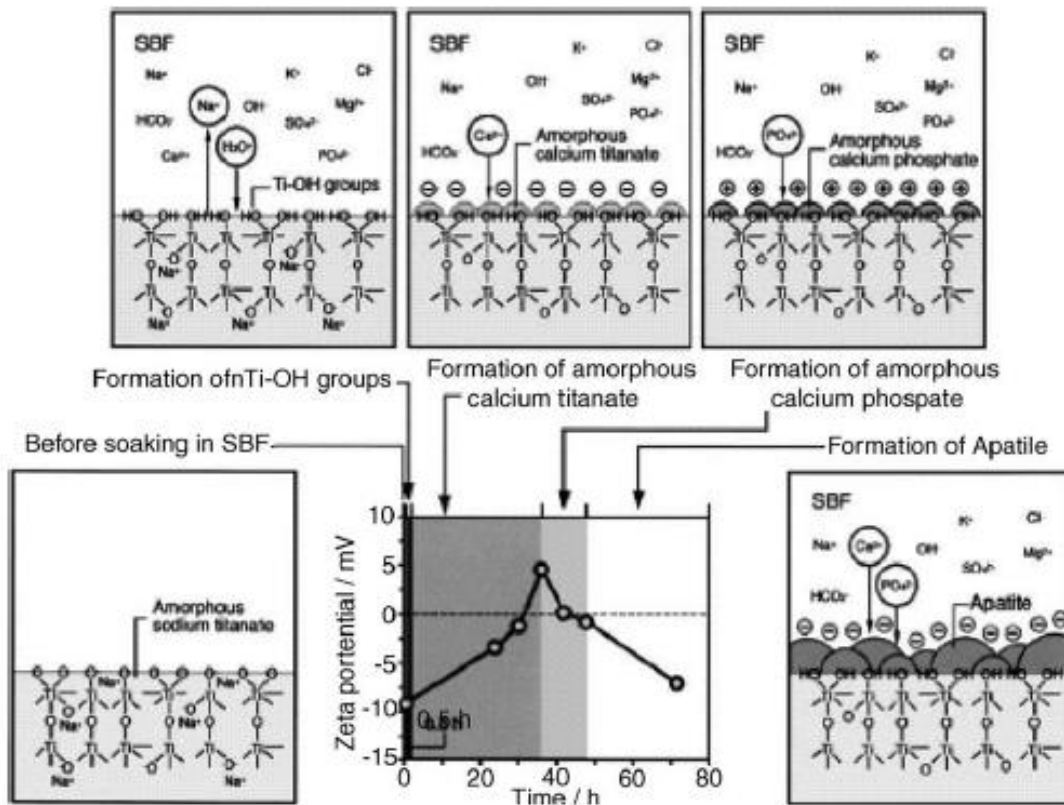
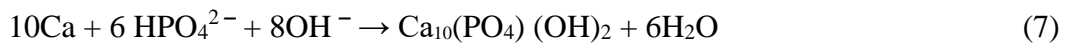


**Fig. 2.21: Schematic representation of changes in surface structure as hydroxyapatite formation on the surface of Ti alloy after immersion in SBF (Liu et al. 2004).**

The mechanism of hydroxyapatite formation on the surface of implants is highly dependent on surface treatment by the alkaline solution, which assists the surface of Ti alloy for nucleation and increase the growth of hydroxyapatite. The alkali treatment increases the ability to absorb  $\text{OH}^-$  ions on the surface.  $\text{Na}^+$  ions are released from the sodium titanate into SBF and increase the pH. The negatively charged ions are formed due to the presence of  $\text{HTiO}_3^-$  on the alloy surface, which combines with  $\text{Ca}^{2+}$  ions by Coulomb's force (Gao et al. 2012a).

Meanwhile,  $\text{HPO}_4^{2-}$  group of ions from the hydrogen bond, are attracted by  $\text{Ca}^{2+}$  ions in SBF. The enhancement of  $\text{Ca}^{2+}$ ,  $\text{HPO}_4^{2-}$ , and  $\text{OH}^-$  ions in the aqueous solution improve the degree of supersaturation with respect to hydroxyapatite. Once the apatite starts nucleating, it consumes  $\text{Ca}^{2+}$ ,  $\text{HPO}_4^{2-}$ ,  $\text{OH}^-$  ions and spontaneously grows on the alloy surface. The hydroxyapatite formation can be produced according to the following reaction in SBF (Kohn 1998).



Several studies have been investigated for surface modification and bioactive surface modification of porous Ti alloys using alkali treatment and immersion in SBF (Kohn 1998) (Butev et al., 2015).

Gao et al.,(2012) have developed porous Ti-Mo alloy through PM method using  $\text{NH}_4\text{HCO}_3$  (25 wt. % ) space holder materials. This porous alloy sample was evaluated for bioactive surface by immersing in SBF at 37 °C for various immersion time of 7, 14 and 28 days. SEM microstructure revealed that the formation of bone-like hydroxyapatite formation on the porous alloy surface as seen in Fig. 2.22(a). Also, it is found that the deposition of more apatite granules became larger deposition on the alloy surface with increasing the immersion time in SBF solution. These hydroxyapatite particles facilitate the new bone in growth which enhance the chemical bonding of interfaces. They also examined the surface tomography of the porous alloys after immersion in SBF for different immersion time. It was observed that there was decrease in the ridges and roughness of the surface due to the formation of large hydroxyapatite particle formation on the porous alloy surface as shown in Fig. 2.22(b). Many researchers have developed different porous Ti-based alloys and examined their hydroxyapatite formation on surface of alloys as listed in Table. 2.6.



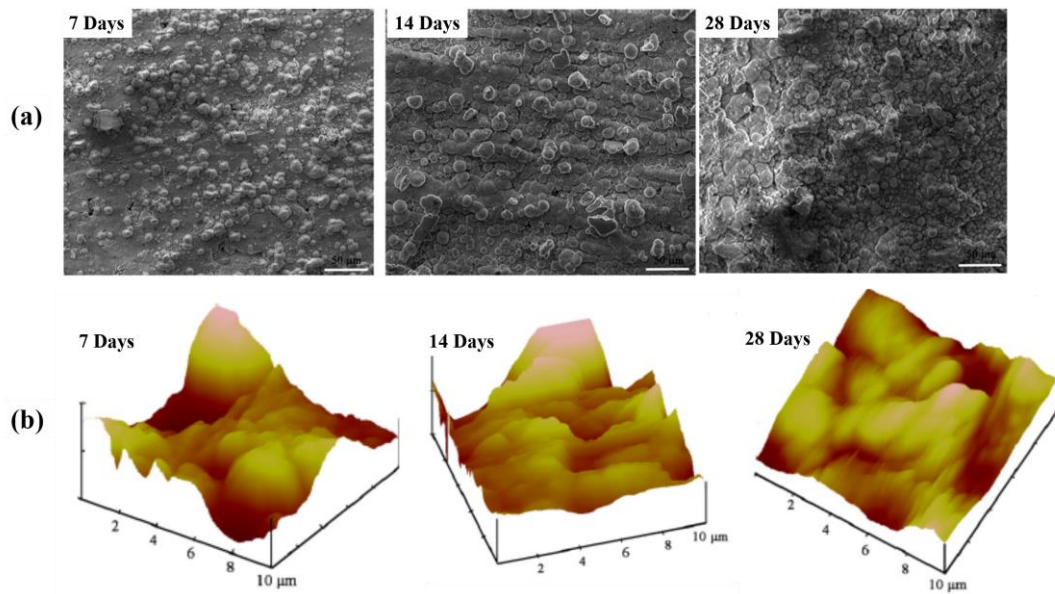


**Fig. 2.22: Porous Ti-Mo alloy after immersion in SBF for 7, 14, and 21 days: (a) SEM microstructure of hydroxyapatite formation, and (b) AFM tomography (Gao et al. 2012).**

**Table 2.6: Surface modification and hydroxyapatite formation on various porous Ti alloys in SBF solution.**

Alloys	Environment	Summary	References
Porous Ti	Alkali treatment 5 M NaOH aqueous solution at 60 °C for 24 h. Samples were immersed in SBF at 37 °C for 14 days.	Results indicated that, a dense and uniform apatite layer covered the surface of NaOH treated sample. There is no obvious formation of apatite on the untreated sample after 14 days.	Hsu et al. (2013)
Porous Ti-3Ag	Four different (Ball milling time 1-10 h) samples were treated	The results, indicate that longer ball milling time provides higher surface energy by powder refinement. Hence, the	Hou et al. (2013)

	Hydrothermally using 5.0 M NaOH solution and followed by immersion in SBF.	samples with longer ball milling time and little Ag content possess better apatite-inducing ability.	
Porous Ti-6Al7Nb	Alkali treated using 5 M of NaOH for 24 h. All the porous samples were immersed in SBF for 5 and 15 days to examined the hydroxyapatite formation.	It was found that the excellent bioactive surfaces were developed after immersion SBF. The porous alloy after 15 days of immersion showed that the excellent hydroxyapatite particles by accumulating more particle growth with increasing immersion time.	(Butev et al. 2015).
Porous Ti-6Al-7Nb	Treated with 10 M NaOH solution at 60 °C for 24 h samples were soaked in SBF at 37 °C for 5 and 15 days.	The surface exhibits the bioactivity and allow apatite formation within 5 days and having Ca/P ratio of 1.3 was obtained after 15 days in SBF.	Ezgi et al. (2016)
Porous Ti-27Nb-13Zr	Alkali NaOH (5 M) solution at 60 °C for 24 h and samples immersed in SBF for 3, 7, 11 and 15 days.	Analysis of the coating revealed the presence of calcium phosphate layers on samples immersed for 3 days in the SBF solution and gradually covered by increasing in immersion time.	Mendes et al. (2016)

Sri Maha Vishnu et al., (2019) have investigated the electrochemical corrosion properties of porous Ti-42Nb alloy (with 39% porosity through PM method) after immersion in Hank's solution for 1 h, 160 h, and 360 h. The electrochemical corrosion properties of the porous alloy in Hank's solution were determined by means of potentiodynamic polarization [Fig. 2.23(a)], EIS study [Fig. 2.23(b&c)] and equivalent circuit model as depicted in Fig. 2.23(d). They have found wide passivation region from around +0.5 to around +2.2 V in all three h cases, inside which the currents only varied and slightly changing potential with increasing immersion time. It shows that the corrosion potentials, ( $E_{corr}$ ) shifted towards more positive values (from -440.2 to -185 mV) and lower the corrosion current density ( $i_{corr}$ ) values (from 4.56 to 4.02  $\mu\text{A}/\text{cm}^2$ ) with increasing immersion time, indicating that the passivating oxide films grew over time.

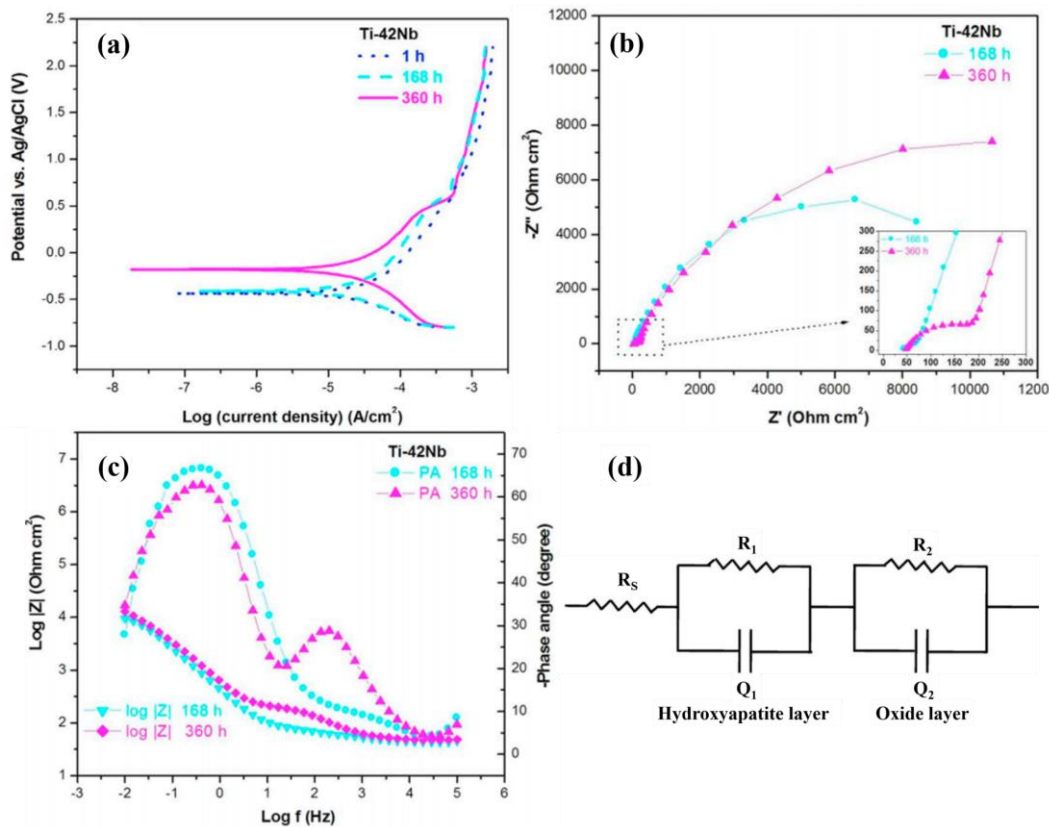


**Fig. 2.23: Porous Ti-42Nb alloys immersed in Hank's solution for 1 h, 168h, and 360 h: (a) potentiodynamic polarisation curves, (b) Nyquist, (c) Bode magnitude and phase angle plot, and (d) equivalent circuit model (Sri Maha Vishnu et al. 2019b).**

The Nyquist plots show high frequencies with increase the diameter of the curves with increase the immersion time in solution. This indicates that the formation of apatite significantly influence to increase the corrosion resistance. The Bode plots show that for immersion time (168h, and 360 h) exhibited nearly similar trends, however, a small improvement of modulus of impedance with respect to 360 h of immersion. In each case, the phase angle curves display two phase constant (maxima), it can be seen first one at the medium-frequency region ( $10\text{--}35^\circ$ ) and another at the low frequency region ( $55\text{--}70^\circ$ ). Hydroxyapatite formation has been formed on the native metal oxide layer during the immersion. The medium frequency feature may be attributed to the hydroxyapatite layer and the low frequency feature to the native surface oxide layer. Results indicate that the formation of hydroxyapatite increase with the increase in immersion time as well directly control corrosion resistance of the porous implants.

X-ray photo spectroscopy (XPS) is powerful tool to understand the chemistry at surface of metal substrate due to chemical reaction with the environments. XPS survey spectra of the surface of the porous Ti-42Nb alloy after immersion in Hank's solution for 360 h is given in Fig. 2.24. It clearly indicates the presence of Ti, Nb, Ca, P and O within the typical XPS penetration depth of 1–2 nm. Also, it revealed the binding energy levels of individual elements of Ti 2p, Nb 3d, Ca 2p, P 2p and O 1s energy levels. These results are indicating a possibility of and the presence of various oxides such as  $\text{TiO}_2$  and  $\text{Nb}_2\text{O}_5$  at the surface. Altogether, these observations indicate that the formation of the protective oxide layer occurs gradually with respect to immersion time.

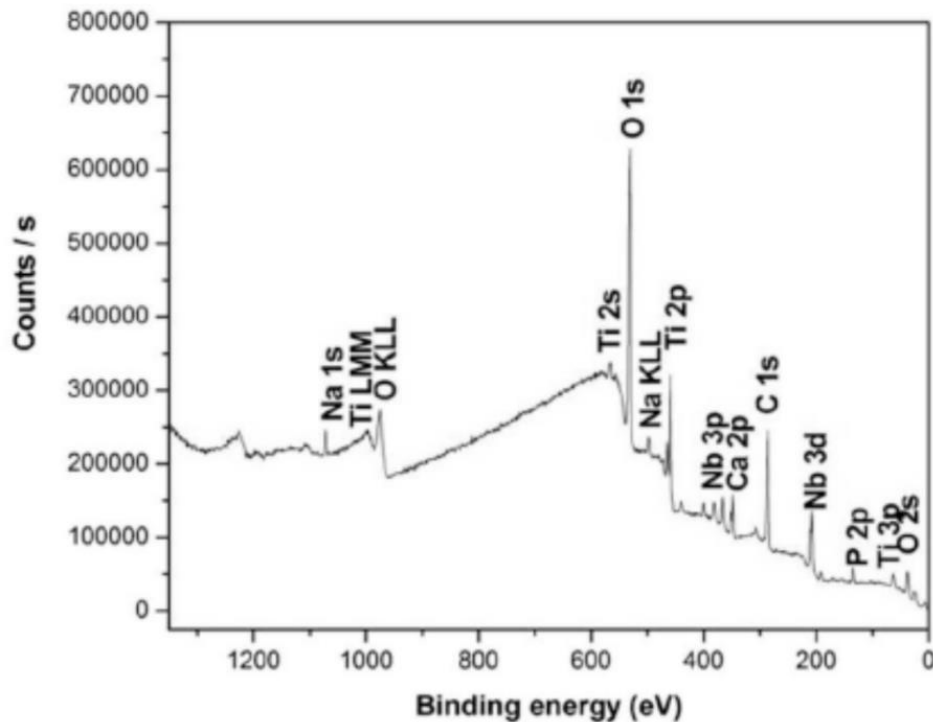


**Fig. 2.24:** XPS survey spectra of the surface of porous Ti-42Nb alloy after immersion in Hanks' solution for 360 h (Sri Maha Vishnu et al. 2019b).

### 2.6.5. Cytotoxicity performance

Quite a few investigations were reported to appreciate a biological compatibility (in-vitro test) of titanium implant due to the release of toxic metal ions and corrosion products, which is significantly affected by the surrounding biological environments (Montanaro et al. 2002). It is important to know as new tissue ingrowth needs that the bone graft is osteoconductive through providing the various human osteoblast cells to stimulate the cell adhesion and cell proliferation on the surface implants (Majumdar et al. 2015; Wang et al. 2009). However, cytotoxicity test is performed to examine the characteristics of cell adhesion, and cell proliferation using the various human osteoblast cells to ensure that the implants are non-toxic and it can be used as bio-implant without any adverse reaction with the surrounding tissues.

Xiaojian Wang et al., (2009) demonstrated the MTT assay to determine cell viability and the proliferation of cell on bulk and porous Ti-10Nb-10Zr alloys with 69% porosity using SaOS<sub>2</sub> osteoblast-like cells. After cell culture for 14 days, cells on the porous alloys were observed to be spreading well, both on the surface of the porous

scaffold and inside the pores [Fig. 2.25 (a and b)]. Also, they noticed that cell attachment on the porous alloy with more cells grown and good spreading compared to bulk alloy. Similarly, various researchers developed the porous Ti alloys and investigated that the cytotoxicity behavior of the alloy by incubating in various human osteoblast cell and few studies have been presented in Table. 2.7.

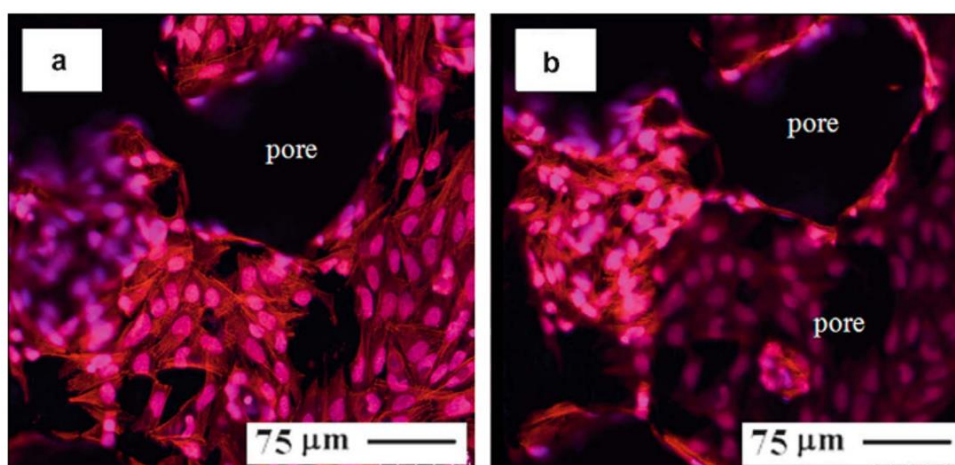


**Fig. 2.25.** Confocal micrographs of cell growth on the porous Ti-Nb-Zr alloy; (a) inside pores of porous Ti-Nb-Zr alloy and (b) on the surface of the porous alloy (Wang et al. 2009).

**Table 2.7.** Cytotoxicity studies conducted on various porous Ti alloys using human osteoblast cell by means of cell growth and cell proliferation.

Alloys	Environment	Summary	References
Porous Ti-7.5Mo	Sample with the 50% porosity used to examine the cytotoxicity by incubating in human osteo-blast cell MG-63 for 7 days.	It was noticed that the rough surface can provide a better cell adhesion than the smooth one. Furthermore, the large surface area of porous scaffold is more favorable for the cell adhesion and proliferation. The porous alloy surface	(Hsu et al. 2013)

		exhibit excellent cell attachment inside the pores after 7 days.	
Porous Ti-6Al-4V	Test was performed on porous Ti-6Al-4V alloy have porosity of 47%, 54%, and 64% by immersing for 7 days in MG-63 osteoblast cell.	Porous alloy surface showed cell growth and proliferation. It was reported that larger pore size did not affect the cell growth but it increased the faster cell migrate inside the pores. However, it exhibited more than 70% cell attachment compared to control, which confirms the non toxicity of developed porous alloys.	(Kalantari et al. 2015b)
Porous Ti-35Nb-4Sn	Examined the effect of porosity( 30% to 70%) and pore size on the cell growth proliferation on the surface of porous alloy after immersion in Alamar blue solution for 1, 3, and 7 days.	Results showed that the cells seeded on the scaffolds for day 1 exhibited a lower fluorescence value, which is likely due to the low cell adherence onto the porous surface. With, increase in the immersion time, it showed more cell adhesion on the surface. However, porous alloy with 50% porosity and average pore range 300-500 $\mu\text{m}$ performed best for cell proliferation.	(Torres-Sanchez et al. 2018)

## 2.7 Motivations

Ti and its alloys exhibit good mechanical properties, high corrosion resistance and excellent biocompatibility as compared to stainless steel or Co–Cr alloys. The most popular biomedical candidate is Ti–6Al–4V alloy. However, it releases the toxic metal ions which is harmful to human body. Also, various Ti and its alloys are suffering from the *stress-shielding effect* due to the mismatch of elastic modulus between the bone and implant materials. Therefore, with the aim to rectify these concerning drawbacks of Ti, the pore structures are introduced in the bulk alloy. In the present work,  $\beta$ -stabilizing elements Nb and antibacterial element Ag were added into Ti to develop the porous implant alloy to make the elastic modulus closer to that of human bone.

- According to literature,  $\alpha+\beta$  type Ti alloy are more suitable for implant applications, due to exhibit low elastic modulus.
- According to literature, Nb and Ag are identified as excellent alloying elements in Ti matrix,
- Addition of  $\beta$ -stabilizing elements Nb in Ti matrix significantly increases the corrosion and wear resistance, as well help to reduce the elastic modulus of Ti based alloys.
- Addition of Ag in Ti matrix is helps to enhance the corrosion resistance and antibacterial properties of implant materials.
- A limited research carried out on Ti–Nb–Ag alloy system, which may produce the  $\alpha+\beta$  type alloy.





## CHAPTER 3

### 3. EXPERIMENTAL DETAILS

In this chapter, describes the detail experimental tools and procedure for processing porous Ti–Nb–Ag alloy through powder metallurgy (PM) method. The microstructural characterization, mechanical properties, electrochemical corrosion study, tribocorrosion behavior, biocompatible studies and cytotoxicity behavior of the prepared porous alloys were examined. The schematic representation of the work flow is shown in Fig. 3.1.

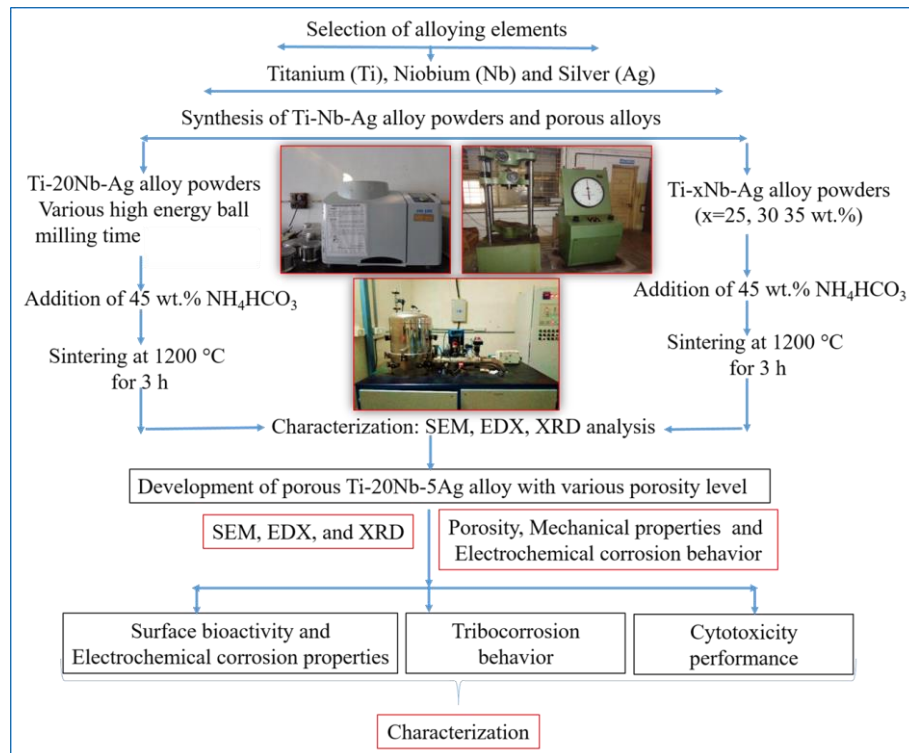


**Fig. 3.1: Schematic representation of development of synthesis of Ti–Nb–Ag alloy powders, porous Ti–Nb–Ag alloys and characterization.**

#### 3.1 Raw materials

In the present research, elemental powders of Ti (99.5% purity, particle size ~45  $\mu\text{m}$ ), procured from Alfa aesar, Nb (99.8% purity, particle size ~45  $\mu\text{m}$ ) procured from Excell materials, and Ag (99.9% purity, particle size ~45  $\mu\text{m}$ ) procured from Next-Gen steels to prepare the porous Ti–Nb–Ag alloys.

Fig. 3.2 (a-c) shows SEM micrographs of the raw materials used to prepare the porous alloys such as Ti, Nb and Ag. Microstructure revealed that all are in irregular shape and the particle size about of  $<45 \mu\text{m}$ . Fig. 3.2 (d-f) shows that the energy dispersive X-Ray (EDX) analysis which confirms the presence of pure elemental powders of Ti, Nb and Ag. Fig. 3.3 shows that SEM micrographs of ammonium bicarbonate ( $\text{NH}_4\text{HCO}_3$ ) particles which are used as space holder to create the porous structures. The microstructure reveals that the particles are of irregular shape with particle size ranging from  $150\text{--}500 \mu\text{m}$ .

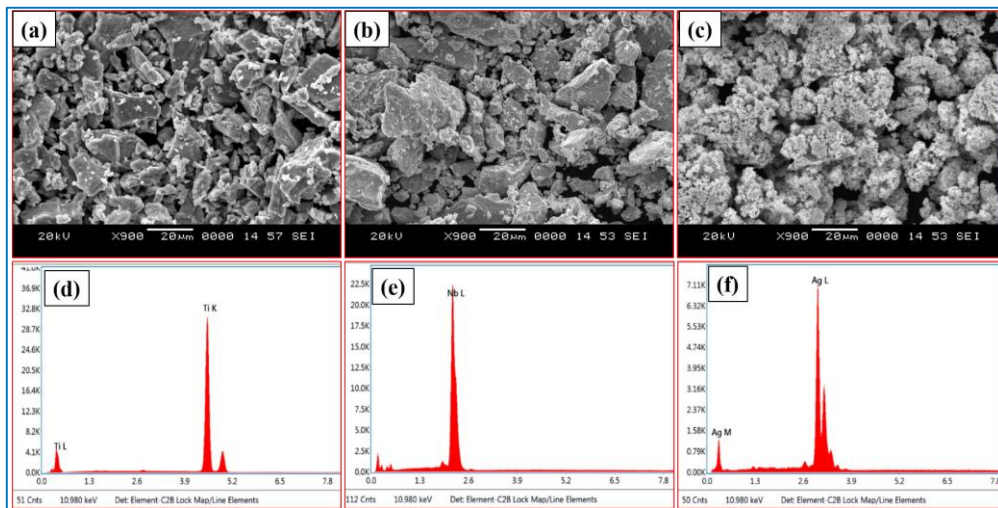


**Fig. 3.2: SEM and EDX analysis of as-procured elemental powders SEM and EDX: (a & d) Ti, (b & e) Nb, and (c & f) Ag.**

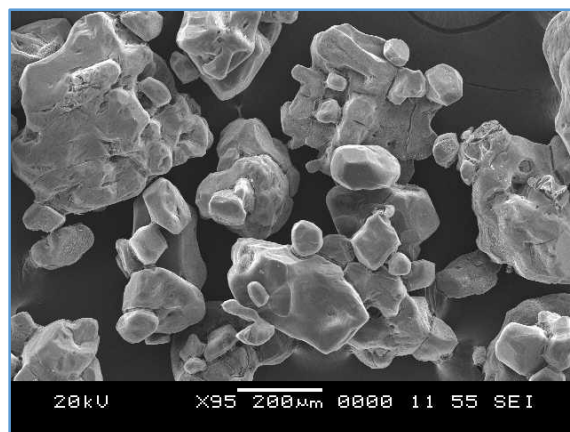


**Fig. 3.3: SEM micrograph of as-procured ammonium bicarbonate ( $\text{NH}_4\text{HCO}_3$ ) used as space holder material.**

### 3.2. Synthesis of Ti–Nb–Ag alloy powder using ball mill

In this present research work synthesized various Ti–Nb–Ag based alloy powders were developed using high-energy ball mill such as; (i) Ti–20Nb–5Ag alloy powder with different ball milling times for 1 h, 5 h, 10 h, 15 h, and 20 h, and (ii) Ti– $x$ Nb–5Ag alloy powders ( $x=25, 30$  and  $35$  wt. %) were developed by milling for 20 h using high-energy planetary ball mill. During the milling process the alloy powders the ball to powder weight ratio of 10:1, and rotating speed of about 250 rpm (High-energy planetary ball mill, RX-100, Germany). Hardened stainless steel balls and vial was used to carry out ball milling process.

### 3.3 Preparation of porous Ti-Nb-Ag alloy through powder metallurgy

Synthesis powders of Ti–20Nb–5Ag for different milling time such as 1 h, 5 h, 10 h, 15 h and Ti– $x$ Nb–5Ag alloy powders ( $x=25, 30$  and  $35$  wt.% ) were added 45 wt.% of ammonium bicarbonate ( $\text{NH}_4\text{HCO}_3$ ), which used as space holder material to create pore structures. Also, Ti–20Nb–5Ag alloy powder with 20 h of ball milling added various amounts of  $\text{NH}_4\text{HCO}_3$  such as 15%, 30%, 45% and 60 wt. % to develop the various porosity levels. Mixed Ti-Nb-Ag powders and  $\text{NH}_4\text{HCO}_3$  was loaded in to steel die and compacted at an applied load of 500 MPa to make green pellets. Sintering operation was carried out in stages, (i) all the green pellets were first heated to 200 °C for 2 h to burn the space holder particles. (ii) Temperature was raised to 1200 °C for 3 h to obtain porous alloys. During the sintering process the heating and cooling rate was maintained 10 °C /min. The sintering process was conducted under high vacuum atmosphere at the vacuum level of  $10^{-5}$  mbar to avoid the contamination (High temperature vacuum furnace, V.T Technologies, Bangalore). Fig. 3.4 shows that schematic representation of fabrication of porous Ti-Nb-Ag alloys through PM space holder method.

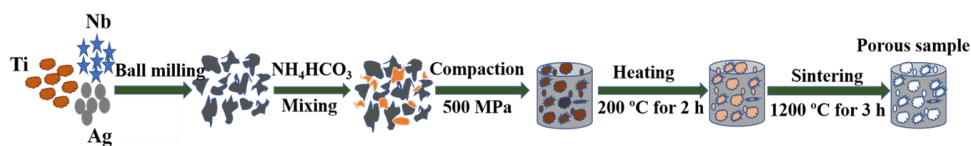


**Fig. 3.4: Schematic representation of fabrication of porous Ti–Nb–Ag alloys through PM method.**

### 3.4 Characterization of developed alloy powders and porous Ti-Nb-Ag alloys

#### 3.4.1. Porosity, density and mechanical properties of porous alloys

Porosity and density of all the developed porous Ti-Nb-Ag alloys were measured by using Archimedes' immersion technique. Pore size of the developed porous alloys was determined using the Image-J software and more than 100 pores was measured for to determine the mean pore size. The following equations used to measure the porosity and density.

$$\text{Porosity (\%)} = ((W_{\text{sat}} - W_{\text{dry}}) / (W_{\text{sat}} - W_{\text{sus}})) \times 100 \quad (8)$$

$$\text{Density (g/cm}^3\text{)} = ((W_{\text{dry}} / (W_{\text{sat}} - W_{\text{sus}})) \times 100 \quad (9)$$

Where,  $W_{\text{sat}}$  = saturate weight,  $W_{\text{s}}$  = suspended weight, and  $W_{\text{dry}}$  = dry weight.

The compression strength and elastic modulus of the various prepared porous Ti-Nb-5Ag alloys were conducted using universal testing machine (Shimadzu, Autograph AG-X plus, 100KN, Japan) at a strain rate of  $10^{-3} \text{ s}^{-1}$ . The samples were prepared according to ASTM standard E9-09 (Gao et al. 2012a). The origin software was used to measure the elastic modulus of the developed porous alloy by using the linear portion of the compressive stress-strain curves.

#### 3.4.2. Electrochemical corrosion properties of porous alloys

The conventional three electrode system was used for examine the electrochemical corrosion and impedance measurement of porous Ti-20Nb-5Ag alloys. It consists of a saturated calomel electrode (SCE) as reference electrode, a platinum as counter electrode, and a working electrode as porous alloys. Prior to conduct the electrochemical corrosion test, one side of the prepared porous sample was mechanically polished using SiC grit paper (up to 1200) and followed by cloth polishing using with  $0.5 \mu\text{m}$  diamond paste. The porous sample was immersed in aqueous electrolyte i.e. simulated body fluid (SBF) to measure the electrochemical corrosion properties. Electrolyte was prepared with the similar ionic concentration as human blood plasma fluids (pH=7.4) (Å and Takadama 2006). Electrolyte was prepared using the various chemical reagents as presented in Table.3.1.

Electrochemical corrosion behavior of the porous alloys was examined using the electrochemical potentiostat (Biologic, SP-150, France), as shown in Fig. 3.5 (a). All the experiments was conducted at 37 °C and water bath used to maintain the temperature [Fig. 3.5 (b)].

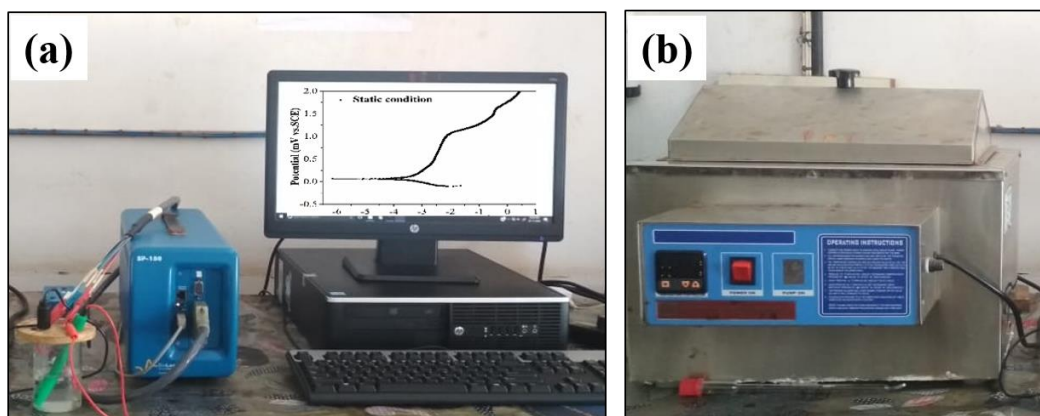


**Fig. 3.5:** (a) Photographs of electrochemical potentiostat (Biologic-150), and (b) temperature-controlled water bath.

**Table 3.1:** Chemical reagents used to prepare 1000 ml of simulated body fluids (Å and Takadama 2006).

Chemical reagents	Amount	Purity	Formula weight
NaCl	8.036 g	99.5%	58.44
NaHCO <sub>3</sub>	0.352 g	99.7%	84.01
KCl	0.225 g	99.0%	74.56
K <sub>2</sub> HPO <sub>4</sub> ·3H <sub>2</sub> O	0.230 g	99.0%	228.23
MgCl <sub>2</sub> ·6H <sub>2</sub> O	0.311 g	99.0%	203.30
1 M HCl	39.ml	.....	.....
CaCl <sub>2</sub>	0.293 g	98.0%	110.98
Na <sub>2</sub> SO <sub>4</sub>	0.072 g	99.0%	142.04
Tris	6.063 g	99.8%	121.14

### 3.4.3. Tribocorrosion behavior of porous alloys

Prior to tribocorrosion study, the porous samples prepared with diameter of 10 mm and length of 15 mm. A custom-made tribometer (pin-on-disc type) and which is connected potentiostat to perform the tribocorrosion test as shown in Fig. 3.6. The rig of the tribometer consists balancing lever on one end and at the other end contact with sample holder where the working electrode was fixed (porous Ti-20Nb-5Ag alloy).

Alumina disc 100 mm in diameter and 5 mm thickness (Ant ceramics, India) with the surface roughness ( $R_a$ ) is  $0.02 \mu\text{m}$  (according to manufacturer), was used as a counter surface due to high electrochemical stability in the corrosive environment. The installed pin-on-disc tribometer with the exposed surface area of  $1 \text{ cm}^2$  to the counter surface which is rotating at speed of 2 rpm in the media of electrolyte (SBF). The loads applied (1 N, 5 N and 10 N) by placing standard weights on the balancing lever of tribometer which is connected with potentiostat.

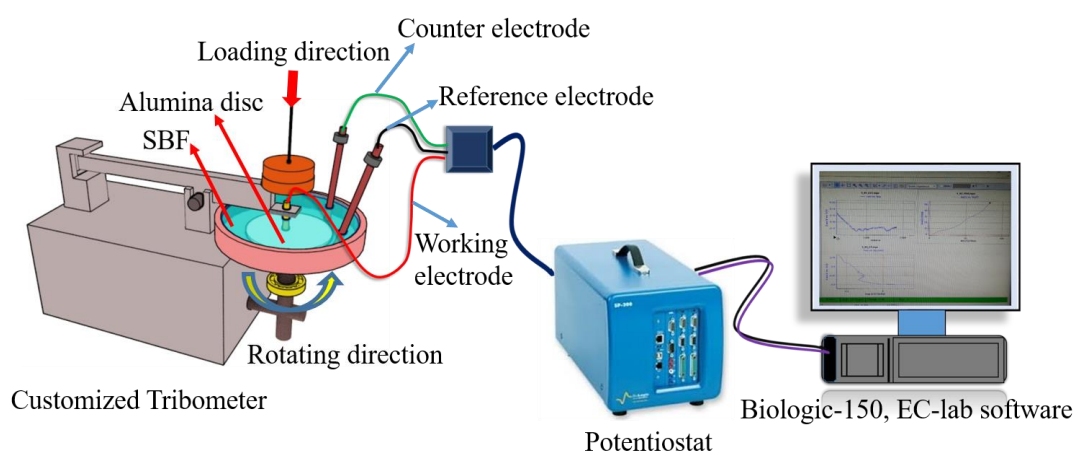


**Fig. 3.6: Schematic diagram of custom-made Tribometer.**

#### **3.4.4. Surface modification through alkali treatment**

Porous Ti–20Nb–5Ag alloy samples were prepared to the dimensions of 10 mm diameter and 3 mm thickness, and mechanically polished up to 1200-grit finish and were cleaned ultrasonically and dried. The alkali treatment was conducted by soaking the samples in aqueous solution of 5 M of NaOH at  $60 \text{ }^\circ\text{C}$  for 24 h. Then, alkali treated samples were washed using distilled water. Further, heat treatment was conducted at  $600 \text{ }^\circ\text{C}$  for 1 h and cooled to room temperature. Then all the samples were taken out rinsed in distilled water and dried.

#### **3.4.5. Evaluation of hydroxyapatite formation**

Alkali-heat treated porous Ti–20Nb–5Ag samples were immersed in a beaker which contains 25 ml of SBF (as listed in Table. 1) to examine the apatite forming ability on the surface of porous alloy. The porous samples were immersed in SBF solution for 7, 14 and 21 days at  $37 \text{ }^\circ\text{C}$ . Water bath was used to control the temperature.

The solution was refreshed for every 24 h to maintain the ionic concentration. All the samples were taken out after the predetermined immersion time and rinsed in distilled water and dried.

#### **3.4.6. In-vitro corrosion behavior**

Porous Ti–20Nb–5Ag alloy are immersed in SBF for various times such as 7, 14 and 21 days at 37 °C, to examine the influence of hydroxyl apatite coating on the electrochemical corrosion properties. The electrochemical corrosion behaviour of sample was investigated using potentiodynamic polarization and electrochemical impedance spectroscopy (EIS). The conventional three electrode system used to examine the electrochemical properties (Fig. 3.5). For potentiodynamic polarization study conducted in a potential range of 2 V (vs. SCE) at the scan rate of 0.5 mV/min. The corrosion parameters were determined by Tafel approximation method using EC-Lab software from the potentiodynamic plot. For electrochemical impedance spectroscopy (EIS), performed in the frequency range from 100 kHz to 5 m Hz with amplitude of 10 mV.

#### **3.4.7. Cytotoxicity performance**

For **cytotoxicity** test, the as-synthesized porous sample was cut in the form of the disc (10 mm diameter and 2 mm height), in a selected porous specimen. The sample was cleaned ultrasonically using acetone and distilled water. Prior to cell culture, porous samples were sterilized in an autoclave and rinsed using deionized water and phosphate-buffered saline (PBS) solution. Cell culture experiments were performed using osteoblast-like Osteosarcoma cells (MG-63) procured from National Centre for Cell Science (NCCS, Pune, India). Cells were cultured using Dulbecco's Modified Eagle Medium (DMEM, Himedia, Mumbai, India), with 10% Fetal Bovine Serum (FBS) and 2% antibiotic/antimycotic solution at 37 °C and 5% CO<sub>2</sub>. Media was refreshed once in two days. Briefly, MG–63 human osteoblast cells were grown using DMEM with 10% FBS and 2% antibiotic/antimycotic solution. Cells were seeded at the density of  $25 \times 10^3$ ,  $7.5 \times 10^3$ ,  $5 \times 10^3$ /well in 24 well plates to check cytotoxicity at 1<sup>st</sup>, 4<sup>th</sup>, and 7<sup>th</sup> day respectively and allowed to attain confluence. Low seeding densities for prolonged incubation were used to avoid detachment of cells due to over confluency over 4 and 7 days of incubation. Later, cells were incubated at 37 °C and 5% CO<sub>2</sub>. After



each time interval, the supernatant was removed, cells were incubated with acridine orange-ethidium bromide mixture (1 µg/mL each) for 20 min without exposing to light. Then, washed with PBS thrice and microstructure was observed under Zoe-fluorescent microscope (FM) (Bio-Rad, USA). Hemocytometer inverted microscope (Primovert, Zeiss) was used to count live cells and dead cells. After each predetermined incubation time, cells were trypsinized, stained with trypan blue and count the cells. Trypan blue dye is able to enter only to the dead cells. Hence cells attaining blue (i.e., dead cells) were excluded, and only viable cells were counted using four corner chambers of a hemocytometer. Total viable cell count was calculated using the formula:

$$\text{Cell count} = \frac{\text{sum of cells in 4 chambers} \times \text{dilution factor} \times 10^4}{4} \text{ cells/mL} \quad (10)$$

### 3.5. Microstructural analysis

A phase analysis of developed Ti–Nb–Ag powder and prepared porous Ti–Nb–Ag alloy was investigated by X–ray diffractometer (DX GE-2P, Japan). The microstructures of all the prepared Ti–Nb–Ag alloy powders and porous alloys were examined in a scanning electron microscope (SEM) (JEOL, JSM-638OLA) with energy dispersive X-ray spectroscopy (EDX) (EDAX- Smart Insight) and optical microscopy. The surface topography of the samples after immersion in SBF for various times was analysed using Atomic Force Microscopy (AFM). The surface topography and roughness of the apatite coating on the porous Ti–20Nb–5Ag alloy after immersing in SBF for various times. X-ray Photoelectron Spectroscopy (XPS) used to investigate the stoichiometry of hydroxyapatite coated surface of porous Ti–20Nb–5Ag alloy.

#### *Analysis of X-Ray Diffractometer*

X-Ray diffraction (XRD) profile was generated using a computer controlled diffractometer (Make JEOL, Model-JDX 8P, Japan) with Ni filter operated at 30 kV and 20 mA with a Cu- $\alpha$  radiation with diffraction angle ( $2\theta$ ) range from 30° to 90° and at scanning speed of 2° per minute.

Samples were scanned from 30° to 90° at the scan rate of 2°/min. From the literature, it was found that major peaks of the phases for Ti–Nb–Ag alloy system is obtained within the above mentioned diffraction angle range (Wen et al. 2014).



**Fig. 3.7: Photograph of X-ray diffractometer.**

### ***X-ray photoelectron spectroscopy (XPS)***

XPS can provide the significant information of surface properties being up to three atomic layers thickness (~1 nm), depending upon the material. A layers thickness up to 10 nm are considered ultra-thin films, which gives the chemical properties of the surface of sample. Basically, the XPS belongs to photoemission spectroscopies where the electron population spectra are attained by irradiating a sample surface with a beam of X-rays. Sample properties are measured from the kinetic energy and the number of ejected electrons. To perform the operations using XPS needs high vacuum ( $p \sim 10^{-6}$  Pa) or ultra-high vacuum ( $p < 10^{-7}$  Pa) conditions.

However, in the present study XPS (AXIS ULTRA, KRATOS analytical) [Fig. 3.8] used to investigate the stoichiometry (binding energy) of sintered porous Ti-20Nb-5Ag alloy which is coated with hydroxyapatite by immersion in SBF solution for 21 days at 37 °C.



**Fig. 3.8: Photograph of X-ray photoelectron spectroscopy.**

## CHAPTER 4

### RESULTS AND DISCUSSION

#### 4.1 Effect of ball milling times on sintered porous Ti–20Nb–5Ag alloys

*It is very important to examine the powder particle size, after obtaining through mechanical alloying, which significantly influences the microstructural and mechanical properties of the sintered alloys prepared through powder metallurgy process. In the present work, Ti–20Nb–5Ag alloy powders are used and size reduction was carried out by ball milling for 1, 5, 10, 15 and 20 h. The ball milled powders were mixed with space holders (45 wt. %  $\text{NH}_4\text{HCO}_3$ ) to generate porosity and were subjected for sintering. Microstructure, mechanical properties and electrochemical corrosion properties of the mechanically alloyed powders and sintered porous Ti–20Nb–5Ag alloys were examined and discussed in details.*

##### 4.1.1 Microstructure analysis

SEM micrographs of Ti–20Nb–5Ag alloy powders at various ball milling times of 1, 5, 10, 15 and 20 h are depicted in Fig. 4.1. It can be seen from the micrograph that there is variation in the morphology due to the effect of ball milling time. It is noticed that ball milling up to 5 h, the powder particles are quite irregularly shaped and also all the particles retained their original shape as shown in Fig. 4.1 (a and b). This may be due to insufficient collide between the powder particles and balls in the milling chamber. However, these particles are slightly work hardened due to continuous impact through the ball and powders which can be explained by the small changes in shape and size (Aguilar et al., 2016c; Nouri et al., 2011). Further, when the milling time was increased to 10 h and 15 h [Fig. 4.1 (c and d)], the morphology of powders is still heterogeneous and did not show any remarkable changes on refinement in the milled powder particles. Microstructure of the powder particles show a quite flattened and smaller in size as compared to that of initial ball milling times of 1 and 5 h. This may be due to the fact that the powder particles had an effect of micro-forging and cold welding at the initial stage of impact due to balls. However, it is noticed a severe change in the powder morphology along with reduction in size of powder particles after 20 h of ball milling as compared to 1, 5, 10 and 15 h.

It could be seen from Fig. 4.1 (e) the edges of these particles became smooth due to the disappearance of sharp edges as a result of continuous fracture and cold welding between the powder particles when the time of milling is the highest. It is well known that the ball milling for longer durations leads to severe plastic deformation and also work-hardening resulting in brittleness of powder particles to commute in small size. It is also observed that there is significant change in the shape which indicates effective fracture and cold-welding between the particles. These results are in good agreement with the previous reports (Aguilar et al., 2016c; Nouri et al., 2011).

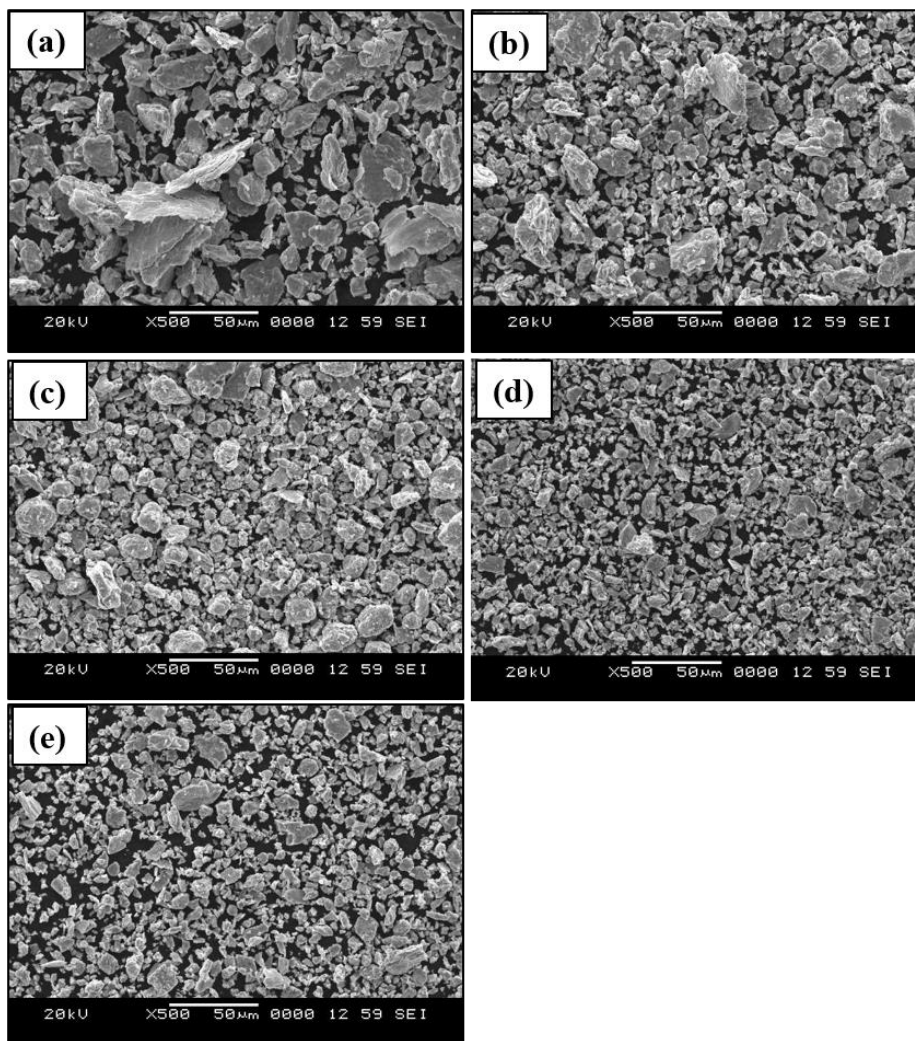


**Fig. 4.1:** SEM images of Ti–20Nb–5Ag alloy powders developed by ball milling at different times of (a) 1 h, (b) 5 h, (c) 10 h, (d) 15 h and (e) 20 h.

Fig. 4.2 shows the relationship between particle-size of Ti–20Nb–5Ag alloy powders and milling times of 1, 5, 10, 15 and 20 h. It can be seen that there is a decrease in particle size with time. However, the slope change is not much at initial period and higher milling time plays an important role in reduction of size. It is found that the particle size reduction was not significant for shorter milling times (32  $\mu\text{m}$  and 28  $\mu\text{m}$  at 1 and 5 h milling time respectively). At this stage of ball milling, it might flatten the elemental particles due to the shearing and the compressive force during the colliding of balls. However, the particle size gradually decreases after 5 h of ball milling. It can be seen that the particle size is reduced from 32  $\mu\text{m}$  to 7  $\mu\text{m}$  for the ball milling time of 1 h to 20 h respectively. A significant reduction of about 4.5 times for 20 h of milling as compared to 1 h of milling indicates a severe micro-forging and cold welding between the powder particles at this stage of ball milling (Dercz & Matuła, 2017; Hou et al., 2013; Nouri et al., 2011). The relationship between the ball milling time particles size using linear equation is as follows:

$$y = -1.37x + 33.63 \quad (11)$$

Where,  $y$  is the particle size of the ball milled powders,  $x$  given is ball milling time.

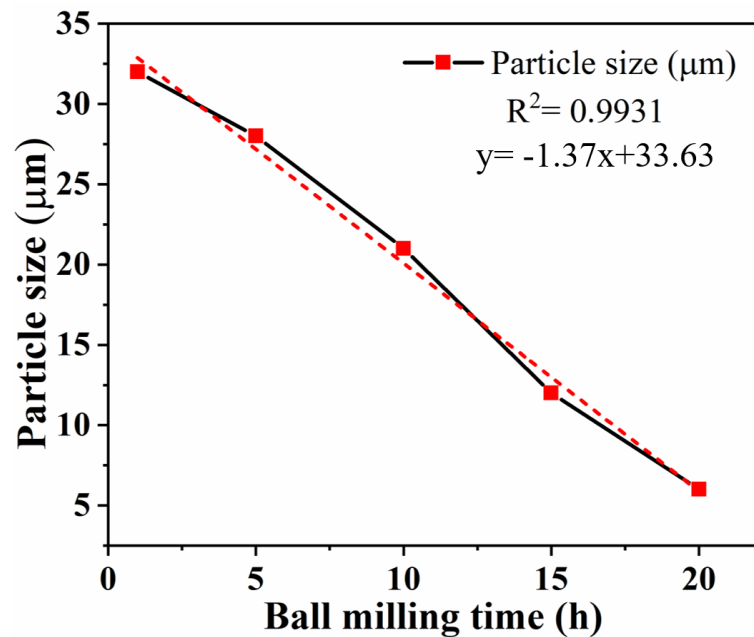


**Fig. 4.2:** A corelationship of particle size with ball milling time for developed Ti–20Nb–5Ag alloy powders.

Fig. 4.3 shows the backscattered SEM images of Ti–20Nb–5Ag alloy powders for different ball milling time (1–20 h). It is revealed that the powders remained unalloyed for ball milling time of 1 and 5 h [Fig. 4.3 (a) and (b)], at this point, alloy formation is difficult because the duration of ball milling time is short. Due to the short ball milling time, the powder particles were not exposed for required compressive forces or kinetic energy to get altered (Nazari et al., 2015a; Salvo et al., 2017a). Particles of Ti appear in the dark contrast region and bright contrast region is attributed to as Nb/Ag particles (as arrows shows in Fig. 4.3). Further, with increasing ball milling time, it can be observed that most of the bright region disappeared as compared to initial ball milling time. It is indicating that the solute atoms of Nb and Ag were incorporated into the Ti matrix, which show noticeable mechanical alloying of the powder particles at higher ball milling time (Nouri et al., 2011).

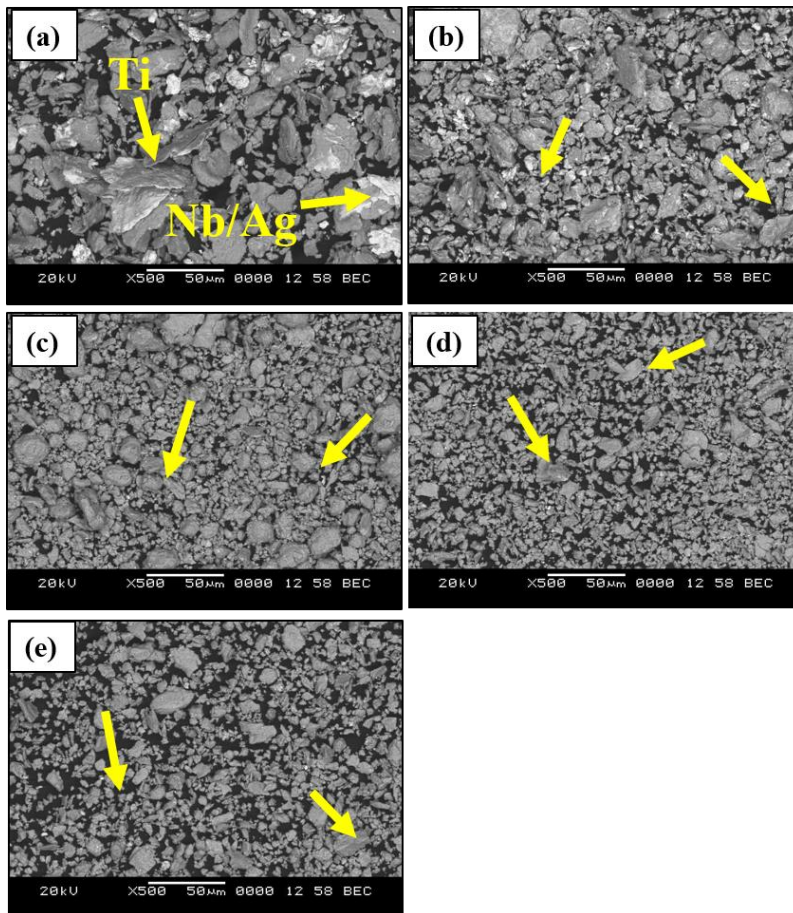


**Fig. 4.3: Backscattered SEM images of the Ti–20Nb–5Ag alloy powders developed from different ball milling times: (a) 1 h, (b) 5 h, (c) 10 h, (d) 15 h and (e) 20 h.**



Elemental mapping was performed using EDX for Ti–20Nb–5Ag alloy powders after various ball milling times of 1, 5, 10, 15 and 20 h is presented in Fig. 4.4. All the elemental powders Ti, Nb, and Ag are distributed homogeneously for all ball milling times. However, after 15 and 20 h of ball milling, a more uniformity in distribution is observed due to the effectiveness of ball milling and it could enhance the sintering ability during the heat treatment process (Wen at el., 2014).

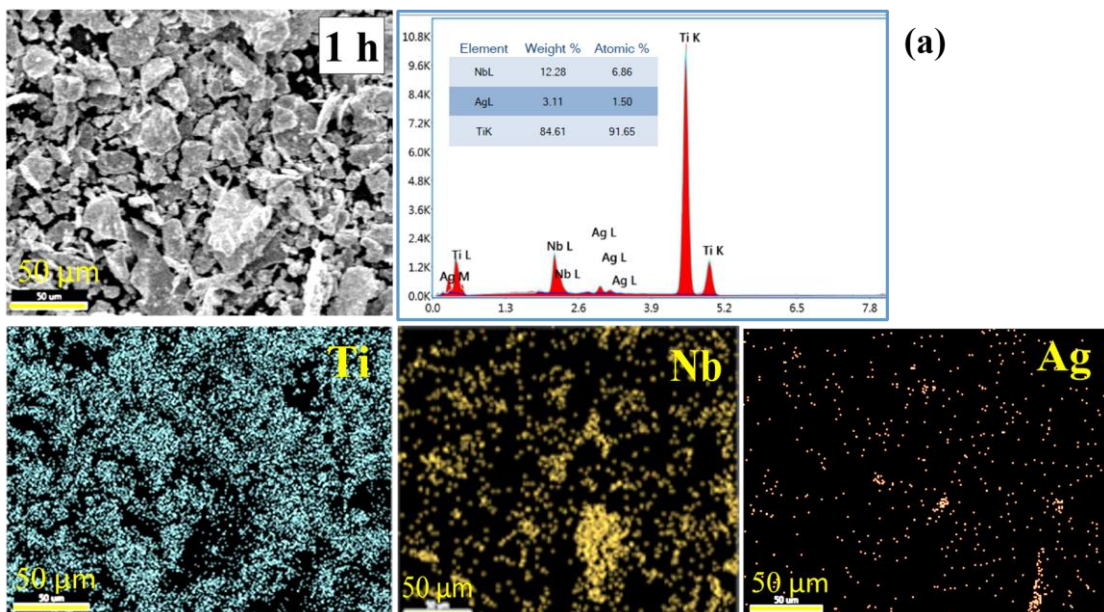


**Fig. 4.4 (a): EDX elemental mapping of Ti–20Nb–5Ag alloy powders obtained after 1 h of ball milling time.**



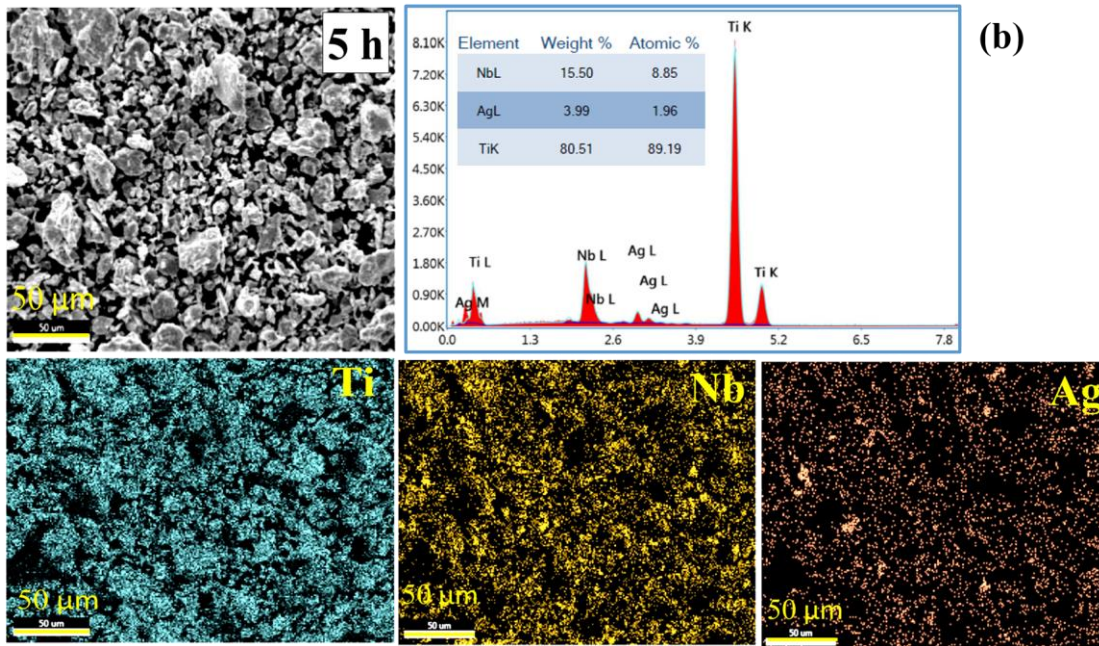


Fig. 4.4 (b): EDX elemental mapping of Ti-20Nb-5Ag alloy powders obtained after different ball milling times 5 h.

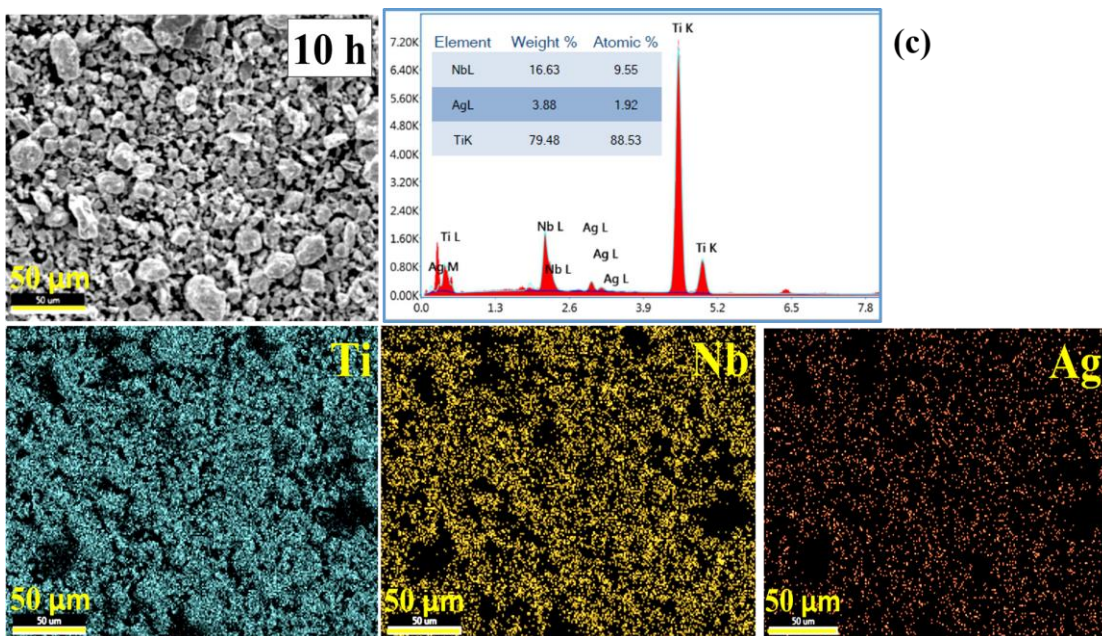


Fig. 4.4 (c): EDX elemental mapping of Ti-20Nb-5Ag alloy powders obtained after different ball milling times 10 h.



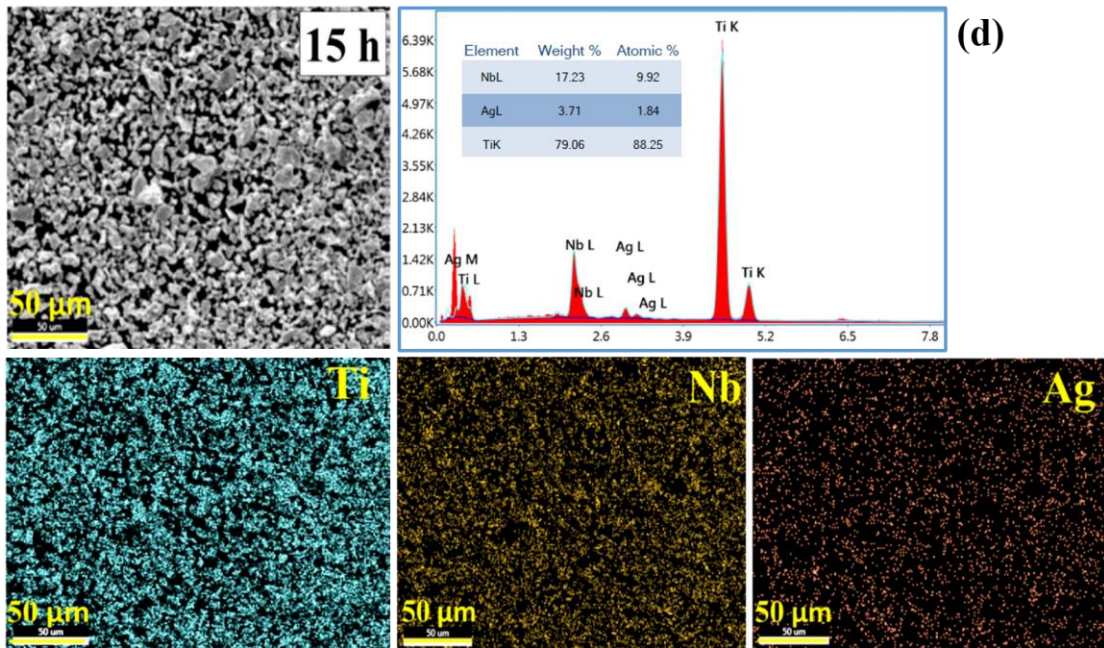


Fig. 4.4 (d): EDX elemental mapping of Ti-20Nb-5Ag alloy powders obtained after different ball milling times 15 h.

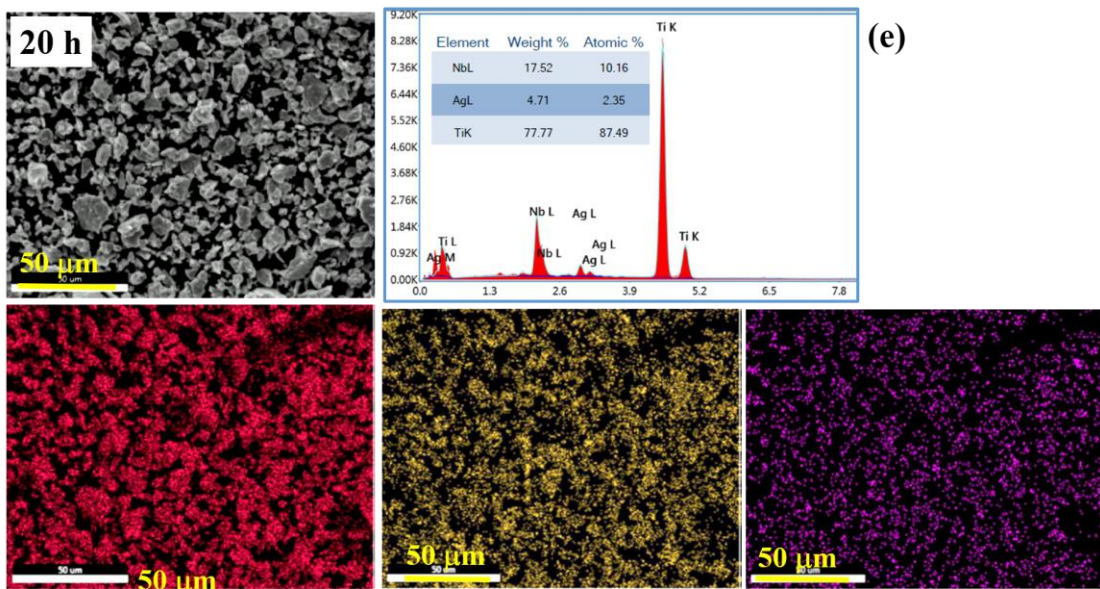
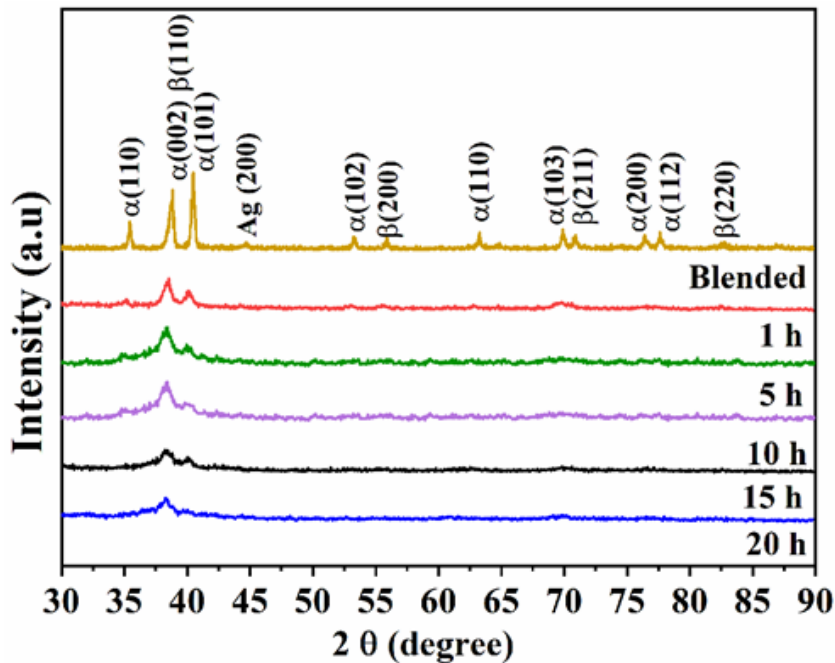


Fig. 4.4 (e): EDX elemental mapping of Ti-20Nb-5Ag alloy powders obtained after different ball milling times 20 h.

#### 4.1.2 XRD analysis

XRD patterns of the ball milled powders of Ti–20Nb–5Ag as a function of ball milling times (1, 5, 10, 15 and 20 h) is shown Fig. 4.5. With increasing ball milling times, it is clearly observed that there is diminution in the intensity of the peaks, peak shift, peak broadening and also vanishing of peaks. This is due to significant reduction in the crystalline size along with development of lattice strain. It is noticed that there is formation of  $\alpha$  and  $\beta$  phases in various ball milled powders. It is also found that a near amorphous phase occurred after 15 and 20 h of ball milling as compared to ball milling times of 1, 5 and 10 h. Interestingly it is noticed that the peak of pure Ag which was present in a blended and 1 h ball milled sample dispersed in Ti matrix with increasing in the ball milling time (Wen et al., 2014). It is a well-established fact that the tendency of peak broadening with increasing the milling time is an indication of the grain refinement. A Williamson-Hall refinement analysis is performed to determine the crystallite size and lattice strain from XRD data. These results are presented in Table. 4.1 (a-e).



**Fig. 4.5: XRD diffraction patterns of Ti–20Nb–5Ag alloy powders with different ball milling times.**

As milled and sintered porous alloys were analysed by XRD, using Cu-K $\alpha$  radiation (1.542 Å) at 2 $\theta$  with scan rate of 2° /min. The crystallite size and lattice parameters were calculated for the XRD data obtained using Williamson-Hall equation ( $\beta_{hkl} \cdot \cos\theta = \frac{K\lambda}{D} + 4\varepsilon \sin\theta$ ) where  $\beta_{hkl}$  is corrected instrumental broadening, D is the crystallite size,  $\lambda$  is the wavelength of X-ray source,  $\varepsilon$  is the lattice strain, and K is the shape factor (K=0.9). For  $\alpha$  and  $\beta$  phases, it is noticed that the slight reduction in the crystalline size increases with increasing the ball milling times. However, in the case of the  $\beta$  phase it is clearly observed that there is increase in the lattice strain with ball milling times. These variations are mainly due to the significant grain refinements during the ball milling process, and increasing kinetic energy of the powder particles. The investigation of the diffraction patterns obtained using Williamson-Hall method showed significant influence of high energy ball milling time on the lattice parameters. G. Dercz et al., (2017) have developed porous Ti–26Nb alloy from the various ball milled powders and found reduction in the crystallite size and lattice parameters when ball milling times are increased.

**Table. 4.1 (a): Parameters obtained from the XRD analysis of the Ti–20Nb–5Ag ball milled powder for 1 h by using Williamson-Hall method.**

Ball milling time: 1 h							
	2 $\theta$ (degree)	hkl	d (Å)	Lattice parameter (Å)	FWHM $\beta_{hkl}$	Crystallite Size (D) nm	Dislocation density $\times 10^{-3} \text{ nm}^{-2}$
$\beta$ - phase	38.42	110	2.342	3.885	0.314	26.972	1.3744
	44.31	200	2.044		0.551	14.614	4.6819
	77.45	211	1.231		0.576	26.626	1.4105
	82.91	220	1.169		0.768	11.060	8.1735

$\alpha$ -phase	$2\theta$ (degree)	hkl	d (Å)	Lattice parameter (Å)		FWHM $\beta_{hkl}$ (degree)	Crystallite Size (D) nm	Dislocation density $\times 10^{-3} \text{ nm}^{-2}$
				$a_0$	$c_0$			
	35.05	100	2.559	3.04	4.87	0.314	102.513	0.095
	38.42	002	1.253			0.318	26.972	1.374
	40.04	101	1.12			0.275	74.533	0.180
	52.89	102	1.729			0.672	46.432	0.4638
	63.11	110	1.471			0.480	16.715	3.5788
	70.66	103	1.331			0.481	23.185	1.860

**Table. 4.1 (b): Parameters obtained from the XRD analysis of Ti–20Nb–5Ag ball milled powders for 5 h by using Williamson-Hall method.**

Ball milling time: 5 h								
$\beta$ -phase	$2\theta$ (degree)	hkl	d (Å)	Lattice parameter (Å)		FWHM $\beta_{hkl}$ (degree)	Crystallite Size (D) nm	Dislocation density $\times 10^{-3} \text{ nm}^{-2}$
				$a_0$	$c_0$			
	38.42	110	2.343	3.385		0.629	13.543	5.4517
	44.32	200	2.044			0.472	17.003	3.4588
	55.3	211	1.66			0.196	56.071	0.3180
	77.45	220	1.231			0.072	193.24	0.0267
	82.41	211	1.350			0.787	10.431	9.1910
	35.05	100	2.559			2.31	4.64	0.314

<b><math>\alpha</math>- phase</b>	38.44	002	2.342		0.629	13.543	5.4518
	40.05	101	2.251		0.551	39.915	0.6277
	52.89	102	1.729		0.629	83.743	0.1426
	63.12	110	1.471		0.472	16.820	3.5343
	70.67	103	1.331		0.944	8.838	12.801
	76.16	200	1.248		0.157	50.481	0.3924

**Table. 4.1 (c): Parameters obtained from the XRD analysis of Ti–20Nb–5Ag ball milled powders for 10 h by using Williamson-Hall method.**

Ball milling time: 10 h									
<b><math>\beta</math>- phase</b>	<b>2<math>\theta</math></b>	<b>hkl</b>	<b>d Å</b>	<b>Lattice parameter Å</b>		<b>FWHM <math>\beta_{hkl}</math> (degree)</b>	<b>Crystallite Size (D) nm</b>	<b>Dislocation density <math>\times 10^{-3} \text{ nm}^{-2}</math></b>	
		38.44	110	2.341	3.3461		0.629	13.543	5.4517
	56.28	200	2.045	0.472			17.003	3.4588	
	70.62	211	1.350	0.787			10.431	9.1910	
	82.50	220	1.169	0.5234			36.672	0.7435	
<b><math>\alpha</math>- phase</b>	<b>2<math>\theta</math> (degree)</b>	<b>hkl</b>	<b>d Å</b>	<b>Lattice parameter Å</b>		<b>FWHM <math>\beta_{hkl}</math> (degree)</b>	<b>Crystallite Size (D) nm</b>	<b>Dislocation density <math>\times 10^{-3} \text{ nm}^{-2}</math></b>	
				<b>a<sub>o</sub></b>	<b>c<sub>o</sub></b>				
		35.20	100	2.559	2.31	4.64	0.314	79.704	0.1574
		38.44	002	2.342			0.629	13.543	5.4518
		40.10	101	2.251			0.551	39.915	0.6277
		53.10	102	1.729			0.629	83.743	0.1426

	62.77	110	1.471			0.472	16.820	3.5343
	76.02	112	1.331			0.944	8.838	12.801
	81.76	004	1.248			0.157	50.481	0.3924

**Table. 4.1 (d): Parameters obtained from the XRD analysis of Ti–20Nb–5Ag ball milled powders for 15 h by using Williamson-Hall method.**

Ball milling time: 15 h								
$\beta$ - phase	2 $\theta$ (degree)	hkl	d Å	Lattice parameter Å		FWHM $\beta_{hkl}$ (degree)	Crystallite Size (D) nm	Dislocation density $\times 10^{-3} \text{ nm}^{-2}$
	38.40	110	2.343	3.219		0.236	35.850	0.7780
	44.28	111	2.045			0.314	25.512	1.5364
	55.73	110	1.649			0.118	73.261	0.1863
	64.32	211	1.447			0.096	112.540	0.0789
	69.98	211	1.343			0.576	15.192	4.3326
	82.91	220	1.163			0.072	135.140	0.0547
	$\alpha$ - phase	2 $\theta$ (degree)	hkl			d Å	Lattice parameter Å	
				a <sub>o</sub>	c <sub>o</sub>			
38.407		002	2.343	2.50	4.5	0.236	35.850	0.7781
75.837		002	1.253			0.072	113	0.0783
86.906	202	1.12	0.96			9.583	10.889	



**Table. 4.1 (e): Parameters obtained from the XRD analysis of Ti–20Nb–5Ag ball milled powders for 20 h by using Williamson-Hall method.**

Ball milling time: 20 h								
$\beta$ - phase	$2\theta$ (degree)	hkl	d Å	Lattice parameter Å		FWHM $\beta_{hkl}$ (degree)	Crystallite Size (D) nm	Dislocation density $\times 10^{-3} \text{ nm}^{-2}$
	38.40	110	2.342	3.311		0.236	19.23	2.7042
	69.79	200	1.659			0.944	16.97	3.4724
$\alpha$ - phase	$2\theta$ (degree)	hkl	d Å	Lattice parameter Å		FWHM $\beta_{hkl}$ (degree)	Crystallite Size (D) nm	Dislocation density $\cdot 10^{-3} \text{ nm}^{-2}$
				$a_0$	$c_0$			
	38.21	100	1.88	2.95	4.68	0.551	15.67	4.0725

#### 4.1.3 Microstructure analysis of sintered porous Ti–20Nb–5Ag alloys

Fig. 4.6 shows the SEM micrographs of sintered porous Ti–20Nb–5Ag alloy developed from the various ball milled powders (1, 5, 10 15 and 20 h). It is noticed that the morphology of powders would significantly influence the pore characteristics of the sintered porous alloys. All the sintered porous alloys exhibited a uniform distribution of macropores throughout the surface, and all are well connected through a micropore which indicate the presence of interconnected pores in the sintered porous alloys. These interconnected pores play a necessary role to improve new bone ingrowth and osseointegration properties of implants (Gao et al., 2012b; Yue-qin et al., 2010). The microstructure of the sintered porous alloys which is made from low ball milling times show a smooth pore surface, sintering neck, and a few un-sintered particles which is possibly due to larger particle size which could significantly reduce the contact between the particles and thus hinder the densification during the sintering process (Aguilar et al., 2016c; H. Hsu et al., 2014).



On the other hand, the microstructure of the sintered porous alloy after prolonging milled powders, shows rough and corrugated pore surface, along with micropores were observed on macropore. It clearly suggests that there is very good interconnectivity between the pores. Fine particles significantly improve the surface area, sintering ability in the absence of any sintering neck and un-sintered particles (Aguilar et al., 2016c; H. Hsu et al., 2014). The average pore size of the sintered porous alloys was estimated using Image-J analysis software. With increasing ball milling time, the average pore size decreased from 139  $\mu\text{m}$  to 122  $\mu\text{m}$  for 1 h to 20 h time respectively.

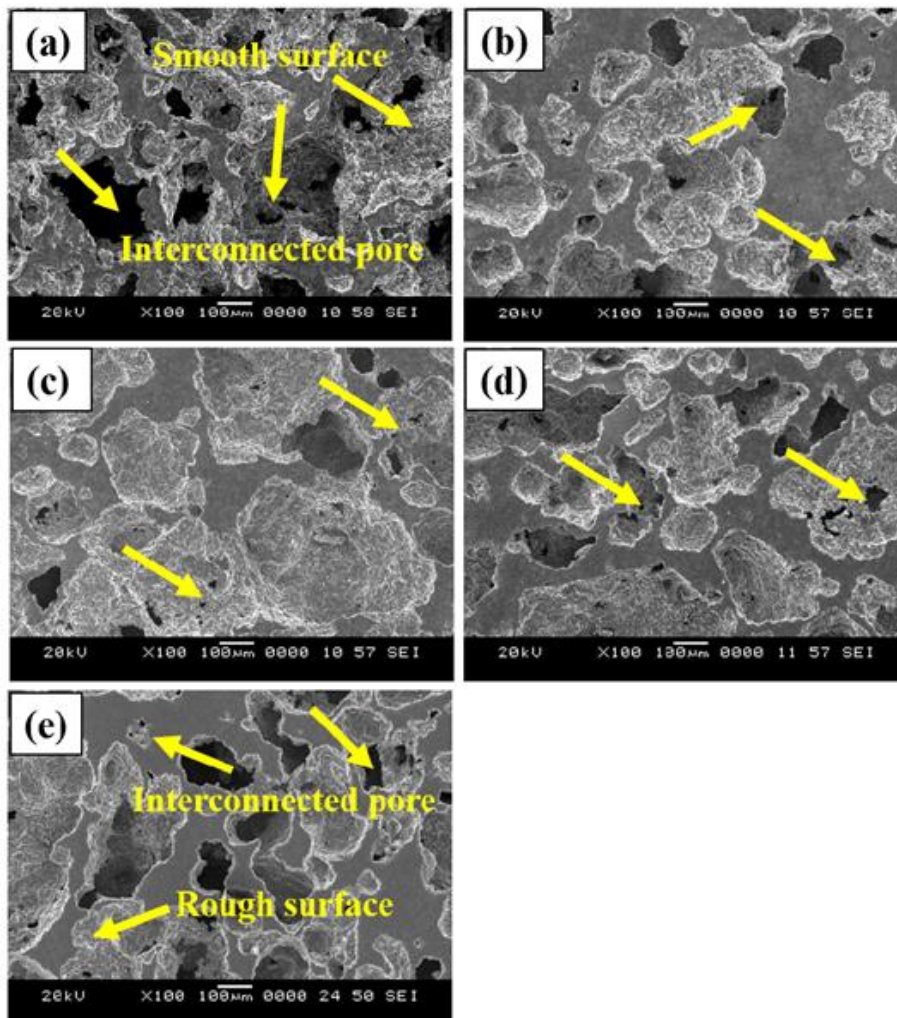


**Fig. 4.6: SEM micrographs of porous Ti–20Nb–5Ag alloy developed from various ball milled powders for: (a) 1 h, (b) 5 h, (c) 10 h (d) 15 h, and (e) 20 h.**

Fig. 4.7 shows the backscattered SEM images of the porous Ti-20Nb-5Ag alloy developed from different ball milling times for 1, 5, 10, 15 and 20 h. The microstructure of the porous alloys made by lower milling times (1, 5 and 10 h) exhibited a heterogeneous microstructure, as evidenced by high volume fraction of  $\beta$  Nb-rich phase (bright region) in  $\alpha$ -Ti (dark region). With increasing ball milling time for 15 and 20 h, the volume fraction of  $\beta$  phase marginally decreased, and exhibits the bright Nb-rich phase colonies were mostly homogenized, where dark Ti matrix showing a decrease in size and volume fraction of  $\alpha$ -Ti phase. (F. X. Xie et al., 2013).

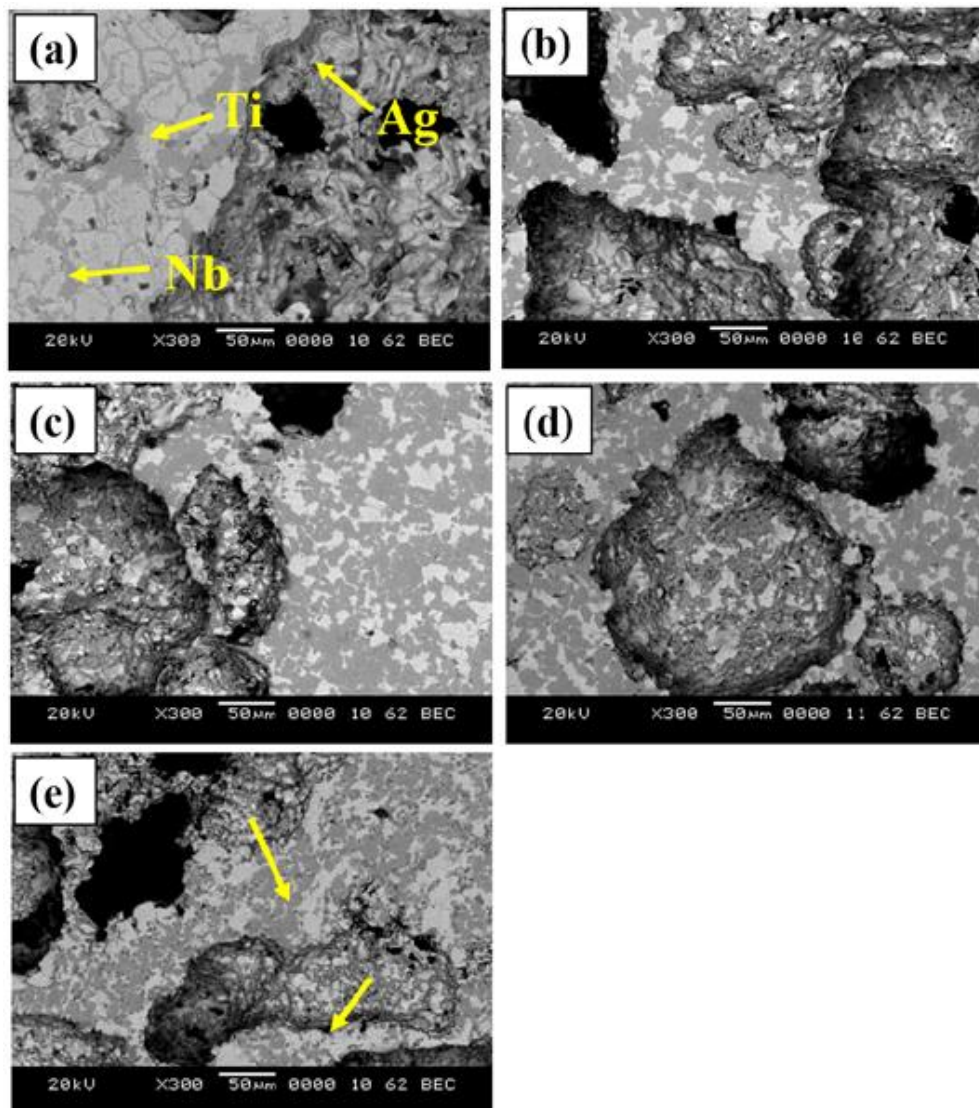


**Fig. 4.7: Backscattered SEM microstructure of the porous Ti-20Nb-5Ag alloy with different ball milling times: (a) 1 h, (b) 5 h, (c) 10 h (d) 15 h, and (e) 20 h.**

The sintered porous alloys made from lower duration milled powders has less diffusion between the particles, it is due to the bigger particle. This lead to lower surface area and low sintering ability, result in the formation of more  $\beta$  Nb-rich phase (bright region) with heterogeneous microstructure. On other hand, the porous alloys made from the higher duration ball milled powders had smaller particles which showed high diffusion rate. Resulting in slight reduction in  $\beta$  Nb-reach phase, which considerably increases homogeneous microstructure throughout the surface. The results show good agreement with the previous study on porous Ti-Sn-Nb alloy reported by (Nouri et al., 2011).

#### 4.1.4 XRD analysis

Fig. 4.8 shows the XRD patterns of porous Ti–20Nb–5Ag alloys made from various ball milled powders (1, 5, 10, 15 and 20 h) and sintered at 1200 °C for 3 h. The patterns did not reveal significant diffraction peaks of individual elemental Nb and Ag which indicating a complete dissolution in Ti matrix after the sintering. (Aguilar et al., 2016a; M. Wen et al., 2014b).

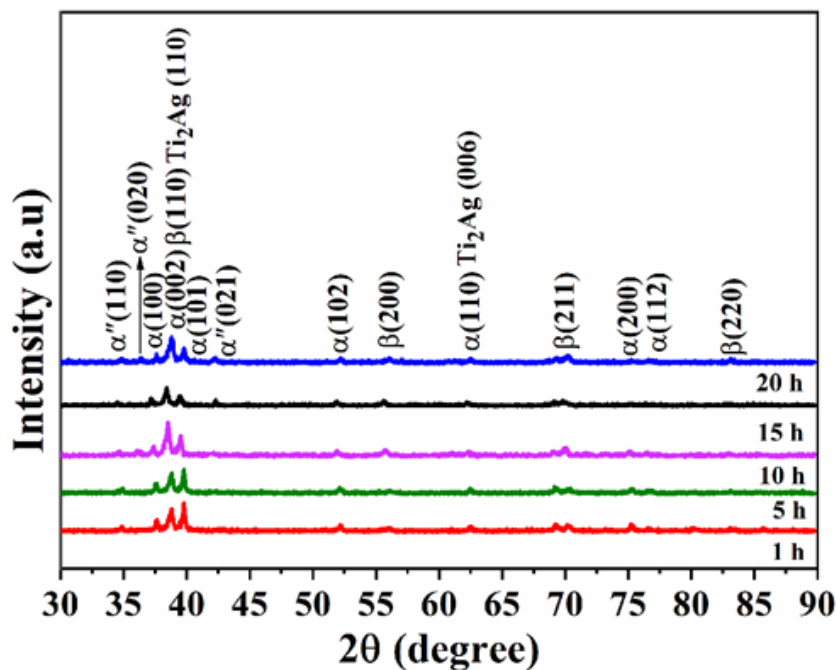


**Fig. 4.8: XRD patterns of sintered porous Ti–20Nb–5Ag alloy developed using different ball milling time.**

The diffraction patterns of sintered alloy were predominantly composed with  $\beta$  phases and formation of minor  $\alpha$  phases indicating complete diffusion of Nb into Ti after sintering in a high vacuum atmosphere ( $10^{-5}$  mbar). However, a small amount of  $\alpha'$  martensite phase, and small fraction of  $Ti_2Ag$  phase along with  $\alpha$  and  $\beta$  phase in the sintered porous alloy made from the 15 and 20 h ball milled powder could be located (M. Chen et al., 2016; Szaraniec & Goryczka, 2017). Interestingly, formation of  $\alpha'$  martensite phase significantly helps to reduce the elastic modulus of Ti-based alloys (Q. Liu et al., 2013; Mendes et al., 2016).

These results are in good agreement with the previous study reported by Wen et al. (M. Wen et al., 2014b). Moreover, the XRD results are examined to investigate the lattice strain and crystallite size of sintered porous alloys using Williamson-Hall method. The obtained lattice parameters crystallite size and dislocation density of sintered porous alloys are summarized in the Table. 4.2 (a-e). It showed that there is gradual decrease in lattice parameters of sintered porous alloys with increase in ball milling time, which is due to the sintering effect. The lattice parameters of the sintered porous alloys are presented in Table. 4.2. It is observed that as the high energy ball milling time increases, the lattice parameters of the unit cell of  $\alpha$  and  $\beta$  phases are slightly reduced.

**Table. 4.2 (a): Parameters obtained from the XRD analysis of the sintered porous alloys using 1 h ball milled powder analysed using Williamson-Hall method.**

Sintered porous alloy using 1 h ball milled powder							
	2 $\theta$ (degree )	Hkl	d Å	Lattice parameter Å	FWHM $\beta_{hkl}$ (degree)	Crystallite Size (D) nm	Dislocation density $\times 10^{-3} \text{ nm}^{-2}$
$\beta$ - phase	38.42	110	2.342	3.367	0.314	26.972	1.3744
	44.31	200	2044		0.551	14.614	4.6819
	77.45	211	1.231		0.576	26.623	1.4105
	82.40	220	1.169		0.768	11.060	8.1735

	83.04	220	1.230			0.118	151.46	0.0435
	81.43	220	1.181			0.236	33.879	0.8712
	82.58	220	1.168			0.314	28.013	1.2743
<b><math>\alpha</math>- phase</b>	<b>2<math>\theta</math></b> (degree)	<b>hkl</b>	<b>d Å</b>	<b>Lattice parameter Å</b>		<b>FWHM <math>\beta_{hkl}</math> (degree)</b>	<b>Crystallite Size D nm</b>	<b>Dislocation density <math>\times 10^{-3} \text{ nm}^{-2}</math></b>
				<b>a<sub>o</sub></b>	<b>c<sub>o</sub></b>			
	38.41	002	2.34313	3.69	4.49	0.196	43.112	0.5380
	75.81	112	1.25486			0.157	51.535	0.3765
	76.25	112	1.24863			0.314	27.736	1.2998
	77.61	201	1.23008			0.118	151.46	0.0435
	81.43	004	1.1818			0.236	33.879	0.8712
76.45	112	1.244					0.144	63.8

**Table. 4.2 (b): Parameters obtained from the XRD analysis of the sintered porous alloys using 5 h ball milled powder analysed using Williamson-Hall method.**

<b>Sintered porous alloy using 5 h ball milled alloy powder</b>							
	<b>2<math>\theta</math></b> (degree)	<b>hkl</b>	<b>d Å</b>	<b>Lattice parameter Å</b>	<b>FWHM <math>\beta_{hkl}</math> (degree)</b>	<b>Crystallite Size (D) nm</b>	<b>Dislocation density <math>\times 10^{-3} \text{ nm}^{-2}</math></b>
<b><math>\beta</math>- phase</b>	38.44	110	2.341	3.3461	0.629	13.543	5.4517
	44.28	111	2.045		0.472	17.003	3.4588
	44.64	111	2.029		0.059	142.25	0.0494
	64.36	210	1.447		0.196	56.071	0.3180
	64.75	210	1.438		0.072	193.24	0.0267

	69.62	211	1.350			0.787	10.431	9.1910
	81.76	220	1.177			0.157	50.482	0.3923
	82.50	220	1.169			0.236	36.672	0.7435
<b><math>\alpha</math>-phase</b>	<b>2<math>\theta</math></b> <b>(degree)</b>	<b>hkl</b>	<b>d Å</b>	<b>Lattice parameter Å</b>		<b>FWHM <math>\beta_{hkl}</math></b> <b>(degree)</b>	<b>Crystallite Size (D)</b> <b>nm</b>	<b>Dislocation density</b> <b><math>\times 10^{-3} \text{ nm}^{-2}</math></b>
				<b>a<sub>o</sub></b>	<b>c<sub>o</sub></b>			
	35.20	100	2.559	2.31	4.64	0.314	79.704	0.1574
	38.44	002	2.342			0.629	13.543	5.4518
	40.10	101	2.251			0.551	39.915	0.6277
53.10	102	1.729	0.629			83.743	0.1426	
	62.77	110	1.471			0.472	16.820	3.5343
	76.02	112	1.331			0.944	8.838	12.801

**Table. 4.2 (c): Parameters obtained from the XRD analysis of the sintered porous alloys using 10 h ball milled powders analysed using Williamson-Hall method.**

<b>Sintered porous alloy using 10 h ball milled alloy powder</b>							
	<b>2<math>\theta</math></b> <b>(degree)</b>	<b>hkl</b>	<b>d Å</b>	<b>Lattice parameter Å</b>	<b>FWHM <math>\beta_{hkl}</math></b> <b>(degree)</b>	<b>Crystallite Size (D)</b> <b>nm</b>	<b>Dislocation density</b> <b><math>\times 10^{-3} \text{ nm}^{-2}</math></b>
<b><math>\beta</math>-phase</b>	38.79	110	2.321	3.291	0.197	47.321	0.4465
	55.98	200	1.642		0.196	42.007	0.5667
	70.21	211	1.340		0.393	23.663	1.7858
	83.10	220	1.162		0.944	11.1	8.1163

	$2\theta$ (degree)	hkl	d Å	Lattice parameter Å		FWHM $\beta_{hkl}$ (degree)	Crystallite Size (D) nm	Dislocation density $\times 10^{-3} \text{ nm}^{-2}$
				$a_0$	$c_0$			
$\alpha$ -phase	38.79	101	2.321	3.28	4.25	0.196	47.321	0.4465
	70.21	300	1.340			0.393	23.663	1.7858
	79.58	112	1.204			0.195	80.952	0.1525
	83.10	220	1.162			0.944	11.1	8.1163

**Table. 4.2 (d): Parameters obtained from the XRD analysis of the sintered porous alloys using 15 h ball milled powders analysed using Williamson-Hall method.**

Sintered porous alloy using 15 h ball milled powder								
	$2\theta$ (degree)	hkl	d Å	Lattice parameter Å		FWHM $\beta_{hkl}$ (degree)	Crystallite Size (D) nm	Dislocation density $\times 10^{-3} \text{ nm}^{-2}$
				$a_0$	$c_0$			
$\beta$ -phase	38.83	110	2.319			0.196	47.845	0.4368
	56.08	200	1.639			0.236	34.553	0.8375
	70.21	211	1.340			0.393	23.674	1.7842
	83.24	220	1.160			0.314	35.463	0.7951
$\alpha$ -phase	$2\theta$ (degree)	hkl	d Å	Lattice parameter Å		FWHM $\beta_{hkl}$ (degree)	Crystallite Size (D) nm	Dislocation density $\times 10^{-3} \text{ nm}^{-2}$
	$a_0$	$c_0$						
	40.62	101	2.220	4.44	5.16	0.196	4.143	58.2519
53.21	102	1.721		0.157		9.390	11.3407	



**Table. 4.2 (e): Parameters obtained from the XRD analysis of the sintered porous alloys using 20 h ball milled powders analysed using Williamson-Hall method.**

Sintered porous alloy using 20 h ball milled powder								
$\beta$ - phase	2 $\theta$ (degree)	hkl	d Å	Lattice parameter Å		FWHM $\beta_{hkl}$ (degree)	Crystallite Size (D) nm	Dislocation density $\times 10^{-3} \text{ nm}^{-2}$
				$a_0$	$c_0$			
	38.76	110	2.322			0.236	39.05	0.6557
	44.59	111	2.031			0.235	35.274	0.8037
	56.09	110	1.639			0.472	17.253	3.3593
	70.31	211	1.338			0.314	30.512	1.0741
$\alpha$ - phase	2 $\theta$ (degree)	hkl	d Å	Lattice parameter Å		FWHM $\beta_{hkl}$ (degree)	Crystallite Size (D) nm	Dislocation density $\times 10^{-3} \text{ nm}^{-2}$
				$a_0$	$c_0$			
		34.89	100	2.571	2.5	4.25	0.236	199.47
	76.45	112	1.244			0.144	63.8	0.2457

Fig. 4.9 (a) shows the optical micrograph of the sintered porous Ti–20Nb–5Ag alloy made from 15 h ball milled powder (low magnification). The porous alloy was etched by Keller’s reagents (N. Jha et al., 2014). Fig. 4.9 (b) presents the microstructure of the porous alloy (high magnification) and it is clearly seen that  $\alpha$  (dark region) and  $\beta$  (bright region) grains, and rarely  $\alpha''$  grain formation was observed. Microstructure predominantly consists of  $\beta$  region, also revealing the formation of  $\alpha$  on the  $\beta$  region, which indicates that the porous alloy mainly composed with the  $\beta$  phase structure.

The effects of ball milling time on the porosity and density of porous Ti–20Nb–5Ag alloy are shown in Fig. 4.10. Porosity and density of the sintered porous alloys measured using Archimedes’ principle. The porosity of samples decreased from 71 % to 56 % with increasing HEBM time from 1 h to 20 h, respectively. On the other hand, the density increased from 1.5 g/cm<sup>3</sup> (1 h) to 2.2 g/cm<sup>3</sup> (20 h), which fairly



matches with the elastic modulus of natural bone (Y. Li & Shang, 2020). The relationship between the ball milling time with the porosity and density of the developed porous alloys using linear equation is as follows:

$$y = -1.06x + 73.25 \quad (12)$$

$$y = -0.04x + 1.42 \quad (13)$$

Where, the  $y$  is porosity and density of the developed porous alloys, and  $x$  is given ball milling time.

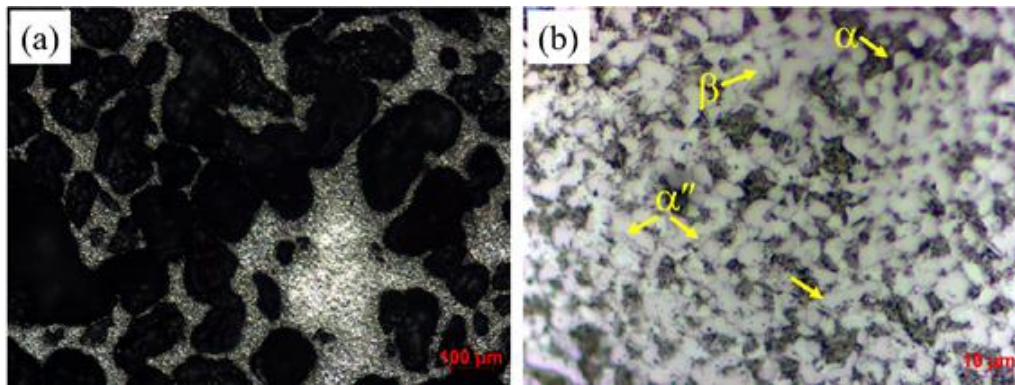


**Fig. 4.9:** Optical images of the sintered porous Ti-20Nb-5Ag alloy made from the 15 h of ball milled powder.

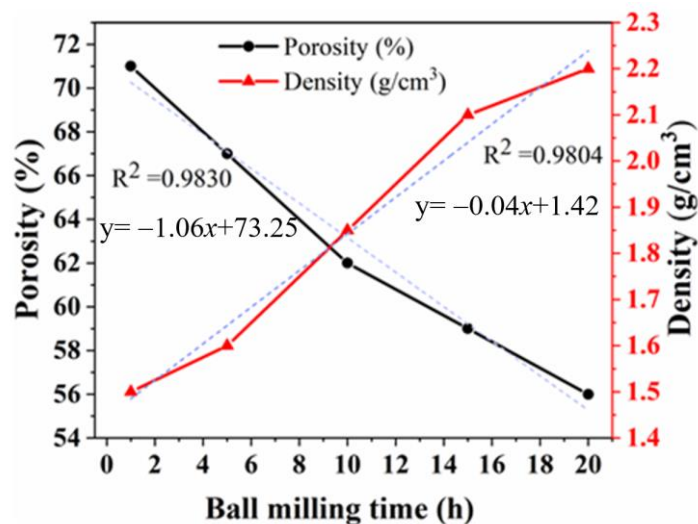


**Fig. 4.10:** Porosity and density of the sintered porous Ti-20Nb-5Ag alloy developed with various ball milling times for 1, 5, 10, 15 h and 20 h.

#### 4.1.5 Mechanical properties of porous Ti–20Nb–5Ag alloys

Typical compressive stress-strain curve and mechanical properties of the porous Ti–20Nb–5Ag alloy made from the various ball milled powders (for 1, 5, 10, 15, and 20 h) are shown in Fig. 4.11. It is noticed that the ball milling time has a direct effect on the compression strength and elastic modulus, which are increased from 21 MPa to 83 MPa, and 0.5 GPa to 3.3 GPa with increase ball milling time from 1 h to 20 h, respectively. The relationship between the ball milling time with the compression strength and elastic modulus of the developed porous alloys using linear equation is as follows:

$$y = -4.35x + 21.50 \quad (13)$$

$$y = 0.11x + 0.53 \quad (14)$$

Where, the  $y$  is compression strength and elastic modulus of the developed porous alloys, and  $x$  is given ball milling time.

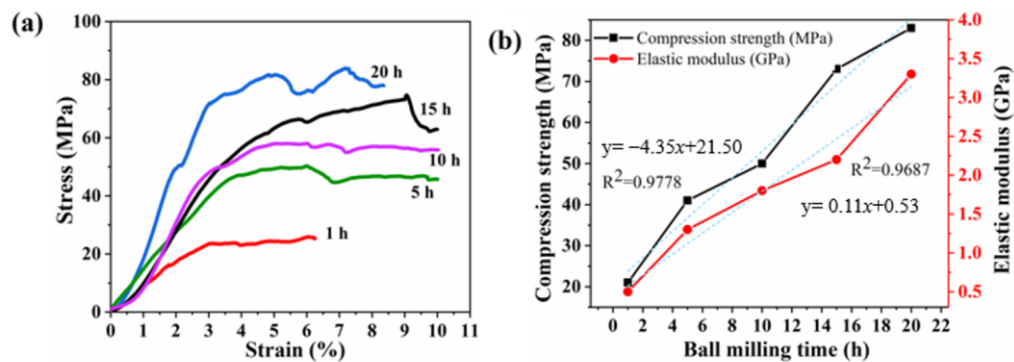


**Fig. 4.11: Sintered porous Ti–20Nb–5Ag alloy made from the various ball mill powders (a) Typical compressive stress–strain curve and (b) mechanical properties.**

Compared to a sintered porous alloy made from 1, 5, 10, and 15 h ball milled powders, the alloy made from 20 h ball milled powder possessed enhanced properties, due to the finer particles. This is due to increase in contact between the particles, which lead to faster densification during the sintering at high temperature under vacuum. Moreover, these results of elastic modulus are much lower as compared to conventional

metallic bulk biomaterials such as stainless steel (200 GPa), Co–Cr based alloys (200 GPa) and Ti–based alloys (90–110 GPa) (Geetha et al., 2009; Gepreel & Niinomi, 2013). Hou et al. (Hou et al., 2013) have developed the porous Ti–3Ag alloys and found a reduction in the porosity of about 64 % to 54 % with an increase in ball milling time from 1 h to 10 h. The study reported an increase of compression strength from 16 MPa to 53 MPa, as well as elastic modulus from 1 GPa to 1.9 GPa, with increase in ball milling time. The results suggested that the mechanical properties of the sintered alloys greatly depended on the particle size rather than addition of space holder materials. In the present study, we are able to achieve compression strength and elastic modulus of the porous Ti–20Nb–5Ag alloy close to that of human bone (Q. Chen & Thouas, 2015; Yue-qin et al., 2010).

#### **4.1.6. In-vitro electrochemical corrosion behavior of porous Ti–20Nb–5Ag alloys**

Fig. 4.12 shows typical electrochemical corrosion polarization behavior of porous Ti–20Nb–5Ag alloys made from various ball milled powders at 1, 5, 10, 15 and 20 h performed in SBF solution at 37 °C according to ASTM standard ASTM-G31-72 (Razavi et al., 2014). The results show similar polarization curves and typical self-passivation behavior for all the porous alloys, indicating the high protective passive film formation in electrolytes. The curves also exhibited active-passive transition regions along with stable passivation regions with higher potential (Fekry & El-Sherif, 2009). As observed in the polarization behavior of the porous alloys, a less negative corrosion potential value is noticed for the 20 h milled samples as compared to 1, 5, 10 and 15 h milled samples. The results indicate that increase in ball milling time lead to the more homogeneous distribution of the powder particles, which is significantly affecting the corrosion behavior of porous samples (Zamani et al., 2014).

It is also found that there is a shift in corrosion potential towards the nobler direction for the porous alloys when the ball milling time is increased. The corrosion parameters of the porous alloys deduced from the polarization curves as a function of ball milling time in SBF solution are summarized in Table 4.3. The results indicated that the corrosion potential ( $E_{\text{corr}}$ ) values of porous alloys shifted to positive direction (–0.56 to –0.32  $V_{\text{SCE}}$ ) and more importantly the corrosion current density ( $i_{\text{corr}}$ ) value

decreased (5.21 to 0.52  $\mu\text{A}/\text{cm}^2$ ) with increasing the ball milling time from 1 h to 20 h. Similarly, corrosion rate decreases when ball milling time is increased. It confirms that increasing ball milling times can significantly enhance the corrosion resistance of the developed sintered porous alloys, which is due to the presence of fine particle size and also significant homogeneous distribution of elemental particles after ball milling (Grosjean et al., 2004; Zamani et al., 2014) (F. X. Xie et al., 2013).

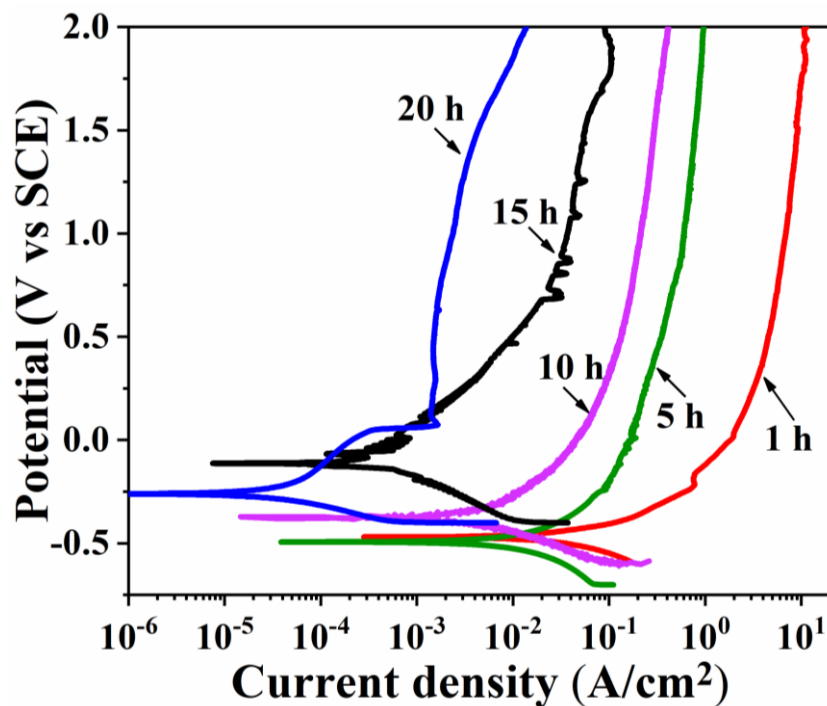


**Fig. 4.12: Potentiodynamic polarization curves in SBF solution at 37 °C for the sintered porous Ti-20Nb-5Ag alloy made from various ball milling times.**

However, the porous structure is also a very critical factor to consider in corrosion behavior. The porous alloys are more susceptible to corrosion as they provide a large area for electrolyte attack as compared to bulk samples (Fojt et al., 2013; Sun et al., 2011a). An interestingly active-passive plot, could show stable passivation at higher potential regions with the presence of porosities. Mostly, it is found even bulk alloy with any negligible porosity showed unstable polarization plot. Also, severe fluctuation in current as metastable passivity.

Moreover, it does not reflect any porous alloy and it only shows a reduction in passive current density ( $i_{\text{pass}}$ ) for  $4.89 \mu\text{A}/\text{cm}^2$  (1 h) to  $3.30 \mu\text{A}/\text{cm}^2$  (15 h). Corrosion rate of the sintered porous alloys reduced with ball milling time increased.

**Table 4.3: Potentiodynamic polarization parameters of porous Ti–20Nb–5Ag alloys made from various ball milled powders in SBF solution at 37 °C.**

Ball milling time (h)	$E_{\text{corr}}$ (V <sub>SCE</sub> )	$\beta_a$ (V/dec)	$\beta_c$ (V/dec)	$i_{\text{corr}}$ ( $\mu\text{A}/\text{cm}^2$ )	$i_{\text{pass}}$ at 0.5 V ( $\mu\text{A}/\text{cm}^2$ )	Corrosion rate (mm/y) x $10^{-3}$
1	-0.56	0.14	0.13	5.21	4.891	11.870
5	-0.51	0.10	0.09	2.18	3.603	4.656
10	-0.49	0.26	0.11	1.53	3.570	2.752
15	-0.41	0.14	0.12	0.61	3.501	0.982
20	-0.32	0.10	0.13	0.52	3.30	0.84

Fig. 4.13 shows the SEM micrographs of porous Ti–20Nb–5Ag alloy of 15 h milled powder after in vitro corrosion test and the EDX analysis of corroded surface. It exhibits morphological variations on the porous alloy surface. Small globular shape products are formed on the surface as corrosion products, which are identified as hydroxyapatite (Ca/P) and sodium (Na), due to the presence in the electrolytes (SBF) solution as revealed after EDX analysis [(Fig. 4.13(c)] (Sherif et al., 2020).

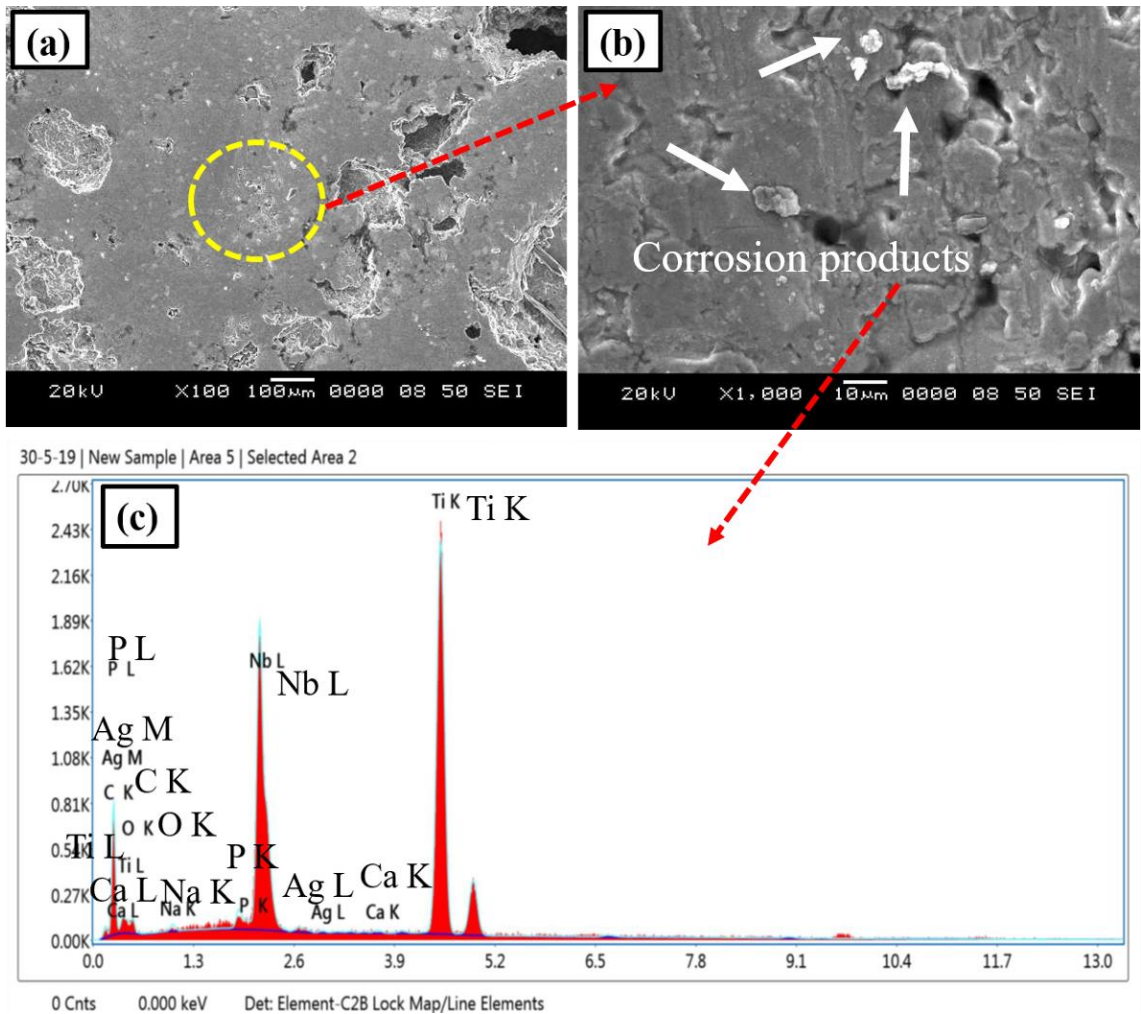


**Fig. 4.13: SEM micrographs of porous Ti–20Nb–5Ag alloy after corrosion test in SBF solution: (a) low and (b) high magnification region, (c) EDX analysis after corrosion test.**

## Summary

The effects of various high–energy ball milling times (1, 5, 10, 15 and 20 h) on microstructure, mechanical properties and in vitro corrosion behavior of porous Ti–20Nb–5Ag alloys have been studied and summary is presented follows:

- The distribution of the elemental powder particles significantly increases with increase in ball milling time.

- With increasing ball milling times, the porosity and pore size decreased from 71% to 56% and from 139  $\mu\text{m}$  to 122  $\mu\text{m}$ , respectively.
- After 15 and 20 h of ball milling time, XRD shows the formation of a small amount of  $\alpha''$  martensite and intermetallic compound of  $\text{Ti}_2\text{Ag}$  along with  $\alpha$  and  $\beta$  phases.
- The compression strength increased from 21 MPa to 83 MPa, and elastic modulus increased from 0.5 GPa to 3.3 GPa when ball milling time increased from 1 h to 20 h.
- The corrosion potentials shifting towards the nobler direction and remarkable reduction in corrosion current density, and passivation current density in SBF suggest significant improvement of in vitro corrosion resistance with increase in ball milling time.

## CHAPTER 4.2

### 4.2. Influence of addition of various Nb content on sintered porous Ti-xNb-5Ag alloys

*It is well reported that the amount of Nb in Ti based alloys plays an important role on the relevant properties. Among the several properties, Nb significantly influences on reducing the elastic modulus which minimizes the stress-shielding effect. The present study is focused to develop the porous Ti-xNb-5Ag alloys ( $x=25, 30$  and  $35$  wt. %) and to investigate the role of Nb content on Microstructure, mechanical properties and electrochemical corrosion behavior.*

#### 4.2.1 Synthesis and characterization of Ti-xNb-5Ag alloys powders

SEM micrographs of Ti-xNb-5Ag alloy powders ( $x=25, 30$  and  $35$  wt. %) developed after 20 h of ball milling as shown in Fig. 4.14 (a-c). Microstructure of the developed powders revealed dispersed particles of irregular shape which are slightly agglomerated. This is due to the intense plastic deformation by micro-forging between the powder particles and balls during the high energy ball milling process (Aguilar et al., 2016b; Salvo et al., 2017b).

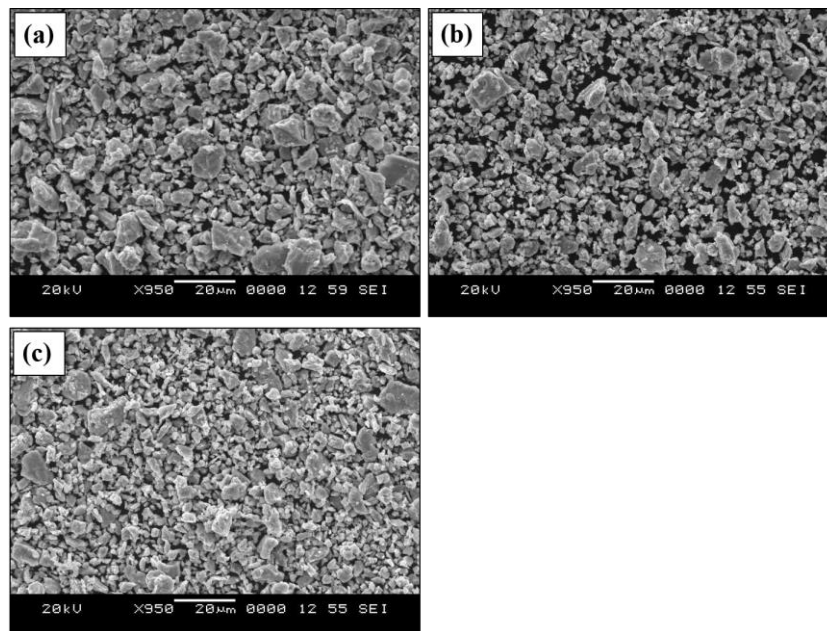


**Fig. 4.14: SEM micrographs of developed Ti-xNb-5Ag alloy powders after 20 h ball milling: (a) 25 wt. %, (b) 30 wt. %, and (c) 35 wt.%.**



The backscattered SEM images of the developed Ti-xNb-5Ag alloy powders with the addition of various Nb content (25–35 wt. %) after 20 h of ball milling are shown in Fig 4.15 (a–c). It can be seen that the solute elements of Nb and Ag are well incorporated into the Ti matrix during the ball milling process. The constituent elements of the ball milled powders can be easily distinguished by dark (Ti) and bright (Nb/Ag) regions as seen in Fig. 4.15 (a). It is observed that the solutes viz, Nb from 25 to 35 wt. % and 5 wt. % of Ag are significantly mixed into the Ti matrix. It could also be seen that more interfacial boundaries were formed after proper mixing using ball milling because of increase of collision frequency at longer ball milling times leading to a faster diffusion process (Nazari et al., 2015a; Nouri et al., 2011; M. Wen et al., 2014c). Prolonged milling time could refine and homogenize the powder particles. However, alloy with 35 wt. % of Nb content [(Fig. 4.15 (c)] seems to be more agglomerated as compared to alloy with smaller amounts of Nb content [Fig. 4.15 (a & b)]. This may be due to the predominance of cold welding of the added powder particles (Dercz & Matuła, 2017; Nazari et al., 2015a).

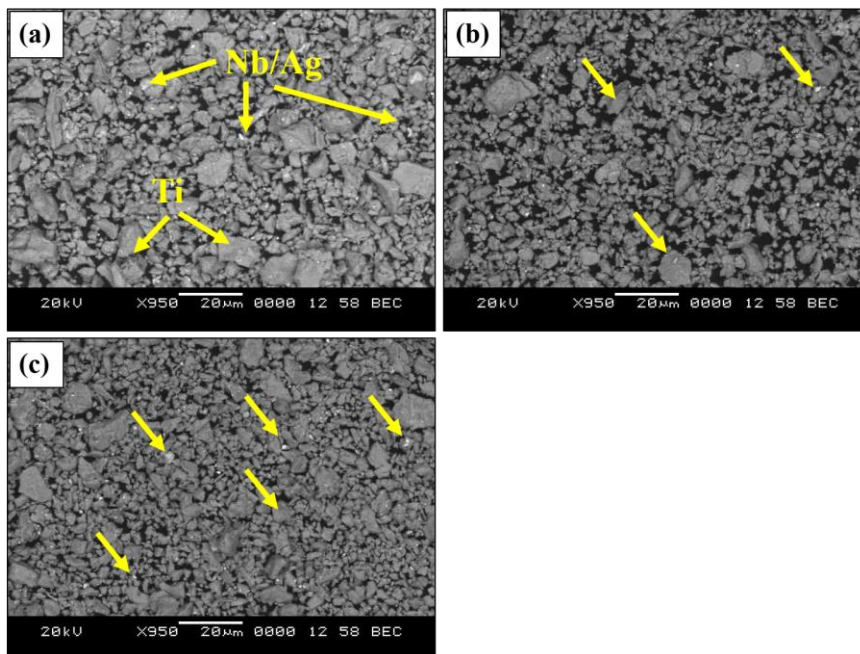


**Fig. 4.15: Backscattered SEM images of developed Ti-xNb-5Ag alloy powders after 20 h ball milling: (a) 25 wt. % Nb, (b) 30 wt. % Nb, and (c) 35 wt. % Nb.**

Fig. 4.16 shows the particle size distribution of Ti-xNb-5Ag alloy powders of various Nb content of 25, 30 and 35 wt. %. The laser particle size analyzer was used to measure the particle size distribution of the alloy powder after 20 h of ball milling. It is observed that there is a slight variation in the particle size after 20 h of ball milling. The particle size mainly gathered at a single peak and also it can be noticed that there is a slight shift towards the right-hand side of scale due to the addition of Nb content into alloy powder, indicating that the fraction increments in the particle size. This is mainly attributed to the agglomeration of powder particles after the ball milling. It is in good agreement with the SEM results presented in Fig. 4.15. However, the peak of the particle size distribution occurs at 6  $\mu\text{m}$ , 9  $\mu\text{m}$ , and 12  $\mu\text{m}$  for 25, 30 and 35 wt. % of Nb content, respectively after ball milling for 20 h.

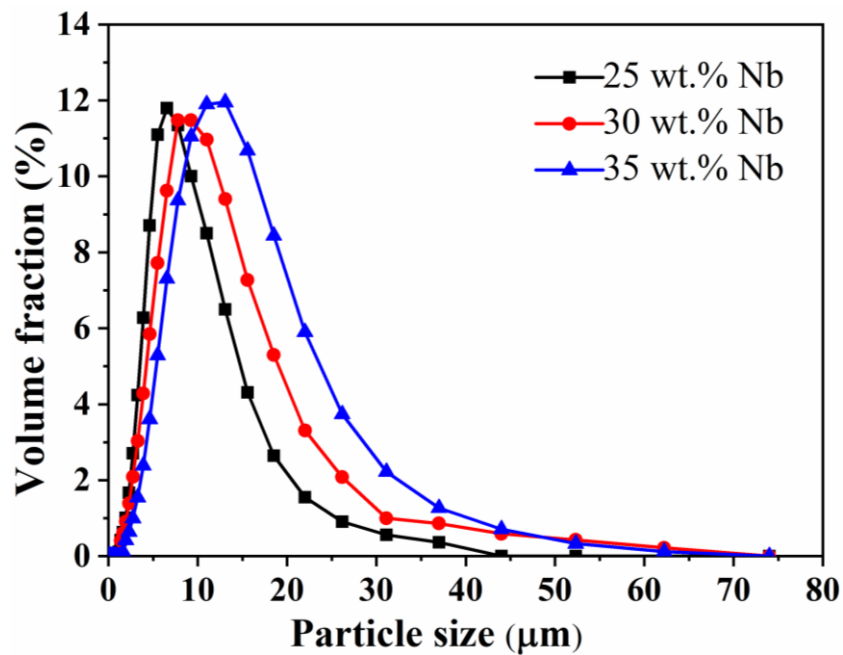


**Fig. 4.16: Particle size distribution of Ti-xNb-5Ag alloy powders developed with addition of various Nb content after 20 h of ball milling.**

#### 4.2.2 XRD analysis

The X-ray diffractograms for Ti- $x$ Nb-5Ag alloy powders ( $x=25, 30$  and  $35$  wt. %) after 20 h of ball milling are shown in Fig. 4.17. The patterns of ball milled powders exhibit various phases such as  $\alpha$ -Ti at  $2\theta$  values of  $38.8^\circ$ ,  $40.1^\circ$  and  $76.1^\circ$ , the corresponding planes of (002), (101) and (112) respectively. Similarly, the  $\beta$ -Ti obtained at  $2\theta$  values approximately  $38.7^\circ$ ,  $55.9^\circ$ ,  $70.1^\circ$  and  $83.1^\circ$  and their corresponding planes are of (110), (211) and (221), respectively. Interestingly, peaks of  $Ti_4Nb$  and  $TiO_2$  at  $2\theta$  values of  $39^\circ$ , and  $61.1^\circ$  respectively were also observed. On examining the X-ray diffractograms, it is observed that there is peak broadening and small peak shift due to the reduction in the crystalline size and also due to the presence of lattice strain, which is commonly observed at prolonged ball milling. The results are in good agreement with the previous work reported on the effect of milling (Aguilar et al., 2016c; Nazari et al., 2015a; M. Wen et al., 2014c).

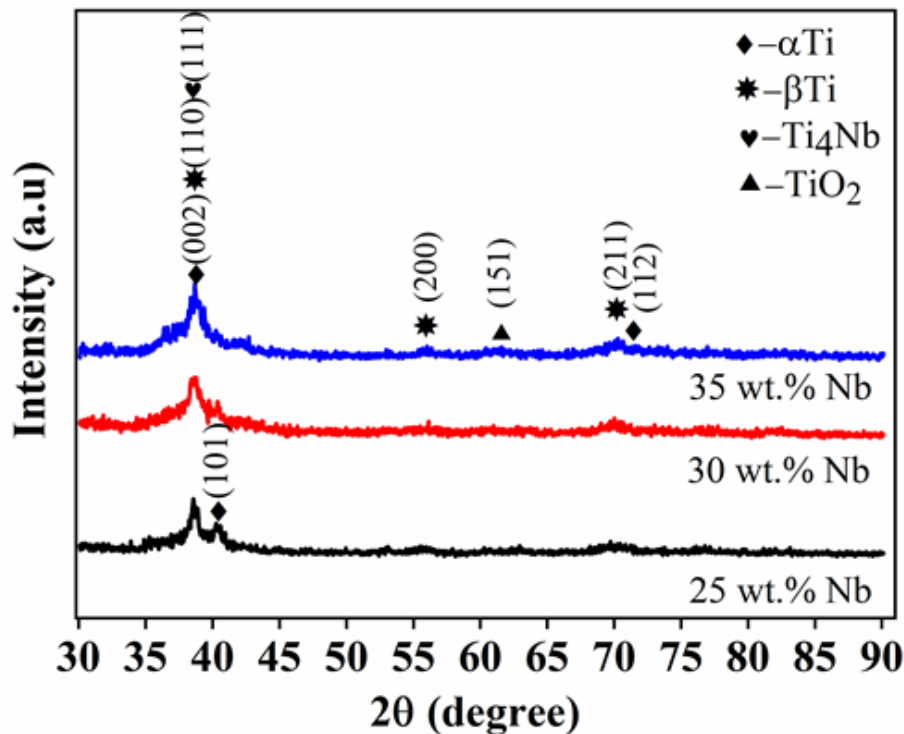


**Fig. 4.17:** X-ray diffractograms of developed Ti- $x$ Nb-5Ag alloy powders with the addition of various Nb content after 20 h ball milling: (a) 25 wt. %, (b) 30 wt. %, and (c) 35 wt.%.

### 4.2.3 Microstructural characterization of porous alloys

SEM micrographs and pore size distribution of the porous Ti- $x$ Nb-5Ag alloy ( $x=25, 30$  and  $35$  wt. %) are shown in Fig. 4.18. All these porous alloys exhibit homogeneous distribution of pores throughout the surface with irregular shape due to evaporation of space holder material (Nidhi Jha et al., 2013; B. Q. Li et al., 2015; Y. Q. Wang et al., 2011). On careful examination of the microstructure of the developed porous alloy surface, it is found many larger pores and small pores which are distributed over the surface, and also it can be seen that there are a number of small pores presented on the cell wall of large pores.

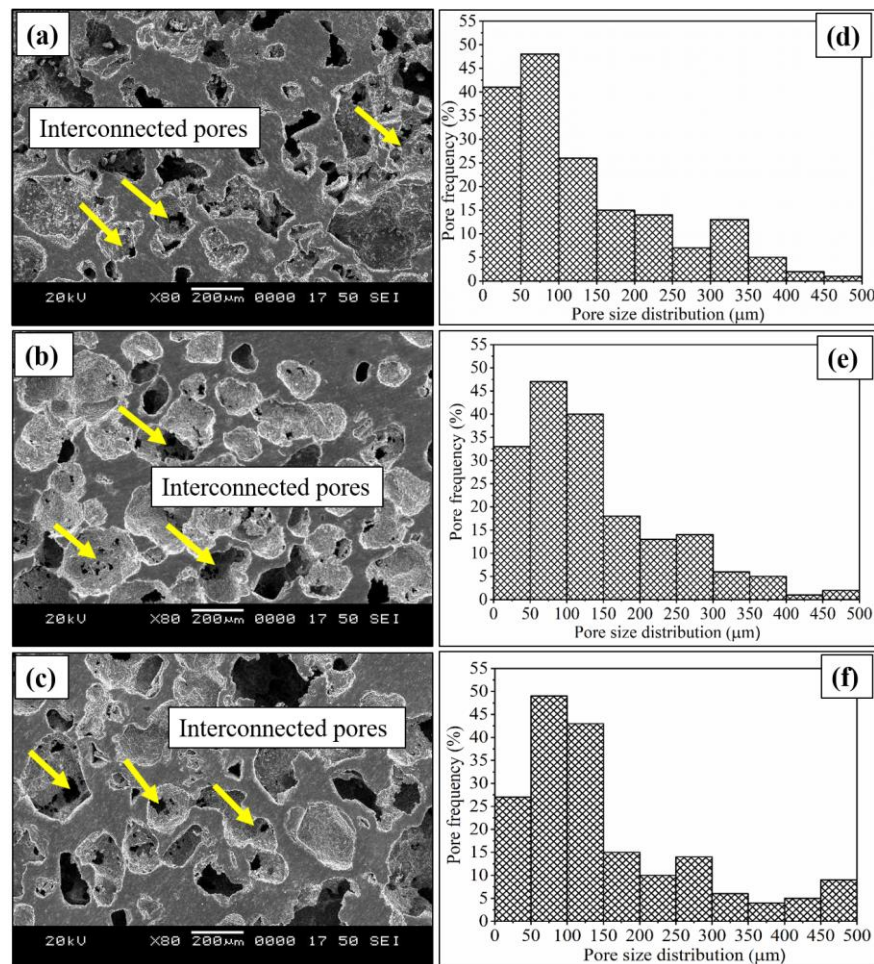


**Fig. 4.18: SEM morphology of developed porous Ti- $x$ Nb-5Ag alloys after 1200 °C: (a) 25 wt. %, (b) 30 wt. %, and (c) 35 wt. %.**

These microstructures indicate the presence of interconnected pores on the developed porous alloys [see the arrows in Fig 4.18 (a–c)]. Pore size distribution of the developed porous Ti–xNb–5Ag alloy is presented in Fig 4.18 (d–f) for 25, 30, and 35 wt. % of Nb content. The minimum three number of SEM micrographs per alloy with different regions were analyzed to measure the average pore size. In each porous alloy more than 100 pores were measured to determine the average pore size by using Image-J software (Rao et al., 2014a). The calculated average pore size of porous alloys is about 130  $\mu\text{m}$ , 136  $\mu\text{m}$  and 142  $\mu\text{m}$  for addition of 25, 30, and 35 wt. % Nb, respectively. The average pore size of each porous alloy is more than 100  $\mu\text{m}$ , which is an important requirement to enhance the osseointegration of developed implant's materials (Gao et al., 2012a; Y. Q. Wang et al., 2011).

Fig. 4.19 (a–c) shows the EDX analysis along with elemental mapping which is performed on an selected area of interest for Ti–xNb–5Mo alloy ( $x=25, 30$  and 35 wt. %) sintered at 1200 °C for 3 h. This illustrates that the distribution of Ti, Nb, Ag and O elements is uniform throughout the developed porous alloy surface. It also indicates noteworthy sintering is done at 1200 °C. It is also noticed that there is more Nb content distribution in the porous sample with the 35 wt. % of Nb [Fig. 4.19 (c)] as compared to the other samples [Fig. 4.19 (a and b)] due to increasing Nb content in the alloys.

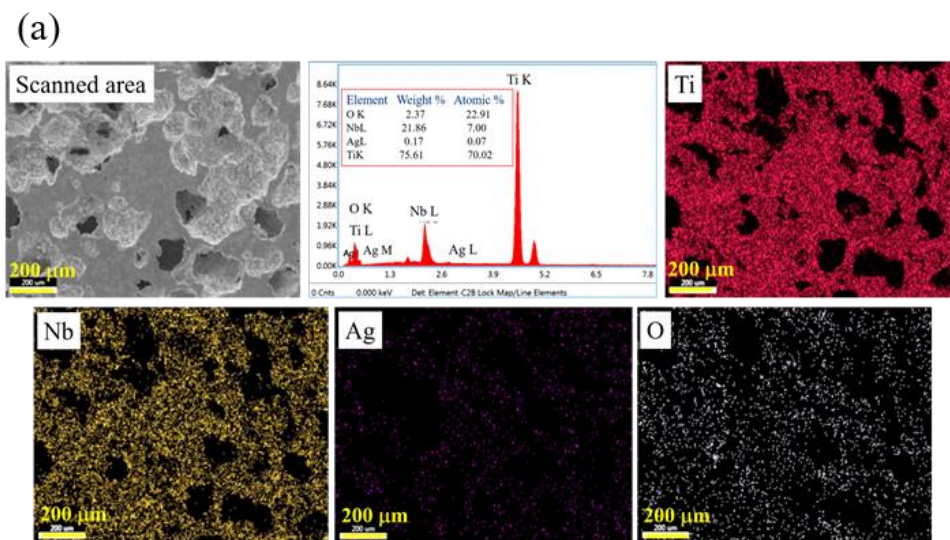


**Fig. 4.19 (a):** Elemental mapping of developed porous Ti–25Nb–5Ag alloys sintered at 1200 °C for 3 h.



(b)

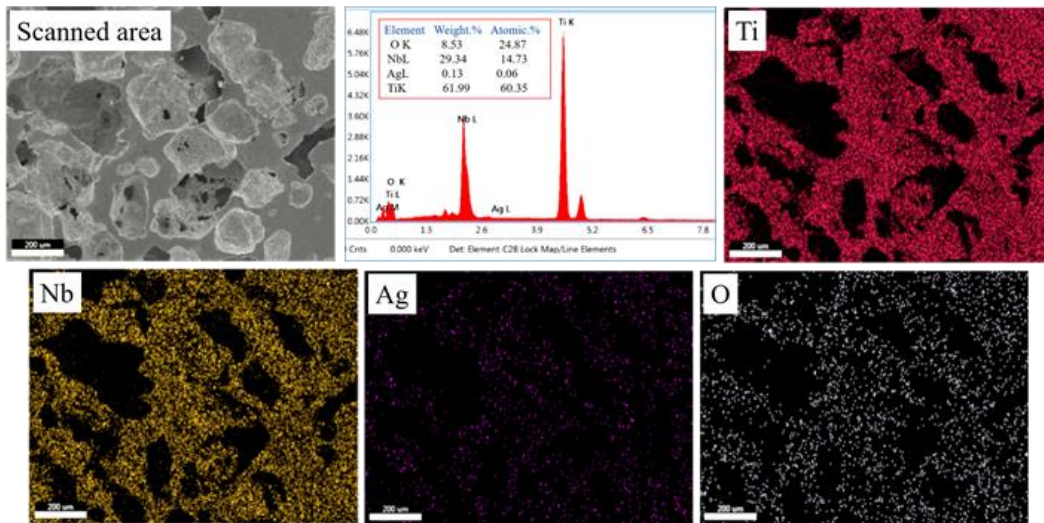


**Fig. 4.19 (b):** Elemental mapping of developed porous Ti-30Nb-5Ag alloys sintered at 1200 °C for 3 h.

(c)

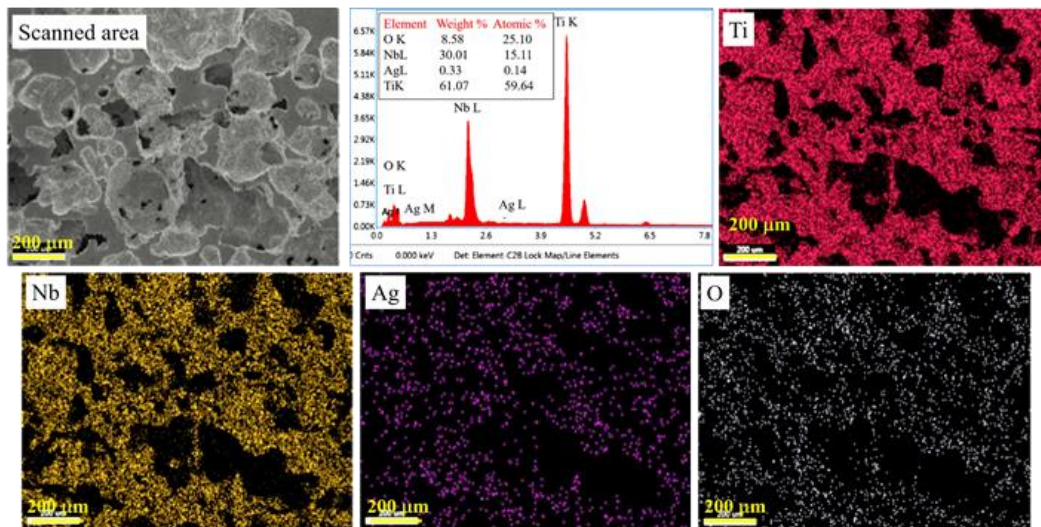


**Fig. 4.19 (c):** Elemental mapping of developed porous Ti-30Nb-5Ag alloys sintered at 1200 °C for 3 h.

XRD patterns of the developed porous Ti- $x$ Nb-5Ag alloys sintered at 1200 °C are presented in Fig. 4.20. It is interesting to notice a formation of intermetallic compounds  $Ti_4Nb$ , and oxides such as NbO and  $TiO_2$  along with  $\alpha$ -Ti and  $\beta$ -Ti phases.

These compounds such as  $Ti_4Nb$ ,  $TiO_2$ , and  $NbO$ , are identified by using the JCPDS codes as  $Ti_4Nb$  (65–7479),  $NbO$  (42–1125), and  $TiO_2$  (49–1433). The formation of the intermetallic compound  $Ti_4Nb$  was confirmed at  $2\theta$  values of  $38.6^\circ$  and  $70.2^\circ$  corresponding to the planes of (111) and (113) respectively. Similarly, formation of oxides is confirmed by the peaks at  $2\theta$  values of  $61.1^\circ$  as  $TiO_2$  [the corresponding plane of (151)] and at  $2\theta$  values of  $36.5^\circ$ ,  $42.5^\circ$  and  $73.9^\circ$  (belong to  $NbO$  compound) corresponding planes of (111) (200) and (311) respectively. However,  $\alpha$ -Ti phase showed lower intensity as compared to the  $\beta$ -Ti phase mainly due to the diffusion of Nb in Ti during the sintering process since Nb element is not detected in the sintered porous alloys due to the overlapping of Nb with the presence of  $\beta$ -Ti. Similar results of intermetallic compounds and oxides were reported in the sintered porous Ti–35Nb alloy sintered at  $1200^\circ C$  (C.S.S. de Oliveira., 2015).

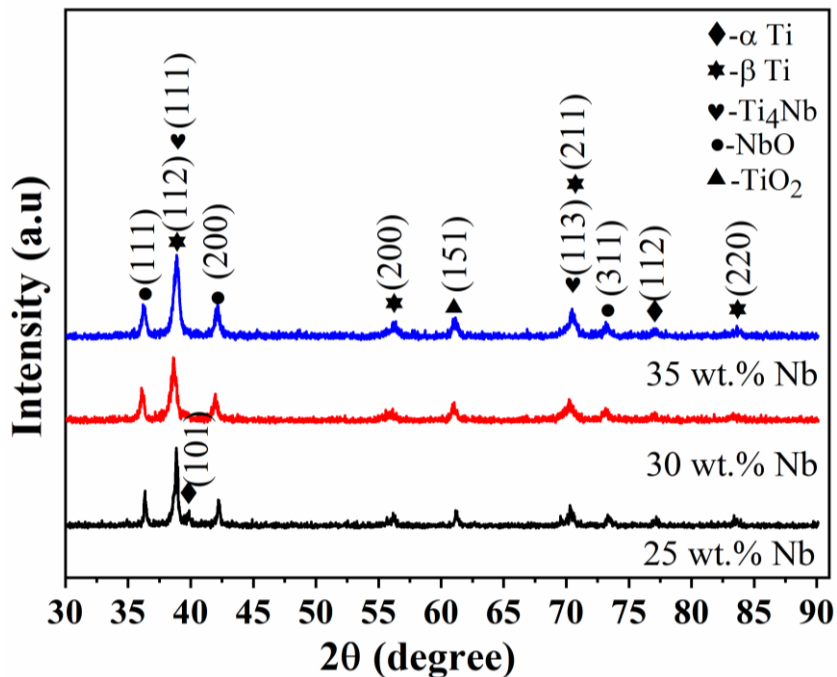


**Fig. 4.20: XRD analysis of developed porous Ti– $x$ Nb–5Ag alloys after sintered at  $1200^\circ C$  for 3 h: (a) 25 wt. % Nb, (b) 30 wt. Nb %, and (c) 35 wt. Nb%.**

Porosity and density of the sintered porous Ti– $x$ Nb–5Ag alloy ( $x=25, 30$  and  $35$  wt. %) with the addition of  $45$  wt. % of  $NH_4HCO_3$  is presented in Fig. 4.21. The porous alloys possessed a porosity ranging from  $57\%$  to  $65\%$ . A slightly higher porosity was found in the sintered porous alloy which is expected due to the addition of  $NH_4HCO_3$ .

A high porosity formation is not only supported by space holders but also due to formation of Kirkendall type pores during the sintering process (Rajamallu et al., 2019; Y. H. Wang et al., 2008; J. L. Xu et al., 2019a). The density of sintered porous alloys drastically reduces from 2.5 g/cm<sup>3</sup> to 1.5 g/cm<sup>3</sup>, for the addition of various Nb content, and the obtained values are found close to the density of human bone as 1.8–2.1 g/cm<sup>3</sup> (Staiger et al., 2006). These porosity and density values developed in porous alloys are fairly suitable to use in bone applications. The relationship between the Nb content with porosity and density of the developed porous Ti–xNb–5Ag alloy using linear equation is as follows:

$$y = -0.8x + 37.33 \quad (15)$$

$$y = -0.1x + 4.96 \quad (16)$$

Where, the  $y$  is porosity and density of the developed porous alloys, and  $x$  is addition of Nb content in the porous alloy.

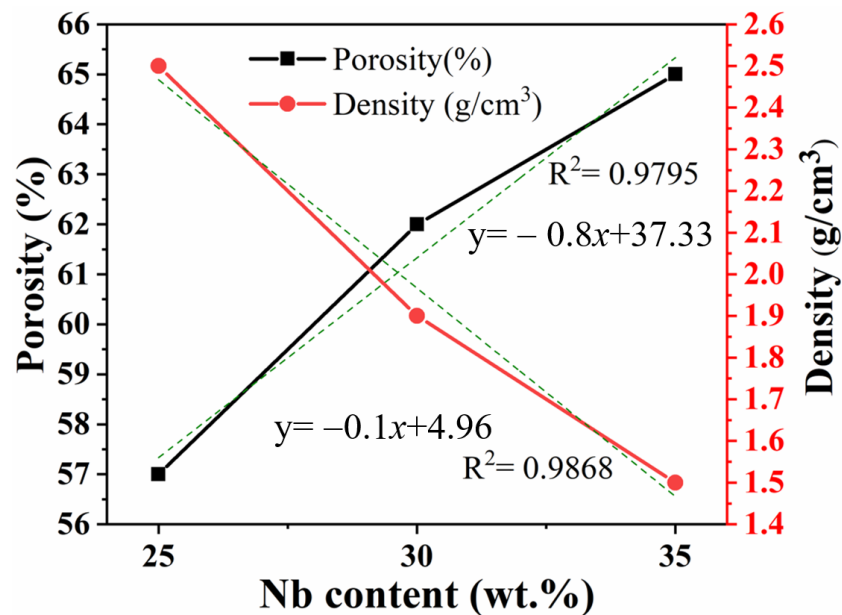


**Fig. 4.21:** Porosity and density values of porous Ti–xNb–5Ag alloy with the addition of various Nb content ( $x=25, 30$  and  $35$  wt. %) after sintered at  $1200$  °C.

#### 4.2.4 Mechanical properties of porous alloys



Mechanical properties of sintered porous Ti- $x$ Nb-5Ag alloy ( $x=25, 30$  and  $35$  wt. %) are obtained using compression stress-strain curves as shown in Fig. 4.22. A typical compression stress-strain curve clearly reveals three distinct regions, such as (i) linear elastic region, (ii) plateau region, and (iii) densification region. However, in the plateau region, it is observed that the fluctuation in stress value remains more constant even at higher strain (average stress in this region is known as plateau stress) and followed by densification. In the densification region, the stress is slightly reduced with increasing strain, where all the pore cell walls collapse due to the continuous applied stresses as seen in Fig. 4.22 (a). Fig. 4.22 (b) shows the elastic modulus and compression strengths of porous alloys, which are measured using compression stress-strain plot. It is observed that elastic modulus varies from 4, to 1.0 GPa, and the compression strength from 64 to 22 MPa for the addition 25 to 35 wt. % of Nb content respectively. These results show that the addition of Nb leads to gradual reduction in the compression strength and elastic modulus of the developed porous alloys (Q. Liu et al., 2013; Rajamallu et al., 2019; Ling-bo Zhang et al., 2015). Similarly, Liu et al. (2019) have produced a Ti- $x$ Nb-9Zr alloys using PM technique with  $x$  being 5, 10 and 15 wt. % Nb. They have reported reduction in elastic modulus from 62 to 38 GPa, for the addition of 5 to 15 wt. % of Nb, respectively. These variations of elastic modulus are responsible due to the addition of Nb content which is a  $\beta$  stabilizer and mainly reduces the bonding forces of the lattice by expanding unit cell volume (Q. Liu et al., 2013; Q. Wang et al., 2017). The relationship between the Nb content with compression strength and elastic modulus of the developed porous Ti- $x$ Nb-5Ag alloy using linear equation is as follows:

$$y = -4.2x + 168 \quad (17)$$

$$y = -0.3x + 11.4 \quad (18)$$

Where, the  $y$  is compression strength (17), and elastic modulus (18) of the developed porous alloys, and  $x$  is addition of Nb content in the porous alloy.

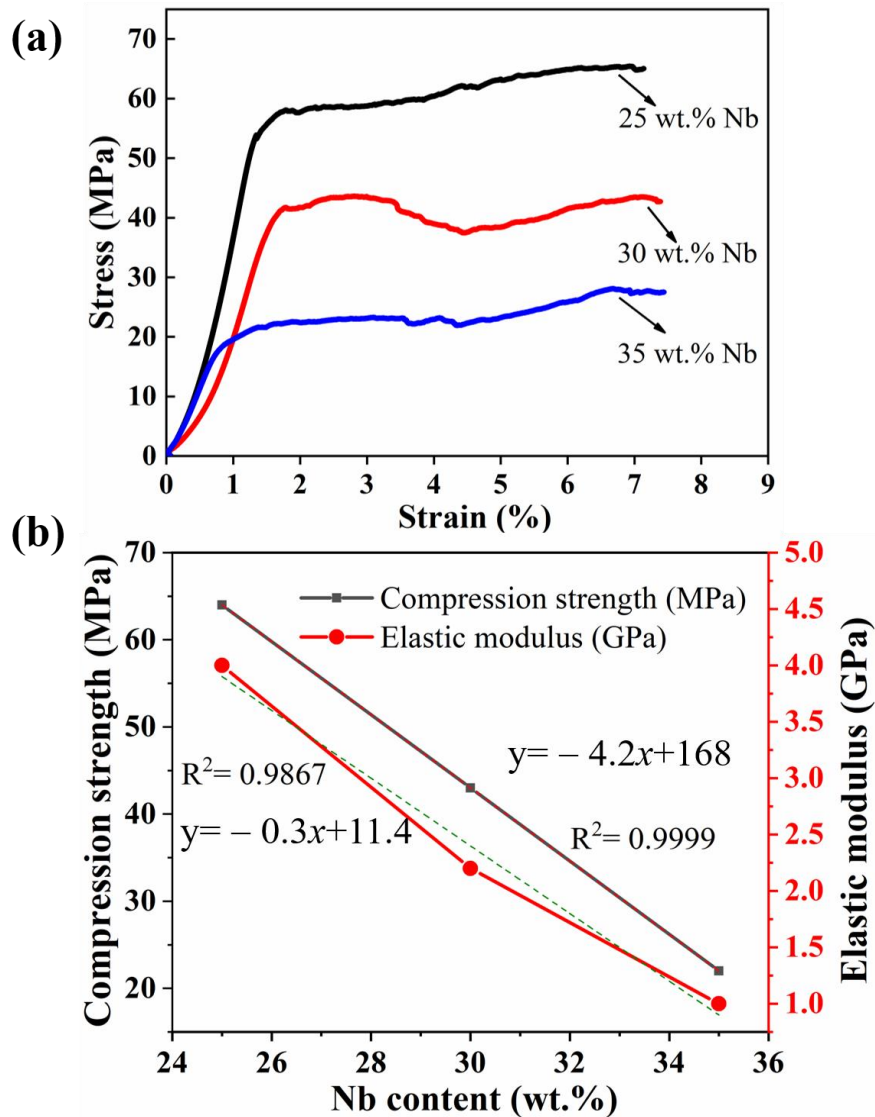


**Fig. 4.22: Stress-strain curves of porous Ti- $x$ Nb-5Ag alloy with the addition of various Nb content ( $x=25, 30$  and  $35$  wt.%), and (b) Compression strength and elastic modulus of porous alloys.**

#### 4.2.5 Role of Nb content on in-vitro corrosion study

Sintered porous Ti- $x$ Nb-5Ag alloy ( $x=25, 30$  and  $35$  wt. %) were immersed in SBF solution and potentiodynamic polarization, and EIS tests were conducted. Fig. 4.23 presents the potentiodynamic polarization curves of the sintered porous Ti- $x(25-35)$  Nb-5Ag alloys in SBF at  $37$  °C.

It is found that all the sintered porous alloys having a different porosity levels showed similar trends in typical active-passive corrosion plots. It contains cathodic region, anodic dissolution, and active-passive regions followed by trans passive regions with respect to changes in potentials. However, it did not show an exponential growth of corrosion current density on the increasing porosity like ferrous alloy and it could be due to high metallic passivity of Ti, Nb and Ag. It is also noticed that a very small fluctuation of corrosion current density at lower potential occurs which is due to the metastable passivation behavior of sintered porous Ti alloy (Xie et al., 2013, Yilmaz et al., 2018).

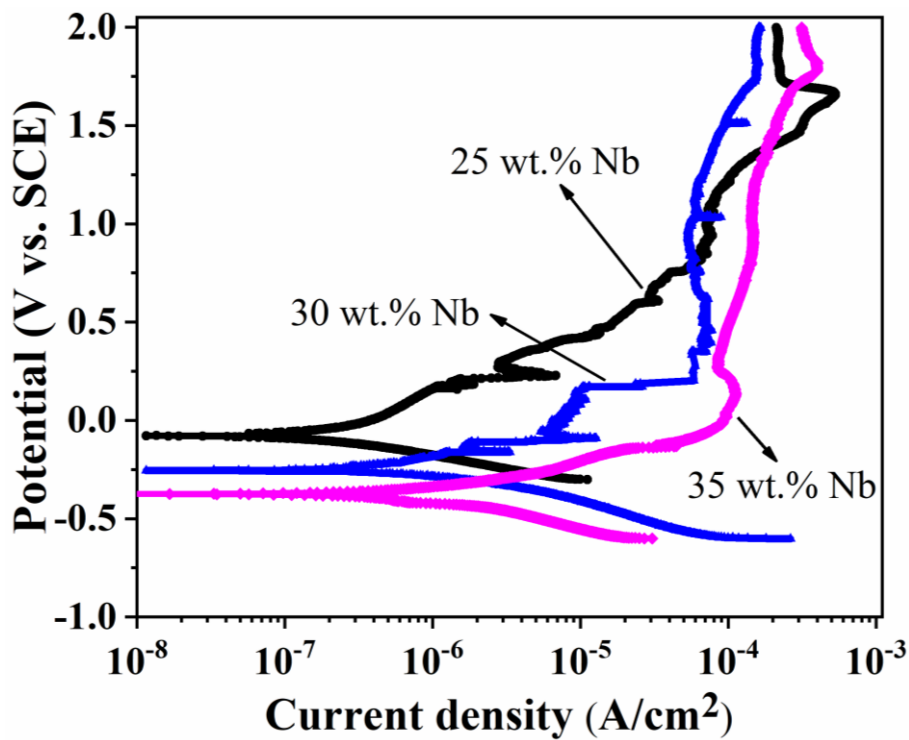


**Fig. 4.23: Potentiodynamic polarization curves of porous Ti- $x$ Nb-5Ag alloy with the addition of various Nb content ( $x=25, 30$  and  $35$  wt. %).**

The corrosion kinetics parameters such as corrosion potential ( $E_{\text{corr}}$ ), corrosion current density ( $i_{\text{corr}}$ ), anodic slope ( $\beta_a$ ), and cathodic slope ( $\beta_c$ ) are determined from the Tafel analysis using both anodic and cathodic branches (Fig. 4.23) and are presented in the Table. 4.4. On observing the  $E_{\text{corr}}$  values, it is noted a significant shift of potential towards negative direction due to unstable film for higher Nb content.

Yilmaz et al., (2019) and Xie et al., (2013) have reported electrochemical studies on sintered porous Ti–Nb alloy and porous Ti– (4–8%)Mo alloys in physiological solution and found that Nb and Mo addition as alloying elements directly control the porosities level and play an important role against the corrosion resistance of alloys. The addition of Nb and Mo in Ti matrix leads to formation of Kirkendall type pores, which increase the porosity in sintered porous alloys. This directly influences the corrosion properties of the porous alloys (Hao et al., 2015; L. Wu et al., 2014; J. L. Xu et al., 2019b). The results suggested that porous alloys having a high porosity exhibited low corrosion resistance as compared to the alloy having less porosity due to the exposure of more surface area to the electrolyte which easily penetrates along the interconnected porosities.

**Table. 4.4: Electrochemical corrosion parameters of the porous Ti–xNb–5Ag alloys (x=25, 30 and 35 wt. %) alloy in SBF solution at 37 °C.**

<b>Porous alloys</b>	<b>E<sub>corr</sub> (V)</b>	<b>β<sub>a</sub> (V/dec)</b>	<b>β<sub>c</sub> (V/dec)</b>	<b>i<sub>corr</sub> (μA/cm<sup>2</sup>)</b>	<b>i<sub>pass</sub> (μA/cm<sup>2</sup>) (at 0.5 V)</b>	<b>Corrosion rate (mm/y) × 10<sup>-3</sup></b>
25 wt.%	-0.13	0.34	0.11	0.20	0.016	1.68
30 wt.%	-0.21	0.15	0.16	0.63	0.069	6.76
35 wt.%	-0.37	0.17	0.18	1.10	0.102	15.84

Further, investigation on the characteristics of the passive film formation on the sintered porous alloys having different porosity levels is presented in the form of the EIS plot (Nyquist and Bode plots) as shown in Fig. 4.24. Nyquist plots [Fig. 4.24 (a)] exhibit an incomplete and large depressed semicircle, which indicates a capacitive response of passive film formation on the sample surface. It also shows that the semicircle radii increase in the sample with less porosity indicating a better impedance behavior of porous alloys with the higher porosity. Similar results were observed using potentiodynamic polarization tests (J. L. Xu et al., 2019).

Bode magnitude and phase angle plot are shown in Fig. 4.24 (b) and Fig. 4.24 (c) respectively. It is a good representation of impedance to see the resistance and capacitance behavior with respect to frequency at lower frequency  $R_s+R_p$ . However, at high frequency only  $R_s$  could be seen.

Porous alloy with the presence of 25 wt. % of Nb exhibits a higher modulus of impedance ( $Z$ ) than other Nb containing porous alloys, which is indicating a stable passivity response. Moreover, it is noticed that initially, the modulus of impedance showed a flat region due to the electrolyte resistance ( $R_s$ ). In the middle and lower frequency ranges, the curves exhibited a linear relationship of modulus with slope close to  $-1$  indicating a characteristic response of a capacitive behavior of passive film (Li et al., 2017). However, the impedance values increase due to reduction in porosity. The result shows that the porous alloy with the low porosity exhibits higher corrosion resistance than highly porous samples. The Bode frequency phase angle plot shows three distinct characteristics, such as high frequency region, middle frequency region, and the low frequency region. In the high frequency region, the phase angle drops towards the  $0^\circ$ , which is indicating the response of electrolyte resistance.

In the middle frequency region, the phase angle near to the  $75^\circ$ ,  $65^\circ$ , and  $60^\circ$  for porous alloy prepared with 25, 30, and 35 wt. % of Nb alloys, respectively which exhibit wide range frequencies indicating the formation of the compact protective passive film on the alloy surface and near capacitive response of the passive film. In the low frequency region, it is observed that the values of the phase angle drastically decreased to lower value due to the influence of resistance of the passive film (Vasilescu et al., 2012; Yilmaz et al., 2017). EIS parameters of experimental data are obtained using an equivalent circuit model [Fig. 4.24 (d)] to fit EIS data and results summarized in Table 4.5. The  $R_s$  is electrolyte resistance (SBF), and a constant phase element representing a shift from the ideal capacitor is used instead of capacitance.  $R_p$  and  $R_b$  are the resistances of the porous and barrier layers, which is associated with the charge transfer resistance through the porous layer.  $Q_p$  and  $Q_b$  correspond to the capacitances of the porous layer and barrier layer, which is related to the formation of the passive film layer.

The model assumed the formation of the oxide film, which was composed of the inner barrier layer ( $R_b$ ) and a porous outer layer ( $R_p$ ). All the ‘n’ values obtained after fitting are close to 1 indicating a near capacitive characteristic of passive film formed on the porous alloys.

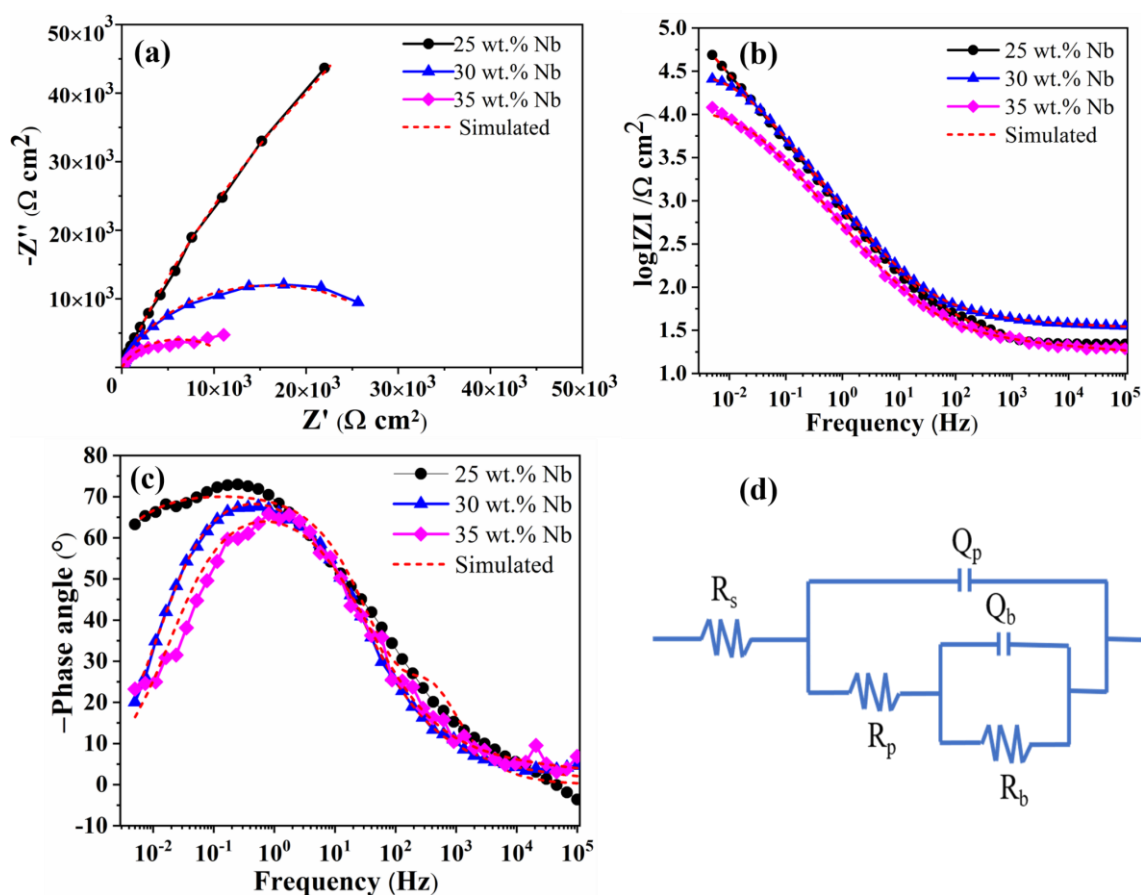


**Fig. 4.24: EIS plots of porous Ti-xNb-5Ag alloys (x=25, 30 and 35 wt. %) in SBF solution at 37 °C: (a) Nyquist impedance plot, (b) Bode magnitude plot, (c) Bode phase plot, and (d) equivalent circuit model.**

The barrier resistance ( $R_b$ ) is strongly dependent on the formation of the passive film. It shows a higher  $R_b$  value for 25 wt.% Nb ( $175 \text{ k}\Omega \text{ cm}^2$ ), which indicates its high corrosion resistance as compared to porous alloy containing 30 wt.% Nb ( $32 \text{ k}\Omega \text{ cm}^2$ ), and porous alloy containing 35 wt.% Nb ( $12 \text{ k}\Omega \text{ cm}^2$ ) alloys. Moreover, the  $R_b$  value of all the porous alloys is much higher than  $R_p$  values (porous layer), which suggest that the porous alloy surface is significantly protected by the thick and compact barrier film. The results show that the capacitance values  $Q_p$  and  $Q_b$  decrease, and the resistances  $R_p$

and  $R_b$  increase with reduction in porosities. The figure also indicates the formation of the total polarization resistance ( $R_t$ ) of passive layers ( $R_t = R_p + R_b$ ) on the porous alloys having more resistance with the decreasing porosity to the electrolytes. The lower capacitances of the porous alloys associated with higher resistance indicate high corrosion resistance of the developed porous alloys.

**Table. 4.5: Impedance parameters obtained by  $R_s(Q_p(R_p(Q_bR_b)))$  model to fit EIS data of porous Ti- $x$ Nb-5Ag alloy ( $x=25, 30$  and  $35$  wt. %) in SBF solution at  $37$  °C.**

Porous Alloy	$R_s$ ( $\Omega\text{cm}^2$ )	$Q_p \times 10^{-6}$ ( $\text{F cm}^{-2}$ )	$n_p$	$R_p$ ( $\Omega\text{cm}^2$ )	$Q_b \times 10^{-6}$ ( $\text{F cm}^{-2}$ )	$n_b$	$R_b$ ( $\text{k}\Omega\text{cm}^2$ )	$R_t = (R_p + R_b)$ ( $\text{k}\Omega\text{cm}^2$ )
25 wt.%	43.1	0.22	0.77	74.80	0.35	0.86	175	175.0
30 wt.%	21.9	1.17	0.73	46.31	0.22	0.85	32	32.0
35 wt.%	19.5	0.29	0.69	40.67	0.16	0.82	12	12.0

### Summary

- The porous porous Ti- $x$ Nb-5Ag alloy ( $x=25, 30$  and  $35$  wt. %) alloys were successfully fabricated from the 20 h ball milled powders with the addition of 45 wt. % of  $\text{NH}_4\text{HCO}_3$  and sintering at  $1200$  °C for 3 hrs.
- The sintered porous Ti- $x$ Nb-5Ag alloys exhibit a variation of porosity ranging from 57%–65% for the addition 25–35 wt. % Nb content and 45 wt. % of  $\text{NH}_4\text{HCO}_3$ .
- XRD analysis revealed that the sintered porous alloys predominantly consist of intermetallic compound  $\text{Ti}_4\text{Nb}$ , oxides  $\text{TiO}_2$ ,  $\text{NbO}$  along with  $\alpha$  and  $\beta$ -Ti phases.
- The significant reduction in the compression strength from 64 MPa to 22 MPa and elastic modulus from 4.2–1 GPa were observed for the addition of 25 wt. % to 35 wt. % Nb content in the sintered porous alloy, respectively.
- The electrochemical corrosion behavior of the porous alloys exhibit excellent corrosion resistance in SBF. It is observed that corrosion potential is decreased away from the noble direction, while corrosion current density increased with

increase in Nb content, where porosity also had an essential role in the corrosion behavior of sintered porous alloys.

- The 8% increment of porosity obtained for the addition of 25 to 35 wt. % Nb in the sintered porous alloys has significant influence on corrosion properties. It significantly reduces the stability of passive film as a 14.5 time reduction in passive film resistance.





## CHAPTER 4.3

### 4.3 Effects of addition of various amount of space holder material

*This chapter describes the role of addition of various amount of space holder material ( $\text{NH}_4\text{HCO}_3$ ) on the characteristics of pore morphology, microstructures, mechanical properties, and electrochemical corrosion behavior of the porous Ti–20Nb–5Ag alloys using 20 h ball milled powder.*

#### 4.3.1. Microstructural analysis

The SEM micrographs of samples with different porosities are developed using space holder materials (15 to 60 wt. % of  $\text{NH}_4\text{HCO}_3$ ) are shown in Fig. 4.25. It is evident that there is significant increment in porosity with increasing  $\text{NH}_4\text{HCO}_3$  (wt. %) contents. Fig. 4.25 (a) shows the microstructure of a porous sample with the addition of 15 wt. % of  $\text{NH}_4\text{HCO}_3$ . Microstructure exhibits the micropores and macropores which are obtained after elimination of space holder material during the sintering process.

The SEM image did not show any interconnected pores though, most of the pores are isolated which may be due to small amounts of  $\text{NH}_4\text{HCO}_3$ . Moreover, using 30 wt. % of  $\text{NH}_4\text{HCO}_3$  showed an increase in micropores and macropores with a very few interconnected pores on the macropores cell wall as shown in Fig. 4.25 (c). Further, the addition of 45 wt. % of  $\text{NH}_4\text{HCO}_3$ , the SEM micrograph showed the micropores on the cell wall of the macropores which is an evidence for the formation of interconnected porosity in the sintered porous alloy. Fig. 4.25 (d) shows SEM micrograph obtained for the highest amount of space holder materials (60 wt. % of  $\text{NH}_4\text{HCO}_3$ ), relatively extra interconnected pores which are connected through the micro and macro size pore on the cell wall. It is well stated that porous implant materials have mixed features, such as micropores, macropores, and interconnected pores. These kinds of pore structures are quite essential to facilitate the osseointegration properties of the implant materials, when inserted into the human body (H. C. Hsu et al., 2013; Xiao-hua Wang et al., 2013).

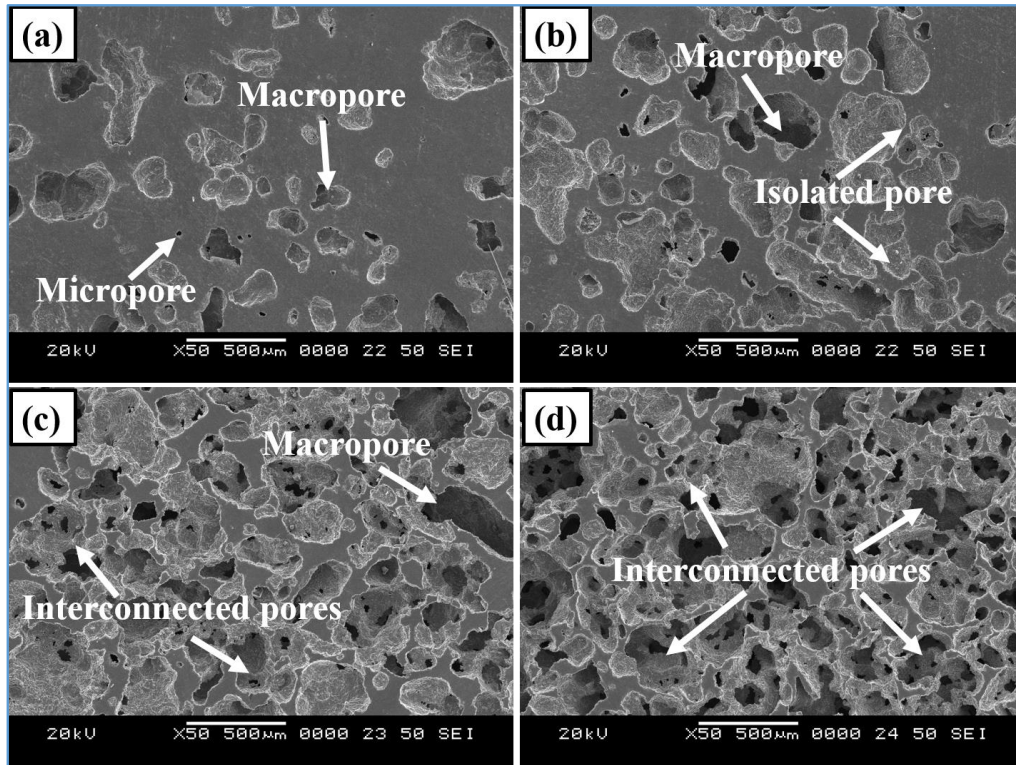


**Fig. 4.25: SEM images of porous Ti–20Nb–5Ag samples synthesized using different amounts of  $\text{NH}_4\text{HCO}_3$  (wt. %): (a) 15%, (b) 30% (c) 45% and (d) 60%.**

Pore size distribution of the developed porous Ti–20Nb–5Ag alloys with the various porosity levels is shown in Fig. 4.26 using Image-J software. Increasing the  $\text{NH}_4\text{HCO}_3$  content, the average pore size increased. The average pore sizes obtained are about 98  $\mu\text{m}$ , 115  $\mu\text{m}$ , 122  $\mu\text{m}$  and 130  $\mu\text{m}$  for the addition of 15%, 30%, 45% and 60 wt. % of  $\text{NH}_4\text{HCO}_3$ , respectively. A pore size as large as 500  $\mu\text{m}$ , could be seen in the sample having 68% porosity. It is reported that 100  $\mu\text{m}$  average pore size or above is required to enhance the osseointegration properties of implant materials (Xiao-hua Wang et al., 2013; Y. Q. Wang et al., 2011).

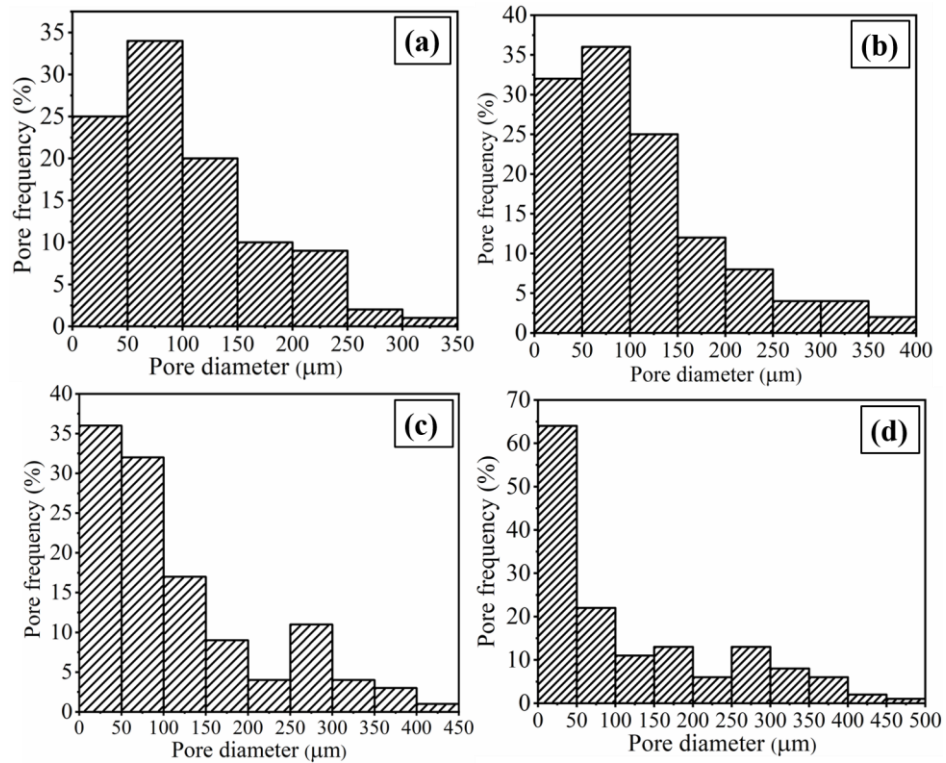


**Fig. 4.26: Pore size distribution of porous Ti–20Nb–5Ag samples synthesized using different amounts of  $\text{NH}_4\text{HCO}_3$  (wt. %): (a) 15%, (b) 30% (c) 45% and (d) 60%.**

The porosity and density of the developed porous Ti–20Nb–5Ag alloys are presented in Fig. 4.27. Porosity of the developed porous alloys are found to be 22%, 43%, 56% and 68% for the addition of 15%, 30%, 45% and 60 wt. % of  $\text{NH}_4\text{HCO}_3$  respectively. It clearly shows that porosity is directly dependent on the amount of space holder materials ( $\text{NH}_4\text{HCO}_3$ ), it is due to the elimination of low melting  $\text{NH}_4\text{HCO}_3$  during the sintering process. Fig. 4.27 also presents the density values (red color) of porous Ti–20Nb–5Ag alloys with the addition of various amounts of  $\text{NH}_4\text{HCO}_3$ . The measured density values revealed that there is significant reduction of about  $3 \text{ g/cm}^3$ ,  $2.6 \text{ g/cm}^3$ ,  $2.2 \text{ g/cm}^3$ , and  $1.5 \text{ g/cm}^3$  for the addition of 15%, 30%, 45% and 60 wt. % of  $\text{NH}_4\text{HCO}_3$ , respectively. It could be seen that there is 50% reduction in the density of the developed porous samples when compared to addition of 15 wt. % and 60 wt. % of  $\text{NH}_4\text{HCO}_3$ . The relationship between the  $\text{NH}_4\text{HCO}_3$  (wt. %) content with porosity and density of the developed porous Ti– $x$ Nb–5Ag alloy using linear equation is as follows:

$$y = 0.99x + 10 \quad (19)$$

$$y = -0.03x + 3.55 \quad (20)$$

Where, the  $y$  is porosity (19), and density (20) of the developed porous alloys, and  $x$  is addition of  $\text{NH}_4\text{HCO}_3$  (Wt. %) content.

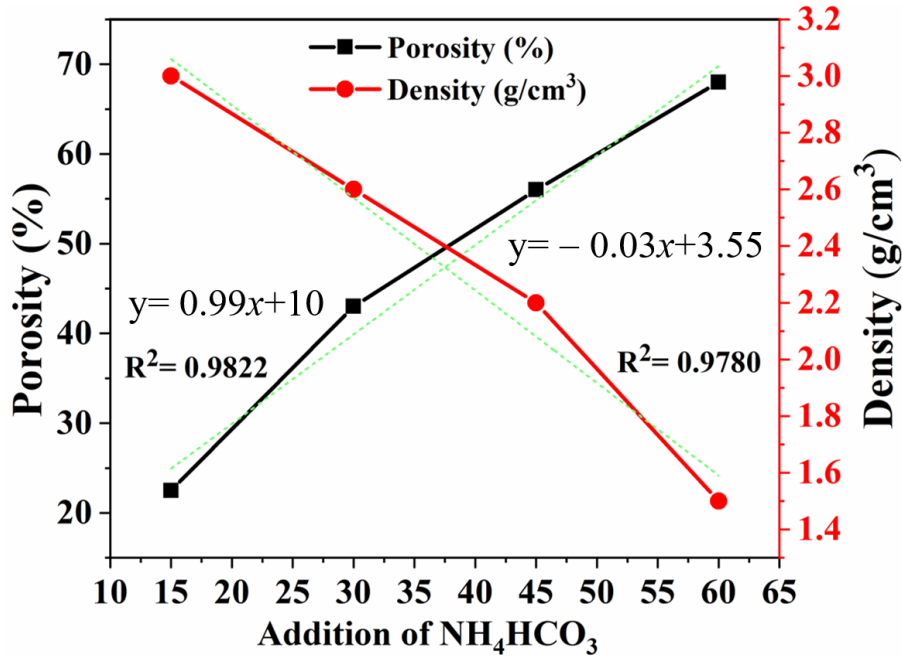


**Fig. 4.27: Influence of different amount of  $\text{NH}_4\text{HCO}_3$  (wt. %) on porosity and density of porous Ti–20Nb–5Ag alloy.**

#### 4.3.2 Mechanical properties of porous alloys

Typical stress-strain curves of developed porous Ti–20Nb–5Ag alloys are shown in Fig. 4.28. It could be seen that the amount of porosity directly affects the compression strength and deformation behavior of these alloys (Gao et al., 2012b; Rao et al., 2014b). The mechanical properties of the developed porous sample are summarized in Table 4.6. A noteworthy variation in the yield strength, compression strength, and elastic modulus were noticed due to the difference in porosities. Yield strength was severely reduced from 221 MPa to 17 MPa when the porosity was increased from 22% to 68%. Similarly, reduction in elastic modulus from 7.8 GPa to 0.5 GPa with increasing porosity.

However, in the present investigation, the maximum compressive strength drop was found between a sample with porosity of 43% and a sample with porosity of 56%. These variations are possible, due to development of porosity level, pore size, isolated pores, and also interconnected pores in porous alloys (Rao et al., 2014b)(Y. Q. Wang et al., 2011)(Yong Hua Li et al., 2009).

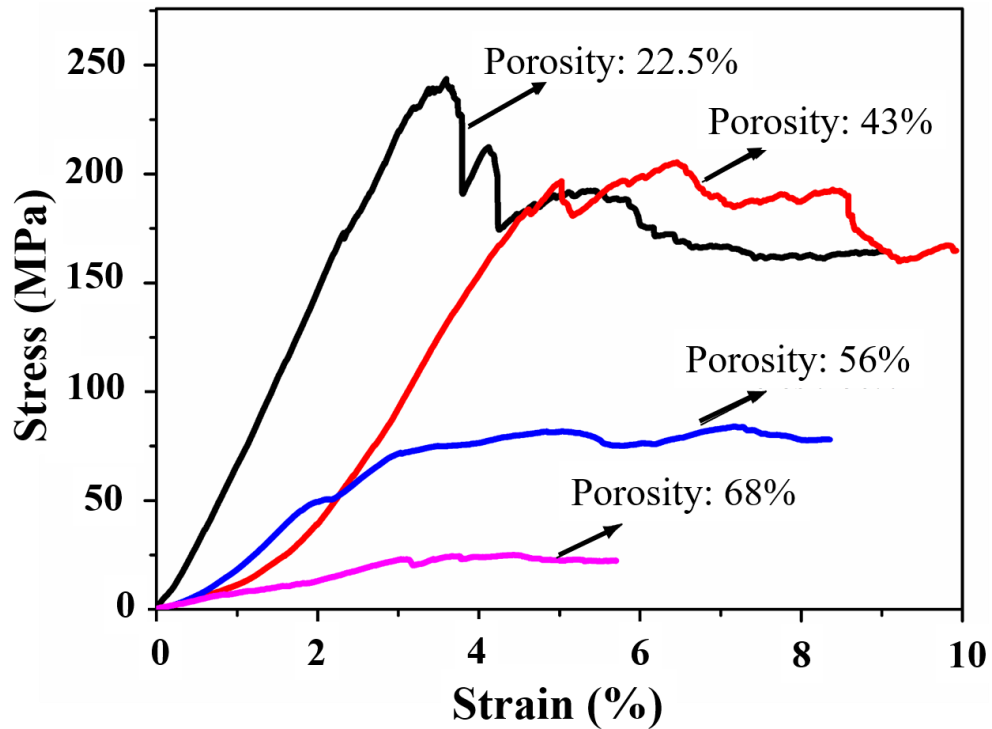


**Fig. 4.28: Compressive stress-strain curve of the porous Ti-20Nb-5Ag alloy with different porosity; prepared using different amounts of  $\text{NH}_4\text{HCO}_3$  (wt. %).**

Moreover, if the sample has low porosity, it contains more isolated pores and less interconnected pores. Porous samples have thick pore cell walls and plastic deformation of these pores are quite difficult under the applied load. It is mainly an obstacle in the sliding moment between the pore cells and strongly resists the fracture of the cell wall (Aguilar et al., 2016b; Rao et al., 2014b). In case of high porosity porous samples, deformation of these pore structures would be easy under the load because the more interconnected pore cells and thin pore cell walls have low strength as compared. According to Rao et al., (2014) when the porosity is relatively low (i.e. 30–50%), it is difficult to deform under the load due to containing more isolated pore in the sample

which reflect on the mechanical properties. Thus, it leads to difficulty in predicting mechanical properties if porosity is lower than 70%. Similar studies have been reported by Wang Yue-qin, et al., (2011) and Y-H. Li et al., (2009) on porous Ti-10Mg alloy and porous Ti-15Mo alloy, respectively. They have produced alloying with different levels of porosities and examined mechanical properties of the porous alloys. It is found that maximum compression strength is dropped down with increase in porosities. It is also reported that the porosity levels, pores size and interconnected porous structures influence the compression strength, due to the variation in the deformation of pores structures. Presented results are in good agreement with the above reported literature.

**Table 4.6: The mechanical properties of the developed porous Ti-20Nb-5Ag alloy.**

Space holder (Wt. %)	Porosity (%)	Yield strength (MPa)	Maximum compression strength (MPa)	Elastic modulus (GPa)
15	22	221	243	7.8
30	43	193	205	5.8
45	56	76	83	3.3
60	68	17	22	0.5

Fig. 4.29 shows the fracture surface of the porous Ti-20Nb-5Ag alloy (porosity of 43%). It indicates the flattening and collapsing of the pore walls [Fig. 4.29 (a)] and suggested that it fractured through mixed mode, i.e. ductile (region-1) and brittle failures (circle), as shown in Fig. 4.29 (b). Dimples having shear lips could also be seen (region 2). Porous implant materials commonly exhibit these kinds of fracture surfaces. This is because porous alloys consists of open and isolated pores, which has thin and thick pore cell wall.



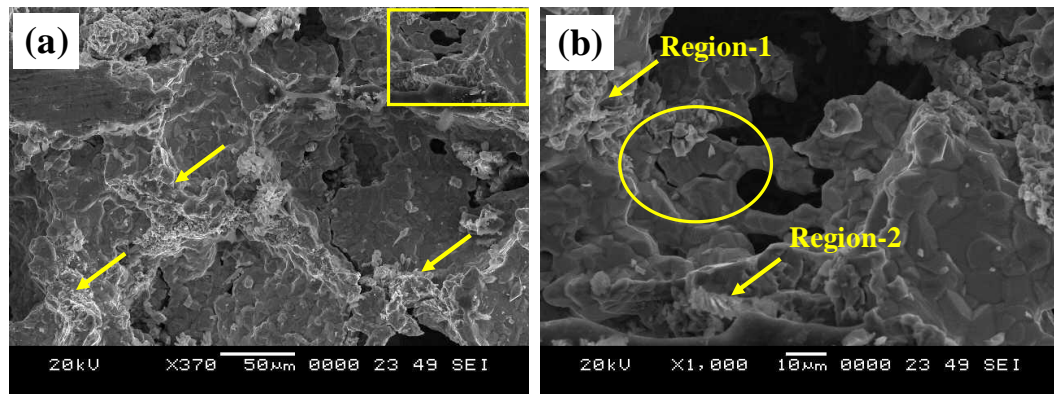


**Fig. 4.29: SEM micrograph of fractured surface of 43% porous Ti–20Nb–5Ag sample: (a) fracture of pore cell walls were indicated by arrows, (b) magnified view of region shown by rectangle in Fig. 6.9 (a): brittle rupture (shown in circle) and ductile failure (region 1) and shear lips (region 2).**

#### **4.3.3. Effect of porosity on electrochemical corrosion properties**

Potentiodynamic polarization curves of the porous Ti–20Nb–5Ag alloys having various porosity levels were obtained in SBF at 37 °C as presented in Fig. 4.30. The electrochemical corrosion kinetics parameters such as  $E_{\text{corr}}$ ,  $i_{\text{corr}}$ ,  $\beta_a$ , and  $\beta_c$  are summarized in Table. 4.7. It can be seen that cathodic reaction is similar for all the porous alloys. On anodic polarization, the current density gradually increases with small fluctuations and tends to reach a stable passivation region. Corrosion potential gradually decreases from the  $-0.18 \text{ V}_{\text{SCE}}$  to  $-0.39 \text{ V}_{\text{SCE}}$  indicating the effect of porosity and the absence of spontaneous film formation. The corrosion current density increases from  $0.20 \mu\text{A}/\text{cm}^2$  to  $1.6 \mu\text{A}/\text{cm}^2$ , with an increase in porosity from 22% to 68%. Corrosion resistance of the implant materials directly depends on the microstructure, composition of alloys, and corrosive environment (Sun et al., 2011b). However, introduction of pore structures into the bulk materials not only eliminates the stress shielding effect, but also significantly improves the new bone ingrowth (Muñoz et al., 2015). The porous implant materials are susceptible to corrosion as compared to the bulk implant materials (F. Xie et al., 2013).



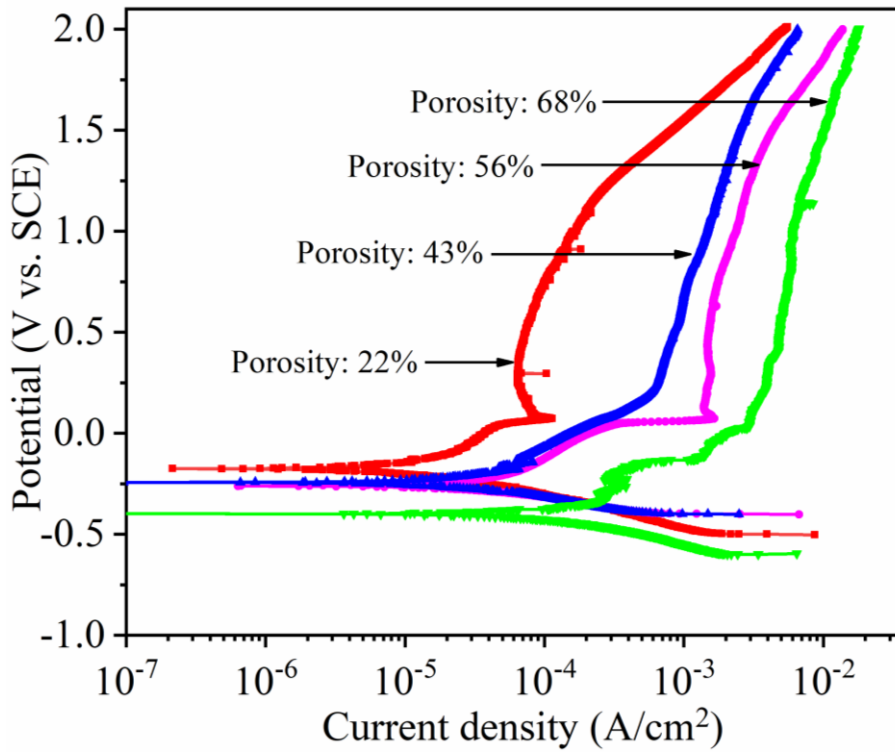


**Fig. 4.30: Potentiodynamic polarization curves of porous Ti–20Nb–5Ag alloy with different porosity in SBF at 37 °C.**

**Table 4.7: Electrochemical corrosion parameter of porous Ti–20Nb–5Ag alloy having different porosity level in SBF solution.**

Porosity (%)	$E_{\text{corr}}$ (V)	$\beta_a$ (V/dec)	$-\beta_c$ (V/dec)	$i_{\text{corr}}$ ( $\mu\text{A}/\text{cm}^2$ )	$i_{\text{pass}}$ ( $\text{A}/\text{cm}^2$ ) (at 0.5 V) $\times 10^{-3}$	Corrosion rate ( $\text{mm}/\text{y}$ ) $\times 10^{-3}$
22	-0.18	0.17	0.38	0.20	0.0074	0.25
43	-0.24	0.14	0.25	0.41	0.870	0.56
56	-0.32	0.10	0.13	0.52	3.30	0.84
68	-0.39	0.15	0.12	1.60	7.39	3.50

Fig. 4.31 shows that the EIS results of the developed porous Ti–20Nb–5Ag alloy having the different porosity in SBF at 37 °C. Fig. 4.31 (a) shows the Nyquist plot. From this plot it could be seen that the diameter of the semicircle gradually decreases due to porosities indicating reduction in corrosion resistance of porous alloys.

This is because of thin passive film formation on the surface which may become easily unstable in the corrosive environment leading to reduction in the corrosion resistance. Bode magnitude and Bode phase angle plots are presented in Fig. 4.31 (b and c). In the high frequency region, it is observed that a constant bode magnitude and bode phase angle near  $0^\circ$  for all the porous alloys indicates the response of electrolyte resistance. At the middle the phase angle approached  $75^\circ$  (for 22% porosity) and  $65^\circ$  (for 68% porosity) which covers a wide frequency. This suggests a typical passive film formation tendency on the surface of a porous alloy surface. At low frequency range, a continuous decrease in the values of phase angle, due to the low response of the passive film (Salehi et al., 2017; Seah et al., 1998). According to the EIS experimental data, the two equivalent circuit models with two-time constants are used to fit plots and calculate the impedance parameters of these alloys. An equivalent circuit model  $[R_s(Q_p R_p)(Q_b R_b)]$  is shown Fig. 4.31 (d) is used to examine practical EIS data. Here,  $R_s$  is electrolyte resistance (simulated body fluids), and a constant phase element (CPE) representing a shift from an ideal capacitor is used instead of the capacitance itself due to non-smooth electrodes surface.  $R_p$  and  $R_b$  represent the resistances of porous and barrier layers respectively. That is associated with the charge transfer resistance through the porous layer and the participation of adsorbed intermediates.  $Q_p$  and  $Q_b$  are the capacitances of the porous and barrier layer, respectively.

After fitting it is found 'n' values are close to 1, indicating a near capacitive behavior of the formed passive film (Yilmaz et al., 2017). The resistance  $R_b$  values of all the alloys is higher than the  $R_p$ , indicating a formation of compact protective layers on the surface. Table 4.8, presents the values of  $Q_p$  and  $Q_b$  which increase with increase in porosity while the resistances  $R_p$  and  $R_b$  decreases. The lower capacitance values are indicating high resistances, which further supports nobler electrochemical corrosion behavior.

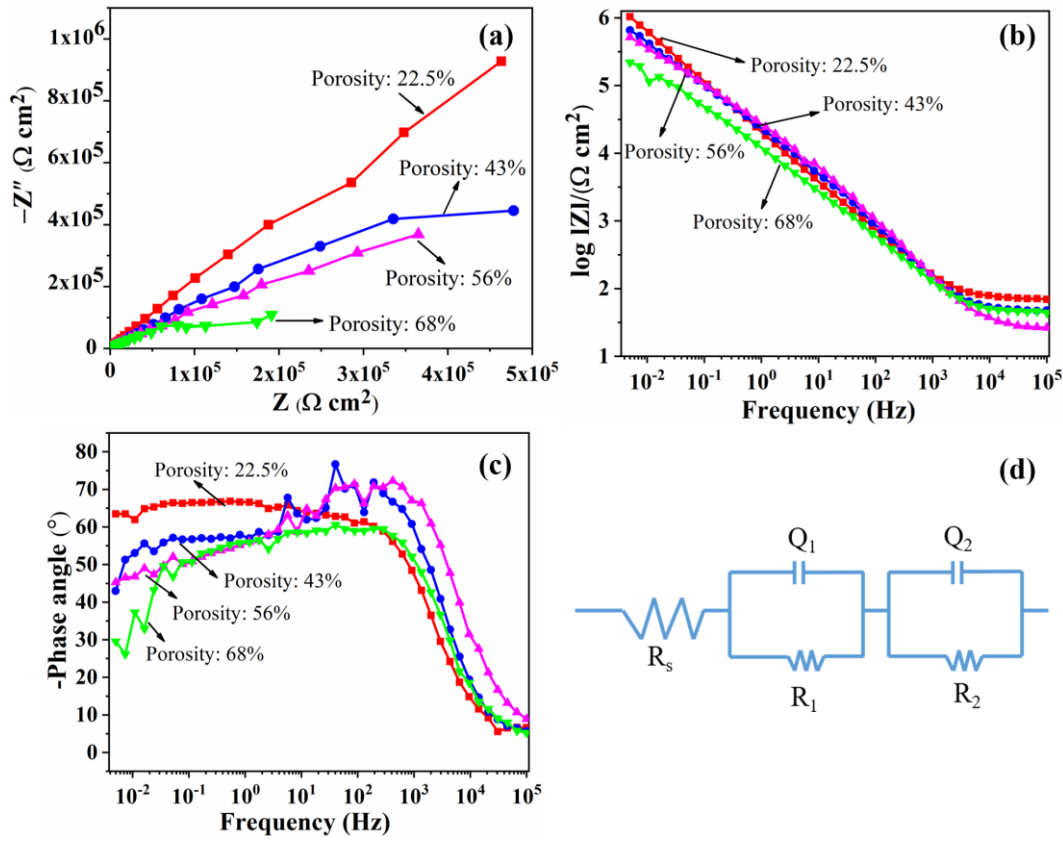


**Fig. 4.31: Electrochemical impedance spectroscopy results of porous Ti-20Nb-5Ag alloy having various porosity in SBF at 37 °C: (a) Nyquist plot; (b) Bode magnitude; (c) Bode phase angle; (d) Equivalent circuit used to analysis EIS data.**

**Table 4.8: Impedance parameters obtained by  $R_s (Q_p R_p) (Q_b R_b)$  model to fit EIS data of porous alloys having various porosities in SBF solution at 37 °C.**

Porosity (%)	$R_s$ ( $\Omega\text{cm}^2$ )	$Q_p \times 10^{-6}$ ( $\text{F cm}^{-2}$ )	$n_p$	$R_p$ ( $\Omega\text{cm}^2$ )	$Q_b \times 10^{-6}$ ( $\text{F cm}^{-2}$ )	$n_b$	$R_b$ ( $\text{k}\Omega\text{cm}^2$ )
22	15.1	0.31	0.8912	62.80	5.73	0.8311	275
43	10.9	0.74	0.8756	40.31	6.88	0.8507	132
56	7.38	0.89	0.8943	58.67	19.4	0.7920	212
68	5.06	12.7	0.9275	24.7	24.0	0.7837	34.8

Seah et al.,(1998) are reported that the corrosion behavior of porous Ti is significantly affected by its pore characteristics in a corrosive environment. Due to the open and interconnected porosity permitted to access more electrolytes, protective layers are unable to maintain titanium oxide layer on the alloy surface. Similarly, Yilmaz et al., (2018) have studied the polarization behavior of the porous Ti-Nb alloy having porosity of 23 % and 60%. It is also reported that the low porosity samples show a high corrosion resistance, while the high porosity samples exhibit high corrosion rate. This is due to the insufficient thickness of oxide film or heterogeneous oxide layer formation on the surface of porous alloys.

Further, the formation of  $\beta$ -martensite and intermetallic compounds in the sintered Ti alloys is responsible to enhance the corrosion resistance of alloys as reported in the previous studies (Takahashi et al., 2011; Xia et al., 2016). Xia et al.,(2016) have developed Ti-6Al-4V-xZr alloys ( $x = 0, 10, 20, 30, 50$  wt%) to examine the microstructure and corrosion behavior of the alloys in physiological solution. The XRD analysis revealed the formation of  $\alpha''$  martensite in Ti-6Al-4V-xZr alloys. It is found that the higher corrosion resistance in Ti-6Al-4V-50Zr alloy than other developed alloy, is due to the presence of  $\alpha''$  martensite. In a study Takahashi et al.,(2011) investigated the microstructure and corrosion study on pure Ti and Ti-22.5Ag (wt. %) alloy in physiological solution. They have revealed that the formation of  $\alpha$ -Ti and intermetallic compounds of Ti<sub>2</sub>Ag peak and a high corrosion resistance in Ag added more samples than only pure Ti sample, this is due to the formation of intermetallic Ti<sub>2</sub>Ag and oxides.

## Summary

The powder of Ti-20Nb-5Ag ball milled for 20 h and sintered at 1200 C for 3 h to prepare porous through powder metallurgy space holder technique.

- Various porosity levels (22% to 68%) are achieved by adding different amounts of NH<sub>4</sub>HCO<sub>3</sub>.
- Compatible microstructure and mechanical properties were possessed with the porous alloy having porosity of 43%.
- Corrosion resistance of porous alloys decreased with increasing the porosity level.



## CHAPTER 4.4

### 4.4. Tribocorrosion properties of porous Ti–20Nb–5Ag alloy under various applied loads

*In this chapter the effects of applied load on the tribocorrosion properties of the porous Ti–20Nb–5Ag alloys having the porosity of 43% in simulated body fluid have been discussed. It is well known that the tribocorrosion behavior of the implant materials is playing important role on the life of the implants when inserted in to human body. Therefore, the present chapter deals with the tribocorrosion behavior of the developed implant materials under the various applied loads such as 1 N, 5 N and 10 N.*

#### 4.4.1. Microstructure of the porous Ti–20Nb–5Ag alloy

A sintered porous Ti–20Nb–5Ag alloy is selected with an optimum porosity of 43%. The microstructure of porous alloy exhibited an irregular shape and rough surface as shown in Fig. 4.32. It also consists of micro, macro and interconnected pores throughout the surface which is essential to be used as implant applications (Gao et al., 2012b; Torres-Sanchez et al., 2018).

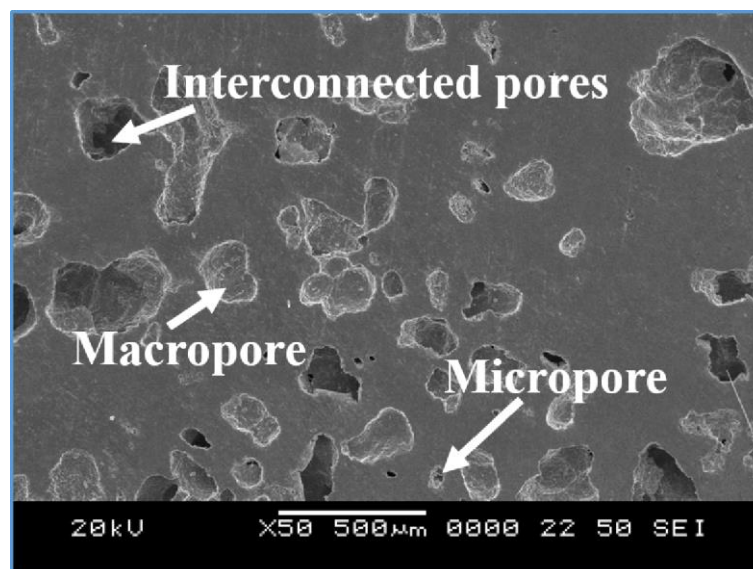


**Fig. 4.32: SEM micrographs of the porous Ti–20Nb–5Ag alloy used for tribocorrosion study.**

#### 4.4.2. Effect of applied loads on open circuit potential

OCP test is carried out under various applied loads of 1 N, 5 N and 10 N in SBF for 900 s as depicted in Fig. 4.33. It is seen in the unloaded condition, the OCP value is about 0.16 V<sub>SCE</sub> which is stable due to the formation of spontaneous passive film on the porous sample. On the other hand, on application of load the OCP values vary with time. It can be seen as three distinct regions as; (i) before sliding (up to 150 s), (ii) during sliding (150–500 s) and (iii) after sliding (500–900 s). Interestingly, OCP of these porous alloys at three different loads were almost stable before applying a load due to the stable passivation film with open circuit potential values of  $-0.14$  V<sub>SCE</sub>,  $-0.32$  V<sub>SCE</sub>, and  $-0.49$  V<sub>SCE</sub> for the applied loads of 1 N, 5 N and 10 N, respectively.

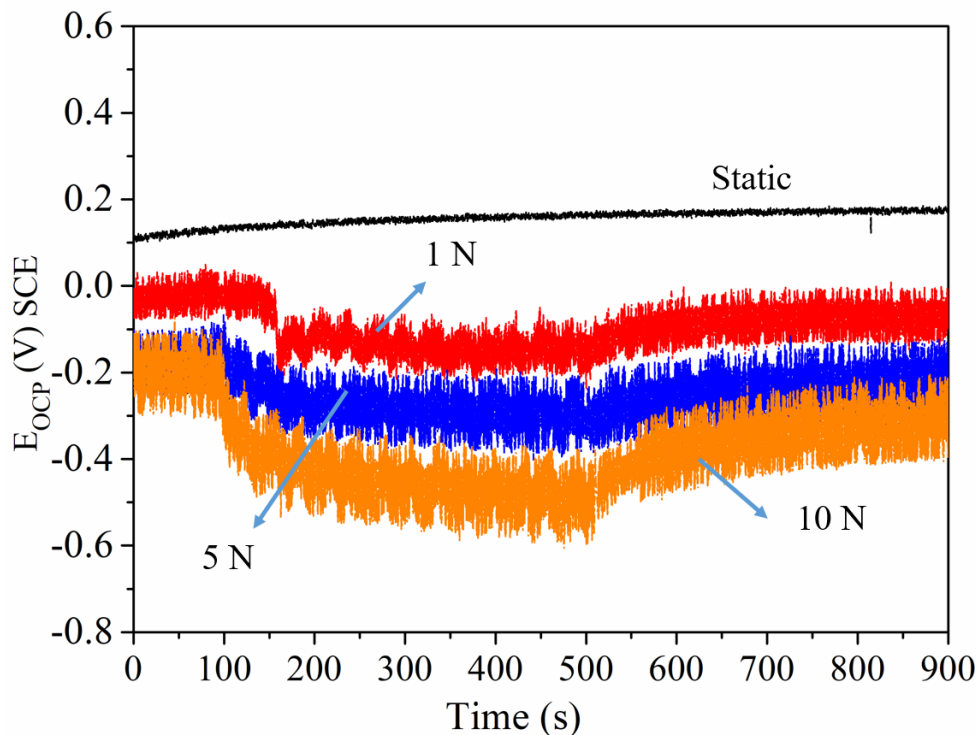


**Fig. 4.33: Open circuit potential (OCP) scan for porous Ti–20Nb–5Ag alloy at static and various applied loading conditions.**

These results indicate that the applied loads are significantly affecting the OCP of the porous alloy and shifted towards a negative direction as compared to unloaded condition. During the sliding process, the higher frictional forces were induced on increasing the application of applied load which makes relative movement difficult

between the metal substrate and counter surface. This can be attributed to the destruction and delamination of passive film under the sliding process. However, high material removal due to wear and corrosion from the surface because of pore structures under the various applied loads (F Toptan, 2017; Z. Wang et al., 2017a, 2018). It is also observed that there are fluctuations in OCP due to the formation of new active surfaces when the material is removed from the surface under the applied load. Further, it is detected that the OCP values obtained during sliding are mixed potential values, which reflect both the active (worn) and passive (unworn) surfaces of the porous alloy (F Toptan, 2017).

#### **4.4.3. Electrochemical corrosion study under the applied load**

Electrochemical polarization plots for porous Ti–20Nb–5Ag alloy were obtained without loading condition and under the influence of applied loads of 1–10 N in the SBF solution is shown in Fig. 4.34. The working electrode (porous alloy) is sliding against a counter surface (alumina disc) with a roughness ( $R_a$ ) of 0.02  $\mu\text{m}$  to understand the tribocorrosion behavior using polarization plot. The potentiodynamic polarization curves of the porous alloy without applying a load is shown in Fig. 4.34 (a). The porous alloy exhibits a typical active–passive transition behaviour with a stable passivation without current fluctuation. It also shows lower passive current density due to spontaneous passive film formation and which is stable even at higher potential regime. Potentiodynamic polarization curves measured under the applied loads of 1 N, 5 N and 10 N are shown in Fig. 4.34 (b), (c) and (d) respectively. Careful observation of these curves, show that there is no significant change in active passive transitions plots of the porous alloys.

However, it is noticed that corrosion potential shifted towards more active regions with increasing the applied loads due to the higher frictional forces which can be attributed to the passive film of porous alloy (Z. Wang et al., 2018). Moreover, severity of current fluctuation was observed in the polarization curves when the applied loads varied from 1–10 N. These fluctuations of currents were started at active dissolution area ( $-0.25$  to  $+0.25$   $V_{\text{SCE}}$ ) at lower weight of loading of 1 N and 5 N [Fig. 4.34 (b) and Fig. 4.34 (c)] indicating initial dissolutions of metal due to higher electrochemical corrosion reaction rates on rubbing action of metal by hard counter



surface. It is accelerated by mechanical abrasion which causes local film thinning or removal of the protective passive film of metallic oxides.

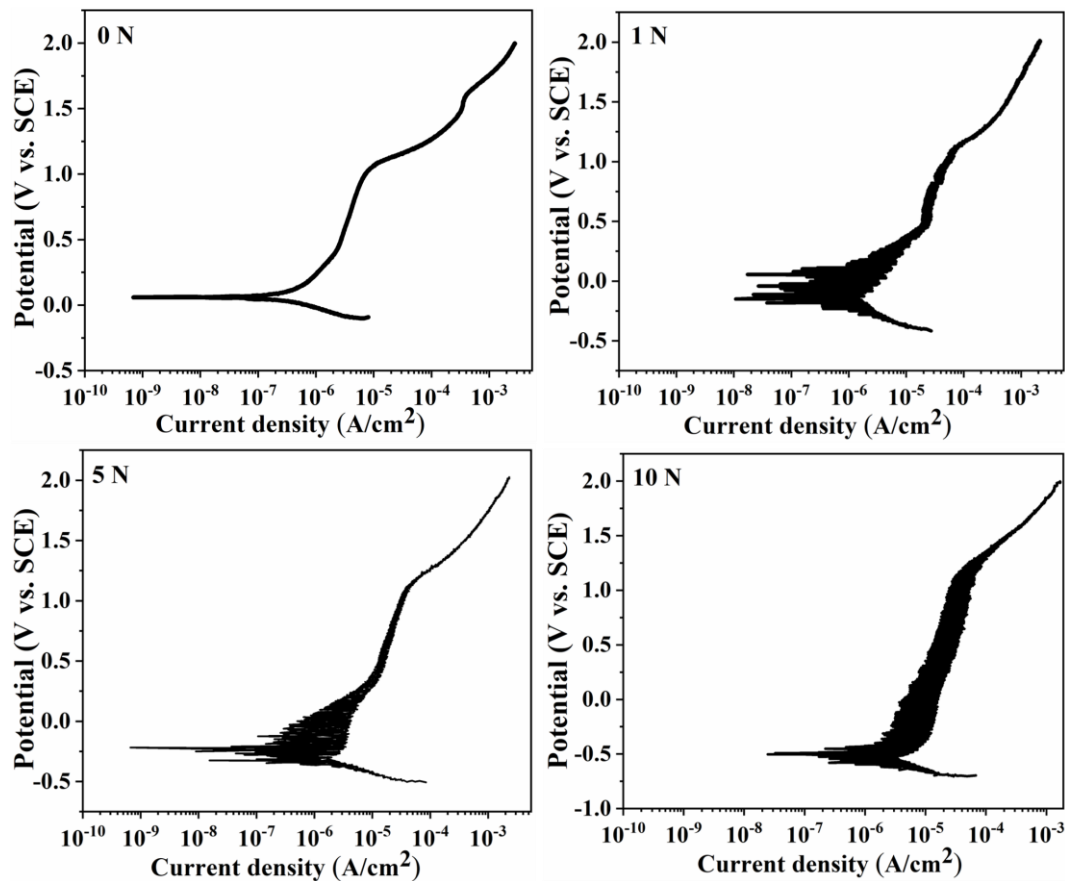


**Fig. 4.34: Potentiodynamic polarization curves of porous Ti-20Nb-5Ag alloy at various applied loads: 0 N, 1 N, 5 N and 10 N.**

However, it was not observed for the sample without loading [Fig. 4.34 (a)] due to the absence of rubbing action and well covered by a thin protective passive film in the SBF solution. Further, at the applied load of 10 N [Fig. 4.34 (d)], it is noticed that the current fluctuation is quite significant and constant up to the higher potential range as compared to 1 N and 5 N. These results indicate that under sliding condition, more oscillations on the current density values occur due to the repeated action of depassivation and repassivation of the metal under sliding against a counter surface. It is known as metastability of passive film of alloy, the current is reduced when it is repassivated and further current is increased significantly on depassivation. Similar

type of behavior is noticed under wear where abrasive particles as well large numbers of inclusions or precipitate particles present in alloy. This is due to the frictional forces occurring between the interfaces (Yenal, 2013). As wear action removes the passive layer from the surface of porous alloy on the local anodic region, passivation occurs simultaneously. However, it was observed that the rapid passivation and removal of passive film resulted in high current fluctuations at lower anodic potentials (F. Toptan et al., 2016; Yenal, 2013).

Corrosion kinetics parameters such as corrosion potential ( $E_{\text{corr}}$ ) and current density ( $i_{\text{corr}}$ ) are measured by analysing the Tafel region through slope of anodic ( $\beta_a$ ) and cathodic ( $\beta_c$ ) branches and the results are presented in Table. 4.9. It can be seen that there is a remarkable shift towards the negative direction of the corrosion potential from the 0.06  $V_{\text{SCE}}$  to  $-0.49 V_{\text{SCE}}$ . It is observed that there is an increment in the corrosion current density ( $i_{\text{corr}}$ ) from 0.17  $\mu\text{A}/\text{cm}^2$  to 0.48  $\mu\text{A}/\text{cm}^2$ . With increasing in the applied loads for 10 N and without loading, there is 64% increment in the corrosion current density which indicates the decline in corrosion resistance with increase in the applied loads. It is also noticed that passive current density ( $i_{\text{pass}}$ ), an important parameter for the stability of passivity and localised corrosion at an applied load of 10 N is about 7 times higher than that of static condition. Similarly, an increase in corrosion rate about 3 times was observed with respect to applied loads.

**Table 4.9: Corrosion parameters of porous Ti–20Nb–5Ag alloy in SBF solution at various applied load.**

Load (N)	$E_{\text{corr}}$ ( $V_{\text{SCE}}$ )	$\beta_a$ (V/dec)	$-\beta_c$ (V/dec)	$i_{\text{corr}}$ ( $\mu\text{A}/\text{cm}^2$ )	$i_{\text{pass}}$ (at 0.5 V) ( $\mu\text{A}/\text{cm}^2$ )	Corrosion (mpy) $\times 10^{-3}$
Static	0.06	0.18	0.09	0.17	0.003	7.14
1	-0.17	0.28	0.11	0.20	0.013	8.40
5	-0.22	0.39	0.13	0.33	0.014	13.8
10	-0.49	0.28	0.14	0.48	0.020	20.17

Fig. 4.35 shows the SEM micrographs of porous alloy after the tribocorrosion test under the applied loads (1, 5 and 10 N). Abrasion is found to be the foremost mechanism under the sliding condition. It can be revealed from SEM image, an increase in narrow ploughing which is caused by applied loads and relative sliding between the interfaces of porous alloy and counter surface. At 10 N load, more narrow wear tracks with the deep groove marks could be seen as compared to 1 N load. However, the wear debris formed due to sliding played an important role in tribocorrosion. It acts as third body abrasive particles, resulting in the increase of wear under the applied loads. Moreover, the porous alloy having irregular and non-homogeneous surface area may lead to more wear debris and wear tracks with increase in applied load (F Toptan, 2017; Fatih Toptan et al., 2019).

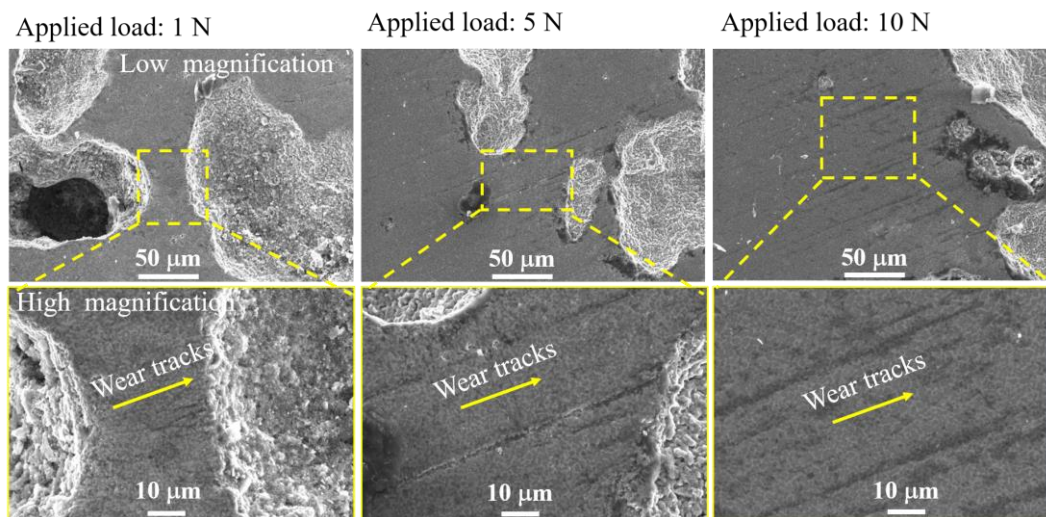


**Fig. 4.35: SEM images of porous Ti–20Nb–5Ag alloy after tribocorrosion at the various applied loads.**

#### 4.4.4 Mechanism of material removal from porous alloy

The mechanism of the tribocorrosion process of porous Ti–20Nb–5Ag alloy in the SBF solution as shown in Fig. 4.36. The tribocorrosion process takes place with both electrochemical corrosion and wear occurring in electrolyte medium. In the

present study, pin-on disc type and SBF used as electrolyte to conduct the tribocorrosion behavior of the porous alloy.

Fig. 4.36 (a) shows the test on porous Ti–20Nb–5Ag in SBF solution in the absence of load. It is reported that Ti and its alloys have strong metallic passivity across the potential range which help to enhance the corrosion resistance (Huang et al., 2015; Pina et al., 2016). In the present study, the high positive potential (OCP) value obtained for unloaded condition, because of spontaneous protective and compact oxide film formation on the alloy as compared to the applied load condition (as seen in Fig. 7.2). On other hand, applying load from the top end, the porous alloy comes into contact with the alumina disc as a counter surface [(Fig. 4.36 (b)].

Once, the porous alloy and counter surface come into contact with each other due to the applied load, frictional forces are generated at the interfaces between working electrode and counter surface subsequently damaging the passive film which is formed on the surface alloy [(Fig. 4.36 (c)]. However, at 1 N, it is seen that a very small wear debris is worn out from the surface due to less damage of passive film under the rubbing action as shown in Fig. 4.36 (d).

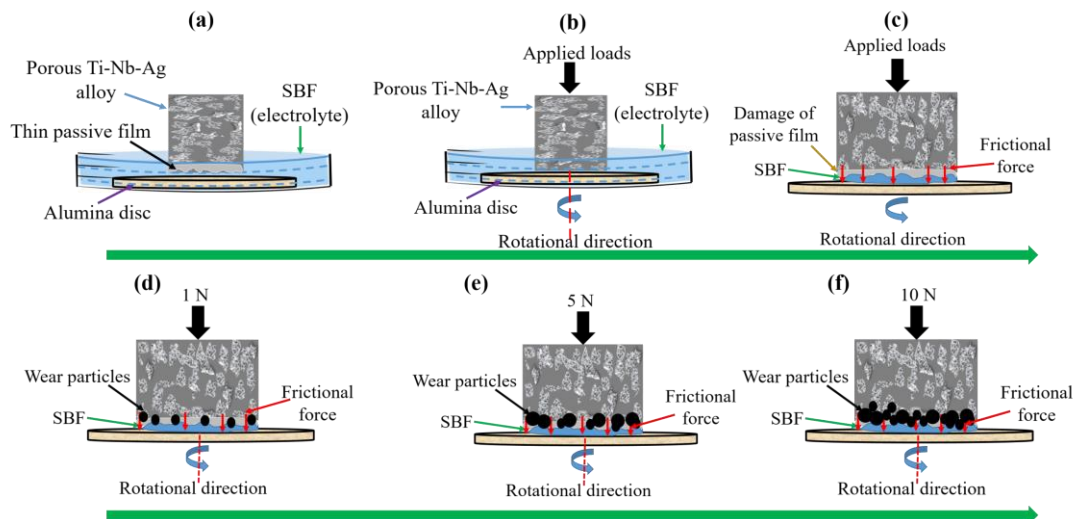


**Fig. 4.36: Mechanism of tribocorrosion process of porous Ti–20Nb–5Ag alloy in SBF solution.**

Further, applying a higher load, it is found debris merely increases at the load of 5 N [Fig. 4.36 (e)] which is clearly evident through the electrochemical corrosion kinetics data as the passive current density did not increase remarkably at 5 N over 1 N. Interestingly, Fig. 4.36 (f) shows more wear particles removal from the surface at the applied load of 10 N as compared to 1 N and 5 N (very high corrosion rate as well as passive current density). This is due to the significant delamination and peeling of natural passive film which is deformed plastically at the higher applied load because of the highest frictional forces at 10 N [Fig. 4.36 (e)].

Pore structures similarly show an important role and contribute significantly for the removal of particles due to corrosive–wear test which acts as a third body (abrasive particles) under the sliding condition. Therefore, the main wear mechanism of the tribocorrosion process is abrasive wear (Fellah, Hezil, Hussein, et al., 2019; F Toptan, 2017). During the tribocorrosion test, a thin passive film is removed from the surface as the applied load is increased which results in the formation of visible wear tracks on the surface. However, the edges of the pore cells consist of sharp edges which may break easily under the application of load. It leads to increase in the surface of the pore area as well as wear debris due to sliding. The accumulation of the wear debris into the pores surface could decrease the effect of the third–body on the wear, and it may cause damage to the passive film. Moreover, the tear of pore cell wall edges directly influences increasing the pore area and slightly increasing in the groove formation.

In the present study, the thin passive film deforms plastically and forms deeper grooves which roughen the surface of porous alloy. The rotational speed used in the present experiment is relatively small, and heat produced by rotation is negligible. However, both the action of loading and rotating cause damage of protective passive film which is formed on the porous alloy surface. Moreover, the edges of these pore cells could be easily removed under the loading condition, which leads to more wear debris from the porous alloy surface and significantly increases the wear tracks under the applied loads (Diomidis et al., 2012; F Toptan, 2017; Z. Wang et al., 2018). Huang et al.,(2015) have conducted the wear–corrosion study of Ti–25Nb–3Mo–3Zr–2Sn alloys in simulated physiological solutions under the synergistic attacks of corrosion and wear.

The result indicates that the corrosion resistance of the alloy is decreased under the sliding conditions as compared to static corrosion. It is reported that the tribological mechanisms were mainly corrosion with adhesive wear. They examined the chemical composition of passive film using X-ray photoelectron spectroscopy (XPS). It is revealed that the passive films primarily consist of the  $\text{TiO}_2$ ,  $\text{Nb}_2\text{O}_5$  as main oxide layers, which is more stable and responsible in protecting against corrosion attack. Similarly, other studies have been reported that chemistry and chemical compositions of these oxides are the governing factors in enhancing the corrosion resistance of Ti–Nb based alloys in simulated physiological solutions (X. Guo et al., 2017; Sri Maha Vishnu et al., 2019b).

Zhang et al., (2008) have studied the effect of various Ag content (14.5 and 20 wt. %) on corrosion behavior of Ti–Ag alloy in artificial body fluid. The result indicates that addition of Ag brings significant reduction in the corrosion current density and increase in the open-circuit potential of Ti–Ag alloy in a nobler direction. It is concluded that passive current densities and corrosion resistance is directly proportional to Ag content. This improvement in corrosion resistance by addition of Ag is attributed mainly to the formation of  $\text{Ti}_2\text{Ag}$  intermetallic precipitates and the formation of  $\text{TiO}_2$  and  $\text{Ag}_2\text{O}$  in artificial body fluid. According to the studies on Ti–based alloys, the alloying elements play an important role in improving the corrosion resistance as they form various stable oxides on their surface. In our present study, porous Ti alloy is developed with the addition of Nb and Ag alloying elements. As reported in the earlier studies there is a possibility of formation of oxides on the porous alloy surface such as  $\text{TiO}_2$ ,  $\text{Nb}_2\text{O}_5$  and  $\text{Ag}_2\text{O}$  in simulated body fluid, which contribute to enhancing the corrosion resistance of the porous alloys.

Moreover, the XRD analysis of the porous Ti–20Nb–5Ag alloy exhibits the formation of  $\text{Ti}_2\text{Ag}$  intermetallic compound, which significantly influences the corrosion resistance of the alloys in SBF. The influence of intermetallic and formation of oxides in SBF solution significantly affect the results in static conditions. However, the synergic effect of corrosion and wear, the stable oxides film breakdown under the applied load which gradually reduces the corrosion resistance of porous alloys.

## Summary

- Porous Ti–20Nb–5Ag alloy having a porosity about 43% was used to study the tribocorrosion properties in the SBF solution.
- It is observed that there is a decrease in OCP values from 0.17 to  $-0.50 V_{SCE}$  with increasing the applied loads.
- The potentiodynamic polarization results revealed that the corrosion potential shifted to the negative direction (from 0.06 to  $-0.50 V_{SCE}$ ) and corrosion current density increased ( $0.12 \mu A/cm^2$  to  $0.47 \mu A/cm^2$ ) with applied load increased.
- The obtained results indicate that increasing the applied loads lead to a material degradation and corrosion

## CHAPTER 4.5

*In this chapter the role of surface modification (through alkali treatment method using 5 M NaOH solution), surface bioactivity (in simulated body fluid) by immersing for various time of interval, and cytotoxicity behavior (using MG-63 osteoblast human cells) on the porous Ti–20Nb–5Ag alloys are discussed.*

### **4.5. Surface modification, Surface bioactivity and cytotoxicity behavior**

Porous Ti–20Nb–5Ag alloy with 43% porosity is selected to investigate the surface modification, surface bioactivity and cytotoxicity properties. The porous alloy with 43% porosity is considered the optimized value among various porosity levels, and also possessed compatible mechanical properties. As it is discussed in the previous sections the porosity ranging from 30–50% is fairly suitable for orthopaedic applications which enhanced osseointegration and significant for cell proliferation properties (Gao et al., 2012b; Kalantari et al., 2015b; Torres-Sanchez et al., 2018; L. Zhang et al., 2017).

#### **4.5.1. Surface modification via alkali treatment**

Fig. 4.37 (a and b) shows the SEM micrographs of as-sintered porous Ti–20Nb–5Ag alloys surface and porous alloy surface after alkali-heat treatment using 5 M NaOH solution, respectively. After alkali-heat treatment, a noticed variation in the surface morphology is seen as compared to the sintered porous alloy surface without treatment. The alkali treated porous alloy surface exhibits the formation of thick oxide layer with spherical precipitate which is identified as sodium titanate layer ( $\text{Na}_2\text{Ti}_5\text{O}_{11}$ ) (Bu, 2016; H. Hsu et al., 2015). During the NaOH solution treatment, the native passive film ( $\text{TiO}_2$ ) on the porous alloy surface is believed to be partially dissolved into NaOH solution. Further, the hydrated  $\text{TiO}_2$  would produce negatively charged hydrates ( $[\text{HTiO}_3]^- \cdot n\text{H}_2\text{O}$ ) on the surfaces of the porous alloy. These  $[\text{HTiO}_3]^- \cdot n\text{H}_2\text{O}$  combine with  $\text{Na}^+$  ions in the NaOH solution, resulting in the formation of a sodium titanate ( $\text{Na}_2\text{Ti}_6\text{O}_{13}$ ) hydro-gel layer as reported by (Hsu et al. 2014). If suitable heat treatment is given to densify, it will lead to formation a stable sodium titanate layer on the porous alloy surface (Gao et al. 2012a; Pattanayak and Yamaguchi 2011). This treatment helps to form functional groups which is quite essential for adhesion of apatite particles, when



the porous alloy is immersed in SBF (Fatehi et al. 2008; Hazwani et al. 2017; Khodaei et al. 2015). EDX analysis confirms that the presence Ti, Nb, Na, and O which are responsible for the formation of sodium titanate layer on the porous alloy surface after alkali-heat treatment as presented in Fig. 4.37 (c).

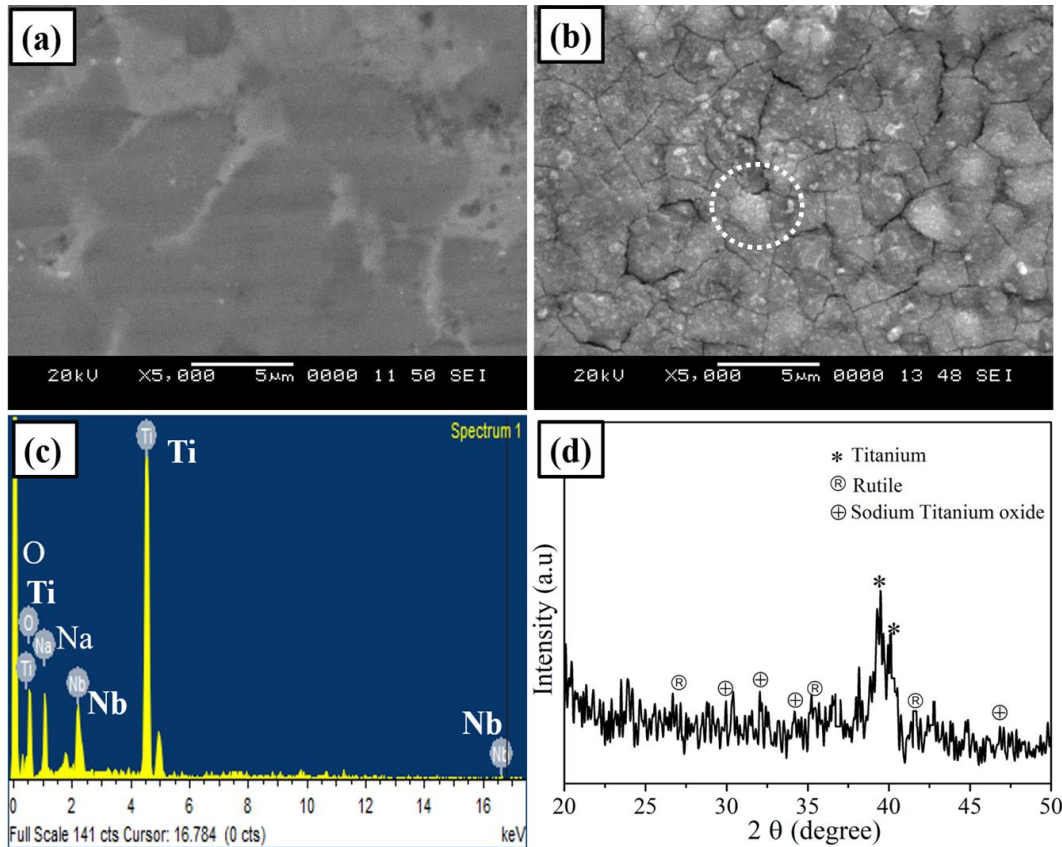


**Fig. 4.37: SEM images of porous Ti–20Nb–5Ag alloy: (a) untreated, (b) after alkali-heat treatment, (c) EDS analysis of the porous surface shown in Fig. (b) and (d) XRD pattern of the surface shown in Fig. (b).**

Further, XRD analysis is conducted to confirm the formation of compounds on the porous alloy surface as shown in Fig. 4.37 (d). It is revealed that the presence of pure Ti, and the formation of oxides such as rutile ( $\text{TiO}_2$ ) and sodium titanate ( $\text{Na}_2\text{Ti}_6\text{O}_{13}$ ), layer on the porous alloy surface after alkali-heat treatment (H. Hsu et al., 2015; H. C. Hsu et al., 2014; Xiong et al., 2008a).

Similar observations have also been reported by the previous study conducted by Gao et al., (2012), and Butev et al., (2016) on the porous Ti–Mo alloy and Ti6Al7Nb alloy foam, respectively. They reported a formation of sodium titanate layer on the surface of the titanium based porous alloys, when the substrate was alkali treated using NaOH solution. This sodium titanate oxide formation is an essential step for the formation of bone-like hydroxyapatite formation on the implant materials (Jonášová et al., 2002; Pattanayak et al., 2012).

#### **4.5.2 Surface bioactivity in simulated body fluid**

Fig. 4.38 shows the SEM micrographs of porous Ti–20Nb–5Ag alloy surface after immersion in an SBF solution at 37 °C for 7, 14 and 21 days after NaOH treatment. After immersion in SBF for various times, it could be seen that drastic changes on the porous alloy surface as compared to alkali-heat treated surface [seen in Fig. 4.37 (b)] (W. Xu et al., 2006). Fig. 4.38 (a) shows SEM micrograph of the porous alloy surface after being exposed for 7 days in the SBF solution. Microstructure reveal that the formation of spherical hydroxyapatite particles on the surface of the porous alloys, which is commonly observed alkali heat treated surface. A small number of spherical particles are observed on the porous surface, which confirms the nucleation of hydroxyapatite particles. With the increase in the immersion time in SBF (for 14 days), the hydroxyapatite particles have grown up to large size, and more clusters could be seen in Fig. 4.38 (b).

Further, on immersion these samples for 21 days [Fig. 4.38 (c)], the growing hydroxyapatite clusters coalesced each other and the porous surface is completely covered by the hydroxyapatite particles. The deposition of hydroxyapatite particles inside the pores significantly supports the propagation of new bone in growth on the surface implant alloys (Butev et al., 2015; Xiong et al., 2008b). XRD analysis revealed the formation of hydroxyapatite on the porous Ti–20Nb–5Ag alloy after 21 days of immersion in the SBF solution as presented in Fig. 4.38 (d). Thus, the present experiment demonstrates that Ca–P deposits are accumulated on the NaOH treated porous alloy surface. However, the XRD pattern detected the peaks of Ti, hydroxyapatite (HA), and TiO<sub>2</sub>. In a study conducted by Xu et al.,(2006) and (Kasuga

et al., 2002) similar results are reported on Ti scaffolds. They found that the formation of hydroxyapatite particles increases with increase in immersion time in SBF.

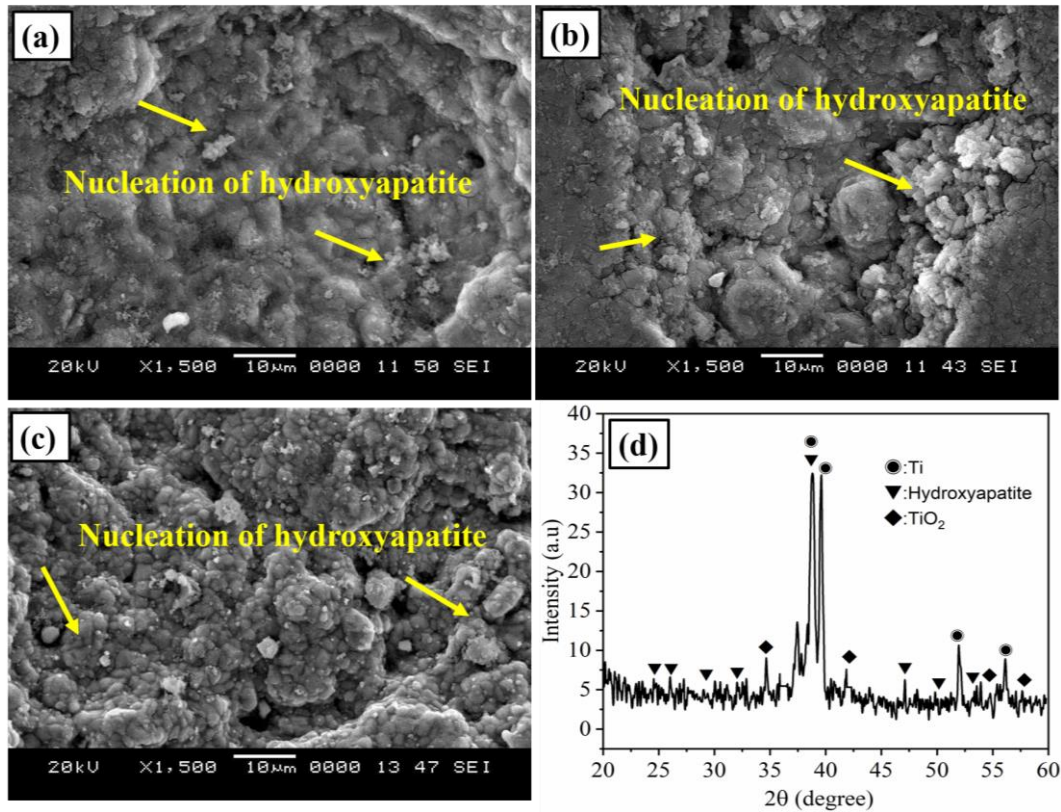


**Fig. 4.38: SEM micrographs of porous Ti–20Nb–5Ag alloy after immersion in SBF solution: (a) 7 days, (b) 14 days, (c) 21 days, and (d) XRD analysis of porous alloy after 21 days of immersion in SBF solution.**

Fig. 4.39 shows that the EDX analysis of hydroxyapatite coated porous Ti–20Nb–5Ag alloy surface after immersion in SBF solution for 7, 14 and 21 days. It shows a presence of elements of the substrate such as Ti, Nb, and Ag along with Ca, P, Na, O and C which obviously form on the surface of the samples due to immersion in the SBF solution. Fig. 4.39 (a) exhibits the presence of large peaks of Ti and small peaks of Ca and P after immersion in SBF for 7 days. However, the peak of Ti is reduced due to an increase in the formation of hydroxyapatite on the porous alloy surface during the immersion time (Gao et al., 2012b; Gu et al., 2009). The elemental peak of Ag has

completely disappeared with increasing immersion time due to the small amount and thick layer of hydroxyapatite formation as shown in Fig. 4.39 (b).

Further, with increasing the immersion time for 21 days, the elemental Ti peak is drastically reduced and large peaks of Ca and P are seen in Fig. 4.39 (c). It is well identified that Ca and P are the main constituents for the formation of hydroxyapatite layers on the implant alloy surface (Benea et al., 2014; H. C. Hsu et al., 2014).

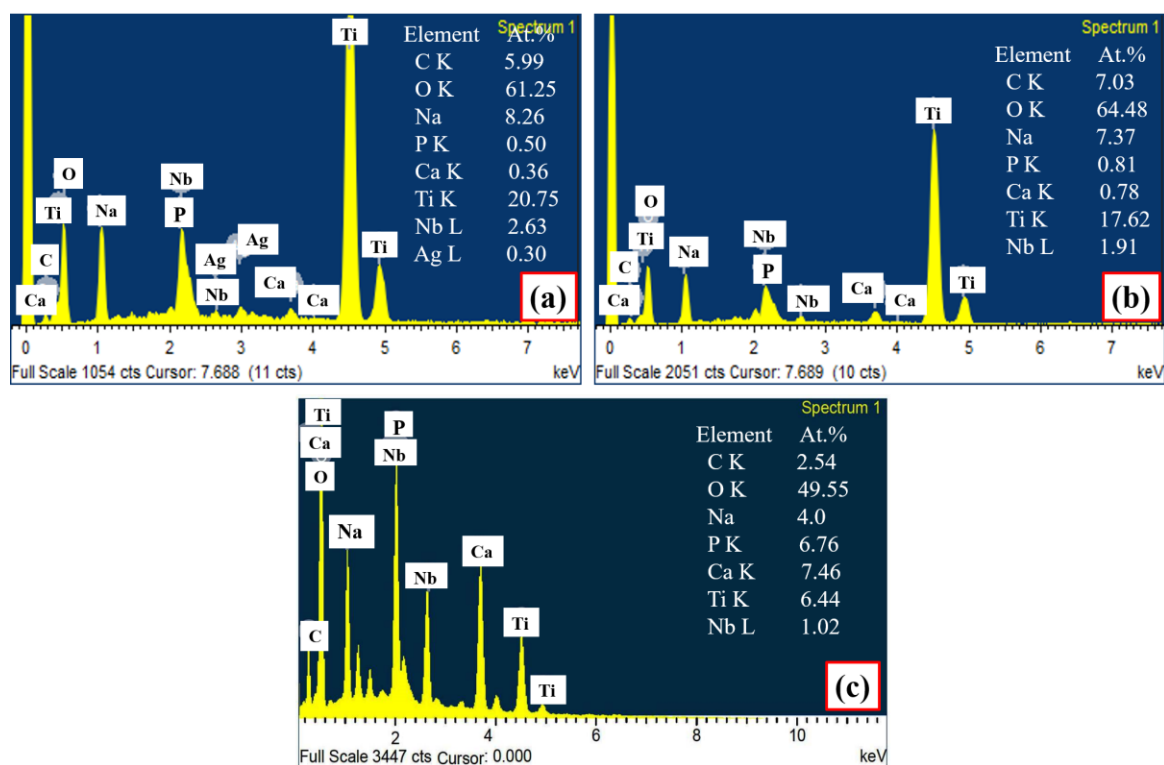


**Fig. 4.39: EDX analysis of porous Ti–20Nb–5Ag alloy after immersion for various time in SBF solution: (a) 7 days, (b) 14 days, and (c) 21 days.**

The EDX analysis confirms the presence of elemental signature and composition of hydroxyapatite layer on the porous alloy surface, which is in good agreement with the SEM micrograph as seen in Fig. 4.38 (c). It is well reported that the formation of a bone-like hydroxyapatite layer on the surface of implant is essential for osseointegration between the implant and living bone tissue. It is also effective in attracting cells and permits osteoblast to form new tissue. Fig. 4.40 shows the elemental mapping of hydroxyapatite coated porous Ti–20Nb–5Ag alloy after 21 days of immersion in the SBF solution. After immersion in SBF solution for 21 days, the



elements obtained such as Ti, Nb, Ca, P, O, C and Na which significantly influence on the formation of hydroxyapatite on the porous alloys surface (Ho et al., 2009; Xiaopeng Wang et al., 2013).

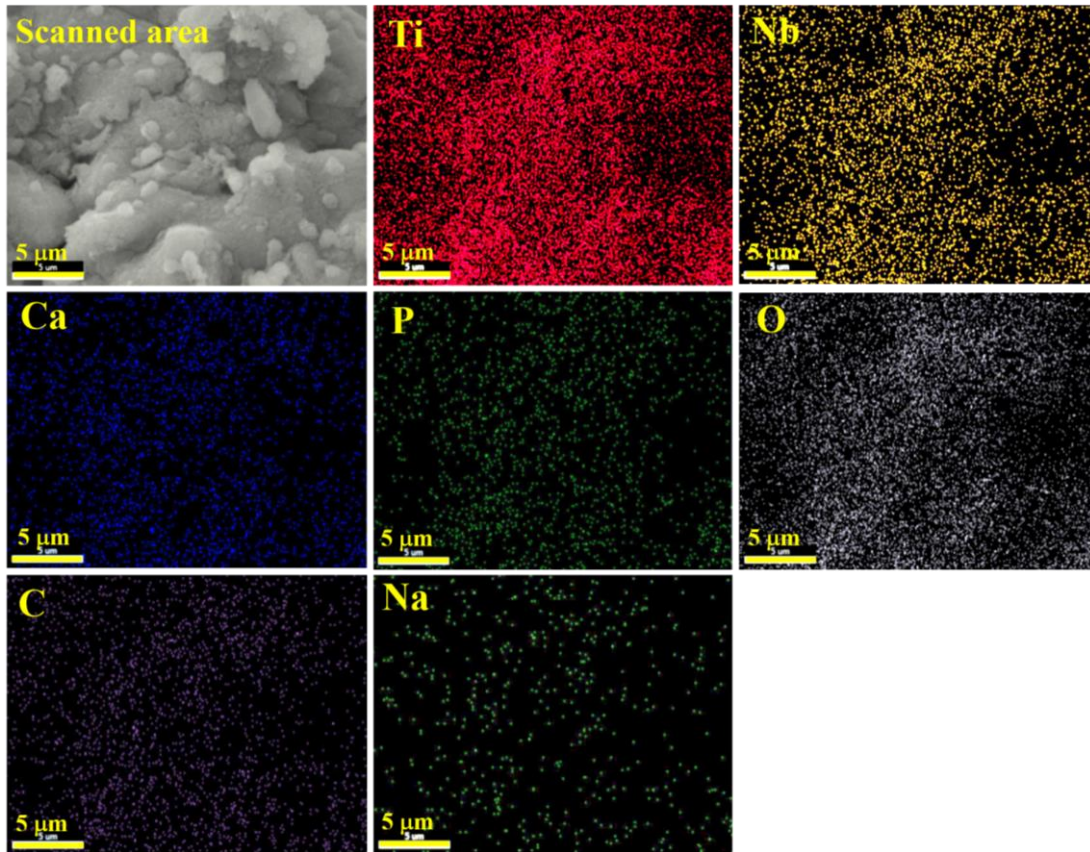


**Fig. 4.40: EDX elemental mapping of porous Ti–20Nb–5Ag alloy after 21 days immersion in SBF solution.**

Fig. 4.41 shows the Ca/P ratio of hydroxyapatite coated porous Ti–20Nb–5Ag alloy after immersion in SBF for 7, 14, and 21 days. These results clearly show that the Ca/P ratio gradually increases with increasing the immersion time in SBF. The Ca/P ratio represented in wt. % (along with at. %). The ratio of Ca/P was found to be 0.83, 1.24, and 1.64 for the immersion time of 7, 14 and 21 days respectively [in terms of wt. %]. It is noticed that, for 21 days of immersion in SBF, the Ca/P ratio is about of 1.64 wt.% which is close to the value of 1.67 and confirming the formation of the hydroxyapatite on the porous alloy (L. Zhang et al., 2017). However, the Ca/P ratio for other immersion times are well within the 0.5–2 (Benea et al., 2014; Gu et al., 2009; W. Xu et al., 2006). These values of the present study are in good support for

hydroxyapatite deposition which is a necessary application as biomaterials. The relationship between the immersion times (h) with hydroxyapatite formation (Ca/P) in SBF solution on the developed porous alloy using linear equation is as follows:

$$y = 0.05x + 0.42 \quad (21)$$

$$y = -0.02x + 0.5 \quad (22)$$

Where, the Ca/P (Wt. %) (19), and Ca/P (At. %) (20) of the developed porous alloys, and  $x$  is immersion time in SBF solution .

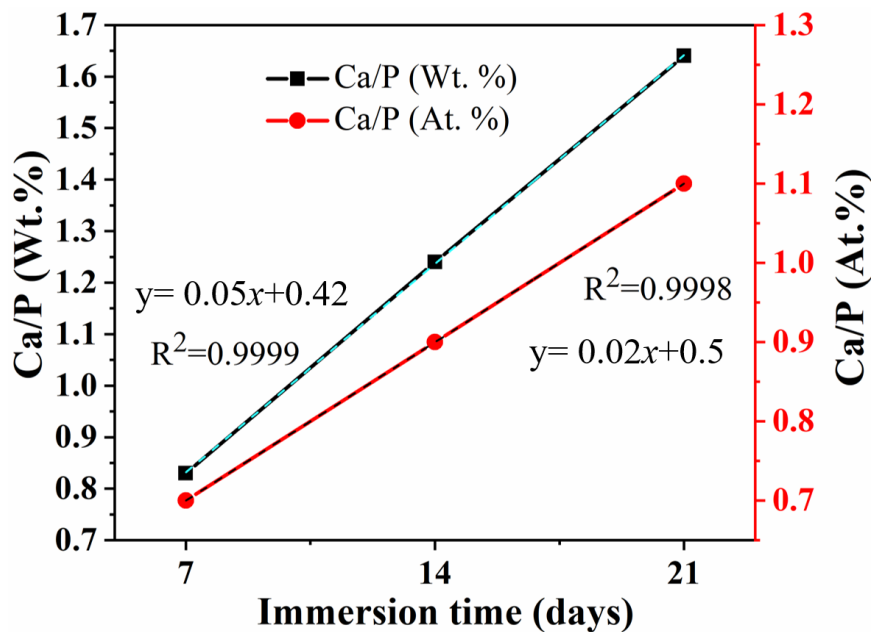


**Fig. 4.41: Ca/P ratio of hydroxyapatite coated porous Ti-20Nb-5Ag alloy after immersion for various time in SBF solution: (a) 7 days, (b) 14 days, (c) 21 days.**

The schematic representation of formation of hydroxyapatite on the porous Ti-20Nb-5Ag alloy in SBF is presented in Fig. 4.42. The apatite formation mechanism is highly dependent on surface treatment by the alkaline solution, which assists the surface of Ti alloy for the nucleation and the growth of apatite (Hou et al., 2013; H. Hsu et al., 2014). The alkali treatment increases the ability to absorb  $\text{OH}^-$  ions on the surface.  $\text{Na}^+$  ions are released from the sodium titanate into the SBF solution and increase the pH.

The negatively charged ions are formed due to the present of  $\text{HTiO}_3^-$  on the alloy surface, which combines with  $\text{Ca}^{2+}$  ions by Coulomb's force. Meanwhile,  $\text{HPO}_4^{2-}$  group of ions from the hydrogen bond, are attracted by  $\text{Ca}^{2+}$  ions in SBF. The enrichment of  $\text{Ca}^{2+}$ ,  $\text{HPO}_4^{2-}$ , and  $\text{OH}^-$  ions in the aqueous solution improve the degree of supersaturation with respect to apatite (Hamzah, 2016; Jonášová et al., 2002).

Once the apatite is starts nucleating, it consumes  $\text{Ca}^{2+}$ ,  $\text{HPO}_4^{2-}$ ,  $\text{OH}^-$  ions and spontaneously grows on the alloy surface (Gao et al., 2012b; Jonášová et al., 2002). The apatite formation can be produced according to the following reaction in SBF (Gao et al., 2012a; Mendes et al., 2016; Yan et al., 2014).

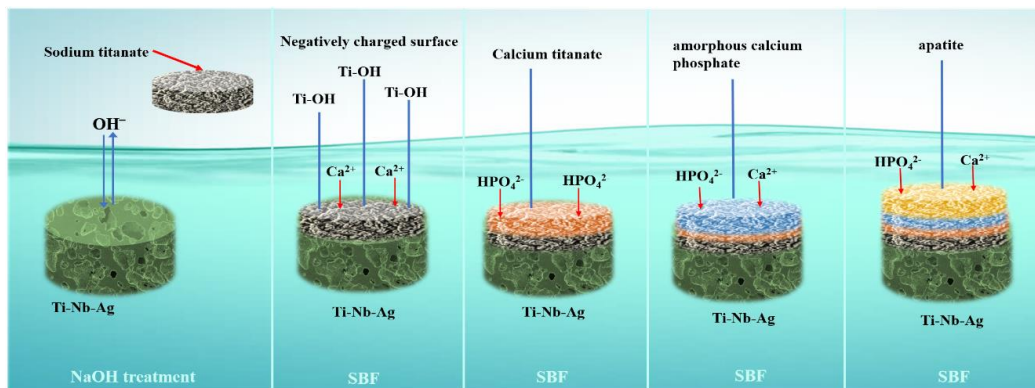


**Fig. 4.42: Schematic representation of hydroxyapatite formation on the porous Ti-20Nb-5Ag alloy in SBF solution.**

#### 4.5.3. AFM and XPS analysis of analysis of hydroxyapatite coated surface

Though, it is difficult to estimate the surface roughness of porous Ti-20Nb-5Ag alloy samples, due to the various pore structures which consist of different shapes and sizes from one region to another. The deposition of hydroxyapatite particles affects measurements because of pore morphology. However, several attempts have been made to observe roughness profile through atomic force microscope (AFM). Fig. 4.43 shows the variation in the surface topography of porous alloy with increasing immersion time in SBF for 7 to 21 days. It is noticed that the formation of smooth surfaces (without ridges) after 21 days [Fig. 4.43 (c)] of immersion in SBF compared to 7 days [Fig. 4.43 (a)] and 14 days [Fig. 4.43 (b)], where more ridges were observed

(Indira et al., 2013). Hence, it is confirmed that the deposition of apatite particles increases with increasing the immersion time in SBF. Fig. 4.43 (d) shows the evaluation of roughness parameters in a sampling scale of  $10\ \mu\text{m} \times 10\ \mu\text{m}$ . The  $R_a$  value (average roughness) decreased from 114 nm to 57 nm, while  $R_{ms}$  (root mean square) was reduced from 148 nm to 73 nm.

It seems that roughness of the surface has gradually decreased and also the ridges were reduced, as thick layers of apatite coating spread on the surface. This result shows a good agreement with the published work of Gao et al., (2012). They analysed the hydroxyapatite coated surface using AFM. It is observed that surface area and surface roughness gradually decrease with increasing the immersion time SBF. Hence, it could be concluded that the modified porous alloy exhibited good potentiality as bone implant material.

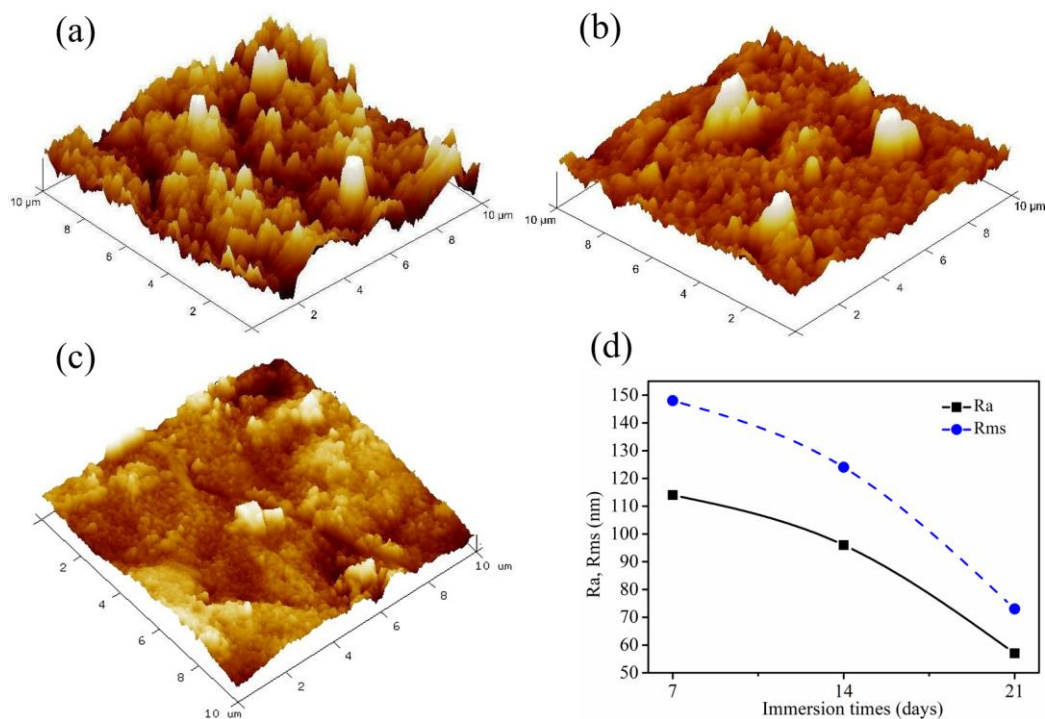


**Fig. 4.43: Surface topography of porous Ti-20Nb-5Ag alloy after immersion in SBF for: (a) 7 days, (b) 14 days, (c) 21 days, and (d) variation in the surface roughness ( $R_a$ ) and root mean square ( $R_{ms}$ ).**



Fig. 4.44 shows XPS survey spectra of the surface of the porous Ti–20Nb–5Ag alloy observed after immersion in the SBF solution at 37 °C for 21 days. The XPS high-resolution spectra exhibit the presence of Ti, Nb, Ag, Ca, P and O. The spectrum shows the unpreventable C 1s element from the carbon contaminant in the surface of the sample. The presence of O 1s is the top most layer which is partially oxidized after the sample surface is exposed to SBF solution (W. Y. Guo et al., 2009; Sri et al., 2018). To investigate systematic analysis, the individual scanning was conducted around the Ti2p, Nb3d, Ag3d, Ca2p, P2p and O 1s energy levels and results are plotted in Fig. 4.45.

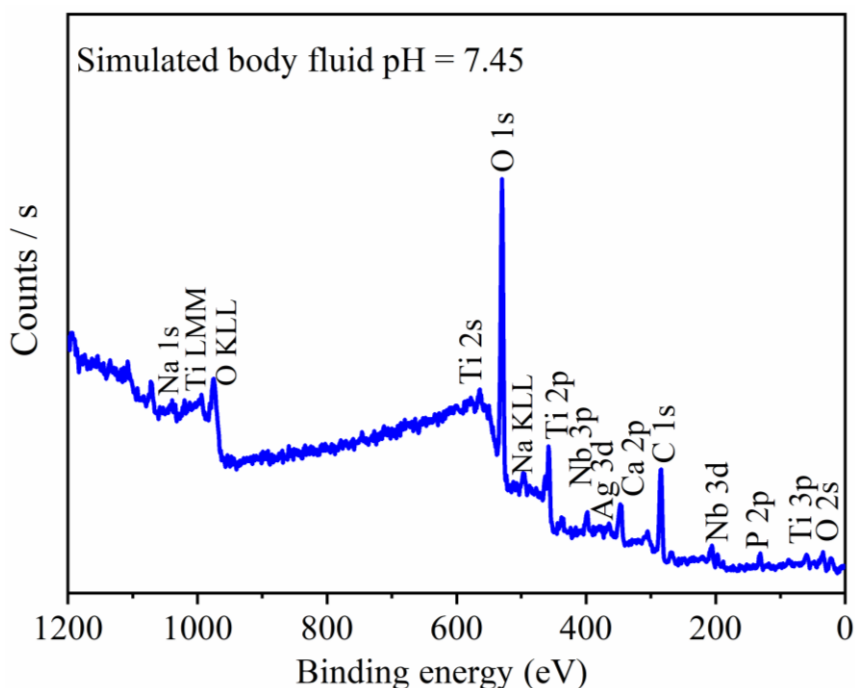


**Fig. 4.44: XPS high-resolution survey spectra obtained for porous Ti–20Nb–5Ag alloy surface after 21 days immersion in simulated body fluids at 37 °C.**

The deconvoluted XPS spectra of the porous alloy surface after immersion in SBF for 21 days as shown in Fig 4.45. From the high-resolution spectra show the presence of Ti 2p [(Fig. 4.45 (a)] of binding energy between 459.2 eV and 464.7 eV. The Ti 2p is an indication for the presence of Ti in the sample. The obtained peak at 459.2 eV is corresponding to  $Ti^{4+}$  oxidation electrons which is the most stable titanium oxide state. The binding energy of the components at 455.1 and 453.07 eV originate in the area relative to metallic Ti 2p electrons.

The two photoelectron peaks of the Nb 3d spectrum [(Fig. 4.45 (b))] located at 206.1 eV and 209.2 eV for Nb 3d<sub>3/2</sub> and Nb 3d<sub>5/2</sub> respectively, obtained from the Nb<sup>5+</sup> oxidation (W. Y. Guo et al., 2009). These two peaks observed at the binding energy of 366.1 eV and 372.5 eV are corresponding to Ag 3d<sub>5/2</sub> and Ag3d<sub>3/2</sub> in porous alloy surface after 21 days immersion in SBF as shown in Fig. 4.45 (c). The peak Ag 3d shifted towards lower binding energy as compared with standard binding energy of Ag 3d<sub>5/2</sub> and Ag 3d<sub>3/2</sub> (368.2 and 374.2 eV) occurred due to the decreasing in the electron density of Ag. The shift of peak Ag 3d is reported by Zhang et al., (2012).

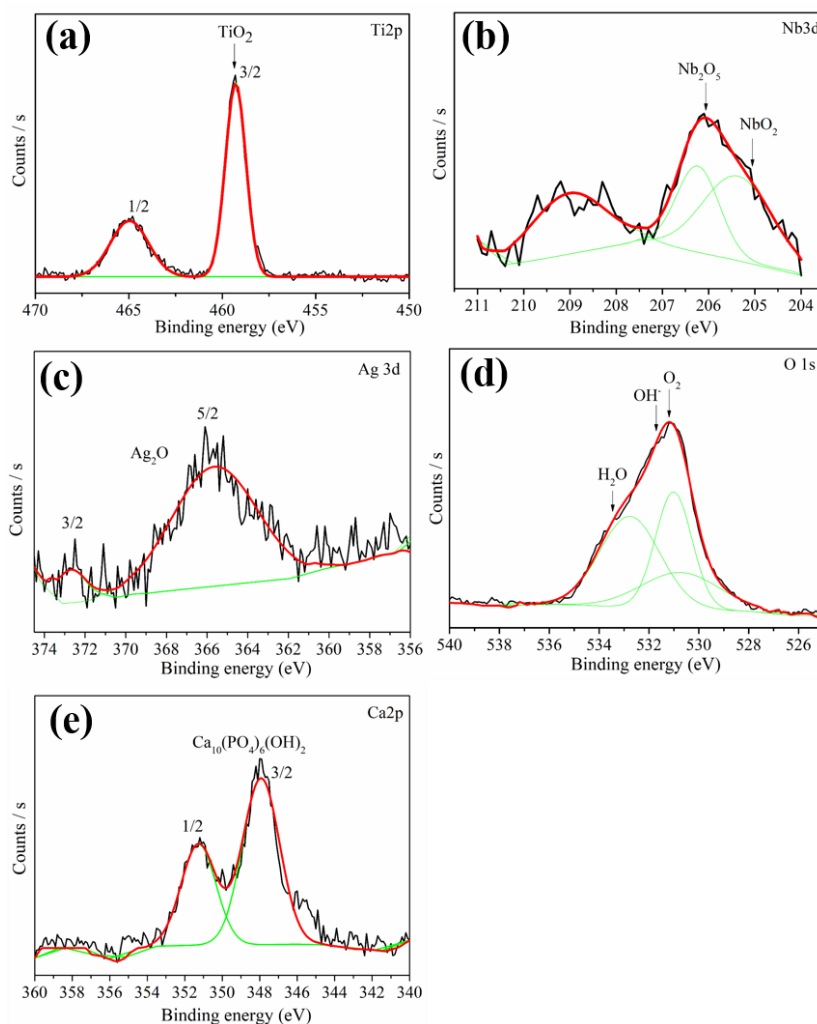


**Fig. 4.45. XPS high resolution individual element spectra of (a) Ti2p, (b) Nb 3d, (c) Ag 3d, (d) O 1s and Ca 2p.**

The binding energies obtained for O<sub>2</sub>, OH<sup>-</sup>, and H<sub>2</sub>O elements are pointed out at 531.1eV, 531.6 eV and 533.4 eV respectively [(Fig. 4.45 (d))], the obtained peaks corresponding to the O 1s spectrum. The O<sup>2-</sup> ions in oxyhydroxide/oxide from the oxygen, OH<sup>-</sup> is represented to the OH oxygen and water in the SBF solution (Han et al., 2011). The high-resolution spectra obtained for calcium element into two peaks of Ca 2p<sub>3/2</sub> (348 eV) and Ca 2p<sub>1/2</sub> (351.2 eV) which is corresponding to hydroxyapatite [Ca<sub>10</sub>(PO<sub>4</sub>)<sub>6</sub>(OH)<sub>2</sub>], obtained from the Ca 2p spectrum (Song et al., 2009).

#### **4.5.4 Effect of hydroxyapatite coating on the electrochemical corrosion behavior**

To study in vitro electrochemical corrosion behavior as a function of immersion time in SBF which is responsible for the formation of hydroxyapatite coating on the porous Ti–20Nb–5Ag alloy after immersion in SBF for 7, 14, and 21 days. The test was performed on the hydroxyapatite coated porous alloys in SBF at 37 °C.

Potentiodynamic polarization test was conducted on the hydroxyapatite coated porous Ti–20Nb–5Ag alloy at a potential of 0.5 V<sub>SCE</sub> which was in the region where the porous alloy showed a passivation tendency in the polarization curve in Fig. 4.46. Both cathodic and anodic branches of polarization curves of porous alloy exhibit appreciably similar behavior, and it revealed that typical active-passive transition. It can be seen that porous alloy shows a spontaneous passivation upon anodic polarization, and increasing in current density with the corrosion potential before entering a stable passive region.

The electrochemical corrosion parameters of porous Ti–20Nb–5Ag alloy after 7-, 14- and 21-days immersion in SBF solution at 37 °C and results are presented in Table 4.10. The corrosion potential (E<sub>corr</sub>), observed for porous Ti–20Nb–5Ag alloy are –0.20 V (at 7 days), –0.14 V (at 14 days), and –0.10 V (at 21 days). The corrosion current density (i<sub>corr</sub>) observed 0.148 μA/cm<sup>2</sup>, 0.053 μA/cm<sup>2</sup>, and 0.007 μA/cm<sup>2</sup> for the immersion of 7, 14 and 21 days respectively. It is observed that the i<sub>corr</sub> is reduced while E<sub>corr</sub> increases towards positive direction with increasing the immersion time in SBF for 7 to 21 days.

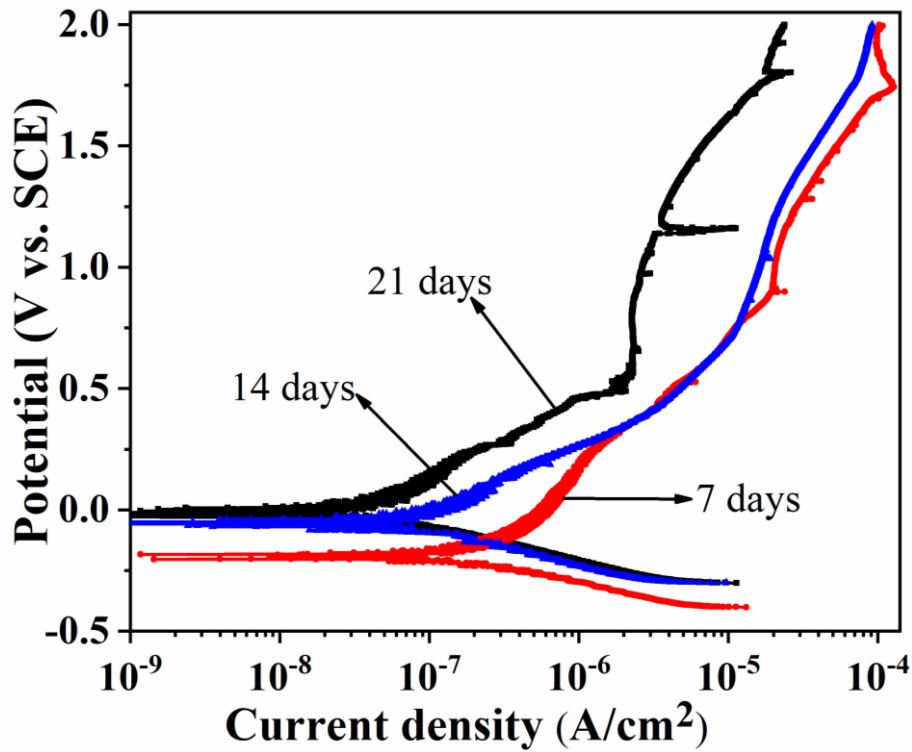


**Fig. 4.46:** Potentiodynamic polarization curves of porous Ti–20Nb–5Ag alloys in SBF solution at 37 °C as a function of immersion time (7, 14 and 21 days).

**Table. 4.10:** Corrosion parameters of the porous Ti-20Nb-5Ag alloy after immersion in SBF solution at 37 °C for 7, 14 and 21 days.

Immersion Time(days)	$E_{\text{corr}}$ (V)	$\beta_a$ (V/dec)	$\beta_c$ (V/dec)	$i_{\text{corr}}$ ( $\mu\text{A}/\text{cm}^2$ )	$i_{\text{pass at 0.5 V}}$ ( $\mu\text{A}/\text{cm}^2$ )	Corrosion ( $\text{mm}/\text{y}) \times 10^{-3}$
7	-0.20	0.31	0.10	0.148	0.0046	0.17
14	-0.14	0.19	0.13	0.053	0.0030	0.09
21	-0.10	0.11	0.08	0.007	0.0011	0.01

From the polarisation curve, as the immersion period increases the alloy showed a very passivity; it means a protective surface film. A very low  $i_{\text{corr}}$  value with a positive shift in  $E_{\text{corr}}$  is found for 21 days of immersion over 7 and 14 days. With increase in immersion time, a steady passive current was observed indicating a stable surface film on porous Ti–20Nb–5Ag alloy.

It is observed a very low passive current density of  $0.004 \mu\text{A}/\text{cm}^2$ ,  $0.003 \mu\text{A}/\text{cm}^2$ ,  $0.001 \mu\text{A}/\text{cm}^2$  for the immersion time in SBF for 7, 14 and 21 days respectively. Further, the corrosion rate decreased with increasing the immersion time of  $0.17$  to  $0.01 \text{ mm}/\text{y} \times 10^{-3}$  for 7 to 21 days respectively. The obtained results show early passive film formation on the porous alloy surface due to the gradual deposition of hydroxyapatite (Indira et al., 2013; Shukla & Balasubramaniam, 2006). Hence, the low current density and high corrosion resistance obtained for porous Ti–20Nb–5Ag alloy after 21 days immersion compared to 7, 14 days might be due to the effect of deposition of more hydroxyapatite particles. The stable current during prolonged immersion is attributed to a continuous interaction of calcium and phosphate ions present in the SBF solution, with the surface film formed on titanium alloys (Raman et al., 2007).

D. Sri Maha Vishnu et al., (2019) reported the interaction of ions present in the SBF solution on the surface of porous Ti-Nb alloy. They found that the corrosion potentials shifted in the more positive direction with increasing immersion time, and also observed that the low corrosion current densities with increasing the immersion time from 1 h, 168 h and 360 h. Similar observations were reported on the Ti and Ti–5Al–2Nb–1Ta alloy in the SBF as carried out by Sasikumar & Rajendran., (2012).

The electrochemical impedance spectroscopy (EIS) technique is a more sophisticated tool for the evaluation of porous alloy surfaces and it is able to explain the characteristics of film formation. Impedance spectra for porous Ti–20Nb–5Ag alloy after immersion in SBF for various times at  $37^\circ\text{C}$  are represented in Fig. 4.47. Using both the Nyquist and the Bode plots to explain the characteristics of the passive film formation on the porous alloy surface. Nyquist plots of the porous alloys after immersion in SBF for various time (7, 14 and 21 days) are shown in Fig. 4.47 (a), and it shows similar behavior that is characterized by an incomplete and large single semicircle, which represents a capacitive response of the passive film in the SBF solution. It is noticed that the semicircle diameter becomes larger with increased immersion time in SBF. The noble electrochemical corrosion properties of porous alloys with respect to immersion times is mainly due to deposition of hydroxyapatite particles on the porous alloy surface (Lu et al., 2018, Wang et al., 2003). Fig. 4.47 (b) shows that the Bode magnitude ( $Z$ ) plots for porous Ti–20Nb–5Ag alloy after various immersions in the SBF. It can be seen that similar nature of magnitude plots for all the

porous alloys. The study revealed that the modulus of impedance values increased with increasing time in SBF. It is also noticed that a large impedance value for 21 days of immersion, which could be attributed to the formation of strongly highly covered hydroxyapatite particles on the porous alloy surface.

The high frequency region in the Bode impedance curve exhibits a region where the slope is  $\approx 0$  due to the characteristics of electrolyte resistance (Tamilselvi et al., 2006). In the intermediate frequency range and low frequency range, the relationship of modulus and the frequency observed with a slope close to  $-1$ . This is a typical capacitive performance of the electrolyte for metallic passivity. It is revealed that the impedance value at high frequency drastically increased due to the more hydroxyapatite particles deposition on the porous alloy surface, which is obtained after immersion in SBF for 21 days (Alves et al., 2009; Vasilescu et al., 2012). C.X. Wang et al., (2003) observed similar results on Ti-6Al-4V alloy after immersion in SBF for various times. With an increase in the exposure time in SBF, the remarkable change in the spectrum coincided with the hydroxyapatite formation and growth of apatite on the porous alloy surface.

Fig. 4.47 (c) presents Bode phase angle spectra obtained for porous alloy immersion in SBF for various times. It was observed that the phase angle increases with immersion time increased in SBF. It is found, 7 days of immersion the phase angle in a middle frequency range shows around  $60^\circ$ . With increasing the immersion time for 14 days, the frequency range increases about  $80^\circ$ , which shows that the frequency range increases with the immersion time. Further, immersion time increases to 21 days, the phase angle value reaches about  $85^\circ$ . However, the high impedance values and phase angle of almost  $85^\circ$  at intermediate frequencies are indicative of a near capacitive response of this biomaterial, which is explained by the presence of a strong hydroxyapatite layer which acts as a stable passive film on the porous alloy surface (barrier layer). The obtained results show that the phase angle is gradually increased. This change is due to the formation of high hydroxyapatite particles deposition and growth on the porous alloy surface with increasing immersion time in the SBF solution. During the EIS, the interaction of solution is generally identified by a phase angle shift at the higher frequency region which influences, physical change of quality of

formation of hydroxyapatite layer formation when it is immersed in SBF. Alves et al., (2009) have described the increasing corrosion resistance of Ti and Ti-6Al-4V alloy as a function of the immersion time in physiological solution. They found that the high impedance values at the phase angle of  $80^\circ$  after the 168 h of immersion as compared to 5 and 24 h of immersion. Which indicates that increasing the immersion time significantly enhances the corrosion resistance due to the formation of passive film with respect to prolonging time. The obtained results in the present investigations are in good agreement with the reports by various researchers (Sasikumar & Rajendran, 2012; Tamilselvi et al., 2006).

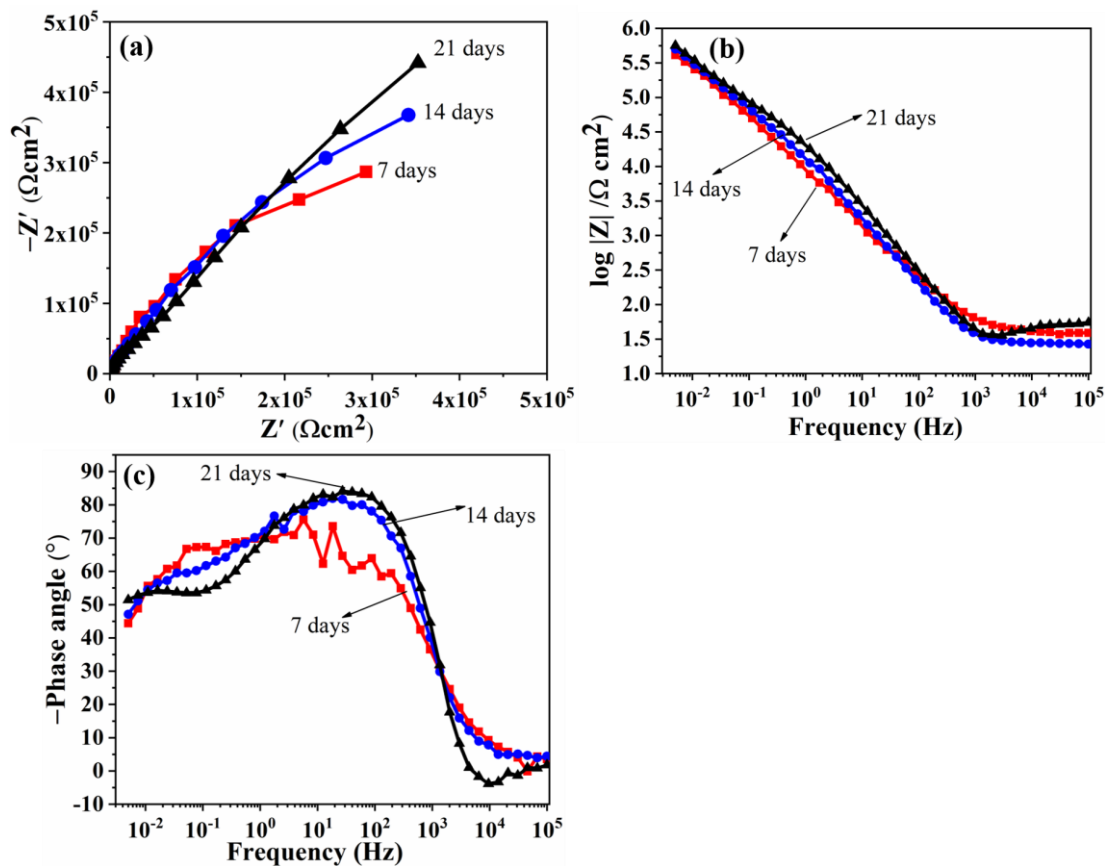


**Fig. 4.47: EIS plots of porous Ti-20Nb-5Ag alloys in SBF solution at 37 °C after 7, 14 and 21 days of immersion: (a) Nyquist impedance plot, (b) Bode magnitude plot, and (c) Bode phase plot.**

The impedance spectra with frequency can be described using an equivalent circuit model as shown in Fig. 4.48. The corresponding impedance values are summarized in Table 4.13. The schematic representation of hydroxyapatite coating on the hydrogel, which is formed on the porous alloy surface as shown in Fig. 4.48 (a). The equivalent circuit used for analysis of the obtained EIS results as presented in Fig. 4.48 (b) (Sasikumar & Rajendran, 2012). The equivalent circuit is composed of various resistances and capacitances. The circuit components are represented as  $R_s$  ( $R_a Q_a$ )( $R_b Q_b$ ), where  $R_s$ ,  $R_a$  and  $R_b$  are related to the solution resistance, resistance of apatite layer, and resistance of barrier layer, respectively. It represents the two-time constant behavior, corresponding to the barrier layer and apatite layer formation. This is due to the adsorption of Ca and P ions over the barrier layer. Q signifies the possibility of a non-ideal capacitance, known as constant phase element (CPE).

In this,  $Q_a$ , and  $Q_b$  are related to capacitance of apatite layer, and capacitance of barrier layer as shown in schematic representation [Fig. 4.48 (b)]. It is used to fit the obtained data of porous Ti–20Nb–5Ag alloy alloys after hydroxyapatite coating on the surface. Here, the constant phase element (CPE) was used in the fitting to instead of capacitance C, due to the previous considers the fact that the barrier film never exhibits the theoretically expected phase shift of  $-90^\circ$  and slope of  $-1$  for an ideal dielectric (Raman et al., 2007). The impedance of the CPE can be represented as follows (Y Bai et al., 2012):

$$Z_{CPE} = C^{-1}(j\omega)^{-n} \quad (11)$$

Where C is the capacitance associated to an ideal capacitor,  $\omega$  is an angular frequency and n is a factor of deviation from the ideal capacitive behaviour due to the irregular surface, roughness factors and absorption effects (Mohan et al., 2015).



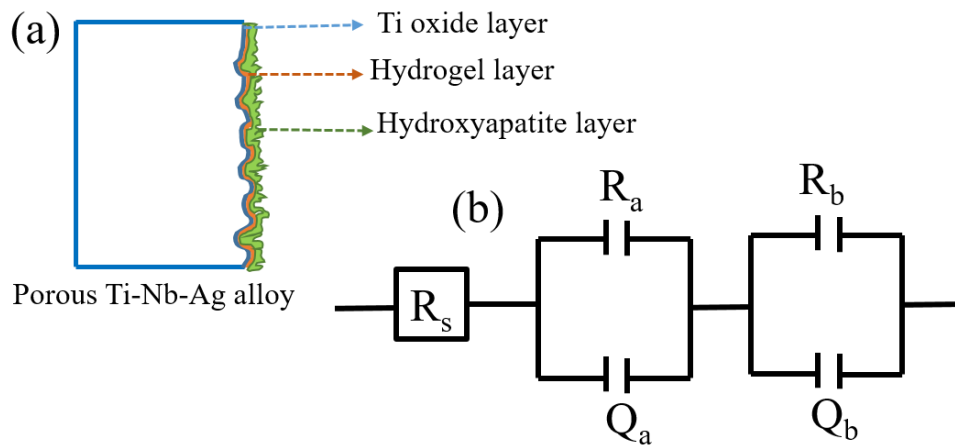


**Fig. 4.48: Physical model and equivalent circuit model of porous Ti–20Nb–5Ag alloy hydrogel layer hydroxyapatite layer/ solution interface at 37 °C.**

Table 4.11 showed changes in the values of the solution resistance ( $R_s$ ) with increasing immersion period from  $26.9 \Omega\text{cm}^2$  to  $103 \Omega\text{cm}^2$  for 7 to 21 days immersion time, respectively. Which can be associated with the change in the ionic strength of the solution with growing time. However, it is noticed that the significant increment in the resistance of hydroxyapatite layer ( $R_a$ ) is about  $105 \text{ k}\Omega\text{cm}^2$  to  $901 \text{ k}\Omega\text{cm}^2$  for 7 to 21 days immersion time, respectively. This suggested that the more hydroxyapatite particles deposited on the surface by the incorporation of Ca and P ions from the solution, which can be made thick film formation during the immersion time. The fact that increasing the immersion time in SBF to the formation of nucleation and apatite growth showed a high corrosion resistance in titanium alloy studied (Sasikumar & Rajendran, 2012). A similar result was observed by V. Raman et al., 2007 (Raman et al., 2007) studied Ti for electrochemical properties after immersion in SBF for various incubation times and found a similar profile as the one obtained in the present study. It is indicating that the alkali treated sample after immersion in SBF for different time. The oxygen beneath the layer increases with immersion time and forming a barrier layer between the sodium titanate hydrogel and titanium surface, it is associated with the formation of parent titanium oxide. Thus, the mixture of alkali heat treatment and immersion in SBF solution induces the formation of hydroxyapatite particles on the porous alloy surface.

Further, increasing the immersion time drives a thickening and roughening of the surface layer. Hence, it can be concluded that the formation of hydroxyapatite layer provides an environment which strongly promotes the high corrosion resistance over the surface of porous Ti–20Nb–5Ag alloy.

**Table 4.11: Impedance parameters of porous Ti–20Nb–5Ag alloy obtained by fitting  $R_s(R_aQ_a)(R_bQ_b)$  models on immersion in SBF.**

Immersion time (days)	$R_s$ ( $\Omega\text{cm}^2$ )	$Q_a$ ( $\mu\text{F cm}^{-2}$ )	$n_a$	$R_a$ ( $\text{k}\Omega\text{cm}^2$ )	$Q_b$ ( $\mu\text{F cm}^{-2}$ )	$n_b$	$R_b$ ( $\Omega\text{cm}^2$ ) $\times 10^5$	$R_{T=}$ ( $R_a + R_b$ ) ( $\Omega\text{cm}^2$ ) $\times 10^5$
7	26.9	9.3	0.81	105	15.10	0.93	185	290
14	40.1	32.1	0.68	659	9.74	0.89	53	59.5
21	103	45.2	0.59	901	2.80	0.76	47	56.0

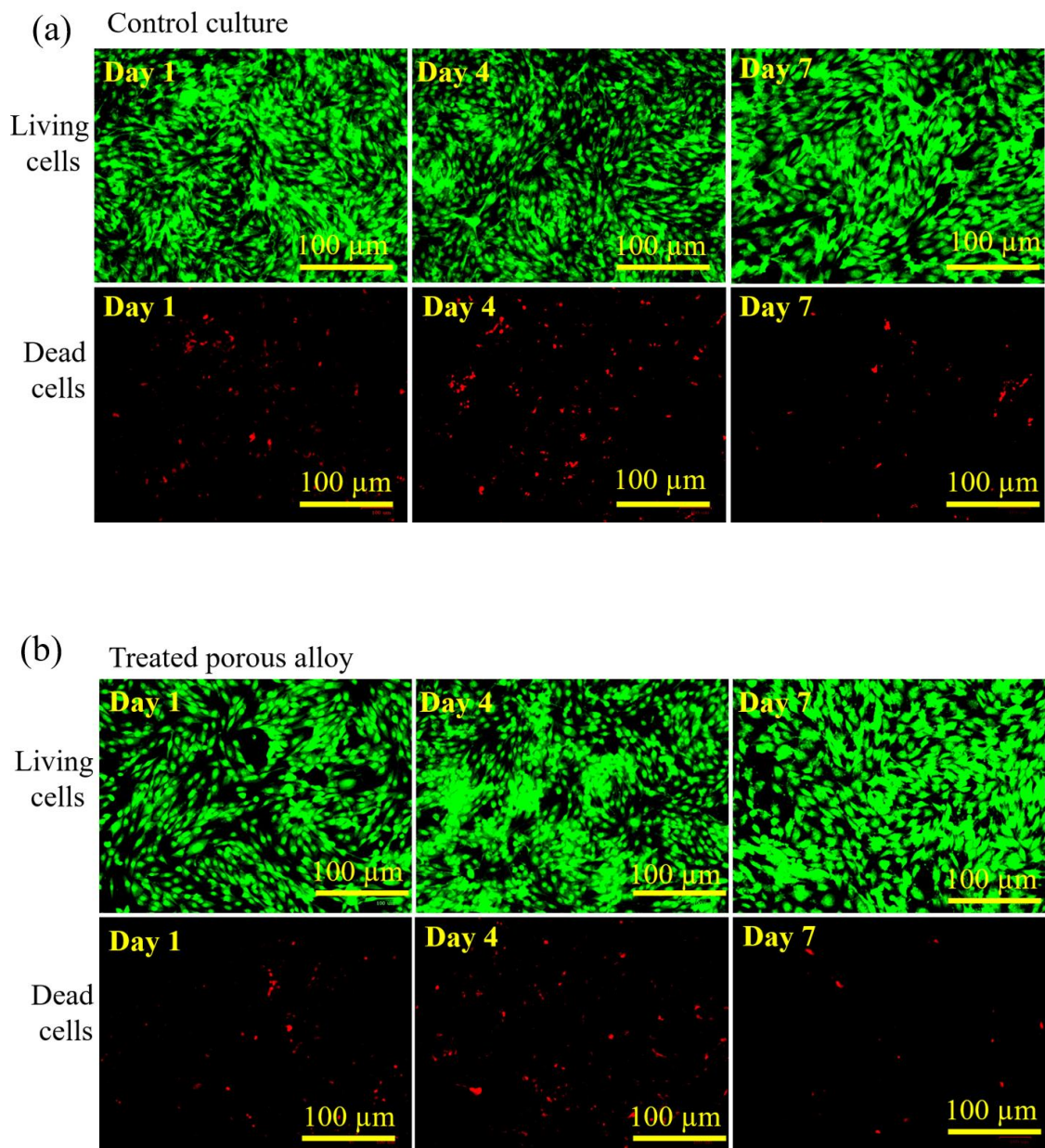
#### 4.5.4 Cytotoxicity performance

Cytotoxicity test provides viability of cells on the implant surface and distinguishes between the living cells and dead cells to assess the biocompatible nature of the implants. In the present study MG-63 cells were used for cytotoxicity tests. Fig. 4.49 shows the typical cell morphology of MG-63 human osteoblast cells; the evidence of cells which are living on the porous alloy surface shown by green fluorescence, and dead cells shown by red fluorescence. It appears that the cells have grown in different shapes, such as spherical, elliptical and polygonal etc. However, the density of cell proliferation increased with increasing incubation times (Fig. 4.49). In a study carried by C. Torres-Sanchez et al., (2018) have fabricated a porous Ti–35Nb–4Sn alloy with the various porosity levels (30%, 40%, 50%, 60% and 70%) and conducted the cytotoxicity test using MG-63 human osteoblast cells. After incubation in 1, 3 and 7 days, the porous alloys exhibited excellent cell propagation on the porous surface. They have reported that the effect of pore size did not influence new tissue in growth as well as not being a controlling factor for bone healing properties. However, it was found that more than 70% cell growth on the surface of all porous alloys, which is indicating that there is no toxic nature of the developed porous alloys. A comparative cell growth at

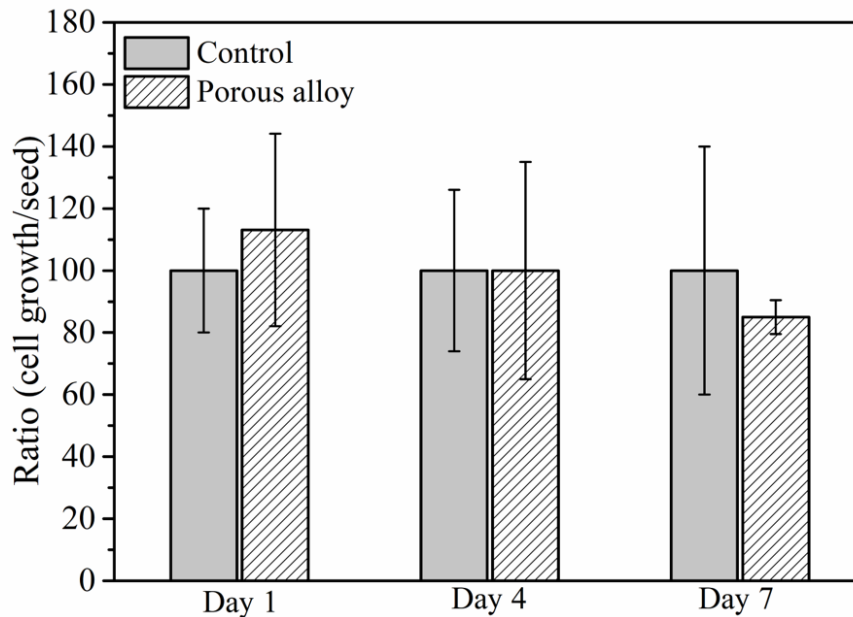
different incubation duration has been shown as the ratio of the final number of grown cells to the initial number of seeding cells.

Fig. 4.50 shows that the high cell propagation rate at the early stage (1<sup>st</sup> day) is due to the initial rate of cell seeding (about  $25 \times 10^3$ /well in 24 well plates). More cell density is provided because initially it required more time to get physical activity and contact among the cells and interface the porous alloy surface. It shows a steady increase in the proliferation with increasing incubation time. When it is compared with the control (reference), current porous alloy shows almost 113% growth at the initial incubation time for one day. Further, increasing an incubation time for the 4th day with the cell seeding rate of  $7.5 \times 10^3$ /well, which shows growth of 100% cell on the porous alloy surface. However, for the 7th day with the cell seeding rate of  $5 \times 10^3$ /well and cell growth was noticed about 85%, which could be attributed to a low seeding cell density. The result shows a slower growth rate due to low seeding cell density. The density of the cell seeding provided lower with increase in incubation time because of avoid detachment of cells due to over confluency. However, the cell attachment on the sample surface showed more than 70%, which is essential to utilize as clinical application. The obtained results are in good agreement with the reports in the works on similar MG-63 osteoblast cells (Yanjie Bai et al., 2016)(Ou et al., 2017).

In a different studies conducted by Bai et al., (2016) and Ou K.L. et al., (2017) have examined the cytotoxicity behavior using MG-63 osteoblast cells on Ti–45Nb alloys and Ti–(25.17 to 26.12)Nb–(0 to 1.24) Ag alloys, respectively. Results show the good cell growth and proliferation on the surface of the developed porous alloys. With increasing incubation time, they reported that the variation in the cell viability was lower than that of control. However, more than 70% of the cell growth was observed for the developed samples to ensure the potential use for clinical applications. From the cytotoxicity study it is well understood that the developed porous alloys are non-toxic in nature and fairly suitable for the clinical applications.



**Fig. 4.49: Fluorescence images of MG-63 human osteoblast cell cultured for different duration: (a) control and, (b) porous Ti-20Nb-5Ag alloy.**



**Fig. 4.50: Human osteoblast MG-63 cell attachments on porous Ti-20Nb-5Ag alloy at different incubation duration: growth of cells with respect to the control.**

### Summary

- Alkali-heat treated porous alloys exhibits a sodium titanate layer formation on the surface, which help to hydroxyapatite growth when immersed into SBF.
- Surface of porous alloys shows that there is deposition of hydroxyapatite particles, and these are increase with immersion time increased.
- Ca/P ratio is increases with immersion time increased in SBF, it is noticed that Ca/P ratio is about of 1.64 wt. % which is close to the hydroxyapatite formation (1.67).
- AFM analysis revealed that roughness ( $R_a$ ) of the porous alloy reduced with immersion time increased in SBF.
- It is noticed that formation of stable oxides of  $TiO_2$  and  $Nb_2O_5$  on hydroxyapatite formed surface (after 21 days).

- Corrosion resistance of the porous alloy increased with immersion time increased, this is due to the more hydroxyapatite particles deposited on the porous alloy surface.
- Cell viability test revealed an excellent proliferation of cells on the surface of porous alloy and it is found to be non-toxic towards MG-63 osteoblast cells.



## CHAPTER 5

### CONCLUSIONS

The development of porous Ti–Nb–Ag alloy through powder metallurgy space holder technique. The microstructural analysis, mechanical properties, in-vitro electrochemical corrosion and tribocorrosion corrosion behavior, and biocompatibility of the developed porous Ti–Nb–Ag alloy was investigated. The major conclusions were drawn from the research work as follows:

- The XRD analysis revealed that formation of a small amount of  $\alpha''$  martensite and intermetallic compound of  $Ti_2Ag$  along with  $\alpha$  and  $\beta$  phases in porous Ti– $x$ Nb–5Ag alloy made from 15 and 20 h of ball milling time.
- The compression strength increased from 21 MPa to 83 MPa, and elastic modulus increased from 0.5 GPa to 3.3 GPa with ball milling time increased.
- The corrosion potentials shifting towards the nobler direction and remarkable reduction in corrosion current density, and passivation current density in SBF suggest significant improvement of in vitro corrosion resistance with increase in ball milling time.
- The sintered porous Ti– $x$ Nb–5Ag alloys exhibit the variation of porosity ranging from 57%–65% for the addition 25–35 wt. % Nb content and 45 wt. % of  $NH_4HCO_3$ .
- XRD analysis revealed that the sintered porous alloys predominantly consist of intermetallic compound  $Ti_4Nb$ , oxides  $TiO_2$ , NbO along with  $\alpha$  and  $\beta$ –Ti phases.
- The significant reduction in the compression strength and corrosion properties were observed for the addition of 25 wt. % to 35 wt. % Nb content in the sintered porous alloy.
- Porous Ti–20Nb–5Ag alloys with various porosity levels (22% to 68%) achieved by adding different amount of 15–60 wt.%  $NH_4HCO_3$ . The compression strength and elastic modulus of the alloys decreased with porosity increased and it is found the compatible microstructure and mechanical properties were possessed with the porous alloy having porosity of 43%.



- Corrosion resistance of porous alloys decreased with increasing the porosity level.
- Porous Ti–20Nb–5Ag alloy having the porosity about of 43% was used to study the tribocorrosion properties in SBF solution and it is observed that there is decrease in OCP values from 0.17 to  $-0.50 V_{SCE}$  with increasing the applied loads.
- The potentiodynamic polarization results revealed that the corrosion potential shifted to the negative direction (from 0.06 to  $-0.50 V_{SCE}$ ) and corrosion current density increases ( $0.12 \mu A/cm^2$  to  $0.47 \mu A/cm^2$ ) with applied load increased. The obtained results indicate that increasing the applied loads lead to a material degradation and corrosion.
- Porous Ti–20Nb–5Ag alloy are alkali-heat treated using NaOH and porous alloys exhibits a sodium titanate layer formation on the surface, which help to hydroxyapatite growth when immersed into SBF.
- Surface of porous alloys shows that there is deposition of hydroxyapatite particles, and these are increase with immersion time increased and it is noticed that Ca/P ratio is increases with immersion time increased in SBF, it is noticed that Ca/P ratio is about of 1.64 wt. % which is close to the hydroxyapatite formation (1.67).
- AFM analysis shown that roughness (Ra) of the porous alloy reduced with immersion time increased in SBF and XPS analysis revealed that formation of stable oxides of  $TiO_2$  and  $Nb_2O_5$  on hydroxyapatite formed surface (after 21 days).
- Corrosion resistance of the porous alloy increased with immersion time increased, this is due to the more hydroxyapatite particles deposited on the porous alloy surface.
- Cell viability test revealed an excellent proliferation of cells on the surface of porous alloy and it is found to be non-toxic towards MG-63 osteoblast cells.

## Scope for Future Work

Porous Ti–Nb–Ag alloy were processed through PM space holder method. Various microstructural analysis were done using optical microscopy, scanning electron microscopy, atomic force microscopy and Fluorescence microscopy. Mechanical properties have been examined in terms of compression strength and elastic modulus. X-Ray diffraction analysis was used to identify the phases of the sintered porous alloys. In vitro electrochemical corrosion and tribocorrosion tests was carried out on sintered porous alloys. Surface modification via alkali treatment was conducted. Hydroxyapatite formation test conducted on sintered porous alloys in SBF, and cytotoxicity test performed using MG-63 human osteoblast cells on the sintered porous alloy, which required to use potentially for biomedical applications. Apart from these characterization and observations, the following various studies can be considered to meet the requirement of the different applications in future.

- Antibacterial test of the sintered porous alloy under various agents can be considered for practical usage of this alloys.
- Micro Computed Tomography (micro-CT) study is in need for clear understanding the interconnected porous structure.
- Mechanical properties can be enhanced by addition of various Ag content to porous Ti–Nb–Ag alloy and further processing through PM space holder method.
- Fretting corrosion test can be done on the sintered porous alloys to know how corrosion will take place under the micro-moment.
- Further, in vivo test can be performed by implanting in animals and studying is very important for considering real time application.



## References

- Aguilar, C., Guerra, C., Lascano, S., Guzman, D., Rojas, P. A., Thirumurugan, M., Bejar, L., and Medina, A. (2016a). "Synthesis and characterization of Ti – Ta – Nb – Mn foams." *Mater. Sci. Eng. C*, 58, 420–431.
- Albayrak, Ç., Hacisalihoğlu, I., Yenal vangölü, S., and Alsaran, A. (2013). "Tribocorrosion behavior of duplex treated pure titanium in Simulated Body Fluid." *Wear*, 302(1–2), 1642–1648.
- Andani, M. T., Shayesteh Moghaddam, N., Haberland, C., Dean, D., Miller, M. J., and Elahinia, M. (2014). "Metals for bone implants. Part 1. Powder metallurgy and implant rendering." *Acta Biomater*, 10(10), 4058–4070.
- Arifvianto, B., LeeFlang, M. a., and Zhou, J. (2015). "The compression behaviors of titanium/carbamide powder mixtures in the preparation of biomedical titanium scaffolds with the space holder method." *Powder Technol*, 284, 112–121.
- Arifvianto, B., and Zhou, J. (2014). "Fabrication of Metallic Biomedical Scaffolds with the Space Holder Method: A Review." *Materials*, 7, 3588-3622.
- Bai, Y., Deng, Y., Zheng, Y., Li, Y., Zhang, R., Lv, Y., Zhao, Q., and Wei, S. (2016). "Characterization, corrosion behavior, cellular response and in vivo bone tissue compatibility of titanium-niobium alloy with low Young's modulus." *Mater. Sci. Eng. C*, 59, 565–576.
- Butev, E., Esen, Z., and Bor, S. (2015). "In vitro bioactivity investigation of alkali treated Ti6Al7Nb alloy foams." *Appl. Surf. Sci*, 327, 437–443.
- Chen, Q., and Thouas, G. a. (2015). "Metallic implant biomaterials." *Mater. Sci. Eng. R Reports*, 87, 1–57.

Chen, S. H., Ho, S. C., Chang, C. H., Chen, C. C., and Say, W. C. (2016). "Influence of roughness on in-vivo properties of titanium implant surface and their electrochemical behavior." *Surf. Coatings Technol.*, 302, 215–226.

Chen, Y. J., Feng, B., Zhu, Y. P., Weng, J., Wang, J. X., and Lu, X. (2009). "Fabrication of porous titanium implants with biomechanical compatibility." *Mater. Lett.*, 63(30), 2659–2661.

Cremaşco, A., Osório, W. R., Freire, C. M. A., Garcia, A., and Caram, R. (2008). "Electrochemical corrosion behavior of a Ti-35Nb alloy for medical prostheses." *Electrochim. Acta*, 53(14), 4867–4874.

C.S.S. de Oliveira, Sandro Griza, Marize Varella de Oliveira, Alexandre Antunes Ribeiro, Mônica Barreto Leite. (2015). "Study of the porous Ti35Nb alloy processing parameters for implant applications." *Powd. Tech.* 281 (2015) 91–98.

Dunand, D. C. (2004). "Processing of titanium foams." *Adv. Eng. Mater.*, 6(6), 369–376.

Eren, Y., Gökçe, A., Findik, F., Ozkan, H., and Osman, İ. (2018). "Mechanical properties and electrochemical behavior of porous Ti-Nb biomaterials." *J Mech Beh of Bio Mat*, 87, 59–67.

Fatehi, K., Moztażadeh, F., Solati-Hashjin, M., Tahriri, M., Rezvannia, M., and Ravarian, R. (2008). "In vitro biomimetic deposition of apatite on alkaline and heat treated Ti6Al4V alloy surface." *Bull. Mater. Sci*, 31(2), 101–108.

Fellah, M., Hezil, N., Hussein, M. A., Abdul, M., Zine, M., Montagne, A., Iost, A., Obrosof, A., and Weiss, S. (2019a). "Preliminary investigation on the bio-tribocorrosion behavior of porous nanostructured b -type titanium based biomedical alloys." *Mater. Lett.*, 257, 126755.

Fojt, J. (2013). "Corrosion behaviour of porous Ti – 39Nb alloy for biomedical applications." *Corr Sci*, 71, 78–83.

Gao, Z., Li, Q., He, F., Huang, Y., and Wan, Y. (2012a). "Mechanical modulation and bioactive surface modification of porous Ti-10Mo alloy for bone implants." *Mater. Des*, 42, 13–20.

Geetha, M., Singh, A. K., Asokamani, R., and Gogia, A. K. (2009). "Ti based biomaterials, the ultimate choice for orthopaedic implants - A review." *Prog. Mater. Sci*, 54(3), 397–425.

Hazwani, N., Universiti, H., Mara, T., and Hanib, N. H. (2017). "Surface characterization on alkali-heat- treatment on titanium alloy." *Malaysian Journal of Analytical Sciences*, 20 (6), 1429 - 1436.

Hou, L., Li, L., and Zheng, Y. (2013). "Effects of ball milling time on porous Ti – 3Ag alloy and its apatite-inducing abilities." *Trans. Nonferrous Met. Soc. China*, 23, 1356–1366.

Hsu, H. C., Hsu, S. K., Tsou, H. K., Wu, S. C., Lai, T. H., and Ho, W. F. (2013). "Fabrication and characterization of porous Ti-7.5Mo alloy scaffolds for biomedical applications." *J. Mater. Sci. Mater. Med*, 24(3), 645–657.

Hsu, H. C., Wu, S. C., Hsu, S. K., Chang, T. Y., and Ho, W. F. (2014). "Effect of ball milling on properties of porous Ti-7.5Mo alloy for biomedical applications." *J. Alloys Compd*, 582, 793–801.

Ibrahim, M. Z., Sarhan, A. A. D., Yusuf, F., and Hamdi, M. (2017). "Biomedical materials and techniques to improve the tribological, mechanical and biomedical properties of orthopedic implants – A review article." *J. Alloys Compd*, 714, 636–667.

Injeti, V. S. Y., Nune, K. C., Reyes, E., Yue, G., Li, S. J., and Misra, R. D. K. (2019). “A comparative study on the tribological behavior of Ti-6Al-4V and Ti-24Nb-4Zr-8Sn alloys in simulated body fluid.” *Mater. Technol*, 34(5), 270–284.

Kalantari, S. M., Arabi, H., Mirdamadi, S., and Mirsalehi, S. A. (2015a). “Biocompatibility and compressive properties of Ti-6Al-4V scaffolds having Mg element.” *J. Mech. Behav. Biomed. Mater*, 48, 183–191.

Karre, R., Kumar, B., Rajendran, A., and Nivedhitha, J. (2019). “Materials Science & Engineering C Comparative study on Ti-Nb binary alloys fabricated through spark plasma sintering and conventional P / M routes for biomedical application.” *Mater. Sci. Eng. C*, 94, 619–627.

Khodaei, M., Meratian, M., Savabi, O., and Fathi, M. (2015). “Comparative evaluation of the effect of different types of surface modifiers on bioactivity of porous titanium implants.” *Russian Journal of Non-Ferrous Metals*, 56 (4), 469–476.

Kohn, D. H. (1998). “Metals in medical applications.” *Curr. Opin. Solid State Mater. Sci.*, 3(3), 309–316.

Kokubo, T., Kim, H. M., and Kawashita, M. (2003). “Novel bioactive materials with different mechanical properties.” *Biomaterials*, 24(13), 2161–2175.

Kokubo, T., Pattanayak, D. K., Yamaguchi, S., Takadama, H., Matsushita, T., Kawai, T., Takemoto, M., and Fujibayashi, S. (2010). “Positively charged bioactive Ti metal prepared by simple chemical and heat treatments.” *J. R. Soc. Interface*, 7, S503–S513.

Lee, C. M., Ju, C. P., and Lin, J. H. C. (2002). “Structure ± property relationship of cast Ti ± Nb alloys.” *Journal of Oral Rehabilitation*, 29, 314–322.

Li, Y. H., Chen, N., Cui, H. T., and Wang, F. (2017). “Fabrication and characterization of porous Ti–10Cu alloy for biomedical application.” *J. Alloys Compd*, 723, 967–973.

Li, Y. H., Yang, C., Kang, L. M., Zhao, H. D., Zhang, W. W., Li, Y. Y., Yang, C., Kang, L. M., W. W., and Li, Y. Y. (2015). "Biomedical porous TiNbZrFe alloys fabricated using NH<sub>4</sub>HCO<sub>3</sub> as pore forming agent through powder metallurgy route." 5899. *Powder Metallurgy*, 58(3), 228-234.

Liu, X., Chu, P. K., and Ding, C. (2004). "Surface modification of titanium, titanium alloys, and related materials for biomedical applications." *Mater. Sci. Eng. R Reports*, 47(3-4), 49-121.

Long, M., and Rack, H. J. (1998). "Titanium alloys in total joint replacement--a materials science perspective." *Biomaterials*, 19(18), 1621-1639.

Majumdar, P., Singh, S. B., Dhara, S., and Chakraborty, M. (2015). "Influence of boron addition to Ti-13Zr-13Nb alloy on MG63 osteoblast cell viability and protein adsorption." *Mater. Sci. Eng. C*, 46, 62-68.

Manivasagam, G., Dhinasekaran, D., and Rajamanickam, A. (2010). "Biomedical Implants : Corrosion and its Prevention - A Review." *Recent Patents on Corrosion Science*, 2, 40-54.

Montanaro, L., Arciola, C. R., Campoccia, D., and Cervellati, M. (2002). "In vitro effects on MG63 osteoblast-like cells following contact with two roughness-differing fluorohydroxyapatite-coated titanium alloys." *Biomaterials*, 23(17), 3651-3659.

Murray, N. G. D., and Dunand, D. C. (2004). "Effect of thermal history on the superplastic expansion of argon-filled pores in titanium: Part I kinetics and microstructure." *Acta Mater*, 52(8), 2269-2278.

Nasab, M. B., Hassan, M. R., and Sahari, B. Bin. (2010). "Metallic biomaterials of knee and hip - A review." *Trends Biomater. Artif. Organs*, 24(2), 69-82.



Nazari, K. A., Nouri, A., and Hilditch, T. (2015). "Mechanical properties and microstructure of powder metallurgy Ti – xNb – yMo alloys for implant materials." *J Mat Des*, 88, 1164–1174.

Niinomi, M. (1998). "Mechanical properties of biomedical titanium alloys." *Mater. Sci. Eng. A*, 243(1–2), 231–236.

Niinomi, M. (2002). "Recent metallic materials for biomedical applications." *Metall. Mater. Trans. A*, 33(3), 477–486.

Nishiguchi, S., Kato, H., Fujita, H., Oka, M., Kim, H., Kokubo, T., and Nakamura, T. (2001). "Titanium metals form direct bonding to bone after alkali and heat treatments." *Biomaterials*, 22, 2525-2533.

Niu, W., Bai, C., Qiu, G., and Wang, Q. (2009). "Processing and properties of porous titanium using space holder technique." *Mater. Sci. Eng. A*, 506(1–2), 148–151.

Nouri, A., Hodgson, P. D., and Wen, C. (2011). "Effect of ball-milling time on the structural characteristics of biomedical porous Ti – Sn – Nb alloy." *Mater. Sci. Eng. C*, 31(5), 921–928.

Oh, I. H., Nomura, N., Masahashi, N., and Hanada, S. (2003). "Mechanical properties of porous titanium compacts prepared by powder sintering." *Scr. Mater*, 49(12), 1197–1202.

Ou, K. L., Weng, C. C., Lin, Y. H., and Huang, M. S. (2017). "A promising of alloying modified beta-type Titanium-Niobium implant for biomedical applications: Microstructural characteristics, in vitro biocompatibility and antibacterial performance." *J. Alloys Compd*, 697, 231–238.

Pattanayak, D. K., and Yamaguchi, S. (2011). "Effect of heat treatments on apatite-forming ability of NaOH- and HCl-treated titanium metal." *J Mater Sci: Mater Med*, 22, 273–278.

Prando, D., Brenna, A., Diamanti, M. V., Beretta, S., Bolzoni, F., Ormellese, M., and Pedefferri, M. P. (2018). "Corrosion of titanium: Part 2: Effects of surface treatments." *J. Appl. Biomater. Funct. Mater.*, 16(1), 3–13.

Raman, V., Tamilselvi, S., and Rajendran, N. (2007). "Electrochemical impedance spectroscopic characterization of titanium during alkali treatment and apatite growth in simulated body fluid." *Electrochim. Acta*, 52(26), 7418–7424.

Rao, X., Chu, C. L., and Zheng, Y. Y. (2014a). "Phase composition, microstructure, and mechanical properties of porous Ti-Nb-Zr alloys prepared by a two-step foaming powder metallurgy method." *J. Mech. Behav. Biomed. Mater*, 34, 27–36.

Ridzwan, M. I. Z., Shuib, S., Hassan, A. Y., Shokri, A. A., and Mohammad Ibrahim, M. N. (2007). "Problem of stress shielding and improvement to the hip implant designs: A review." *J. Med. Sci.*, 7(3), 460–467.

Rubshtein, a. P., Trakhtenberg, I. S., Makarova, E. B., Triphonova, E. B., Bliznets, D. G., Yakovenkova, L. I., and Vladimirov, a. B. (2014). "Porous material based on spongy titanium granules: Structure, mechanical properties, and osseointegration." *Mater. Sci. Eng. C*, 35(1), 363–369.

Ryan, G. E., Pandit, A. S., and Apatsidis, D. P. (2008). "Porous titanium scaffolds fabricated using a rapid prototyping and powder metallurgy technique." *Biomaterials*, 29(27), 3625–3635.

Ryan, G., Pandit, A., and Apatsidis, D. P. (2006). "Fabrication methods of porous metals for use in orthopaedic applications." *Biomaterials*, 27(13), 2651–2670.

Sasikumar, Y., and Rajendran, N. (2012). "Surface modification and in vitro characterization of Cp-Ti and Ti-5Al-2Nb-1Ta alloy in simulated body fluid." *J. Mater. Eng. Perform.*, 21(10), 2177–2187.

Singh, S., and Bhatnagar, N. (2018). "A survey of fabrication and application of metallic foams (1925–2017)." *J. Porous Mater.*, 25(2), 537–554.

Smorygo, O., Marukovich, a., Mikutski, V., Gokhale, a. a., Reddy, G. J., and Kumar, J. V. (2012). "High-porosity titanium foams by powder coated space holder compaction method." *Mater. Lett.*, 83, 17–19.

Sri Maha Vishnu, D., Sure, J., Liu, Y., Vasant Kumar, R., and Schwandt, C. (2019a). "Electrochemical synthesis of porous Ti-Nb alloys for biomedical applications." *Mater. Sci. Eng. C*, 96(October 2018), 466–478.

Srivastava, V. C., and Sahoo, K. L. (2007). "Processing, stabilization and applications of metallic foams. Art of science." *Mater. Sci. Pol.*, 25(3), 733–753.

Staiger, M. P., Pietak, A. M., Huadmai, J., and Dias, G. (2006). "Magnesium and its alloys as orthopedic biomaterials: A review." *Biomaterials*, 27(9), 1728–1734.

Ã, T. K., and Takadama, H. (2006). "How useful is SBF in predicting in vivo bone bioactivity? \$." *Biomaterials*, 27, 2907–2915.

Toptan, F. (2017). "Journal of the Mechanical Behavior of Biomedical Materials Tribocorrosion behavior of bio-functionalized highly porous titanium." *J. Mech. Behav. Biomed. Mater.*, 69, 144–152.

Torres-Sanchez, C., McLaughlin, J., and Fotticchia, A. (2018). "Porosity and pore size effect on the properties of sintered Ti35Nb4Sn alloy scaffolds and their suitability for tissue engineering applications." *J. Alloys Compd*, 731, 189–199.

Torres, Y., Lascano, S., Bris, J., Pavón, J., and Rodríguez, J. a. (2014a). “Development of porous titanium for biomedical applications: A comparison between loose sintering and space-holder techniques.” *Mater. Sci. Eng. C*, 37(1), 148–155.

Torres, Y., Pavón, J. J., and Rodríguez, J. a. (2012). “Processing and characterization of porous titanium for implants by using NaCl as space holder.” *J. Mater. Process. Technol.*, 212(5), 1061–1069.

Wang, C., Chen, H., Zhu, X., Xiao, Z., Zhang, K., and Zhang, X. (2017a). “An improved polymeric sponge replication method for biomedical porous titanium scaffolds.” *Mater. Sci. Eng. C*, 70, 1192–1199.

Wang, X., Li, Y., Xiong, J., Hodgson, P. D., and Wen, C. (2009). “Porous TiNbZr alloy scaffolds for biomedical applications.” *Acta Biomater*, 5(9), 3616–3624.

Wang, Y. Q., Tao, J., Zhang, J. L., and Wang, T. (2011). “Effects of addition of  $\text{NH}_4\text{HCO}_3$  on pore characteristics and compressive properties of porous Ti-10%Mg composites.” *Trans. Nonferrous Met. Soc. China*, 21(5), 1074–1079.

Wang, Z., Huang, W., Li, Y., He, H., Zhou, Y., and Zheng, Z. (2017b). “Tribocorrosion behaviour of a biomedical Ti-25Nb-3Mo-3Zr-2Sn alloy in Ringer’s solution.” *Mater. Sci. Eng. C*, 76, 1094–1102.

Wang, Z., Zhou, Y., Wang, H., Li, Y., and Huang, W. (2018). “Tribocorrosion behavior of Ti-30Zr alloy for dental implants.” *Mater. Lett*, 218, 190–192.

Wen, C. E., Mabuchi, M., Yamada, Y., Shimojima, K., Chino, Y., and Asahina, T. (2001). “Processing of biocompatible porous Ti and Mg.” *Scr. Mater*, 45(10), 1147–1153.

Wen, C. E., Yamada, Y., Shimojima, K., Chino, Y., Asahina, T., and Mabuchi, M. (2002). “Processing and mechanical properties of autogenous titanium implant

materials.” *J Mat Sci: Mater in Med*, 13, 397–401.

Wen, M., Wen, C., Hodgson, P., and Li, Y. (2014). “Fabrication of Ti-Nb-Ag alloy via powder metallurgy for biomedical applications.” *Mater. Des.*, 56, 629–634.

Wu, S., Liu, X., Yeung, K. W. K., Liu, C., and Yang, X. (2014). “Biomimetic porous scaffolds for bone tissue engineering.” *Mater. Sci. Eng. R Reports*, 80, 1–36.

Xie, F., He, X., Lv, Y., Wu, M., He, X., and Qu, X. (2015). “Selective laser sintered porous Ti–(4–10) Mo alloys for biomedical applications : Structural characteristics , mechanical properties and corrosion behaviour.” *Corros. Sci*, 95, 117–124.

Xiong, J., Li, Y., Wang, X., Hodgson, P., and Wen, C. (2008a). “Mechanical properties and bioactive surface modification via alkali-heat treatment of a porous Ti-18Nb-4Sn alloy for biomedical applications.” *Acta Biomater*, 4(6), 1963–1968.

Xiong, J. Y., Li, Y. C., Wang, X. J., Hodgson, P. D., and Wen, C. E. (2008b). “Titanium-nickel shape memory alloy foams for bone tissue engineering.” *J. Mech. Behav. Biomed. Mater*, 1(3), 269–273.

Xu, W., Lu, X., Zhang, B., Liu, C., Lv, S., Yang, S., and Qu, X. (2018). “Effects of porosity on mechanical properties and corrosion resistances of PM-fabricated porous Ti-10Mo Alloy.” *Metals (Basel)*, 8(3), 1–13.

You, D., Wang, Y., Yang, C., and Li, F. (2020). “Comparative analysis of the hot-isostatic-pressing densification behavior of atomized and milled Ti6Al4V powders.” *J. Mater. Res. Technol*, 9(3), 3091–3108.

Yu, T., Jiang, F., Wang, C., Cao, M., Wang, Z., Chang, Y., and Guo, C. (2019). “Investigation on Fabrication and Microstructure of Ti–6Al–4V Alloy Hollow Spheres by Powder Metallurgy.” *Met. Mater. Int*, 27, 1083–1091.

Yue-qin, W., Jie, T. A. O., Jin-long, Z., and Tao, W. (2010). “Effects of addition of  $\text{NH}_4\text{HCO}_3$  on pore characteristics and compressive properties of porous Ti-10 % Mg composites.” *Trans. Nonferrous Met. Soc. China*, 21(5), 1074–1079.

Zhang, L., He, Z. Y., Tan, J., Calin, M., Prashanth, K. G., Sarac, B., Völker, B., Jiang, Y. H., Zhou, R., and Eckert, J. (2017). “Designing a multifunctional Ti-2Cu-4Ca porous biomaterial with favorable mechanical properties and high bioactivity.” *J. Alloys Compd*, 727, 338–345.

Zhao, D., Chang, K., Ebel, T., Nie, H., Willumeit, R., and Pyczak, F. (2015). “Sintering behavior and mechanical properties of a metal injection molded Ti – Nb binary alloy as biomaterial.” *J. Alloys Compd*, 640, 393–400.

## List of Publications based on PhD Research Work

Sl. no.	Title of the paper	Authors (in the same order as in the paper. Underline the Research Scholar's name)	Name of the Journal/Conference / Symposium, Vol., No., pages	Month & Year of Publication	Category*
1	Tribocorrosion Behaviour of Biomedical Porous Ti-20Nb-5Ag Alloy in Simulated Body Fluid	<u>Shivaram M J</u> , S.B Arya, Jagannath Nayak, Bharat B Panigrahi	Journal of Bio-and Tribo-Corrosion 7, (2) 1-9	March, 2021	1
2	Development and characterization of biomedical porous Ti-20Nb-5Ag alloy: Microstructure, mechanical properties, Surface bioactivity and Cell viability studies	<u>Shivaram M J</u> , S.B Arya, Jagannath Nayak, Bharat B Panigrahi	Metals and Materials International 1-11	Jan, 2021	1
3	Electrochemical corrosion and Impedance studies of porous Ti-xNb-Ag alloy in physiological solution"	<u>Shivaram M J</u> , S.B Arya, Jagannath Nayak, Bharat B Panigrahi	Trans Indian Inst Met 73, (4) 921-928	Feb, 2020	1
4	Role of porosity on electrochemical corrosion behavior of porous Ti-20Nb-5Ag alloy in simulated body fluid	<u>Shivaram M J</u> , S.B Arya, Jagannath Nayak, Bharat B Panigrahi	Materials Today: proceedings 33, 5257-5261	February, 2021	3
5	Influence of Ball Milling Time on Mechanical Properties of Porous Ti-20Nb-5Ag Alloy	<u>Shivaram M J</u> , S.B Arya, Jagannath Nayak, Bharat B Panigrahi	International Journal of Materials and Metallurgical Engineering 11 (9) 677-680	Jan, 2018	3

\*Category: 1: Journal paper, full paper reviewed  
 2: Journal paper, Abstract reviewed  
 3: Conference/Symposium paper, full paper reviewed  
 4: Conference/Symposium paper, abstract reviewed  
 5: others (including papers in Workshops, NITK Research Bulletins, Short notes etc.)

(If the paper has been accepted for publication but yet to be published, the supporting documents must be attached.)

Research Scholar



Shivaram M J, 28-10-2021

Name & Signature, with Date.

Research Guide(s)

Dr. Shashi Bhushan Arya

Prof. Jagannath Nayak

Name & Signature, with Date.

# Curriculum Vitae

**Mr. SHIVARAM M.J.**



**Contact Details:**

Near Railway Gate, Mallasandra  
Mallasandra (Po), Tumkuru (Tq)  
Tumkuru (Dist), Karnataka- 572107

**Email-ID:** [shivumj135@gmail.com](mailto:shivumj135@gmail.com), [shivaram.mt14f08@nitk.edu.in](mailto:shivaram.mt14f08@nitk.edu.in)

**Phone Number :** 9620305766

University	National Institute of Technology Karnataka, Surathkal Mangalore 575025, India
Personal Web Sites	<a href="https://mme.nitk.ac.in/student/shivaram-m-j">https://mme.nitk.ac.in/student/shivaram-m-j</a> <a href="https://orcid.org/0000-0003-4327-5699">https://orcid.org/0000-0003-4327-5699</a> <a href="https://scholar.google.com/citations?hl=en&amp;user=t9Nia5AAAAAJ&amp;Shivaram%20MJ">https://scholar.google.com/citations?hl=en&amp;user=t9Nia5AAAAAJ&amp;Shivaram%20MJ</a>
Research Expertise	Metallic materials, Powder metallurgy, Porous biomaterials, Corrosion Engineering.

### **Educational Qualification:**

- **Ph.D.** on Title: “**Development of porous Ti-Nb-Ag alloy through powder metallurgy for biomedical application**” from **National Institute of Technology Karnataka, Surathkal India.**
- **M. Tech in Manufacturing Science and Engineering** form **MSRIT**, Bangalore, Visveswaraiah Technological University, Karnataka. (Completed 2013) (First class with distinction)
- **B.E In Mechanical Engineering** From **SSIT**, Tumakuru, Visveswaraiah Technological University, Karnataka (Completed 2011) (First class with distinction)

### **Profession experience – 6.5 year**

- Worked as Assistant professor in Nagarjuna College of Engineering Technology, Bangalore (August-2013 to July 2014)
- Worked as Research Scholar in National Institute of Technology Karnataka, Surathkal (2014 to 2021)

### **Awards and achievements:**

- Received “**Best Research Award**” from the International Research Awards on New Science Inventions.
- Received “**Student Project Programme**” **Karnataka State Council for Science & Technology (KSCST) funding** for carry out the project entitle “**Manually operated Areca nut cutting machine**” at SSIT, Tumkuru (2011), under the scheme for Bachelor of Engineering.



- Received “**Rajya Puraskar award**” from **Bharat Scouts & Guides** (Government of Karnataka 2004).

#### Recent Journal Publications:

- **M. J Shivaram, S. B Arya, Jagannath Nayak, Barat .B Panigrahi** “Tribo-corrosion behaviour of biomedical porous Ti-20Nb-5Ag alloy in simulated body fluid” **Journal of Bio and Tribo-corrosion (2021)**.
- **M. J Shivaram, S. B Arya, Jagannath Nayak, Barat .B Panigrahi** “Development and characterization of biomedical porous Ti–20Nb–5Ag alloy: Microstructure, mechanical properties, Surface bioactivity and Cell viability studies” **Metals and Materials International (2021)**.
- **M. J Shivaram, S. B Arya, Jagannath Nayak, Barat .B Panigrahi** “Electrochemical corrosion and Impedance studies of porous Ti- xNb-Ag alloy in physiological solution” **Trans Indian Inst Met (2020)**.
- **M. J Shivaram, S. B Arya, Jagannath Nayak, Bharat .B Panigrahi** “Role of porosity on electrochemical corrosion behavior of porous Ti-20Nb-5Ag alloy in simulated body fluid” **Materials Today: proceedings (2020)**.
- **M. J Shivaram, S. B Arya, Jagannath Nayak, Bharat .B Panigrahi** “Influence of Ball Milling Time on Mechanical Properties of Porous Ti-20Nb-5Ag Alloy. **International Journal of Materials and Metallurgical Engineering (2018)** 11 (9), 677-680.
- Ramesh, H Shivananda Nayaka, Sandeep Sahu, K R Gopi, **M. J Shivaram, Shashibhushan Arya** “Influence of Multiaxial Cryoforging on Microstructural, Mechanical, and Corrosion Properties of Copper-Titanium Alloy” **Journal of Materials Engineering and Performance (2019)** 28 (12), 7629-7641.

#### Conference attended:

- International Conference on “**Powder Metallurgy and Particulate Technology**” (IPMPC-19), at Paris, France from 21-24<sup>th</sup> September 2017.
- The International Symposium on "Light weighting for Defence and Transportation" [NMD-ATM], “**BITS Pilani**”, KK Birla Goa campus from 11-14<sup>th</sup> November 2017.
- The 6<sup>th</sup> **Asian Biomaterials Congress, Sree Chitra Tirunal Institute for Medical Science & Technology, Thiruvananthapuram, India** from 25-27<sup>th</sup> October 2017.
- National conference on “**Tribology: Energy, Environment and Efficiency**” at **CSIR-Advance materials and Processes Research Institute, Bhopal, India** during 21-22<sup>nd</sup> Jan, 2016.

- International Conference on “**Advance Materials, Manufacturing, Management and Thermal Sciences**” (AMMMT 2013) at SIT, Tumkuru, from 3<sup>rd</sup> to 4<sup>th</sup> May 2013.
- International Conference on “**Industrial Tribology**”, IndiaTrib-19, Auditorium, **IISc, Bangalore**, India 1-4<sup>th</sup> Dec 2019.
- International Conference on “**Processing and Characterization of Materials, ICPCM-2019**”, at **NIT-Rourkela**, Odisha, India.12-14 December-2019.
- International conference on Emerging Smart Materials in Applied Chemistry [ESMAC-2020], 10<sup>th</sup>-12<sup>th</sup> August-2020, held at KIIT, Bhubaneswar, Odisha, India.

#### Workshop attended:

- Materials in Advanced Applications and Products” during 11-15 July 2016, at National Institute of Technology Karnataka, Surathkal, Mangaluru.
- NRC-M workshop on Advances in Corrosion Engineering, 22-24, Dec 2014. Organized by Dept. of Materials Engineering at IISc Bangalore.
- Material Processing and Degradation, 17-18, Oct 2016 organized by Dept. of MME, NITK Surathkal.
- Material Charecterisation 12-15 July 2016 at IIT Madras, Chennai.
- Engineering Failure Analysis Aug, 1-2, 2014, organized by Dept. of MME, NITK Surathkal.

#### Personal profile:

Date of Birth : 13<sup>th</sup> May 1990  
 Father’s name : Jayaramaiah  
 Mother’s name : Jayamma H.H  
 Nationality : Indian  
 Community : Hindu  
 Gender : Male  
 Marital Status : Single  
 Languages known : English, Kannada, Hindi, Telugu

#### Declaration:

I do hereby affirm that the information furnished above is true to the best of my knowledge.

**Date:** / / 2020

**Place:**



(SHIVARAM M.J)

**Reference :**

Dr. Shashi Bhushan Arya (Ph.D. Supervisor)  
Assistant Professor,  
Department of Metallurgical and Materials Engineering  
NITK Surathkal Mangalore-575025  
Email: [sbarya@nitk.edu.in](mailto:sbarya@nitk.edu.in) Phone no: 8762526500

Dr. Jagannath Nayak (Ph.D. Supervisor)  
Professor, (Dean Student welfare)  
Department of Metallurgical and Materials Engineering  
NITK Surathkal Mangalore-575025  
Email: [jaganmet@gmail.com](mailto:jaganmet@gmail.com) Phone no: 9900711945

Dr. Bharat B Panigrahi  
Professor,  
Department of Materials science and Metallurgical Engineering  
IIT Hyderabad, Telangana-502285  
Email: [barat@iith.ac.in](mailto:barat@iith.ac.in) Phone no: 9441369039